ELECTRONIC STRUCTURE OF ORGANIC MOLECULES CONTAINING TRANSITION-METAL ATOMS

A Thesis Submitted to
the Graduate School of Engineering and Sciences of
İzmir Institute of Technology
in Partial Fulfillment of the Requirements for the Degree of

DOCTOR OF PHILOSOPHY

in Physics

by
Zafer KANDEMİR

July 2019
İZMİR

We approve the thesis of **Zafer KANDEMİR**

Examining Committee Members:

_____
Prof. Dr. Nejat BULUT
Department of Physics, İzmir Institute of Technology

_____
Prof. Dr. Nuran ELMACI IRMAK
Department of Chemistry, İzmir Institute of Technology

_____
Assoc. Prof. Dr. A. Devrim GÜÇLÜ
Department of Physics, İzmir Institute of Technology

_____
Prof. Dr. Oğuz GÜLSEREN
Department of Physics, Bilkent University

_____
Prof. Dr. Sadamichi MAEKAWA
Center for Emergent Matter Science, RIKEN

9 July 2019

_____
Prof. Dr. Nejat BULUT
Supervisor, Department of Physics
İzmir Institute of Technology

_____   _____
Prof. Dr. Lütfi ÖZYÜZER   **Prof. Dr. Aysun SOFUOĞLU**
Head of the Department of   Dean of the Graduate School of
Physics   Engineering and Sciences

ACKNOWLEDGMENTS

ABSTRACT

ELECTRONIC STRUCTURE OF ORGANIC MOLECULES CONTAINING TRANSITION-METAL ATOMS

Hemoglobin including iron atom, vitamin B_{12} containing cobalt atom and ruthenium-based dye molecules are examples of organic molecules. We explore whether electron correlations arising from transition-metal atoms have any special role in the functioning of organic molecules using the effective multi-orbital Anderson model. We choose deoxy and oxy-heme molecules which are examples of hemoglobin derivatives because they have many experimental and theoretical studies. The experimental magnetic susceptibility measurements find that deoxy and oxy-heme molecules exhibit a high-spin to low-spin transition. We use four different computational methods: density functional theory (DFT), DFT+U, DFT+mean-field approximation (DFT+MFA) and DFT+quantum Monte Carlo (DFT+QMC) to study this transition. In this thesis, we compare the results of these methods with each other and the experimental results. DFT and DFT+U methods do not yield the high-spin state for deoxy-heme. DFT method correctly does not find the location of impurity bound state (IBS) known as correlated new electronic states. These methods obtain low-spin for oxy-heme, but they find that magnetic correlations are very small. DFT+MFA works well for high-spin, but this technique does not obtain low-spin because it does not find the location of IBS correctly. DFT+QMC gives the high(low)-spin state for deoxy-heme (oxy-heme) and finds IBS and magnetic correlations. We obtain that DFT+QMC works better among these methods for deoxy and oxy-heme molecules. Moreover, we investigate whether we can observe the IBS and magnetic correlations for vitamin B_{12}, dye molecules and single-atom catalysts by using these computational approaches.

ÖZET

GEÇİŞ ELEMENTİ İÇEREN ORGANİK MOLEKÜLLERİN ELEKTRONİK YAPISI

Demir atomu içeren hemoglobin, kobalt atomu içeren vitamin B_{12} ve rutenyum-bazlı boya molekülleri organik moleküllere örnektir. Geçiş-metali atomlarından kaynaklanan elektron korelasyonlarının, etkin çok-orbitalli Anderson modelini kullanarak organik moleküllerin işleyişinde özel bir rolü olup olmadığını araştırıyoruz. Hemoglobin türevlerinin örnekleri olan deoksi ve oksi-hem moleküllerini, birçok deneysel ve teorik çalışmaları olduğu için seçtik. Deneysel manyetik duyarlılık ölçümleri, deoksi ve oksi-hem molekülleri yüksek-spinden düşük-spine geçiş sergilediğini tespit eder. Bu geçişi çalışmak için dört farklı hesapsal metot kullandık: yoğunluk fonksiyonel teorisi (YFT), YFT+U, YFT+ortalama-alan yaklaşımı (YFT+OAY) ve YFT+kuantum Monte Carlo (YFT+KMC). Bu tezde, bu yöntemlerin sonuçlarını birbirleri ile ve deneysel sonuçlarla karşılaştırıyoruz. YFT ve YFT+U metotları deoksi için yüksek-spin durumunu vermiyor. YFT metodu, korelasyonlu yeni elektronik durum olarak bilinen safsızlık bağıl durumunun (SBD) yerini doğru şekilde bulamaz. Bu metotlar oksi-hem için düşük-spini elde eder, fakat manyetik korelasyonların çok küçük olduğunu bulurlar. YFT+OAY, yüksek-spin için çok iyi çalışır, ancak SBD'nin yerini doğru şekilde bulamadığı için düşük-spin durumunu elde edemez. YFT+KMC, deoksi-hem (oksi-hem) için yüksek(düşük)-spin durumunu verir, ve SBD ve manyetik korelasyonları bulur. YFT+KMC'nin deoksi ve oksi-hem molekülleri için bu yöntemler arasında daha iyi çalıştığını elde ettik. Ayrıca, bu hesapsal yaklaşımları kullanarak vitamin B_{12}, boya molekülleri ve tek-atom katalizörleri için SBD ve manyetik korelasyonları gözlemleyip gözlemleyemeyeceğimizi araştırıyoruz.

TABLE OF CONTENTS

LIST OF FIGURES

LIST OF TABLES

LIST OF ABBREVIATIONS

A-HGNS : Armchair Edge - Hexagonal Graphene Nano Sheet

AF : Antiferromagnetic

CNHbA : Human Cyanomet Hemoglobin

COHbA : Human Carbonmonoxy Hemoglobin

DC : Double Counting

DeoxyHbA : Human Deoxyhemoglobin

DeoxyMb : Deoxymyoglobin

DFT : Density Functional Theory

Hb : Hemoglobin

HbA : Adult Human Hemoglobin

HOMO : Highest Occupied Molecular Orbital

IBS : Impurity Bound State

LUMO : Lowest Unoccupied Molecular Orbital

Mb : Myoglobin

MbCN : Cyanomet Myoglobin

MbCO : Carbonmonoxy Myoglobin

MFA : Mean-field Approximation

OxyHbA : Human Oxyhemoglobin

PDB : Protein Data Bank

QMC : Quantum Monte Carlo

CHAPTER 1

INTRODUCTION

Hemoglobin is a molecule containing transition metal atoms. There are various forms of hemoglobin, for example, deoxyhemoglobin and oxyhemoglobin. These molecules have four heme groups. Each heme group contains an iron (Fe) atom at its center. Oxy-heme is formed with the binding of oxygen molecule to the Fe atom of deoxy-heme molecule. The most important function of the heme molecules is to transport oxygen and carbon dioxide molecules in the blood. These molecules have been studied extensively both experimentally and theoretically due to their magnetic properties. In this thesis, we use the different computational methods to obtain the electronic and magnetic properties of the deoxy and oxy-heme molecules and we compare the results of these different computational methods with each other and the experimental data.

There are two main approaches for electronic structure calculations. The first approach is density functional theory (DFT). DFT is an approach that explains the ground state properties of many-body systems. Kohn and Sham showed ground state energy as a function of electron density. Kohn-Sham equations are a similar form of time independent Schrödinger equation. These equations describe independent particles moving within an effective potential. The other one is due to the Anderson model. This model divides a system into two parts: impurity and host. The impurity part indicates d orbitals of a transition-metal atom and the host part is the remaining orbitals. This model emphasizes the importance of Coulomb repulsions of d orbitals. For the first approach, we perform DFT and DFT+U calculations for deoxy and oxy-heme molecules. For the second approach, we perform DFT+MFA and DFT+QMC by using the effective Anderson impurity model for these molecules.

For deoxy and oxy-heme molecules, we have made various comparisons of the DFT and DFT+U results with the experimental results and computational results from the DFT+QMC and DFT+MFA techniques. From these comparisons, we find that the DFT and DFT+U do not give accurate results for the magnetic properties and electronic state of deoxy and oxy-heme.

There are many experimental works which examine the magnetic properties and spin-states of hemoglobin molecules. The hemoglobin molecule has the mechanism of high-spin to low-spin transition for transporting oxygen molecule. For example, four syn-

thesized deoxyhemoglobin molecules were studied with different temperatures by using Mössbauer spectroscopy (Hu et al. (2005)). It is observed that all synthesized molecules had 0.36 Å out of plane displacement of Fe atom from four nitrogen (N) plane and the spin-states of these models were found as the high-spin (Hu et al. (2005)). The magnetic susceptibilities were measured for deoxyhemoglobin and oxyhemoglobin (Pauling and Coryell (1936); Taylor and Coryell (1938); Alpert and Banerjee (1975)). From the measurement it was seen that deoxyhemoglobin had the high-spin state ($S=2$) (Pauling and Coryell (1936); Alpert and Banerjee (1975)) and each heme of deoxyhemoglobin had 5.46 Bohr magnetons (Pauling and Coryell (1936)) and oxyhemoglobin was diamagnetic (zero magnetic moment) and low-spin state ($S=0$) (Pauling and Coryell (1936); Pauling (1977); Cerdonio et al. (1977); Taylor and Coryell (1938)). The experimental measurements are observed that deoxyhemoglobin has the high-spin state ($S=2$) and oxyhemoglobin is zero magnetic moment and has the low-spin state ($S=0$).

For deoxyhemoglobin and oxyhemoglobin molecules, theoretical calculations were carried out. Hu et al. observed experimentally that five-coordinate heme species have quintet-spin state (high-spin) (Hu et al. (2005)). Hu et al. said that for these heme species DFT calculation did not obtain this spin state and the DFT found as a triplet ground state (Hu et al. (2005)). Spin-states of these molecules by using the density functional theory plus Hubbard U term (DFT+U) method were obtained the high-spin and low-spin, respectively (Scherlis et al. (2007); Novoselov et al. (2016b)). Novoselov et al. obtained that the magnetic moment of the iron atom is 3.5 Bohr magnetons for deoxyHbA and the magnetic moment of the iron atom is 1.5 Bohr magnetons for oxyHbA. While the Hartree-Fock method found the high-spin (quintuplet state) configuration for hemoglobin models (FePIm and FePImO$_2$), the DFT method obtained the triplet and singlet states, respectively (Scherlis et al. (2007); Scherlis and Estrin (2002); Smith et al. (2005)). Besides, Novoselov et al. (2016a) used a combination of density functional theory and dynamical mean-field theory (DFT+DMFT) to describe the variation of the effective spin moment of the Fe atom and produced the spin-state transition from the high-spin to low-spin state in this method. In addition to the DFT method, charge states and transition spin-states of Fe atom in a hemoprotein were studied within the extended Haldane-Anderson (Haldane and Anderson (1976)) model by using unrestricted Hartree-Fock approximation (Yamauchi et al. (2003)). It is shown that multiple charge states and transition from the high-spin to low-spin states are described by this method (Yamauchi et al. (2003)). However, this Anderson model Hamiltonian is not similar to our Hamiltonian.

The density functional theory (DFT) and DFT plus Hubbard U (DFT+U) methods

have been used to study the hemoglobin molecules in many previous theoretical works. These methods find the triplet (S=1) state for the spin state of the deoxy-heme and find the open-shell singlet (S=0) state for the spin state of the oxy-heme molecule. According to the experimental results, the deoxy-heme has high (S=2) spin, and oxy-heme has low (S=0) spin. The DFT and DFT+U methods do not find the high (S=2) spin state for the deoxy-heme molecule. Even if these methods find the low spin state for oxy-heme, they do not find the magnetic moment formations and magnetic correlations as found experimentally. Besides, the DFT method does not find the location of impurity bound state (IBS) correctly which is known as correlated new electronic states with magnetic characteristics for the deoxy and oxy-heme molecules. The IBS plays an important role in determining the magnetic properties of these molecules. Therefore, we find that the DFT and DFT+U do not give accurate results for the magnetic properties and electronic state of deoxy and oxy-heme molecules. Even if we use the different basis sets and energy functionals in our DFT calculations, we can not find the location of IBS correctly, magnetic moment formations and magnetic correlations. Thus, we observe that the DFT method alone does not work for these molecules.

For that reason, we use combined the DFT method plus mean-field approximation (DFT+MFA) to determine the spin-states and magnetic properties of the deoxy and oxy-heme molecules. The DFA+MFA method works very well for the deoxy-heme molecule. This method finds high spin (S=2) for the spin state of deoxy-heme. We find that the IBS of deoxy-heme is below the highest occupied molecular orbital (HOMO) and the IBS is occupied by electrons. This method finds the magnetic moment formation and magnetic correlations for deoxy-heme. The DFT+MFA method does not obtain exactly the IBS of oxy-heme because oxy-heme has the low-spin state. The DFT+MFA method works very well with molecules having high spin, but it does not give correct results for low-spin. In this way, the DFT+MFA method does not work for the oxy-heme while it works very well for the deoxy-heme.

In addition, we use combined the DFT plus quantum Monte Carlo (DFT+QMC) to work out the spin state of the oxy-heme. We find that the spin state of oxy-heme is low from the DFT+QMC method. The IBS of oxy-heme is above the HOMO level and it is unoccupied. Moreover, the DFT+QMC method finds that the spin state of deoxy-heme is high and the IBS is below the HOMO level and occupied by electrons. This method finds the magnetic moment formation and magnetic correlations for deoxy-heme and oxy-heme molecules. These results are consistent with the experimental results. The hemoglobin molecules have the mechanism of high-spin to low-spin transition in experimental results

(Pauling and Coryell (1936); Alpert and Banerjee (1975)). We obtain this mechanism with the DFT+QMC results (Mayda (2019)). We investigate whether we can obtain these results from the DFT, DFT+U and DFT+MFA methods. We want to compare the results of these methods.

If a system contains magnetic moments and magnetic correlations as in deoxy and oxy-heme molecules, we observe that the DFT method does not work well. The DFT method does not take into account the Hund interactions for d orbitals of transition metal atom. If the DFT method is improved these interactions one by one, it will be able to obtain the DFT+QMC results. Then, the DFT method can be used much more widely. For these reasons, the DFT+QMC method can be used for organic molecules instead of using the DFT method alone.

The IBS, magnetic moments and magnetic correlations are not only found in the hemoglobin molecule but also the vitamin B_{12}, Ru-based dye molecules and single-atom catalysts. We think that IBS plays an important role in the hemoglobin molecules. In the same way, we consider that this situation is valid for the other molecules.

1.1. Background of bioinorganic molecules

Metalloproteins and metalloenzymes are bioinorganic molecules which contain transition metal elements. The metal atom in these molecules is usually surrounded by the nitrogen, carbon and oxygen atoms. These molecules play an important role in the chemical reactions in all organisms. Hemoglobin, myoglobin, and vitamin B_{12} can be given as examples for metalloproteins and metalloenzymes. Hemoglobin (Hb) molecule has four heme groups and $\alpha - \beta$ globins. Each heme group consists of a porphyrin ring which contains an iron (Fe) atom. The most important function of the Hb molecule is to transport oxygen and carbon dioxide molecules by binding to Fe atom in the blood. Myoglobin (Mb) has a heme group and contains only one Fe atom as its active center. The Mb is a complex muscle protein that undertakes the task of storing oxygen in the muscles. Vitamin B_{12} is the metalloenzyme which contains a cobalt (Co) atom. It plays an essential role in the production of red blood cells and the functioning of the nervous system and the brain.

Bioinorganic molecules also contain the molecules that are synthesized artificially and have a transition metal atom at their active sites. Ru-based dye molecules are an example of this kind of biological molecules. The molecular structure of the Ru-based dye molecules is similar to the metalloproteins and metalloenzymes. They contain transition

metal atom which is surrounded with the nitrogen and carbon atoms.

Dye molecule is one of the essential parts of dye-sensitized solar cells (DSSCs). In DSSCs, the dye molecule is attached to the semiconductor layer (e.g. TiO_2). The main function of the dye molecule is to provide an electron to the semiconductor layer. When the light hits the dye molecules, the electrons are excited. The electrons leave the dye molecule and reach the surface of the semiconductor layer. The excited state of the dye molecule is reduced again by a redox couple in the electrolyte. The dye molecule regains its lost electrons and thus it continues to run. The studies on sensitizing dyes show that the best results are given by ruthenium-based dyes. Ru-based dye molecules are often preferred because they are well-stimulated by visible and near-infrared spectra of sunlight (Ayalew and Ayele (2016); Hao et al. (2006); Mikroyannidis et al. (2010)). Generally Ru-based dye molecules are used to increase the efficiency of solar cells.

Single-atom catalysts (SAC's) belong to a very important class of artificial catalysts. In recent years, the SAC's have attracted much attention because of their important roles in many chemical reactions such as oxygen reduction reaction and carbon dioxide reduction. SAC's contain transition metal atom at their active sites as in bioinorganic molecules.

Bioinorganic and Ru-based dye molecules and SAC's exhibit an energy gap and contain a transition metal. With these electronic properties, they are similar to diluted magnetic semiconductors. In these materials, transition metal impurities are substituted in a semiconducting host. For example, (Ga,Mn)As is obtained by substituting Mn atoms instead of Ga atoms in GaAs semiconductor. These materials exhibit interesting physical properties. An impurity bound state (IBS), which is a sharp resonant state in the single-particle spectrum, exists 110 meV above the top of the valence band in the semiconducting gap (Jungwirth et al. (2007)). The impurity bound state consists of spectral weight from both the Mn impurity and the host. Calculations performed by using the Haldane-Anderson model show that this new electronic state is important in determining the electronic and magnetic properties of (Ga,Mn)As (Bulut et al. (2007); Tomoda et al. (2009); Ichimura et al. (2006)). Especially, long-range ferromagnetic correlations exist among Mn impurities when the chemical potential is located between the top of the valence band and IBS. When the IBS are occupied by electrons these correlations disappear rapidly.

Bioinorganic and Ru-based dye molecules and SAC's have similar electronic structures with the diluted magnetic semiconductor materials. They have an impurity bound state. Whether the IBS is occupied, plays a significant role in determining the magnetic

and electronic properties of these molecules.

1.2. Comparison of various computational approaches to the electronic structure of bioinorganic molecules

Here, we compare different theoretical approaches to calculate the electronic structure of bioinorganic molecules containing transition-metal atoms. As an example, we study the electronic and magnetic properties of an adult human hemoglobin (HbA). We choose the HbA because there are many experimental results for this molecule. The HbA is divided into two species known as deoxyhemoglobin (deoxyHbA) and oxyhemoglobin (oxyHbA). We use the experimental atomic coordinates of deoxy-heme and oxy-heme molecules which are obtained by X-ray diffraction. We take these molecules from the Protein Data Bank (PDB) with key 2DN2 (Park et al. (2006)) and 2DN1 (Park et al. (2006)), respectively. The hemoglobin molecule consists of four heme groups: two alpha groups and two beta groups. We examine α_1 heme group for both deoxy-heme and oxy-heme molecules. We have explained this procedure in more detail in Chapter 2.

In this thesis, we use the DFT+QMC, DFT+MFA, DFT, and DFT+U methods to study the mechanism of high-spin to low spin transition in the deoxy and oxy-heme molecules. We will compare the results of these methods with each other and the experimental data.

Here, we first study the electronic and magnetic properties of the deoxy-heme and oxy-heme molecules by using the DFT+QMC method. We use the extended multi-orbital Anderson model in this method. We explain this model in Section 1.5. The parameters of the Anderson model are obtained with the DFT calculations. The DFT calculation is carried out by using BP86 exchange-correlation energy functional and 6-31G basis set with the Gaussian program (Frisch et al. (2009)).

Secondly, we calculate the extended multi-orbital Anderson model by combining the DFT and quantum Monte Carlo (DFT+QMC) to determine the spin-states and magnetic properties of deoxy and oxy-heme molecules. In DFT+QMC results, impurity bound state (IBS) known as a new electronic state was found for deoxy and oxy-heme molecules. The IBS plays an important role in determining the magnetic properties of these molecules. We observed that IBS of deoxy-heme is below the highest occupied molecular orbital (HOMO) level and it is occupied by electrons. The spin state of deoxy-heme is a high-spin. IBS of oxy-heme is above the HOMO level and it is unoccupied. The

spin state of oxy-heme is a low-spin. Besides, we obtain the magnetic moment formation and antiferromagnetic correlations for these heme molecules. We will show whether we obtain these results with the DFT+MFA, DFT and DFT+U methods.

Then, we solve the extended multi-orbital Haldane-Anderson model by combining the DFT plus mean-field approximation (DFT+MFA) to determine the spin-states and magnetic properties of these heme molecules. We obtain the same results for deoxy-heme with the DFT+MFA technique, but we don't find a low-spin state for oxy-heme. In DFT+MFA, the IBS is found below the HOMO level for these heme molecules. Thus, the DFT+MFA technique gives accurate results for molecules having only a high-spin state.

With the DFT method, we find that the ground state energy of deoxy-heme is the triplet state (S=1) and the ground state energy of oxy-heme is the open-shell singlet state (S=0). We don't find a high-spin state for deoxy-heme molecule because the location of IBS is above the Fermi level. Although we obtain that the spin state of the oxy-heme is a low-spin with the DFT method, we don't find the IBS. Besides, the values of the magnetic moments of oxy-heme are very smaller than obtaining other methods. Thus, we see that the DFT is not a sufficient method alone.

In addition, we perform the DFT+U method for deoxy and oxy-heme molecules. We find only magnetic moment formation of heme molecules and we don't obtain the parameters of the Anderson model from the DFT+U method. Spin states of deoxy-heme and oxy-heme for the DFT+U is triplet and singlet state, respectively, but the contributions of the magnetic moment are very weak.

In summary, for deoxy and oxy-heme molecules the DFT+QMC is the best method which is obtained the mechanism of high-spin to low-spin transition.

1.3. Electronic correlations in bioinorganic molecules and single-atom catalysts

Like deoxy and oxy-heme molecules, other bioinorganic molecules contain transition metal atoms at their center and surrounded by nitrogen atoms. For example, vitamin B_{12} and Ru-based dye molecules. In addition, we study single-atom catalysts which have attracted much attention due to their essential roles in many chemical reactions such as oxygen or carbon dioxide reduction reactions. SAC's contain transition metal atom at their active sites as bioinorganic molecules. We study the electronic properties of transition metal adatom on graphene systems as an example for SAC's. We investigate whether

we can observe the IBS, magnetic moment formations and antiferromagnetic correlations for these molecules.

In this thesis, we study the electronic and magnetic properties of the deoxy and oxy-heme molecules, the cyanocobalamin (CNCbl) molecule which is a cofactor of the vitamin B_{12} and Ru-based dye molecules as an example for bioinorganic molecules. In addition, we also study the electronic properties of the transition metal adatom on graphene systems as an example for SAC's. We use four different methods: DFT+QMC, DFT+MFA, DFT and DFT+U in order to obtain the electronic and magnetic properties of these models.

1.4. What is the impurity bound state?

Impurity bound state (IBS) is known as the correlated new electronic state. The IBS plays an important role in determining the magnetic properties of a system. Haldane and Anderson examined the electronic properties of gold (Au(5d)) impurity atom in germanium (Ge) semiconductor host. They observed impurity bound states in the semiconductor energy gap by using Hartree-Fock mean-field solution. The impurity bound states correspond to new quantum mechanical electronic states. They used the single-orbital Anderson model. This model emphasizes the importance of Coulomb repulsion of the d orbitals. The single-orbital Anderson model is defined by

$$
\begin{aligned}
H &= \sum_{m,\sigma}(\varepsilon_m - \mu)c_{m\sigma}^\dagger c_{m\sigma} + \sum_\sigma (\varepsilon_d - \mu)d_\sigma^\dagger d_\sigma \\
&+ \sum_{m,\sigma}(V_{md}c_{m\sigma}^\dagger d_\sigma + V_{md}^* d_\sigma^\dagger c_{m\sigma}) \\
&+ U n_{d\uparrow}n_{d\downarrow}
\end{aligned} \tag{1.1}
$$

where $d_\sigma^\dagger$ (d_σ) is the creation (annihilation) operator for impurity atom with spin $\sigma = \uparrow$, $\downarrow$. The electron number operator of impurity atom is $n_{d\sigma} = d_\sigma^\dagger d_\sigma$. $c_{m\sigma}^\dagger$ ($c_{m\sigma}$) creates (annihilates) an electron in host states m with spin σ. Here, ε_d and ε_m are the energies of the impurity and host atoms, respectively.

Magnetic properties of a system critically depend on whether the IBS is occupied by electrons or not. We explain this situation in Fig. 1.1. We are going to discuss the single-orbital Anderson model for semiconductor host. The red line indicates IBS energy. IBS exists in the semiconductor gap. The chemical potential μ is larger than the IBS en-
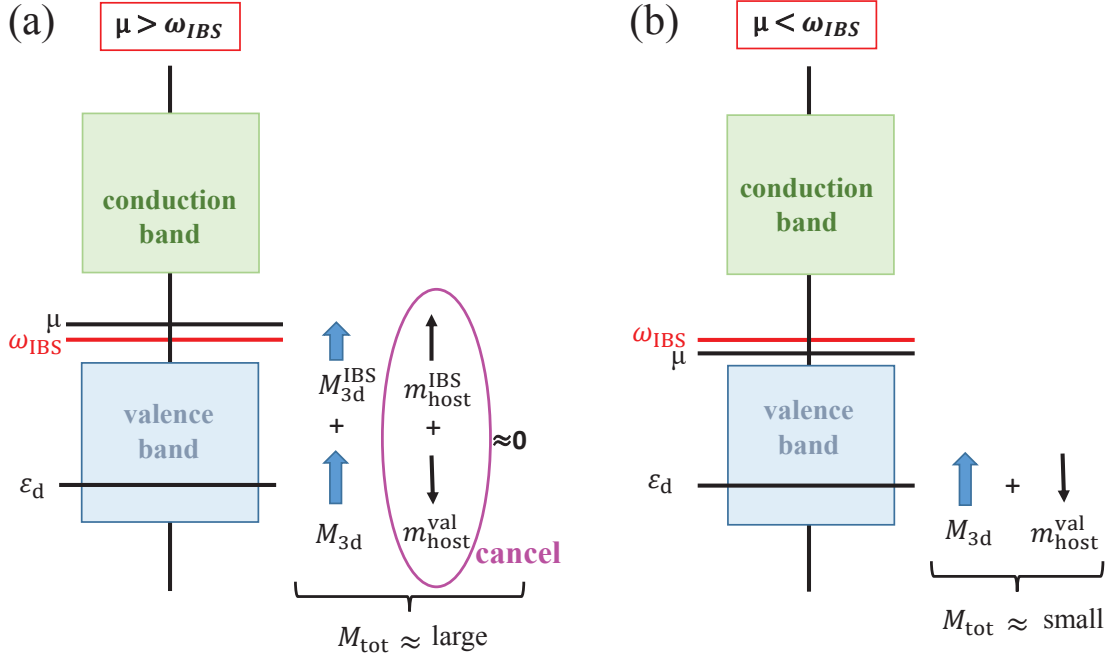
Figure 1.1. The existence of impurity bound state (IBS) in semiconductor energy gap for single-orbital Anderson model. (a) if the chemical potential μ is larger than the frequency of IBS, the IBS is occupied by electrons. Anti-ferromagnetic correlation occurs between host electrons in valence band and host bound states in energy gap, so they cancel each other. Total magnetic moment of this system is large because of strong ferromagnetic correlations formed between 3d orbitals. (b) if the chemical potential μ is less than the frequency of IBS, the IBS is unoccupied. Ferromagnetic correlations between the $3d$ orbitals are destroyed by antiferromagnetic correlations between $3d$ and host electrons. Total magnetic moment of this system is small.

ergy as shown in Fig. 1.1 (a). Here, $3d$ electrons have strong ferromagnetic correlations in the valence band. Impurity bound states (IBS's) of $3d$ electrons also have strong ferromagnetic correlations in the energy gap. Anti-ferromagnetic correlation occurs between host electrons in the valence band and host bound states in the energy gap, so they cancel each other. Thus, the total magnetic moment of host states becomes zero. Due to strong ferromagnetic correlations formed between $3d$ orbitals, a molecule has a high magnetic moment. When the chemical potential μ is above the IBS, the IBS is occupied by electrons. The chemical potential μ is less than the IBS energy as shown in Fig. 1.1 (b). Here, anti-ferromagnetic correlations occur between $3d$ and host electrons. Ferromagnetic correlations between the 3d orbitals are destroyed by antiferromagnetic correlations between $3d$ and host electrons. Thus, a molecule has a low magnetic moment. In addition, when

the chemical potential μ is below the IBS, the IBS is unoccupied.

In this thesis, we use DFT, DFT+U, DFT+MFA and DFT+QMC methods to study IBS. Which methods find IBS correctly? In the following chapters, we will show how to detect IBS with these methods. We are going to concentrate on deoxy and oxy-heme molecules to determine whether these methods give accurate results. We will compare the results of these methods with each other and the experimental data. We try to determine which one works best. We explain what these methods are in Appendix A.

1.5. Extended multi-orbital Anderson Hamiltonian

We study the electronic structures of the deoxy and oxy heme molecules, cyanocobalamin (CNCbl) molecule which is a cofactor of the vitamin B_{12} and Ru-based (e.g. N719 and Z907) dye molecules as an example for bioinorganic molecules. In addition, we also study the electronic structures of the transition metal adatom on graphene systems as an example for single-atom catalysts. We work the electronic structures of these molecules by using the Anderson model. For this purpose, we plan the electronic structures of these molecules on the multi-orbital Anderson model by making use of the density functional theory (DFT).

The extended multi-orbital Anderson Hamiltonian Haldane and Anderson (1976) with the inter and intra-orbital Coulomb interactions is defined by

$$
\begin{aligned}
H \;=\; & \sum_{m,\sigma}(\varepsilon_m - \mu)c_{m\sigma}^{\dagger}c_{m\sigma} + \sum_{\nu,\sigma}(\varepsilon_{d\nu} - \mu)d_{\nu\sigma}^{\dagger}d_{\nu\sigma} \\
& + \sum_{m,\nu,\sigma}(V_{m\nu}c_{m\sigma}^{\dagger}d_{\nu\sigma} + V_{m\nu}^{*}d_{\nu\sigma}^{\dagger}c_{m\sigma}) \\
& + \sum_{\nu}U_{\nu}n_{\nu\uparrow}n_{\nu\downarrow} \\
& + \sum_{\nu>\nu',\sigma}[U'n_{\nu\sigma}n_{\nu'-\sigma} + (U' - J)n_{\nu\sigma}n_{\nu'\sigma}]
\end{aligned}
\tag{1.2}
$$

where $d_{\nu\sigma}^{\dagger}$ ($d_{\nu\sigma}$) is the creation (annihilation) operator for impurity states with spin σ at the d_ν orbitals and $n_{\nu\sigma} = d_{\nu\sigma}^{\dagger}d_{\nu\sigma}$, $c_{m\sigma}^{\dagger}$ ($c_{m\sigma}$) creates (annihilates) an electron in host states m with spin σ. Here, $\varepsilon_{d\nu}$ and ε_m are the energies of the impurity and host states, respectively. The impurity state refers to $3d_\nu$ orbitals for Fe, Co, Ni atoms, $4d_\nu$ orbitals for Ru atom, and $5d_\nu$ orbitals for Pt atom. The hybridization matrix element between host

and impurity states is $V_{m\nu}$. The intra-orbital Coulomb repulsion is U_ν. U' and $(U' - J)$ are the Coulomb interaction between two d electrons in different orbitals with opposite spins and parallel spins, respectively. J is the Hund's coupling term.

1.6. Why do we use the Anderson model?

We use the Anderson model to study the electronic properties of bioinorganic molecules. This model separates d orbitals of a transition metal atom from other orbitals. On-site Coulomb repulsion of the d orbitals is strong. This model emphasizes the importance of Coulomb interactions of d orbitals.

DFT method does not take into account the contribution of on-site Coulomb interactions of d orbitals. For this reason, the DFT does not give the correct electronic properties of systems. Thus, we construct an extended multi-orbital Anderson model to understand the magnetic properties of systems. This model explains the magnetic properties of transition-metal impurities in semiconductors. We use the DFT method to obtain the parameters of Anderson Hamiltonian. Then, we perform the DFT+MFA and DFT+QMC techniques by using these parameters.

1.7. Outline of the thesis

The outline of this thesis is as follows. In Chapter 2, we explain the electronic properties of the human hemoglobin and myoglobin derivatives, cyanocobalamin (CNCbl) molecule, Ru-based dye molecules and transition metal adatoms on a hexagonal graphene nanosheet. For the types of human hemoglobin, we show the molecular structures of truncated α_1 heme group of deoxy-heme, oxy-heme, carbonmonoxy-heme, and cyanomet-heme molecules. The bond distances of these molecules are compared in Table 2.1. For myoglobin derivatives, we examine the molecular structures of horse heart deoxymyoglobin and carbonmonoxy myoglobin and sperm whale cyanomet myoglobin. The bond distances of the myoglobin molecules are compared in Table 2.2. The molecular structures of heme molecules are very similar to the truncated myoglobin molecules as shown in Chapter 2.

In this thesis, we use four different computational methods: density functional theory (DFT), DFT plus Hubbard U potential, DFT plus mean-field approximation (DFT +MFA) and DFT plus quantum Monte Carlo (DFT+QMC). We are going to concentrate

on deoxy and oxy-heme molecules to determine whether these methods give accurate results. Then, we will compare the results of these methods with each other and the experimental data. We try to determine which one works best. In Chapters 3, 4 and 5, we present the results of deoxy and oxy-heme molecules.

In Chapter 3, we will show the DFT results of deoxy and oxy-heme molecules. We perform the DFT calculations by using BP86 exchange correlation energy functional and 6-31G basis set for each heme molecule. We study the electronic correlations of these heme molecules by using the framework of the extended multi-orbital Anderson model. We perform DFT calculations of these heme molecules with the Gaussian program (Frisch et al. (2009)) to obtain the parameters of the Anderson model. DFT method finds the ground state energy of deoxy-heme in the triplet-spin state (intermediate-spin). We will show the results of the triplet-spin state of deoxy-heme. This method does not obtain a high-spin state for deoxy-heme because the DFT method does not find the location of the impurity bound state (IBS) correctly. The IBS corresponds to a new quantum mechanical electronic state and it plays an important role in determining the magnetic properties of a system. The total magnetic moment of deoxy-heme is 2.0 Bohr magnetons with the DFT method. For oxy-heme, the DFT method finds the ground state energy in the open-shell singlet-spin state (low-spin). However, the effective magnetic moments of Fe($3d$) orbitals are very small and the DFT method does not find the IBS correctly. Total magnetic moment of oxy-heme is zero with DFT method. We will show the results of open-shell singlet-spin state of oxy-heme. In addition, we will show the DFT results of deoxy-heme and oxy-heme by using different basis sets: 6-31G(d), 6-31G(d,p), DGDZVP, cc-pVDZ, and LanL2DZ+6-31G. We choose the same energy functional (BP86) for these basis sets. We will compare the results of different basis sets for deoxy and oxy-heme molecules. For these basis sets the DFT method finds the ground state energy of deoxy-heme (oxy-heme) in the triplet-spin state (open-shell singlet-spin state).

In Chapter 4, we show density functional theory plus quantum Monte Carlo (DFT +QMC) results on the extended multi-orbital Anderson model for deoxy-heme and oxy-heme molecules. The DFT+QMC calculations are performed by using the Hirsch-Fye QMC algorithm (Hirsch and Fye (1986)). Detailed explanations of these calculations are shown in Ref. (Mayda (2019)). We observe that the IBS of deoxy-heme is below the Fermi level and the IBS is occupied by electrons. The spin state of deoxy-heme is the high-spin. The IBS of oxy-heme is above the Fermi level and IBS is unoccupied. The spin state of oxy-heme is the low-spin. The experimental results of deoxy and oxy-heme molecules are also in this way. We see that the DFT+QMC technique works better than

the DFT method. DFT method does not obtain the experimental data because this method solves many-body problems using approach. The DFT+QMC method obtains exact solutions by using extended multi-orbital Haldane-Anderson model. Thus, the DFT+QMC results are compatible with the experimental data.

In Chapter 5, we present density functional theory plus mean-field approximation (DFT+MFA) results on the extended multi-orbital Anderson model for deoxy-heme and oxy-heme molecules. We observe that the IBS of deoxy-heme is below the Fermi level and the IBS is occupied by electrons. The spin state of deoxy-heme is the high-spin. The DFA+MFA method works very well for the deoxy-heme molecule. However, we don't find a low-spin state for oxy-heme because the DFT+MFA method does not find the location of IBS correctly. Thus, the DFT+MFA technique gives accurate results for molecules having only a high-spin state.

In Chapter 6, we compare the DFT results of deoxy and oxy-heme molecules with the experimental results and computational results from the DFT+QMC and DFT+MFA techniques. In Chapter 7, we show the DFT+QMC results of cyanocobalamin (CNCbl), ruthenium based dye molecules and transition-metal adatoms on a hexagonal graphene nanosheet. In Chapter 8, we present the DFT results of carbonmonoxy-heme, cyanomet-heme, myoglobin molecules, CNCbl, ruthenium based dye molecules and transition-metal adatoms on a hexagonal graphene nanosheet.

In Chapter 9, we give the summary and conclusions of this thesis. In Appendix A, we explain the four different computational methods: DFT, DFT+U, DFT+MFA, and DFT+QMC techniques. In Appendix B, we show the finite-size effects for deoxy-heme clusters.

CHAPTER 2

STRUCTURES OF BIOINORGANIC MOLECULES

In this chapter, the electronic properties and structural similarities of bioinorganic molecules are explained. These molecules are as follows. In Section 2.1, we show adult human hemoglobin (HbA) derivatives. DeoxyHbA, oxyHbA, carbonmonoxyHbA and cyanometHbA are examples of the HbA derivatives. The types of myoglobin are shown in Section 2.2. They are the horse heart deoxymyoglobin (deoxyMb) and carbonmonoxy myoglobin (MbCO) and sperm whale cyanomet myoglobin (MbCN) molecules. We get the hemoglobin and myoglobin derivatives from the Protein Data Bank (PDB). The PDB codes of these molecules are 2DN1 (Park et al. (2006)) for deoxyHbA, 2DN2 (Park et al. (2006)) for oxyHbA, 2DN3 (Park et al. (2006)) for carbonmonoxyHbA, 1ABY (Kroeger and Kundrot (1997)) for cyanometHbA, 5D5R (Barends et al. (2015)) for horse heart deoxymyoglobin (deoxyMb), 1DWR (Chu et al. (2000)) for horse heart carbonmonoxy myoglobin (MbCO) and 2JHO (Arcovito et al. (2007)) for sperm whale cyanomet myoglobin (MbCN). In Section 2.3, we show the cyanocobalamin (CNCbl) molecule which is a cofactor of the vitamin B_{12}. The ruthenium based dye molecules are shown in Section 2.4. In Section 2.5, we demonstrate the transition-metal adatom on a hexagonal graphene nanosheet. We perform the DFT calculations for these molecules. We will show their DFT results in Chapter 8.

2.1. Human hemoglobin derivatives

The hemoglobin molecule derivatives consist of four heme groups: two alpha groups and two beta groups. The molecular structure of deoxyhemoglobin is shown in Fig. 2.1. It contains about 10,000 atoms. We will examine α_1 heme group for our calculations. The heme group is made up of an iron atom and an organic part. The organic part contains a Fe-protoporphyrin IX and an imidazole part. The structure of the protoporphyrin IX contains eight side chains at the porphyrin plane. In general, these chains are four methyl groups ($-CH_3$), two vinyl ($-CH = CH_2$) and two propionate ($-CH_2 - CH_2 - COO^-(H^+)$) in the side parts. In addition, we add proximal and distal histidine parts. The proximal histidine (His F8) part is located at top of the porphyrin ring.

The distal histidine (His E7) is attached to the imidazole part. The proximal histidine helps to bind or separate O_2 molecule to Fe atom. Moreover, we show the distances between Fe atom and nitrogen atoms, O_2, CO and CN ligands in the porphyrin ring for various human hemoglobin molecules in Table 2.1.

2.1.1. Deoxy and oxy-heme molecules

We use that the experimental atomic coordinates of deoxy-heme and oxy-heme molecules are obtained by X-ray diffraction (Park et al. (2006)). We take these molecules from the Protein Data Bank (PDB) with key 2DN2 and 2DN1 (Park et al. (2006)), respectively.

For the α_1 structure of 2DN2 and 2DN1 (Park et al. (2006)), the eight side chains are different at the porphyrin plane. Therefore, these side parts are replaced by the hydrogen atoms to simplified the sizes of deoxy-heme and oxy-heme molecules. Only these H atoms are optimized in our calculations. In addition, we add proximal and distal histidine parts for deoxy-heme and oxy-heme molecules. Then, we obtain deoxy-heme and oxy-heme molecules in Fig. 2.2.

Figure 2.2 shows the molecular structures of deoxy-heme ($C_{32}H_{30}FeN_{10}O_2$) and oxy-heme ($C_{32}H_{30}FeN_{10}O_4$). The deoxy-heme and oxy-heme have 75 and 77 atoms, respectively. In addition, the total electron numbers of deoxy-heme and oxy-heme are 334 and 350 electrons, respectively. The distance between Fe atom and the average of four nitrogen atoms in the porphyrin ring is 0.4 Å and 0.04 Å for deoxy-heme and oxy-heme, respectively. The bond distances of between Fe and N atoms are shown in the first two columns of Table 2.1.

2.1.2. Carbonmonoxy-heme molecule

Carbon monoxide (CO) is a toxic gas and has no color and smell (Blumenthal (2001)). The CO binds to deoxyhemoglobin with 200 times faster than oxygen (Tanaka et al. (2016)). The CO reduces the oxygen-carrying capacity of the blood and the CO poising occurs. This effect can cause death. The CO interacts with the human deoxyhemoglobin and then carbonmonoxy human hemoglobin (COHbA) occurs. The COHbA molecule has zero magnetic moment Pauling and Coryell (1936). We get the COHbA molecule from the PDB with key 2DN3 (Park et al. (2006)). In the COHbA, α_1 heme
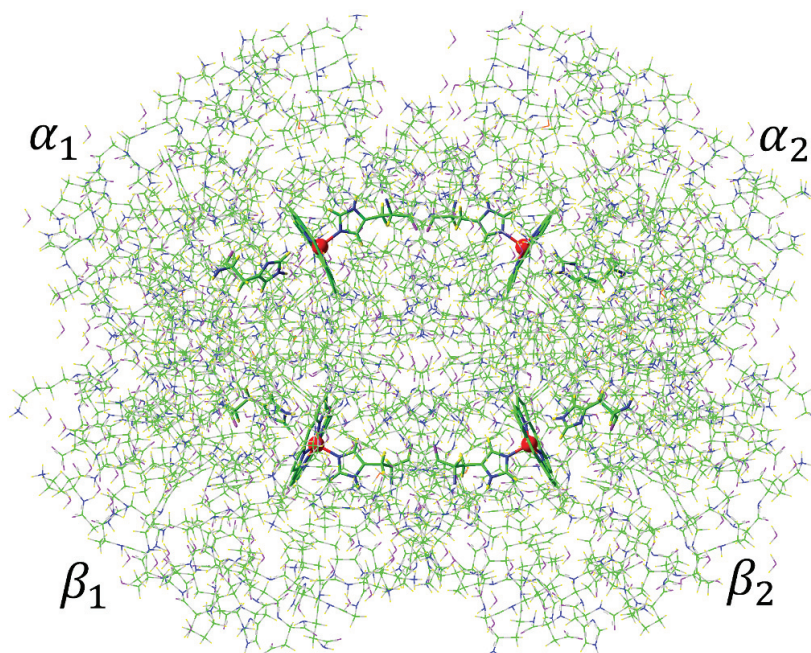
Figure 2.1. Molecular structure of the deoxyhemoglobin (PDB:2DN2). It includes about 10,000 atoms. It contains four inequivalent heme groups: two alpha and two beta. Each heme group has an iron atom (red point). Other atoms are nitrogen (blue), carbon (green), oxygen (purple) and hydrogen (yellow) atoms.
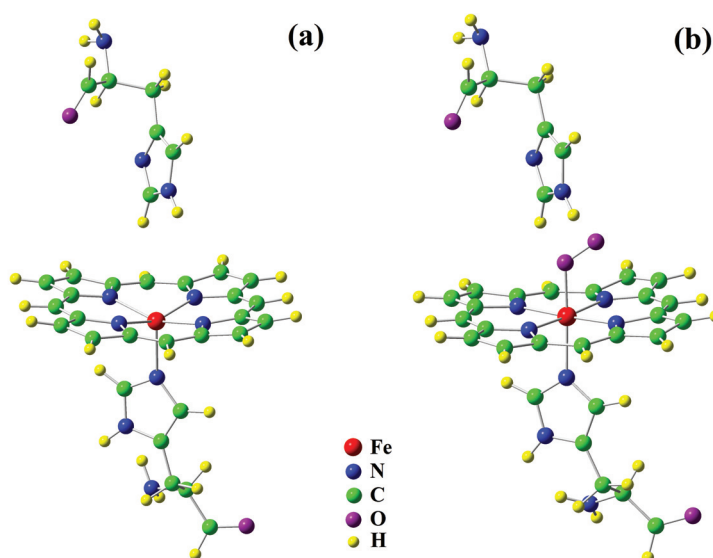
Figure 2.2. Molecular structures of (a) the deoxy-heme ($C_{32}H_{30}FeN_{10}O_2$) and (b) the oxy-heme ($C_{32}H_{30}FeN_{10}O_4$).
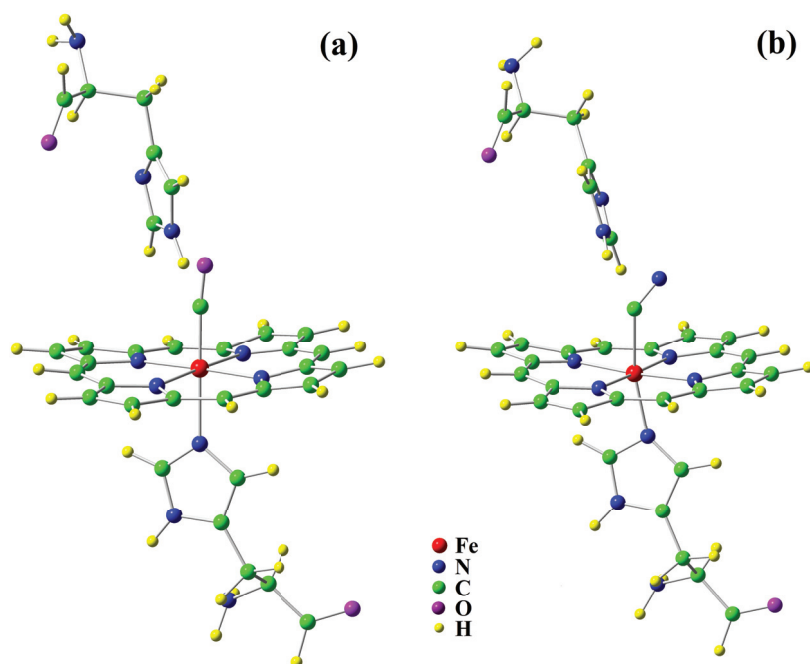
Figure 2.3. Molecular structure of (a) the carbonmonoxy-heme ($C_{33}H_{30}FeN_{10}O_3$) and (b) the cyanomet-heme ($[C_{33}H_{30}FeN_{11}O_2]^-$).

group is used for carbonmonoxy heme (CO-heme) molecule. For our works, we add proximal and distal histidine parts in the CO-heme. The CO-heme molecule is shown in Fig. 2.3 (a) and it has 77 atoms. The structure of the CO-heme is similar to the oxy-heme molecule. In CO-heme molecule, Fe atom binds to CO ligand instead of O_2 molecule. The third column of Table 2.1 denotes the bond distances of between Fe and N atoms.

2.1.3. Cyanomet-heme molecule

K. S. Kroeger and C. E. Kundrot synthesized cyanomet hemoglobin (CNHbA) (Kroeger and Kundrot (1997)). The CNHbA was prepared by using potassium ferricyanide and potassium cyanide with human deoxyhemoglobin (Smith and Simmons (1994); Waterman (1978)). We get the CNHbA molecule from the PDB with key 1ABY (Kroeger and Kundrot (1997)). The effective magnetic moment of HbCN molecule (for lamprey hemoglobin) is 2.42 Bohr magnetons (Hendrickson (1973)). In the CNHbA, α_1 heme group is used for cyanomet-heme (CN-heme) molecule as shown in Fig. 2.3 (b). The total number of electrons of the CN-heme molecule is 347 electrons. If the total number of

Table 2.1. The bond distances between Fe atom and nitrogen (N) atoms, O_2, CO and CN ligands in porphyrin ring for human deoxyhemoglobin, oxyhemoglobin, carbonmonoxy hemoglobin, and cyanomet hemoglobin molecules are shown. The distance between Fe atom and the average of four N atoms in the porphyrin ring refers to d(Fe - 4N's). If the d(Fe - 4N's) value is positive, the Fe atom is located below the 4N's atoms. In addition, we show the number of atom and electron for truncated human hemoglobin molecules. Distances are given in angstroms and bond angles in degrees.

PDB	2DN2 (deoxyHbA)	2DN1 (oxyHbA)	2DN3 (CO-HbA)	1ABY (CN-HbA)
Structure	deoxy-heme 75 atoms 334 electrons	oxy-heme 77 atoms 350 electrons	CO-heme 77 atoms 348 electrons	$[CN\text{-}heme]^-$ 77 atoms 348 electrons
Fe - 2^{nd}N	2.108 Å	2.023 Å	2.031 Å	1.990 Å
Fe - 3^{rd}N	2.121 Å	2.012 Å	2.029 Å	2.065 Å
Fe - 4^{th}N	2.116 Å	1.996 Å	2.024 Å	2.050 Å
Fe - 5^{th}N	2.076 Å	2.020 Å	2.095 Å	1.949 Å
Fe - 10^{th}N	2.196 Å	2.071 Å	2.109 Å	1.931 Å
Fe - X	-	1.817 Å	1.736 Å	2.079 Å
d(Fe - 4N's)	0.40 Å	0.04 Å	-0.03 Å	0.06 Å
Angle Fe- 11^{th}X- 12^{th}Y	-	124.29° X=O, Y=O	172.12° X=C, Y=O	122.90° X=C, Y=N

electrons is odd, the DFT calculations become doublet state. The DFT results are divided into alpha and beta orbitals in the doublet state. We bring singlet state to pass by adding one electron to the $[CN\text{-}heme]^-$ because we use the singlet state in the DFT calculations.

2.2. Myoglobin derivatives

Myoglobin (Mb) molecule has different characteristic properties compared to the hemoglobin (Hb). The Mb is a complex muscle protein that undertakes the task of storing oxygen in the muscles. The structure of the Mb molecule is similar to the Hb. The Mb molecule is about one-fourth the size of the Hb molecule (Nye (2002)). The Mb has a heme group and contains only one Fe atom in its active center. The heme group is made up of an iron atom and an organic part. The organic part contains a Fe-protoporphyrin IX and an imidazole part. The structure of the protoporphyrin IX contains eight side chains at the porphyrin plane. In general, these chains are four methyl groups ($-CH_3$), two vinyl

($-\mathrm{CH} = \mathrm{CH_2}$) and two propionate ($-\mathrm{CH_2} - \mathrm{CH_2} - \mathrm{COO^-}(\mathrm{H^+})$) in the side parts. In addition, we add proximal and distal histidine molecules. The proximal histidine (His F8) part is located at top of the porphyrin ring. The distal histidine (His E7) is attached to the imidazole part.

Here, we examine the horse heart deoxymyoglobin (deoxyMb) and carbonmonoxy myoglobin (MbCO) and sperm whale cyanomet myoglobin (MbCN) molecules (Tsukahara (1986)). We get these myoglobin molecules from the Protein Data Bank (PDB) with key 5D5R (Barends et al. (2015)), 1DWR (Chu et al. (2000)) and 2JHO (Arcovito et al. (2007)), respectively. The spin state of the deoxyMb and MbCO molecules are the high-spin and the low-spin states, respectively (Fiamingo and Alben (1985); Norvell et al. (1975); Roder et al. (1984)). The effective magnetic moment of MbCN molecule is 1.96 Bohr magnetons (McLendon and Sandberg (1978)).

For our works, we add proximal and distal histidine parts in myoglobin derivatives. The deoxyMb molecule is shown in Fig. 2.4 (a) and it has 75 atoms. The deoxyMb molecule is similar to the deoxy-heme molecule. For the deoxyMb molecule, the second column of Table 2.2 shows the bond distances of N atoms which bind to the Fe atom. The structure of the MbCO and MbCN are similar to the CO-heme and CN-heme molecules. Fig. 2.4 (b) and Fig. 2.4 (c) show the structures of the MbCO and MbCN molecules, respectively. The charge of MbCN molecule has minus 1. In the MbCO and MbCN molecules, the Fe atom binds to CO and CN ligands, respectively. The third and fourth columns of Table 2.2 show the bond distances of C and N atoms which bind to the Fe atom.

2.3. Cyanocobalamin molecule

The molecular structure of CNCbl molecule with the chemical formula $\mathrm{C_{63}H_{88}Co}$ $\mathrm{N_{14}O_{14}P}$ is shown in Fig.2.5. This molecule consists of a cobalt (Co) atom at the center and four nitrogen atoms attached to Co atom in the corrin ring. A ligand and a nucleotide are attached to the corrin ring as shown in Fig.2.5. The neutral CNCbl molecule has 718 electrons. It contains 181 atoms.
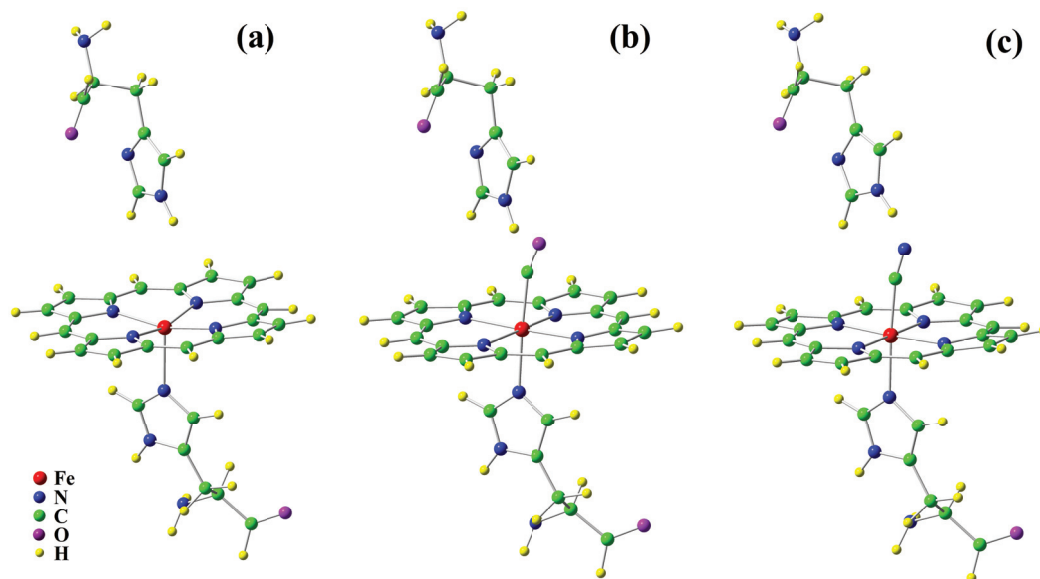
Figure 2.4. Molecular structure of (a) the deoxyMb ($C_{32}H_{30}FeN_{10}O_2$), (b) the MbCO ($C_{33}H_{30}FeN_{10}O_3$) and (c) the MbCN ($[C_{33}H_{30}FeN_{11}O_2]^-$).
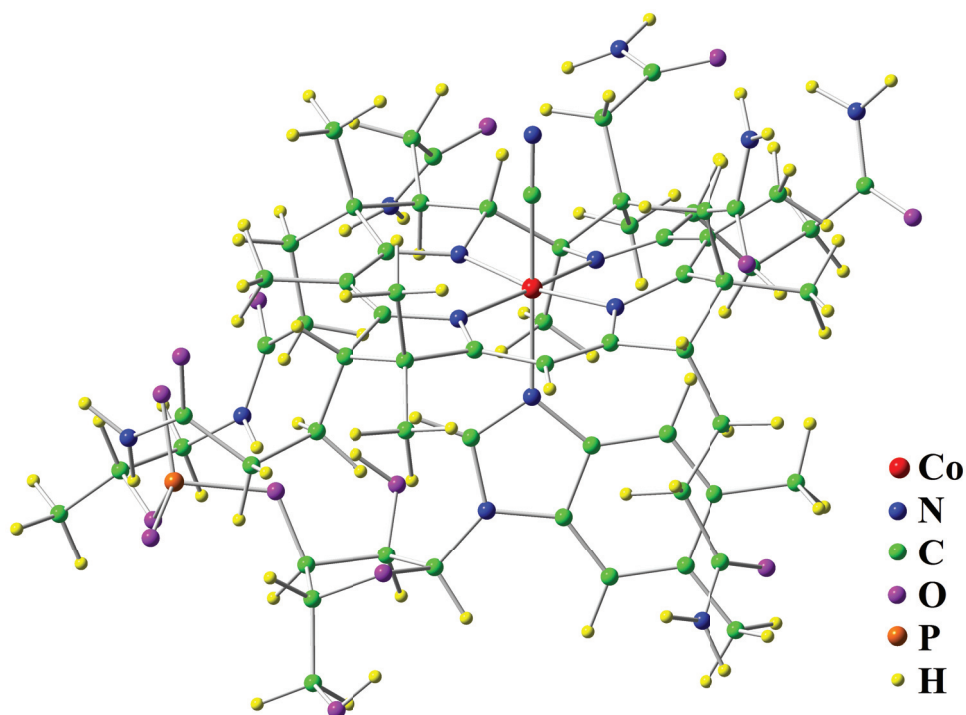
Figure 2.5. Molecular structure of CNCbl ($C_{63}H_{88}Co\,N_{14}O_{14}P$). It contains 181 atoms. Here, the red sphere represents the Co atom located at the center of the molecule.

2.4. Ruthenium-based dye molecules

Dye molecule is one of the essential parts of dye sensitized solar cells (DSSCs). In DSSCs, the dye molecule is attached to the semiconductor layer (e.g. TiO_2). The main function of the dye molecule provides an electron to the semiconductor layer. When the light hits the dye molecules, the electrons are excited. The electrons leave the dye molecule and reach the surface of the semiconductor layer. The excited state of the dye molecule is reduced again by a redox couple in an electrolyte. The dye molecule regains its lost electrons and thus it continues to work. The studies on sensitizing dyes show that the best results are given by ruthenium-based dyes (Mikroyannidis et al. (2010)). Ru-based dye molecules are often preferred because they are well-stimulated by visible and near-infrared spectra of sunlight (Ayalew and Ayele (2016); Hao et al. (2006)). Generally Ru-based dye molecules are used to increase the efficiency of solar cells. The N719 and Z907 dye molecules can be given as examples for the Ru-based dye molecules.

Figure 2.6 shows the molecular structures of N719 and Z907 Ru-based dye molecules. In these molecules, the ruthenium atom is located at the center and six nitrogen atoms neighbor it. N719 dye contains 57 atoms and it has -2 charges and 354 electrons. The chemical formula of N719 dye is $[C_{26}H_{14}N_6O_8RuS_2]^{-2}$. The atomic coordinates of N719 dye are taken from the paper of Schiffmann et al. (Schiffmann et al. (2010)). The molecular structure of Z907 is similar to the structure of the N719 dye. The molecular formula of N719 is $[Ru(dcbpy)_2(NCS)_2]^{-2}$ and where dcbpy is composed of 4-carboxylato-4'-carboxylic acid-2,2'bipyridine (Qin and Peng (2012)). In Z907 dye, one 2,2'-bipyridine ligand binds to nine carbon atoms alkyl chains (C_9H_{19}) instead of one carboxylate and one carboxylic acid ligands (Qin and Peng (2012)). The molecular formula of Z907 is $[RuLL'(NCS)_2]$ (L=4,4'-dicarboxylic acid-2,2'-bipyridine, L'=4,4'-dinonyl-2,2'-bipyridine) (Qin and Peng (2012); Sun (2009)). Z907 dye contains 107 atoms and it has 454 electrons. The chemical formula of Z907 dye is $C_{42}H_{52}N_6O_4RuS_2$.

2.5. Transition-metal adatom on a hexagonal graphene nanosheet

For the calculation of SACs, we use the structure of hexagonal graphene nanosheet with an armchair edge (A-HGNS). n-A-HGNS layer has a low effect of the magnetic moment. n refers to the number of peripheral rings (Deng et al. (2014)). We choose $n = 3$ (3A-HGNS) layer with enough size for us. In addition, we hydrogenated the edges
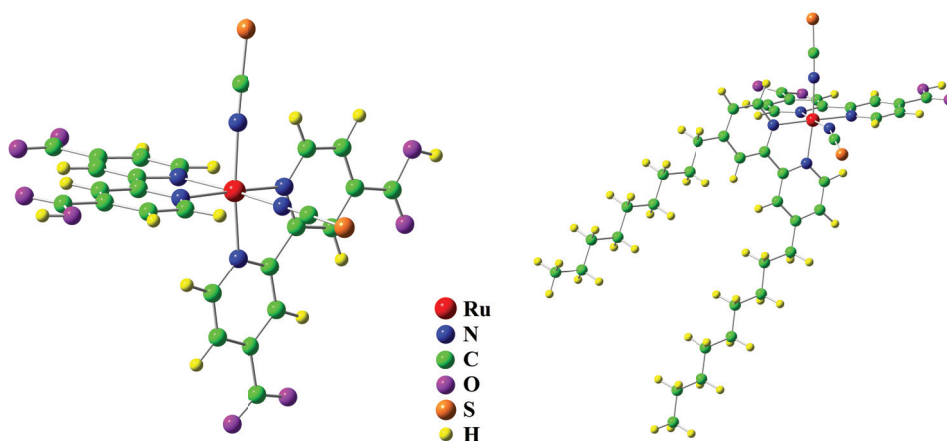
Figure 2.6. Molecular structures of N719 and Z907 Ru-based dye molecules. N719 dye ($[C_{26}H_{14}N_6O_8RuS_2]^{-2}$) contains 57 atoms and has -2 charges. Z907 dye ($C_{42}H_{52}N_6O_4RuS_2$) contains 107 atoms.

of the 3A-HGNS layer. In this layer, the total number of carbon atoms is 42 and the total number of hydrogen atoms is 18. We use the transition metal atoms as Fe, Ni and Pt, which are located different distances and positions on the 3A-HGNS layer. Figure 2.7, 2.8 and 2.9 show the structure of Pt/3A-HGNS ($C_{42}H_{18}Pt$), Fe/3A-HGNS ($C_{42}H_{18}Fe$) and Ni/3A-HGNS ($C_{42}H_{18}Ni$), respectively and they have 61 atoms. As seen in Fig. 2.8 and 2.9, Fe and Ni atoms are located at the hollow site. On the other hand, Figure 2.7 shows that Pt atom is located at the bridge site. We choose these locations for the transition metal atoms because transition metal/graphene systems have the minimum energy at these sites. The structures of Pt/3A-HGNS, Fe/3A-HGNS and Ni/3A-HGNS have 348, 296 and 298 electrons, respectively. The number of basis functions is 436 for each structure.
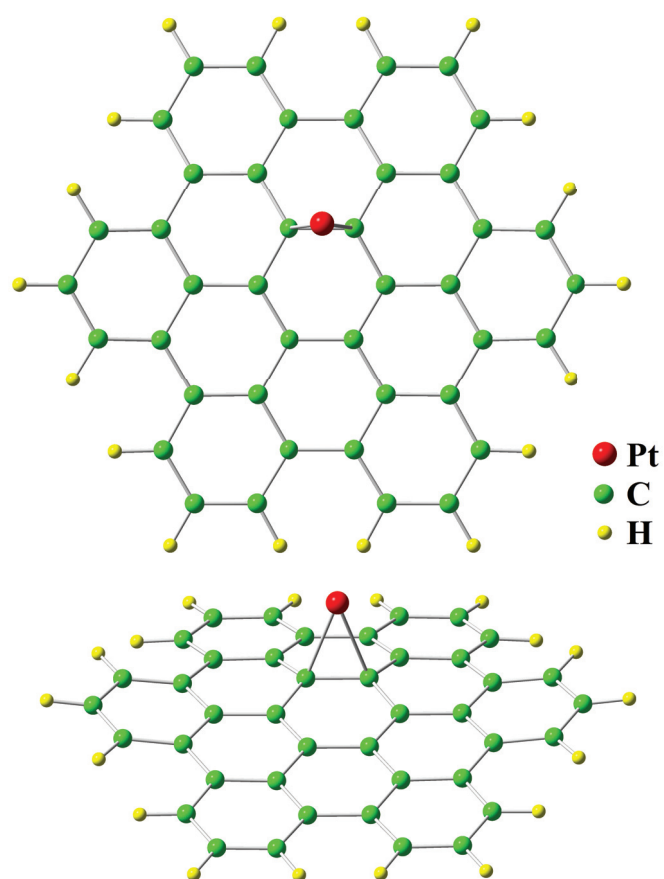
Figure 2.7. Schematic plot of the structure of Pt on 3A-HGNS layer ($C_{42}H_{18}Pt$), which contains 61 atoms. The above figure shows the top view of the Pt/3A-HGNS. The below figure is the side view of Pt/3A-HGNS. The Pt atom is located at the bridge site and 2.04 Å above the current layer.
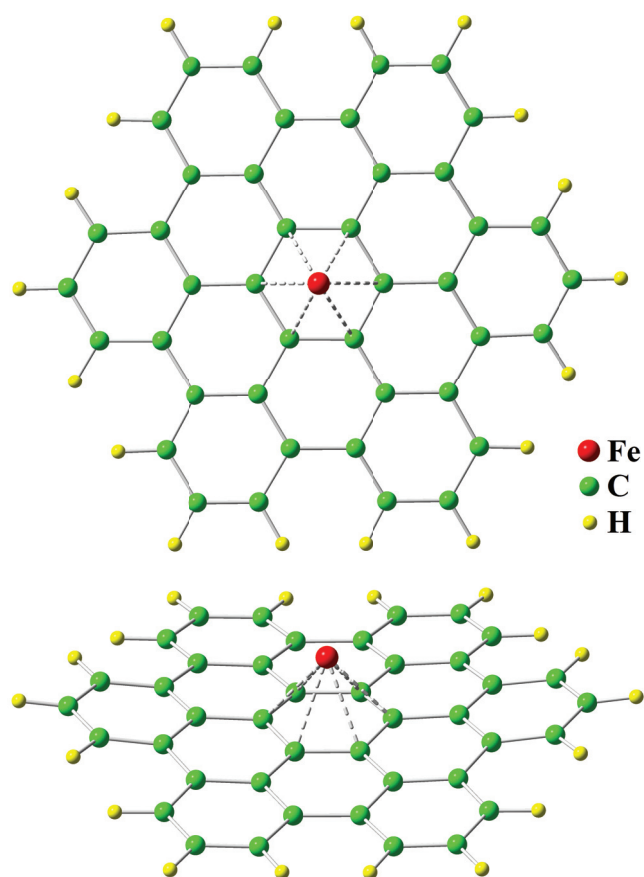
Figure 2.8. Schematic plot of the structure of Fe on 3A-HGNS layer ($C_{42}H_{18}Fe$), which contains 61 atoms. The above figure shows the top view of the Fe/3A-HGNS. The below figure is the side view of Fe/3A-HGNS. The Fe atom is located at the hollow site and 1.56 Å above the current layer.
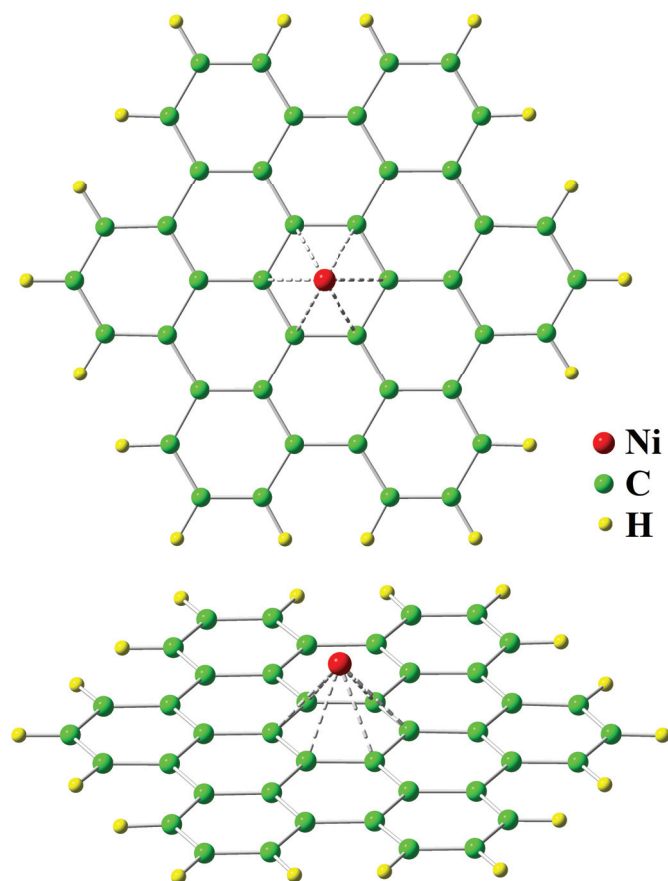
Figure 2.9. Schematic plot of the structure of Ni on 3A-HGNS layer ($C_{42}H_{18}Ni$), which contains 61 atoms. The above figure shows the top view of the Ni/3A-HGNS. The below figure is the side view of Ni/3A-HGNS. The Ni atom is located at the hollow site and 1.66 Å above the current layer.

Table 2.2. The bond distances between Fe atom and nitrogen (N) atoms, CO and CN ligands in porphyrin ring for horse heart deoxymyoglobin and carbonmonoxy myoglobin and sperm whale cyanomet myoglobin molecules are shown. The distance between Fe atom and the average of four N atoms in the porphyrin ring refers to d(Fe - 4N's). If the d(Fe - 4N's) value is positive, the Fe atom is located below the 4N's atoms. In addition, we show the number of atom and electron for truncated myoglobin molecules. Distances are given in angstroms and bond angles in degrees.

PDB	5D5R	1DWR	2JHO
Structure	deoxyMb 75 atoms 334 electrons	MbCO 77 atoms 348 electrons	[MbCN]$^-$ 77 atoms 348 electrons
Fe $- 2^{nd}$N	2.062 Å	2.175 Å	2.046 Å
Fe $- 3^{rd}$N	2.024 Å	2.159 Å	2.038 Å
Fe $- 4^{th}$N	2.070 Å	2.171 Å	2.040 Å
Fe $- 5^{th}$N	2.053 Å	2.161 Å	2.036 Å
Fe $- 10^{th}$N	2.228 Å	2.131 Å	2.080 Å
Fe $-$ X	-	1.902 Å	1.918 Å
d(Fe $-$ 4N's)	0.31 Å	0.03 Å	0.02 Å
Angle Fe $- 11^{th}$X $- 12^{th}$Y	-	162.25° X=C, Y=O	167.28° X=C, Y=N

CHAPTER 3

DFT RESULTS FOR HEME MOLECULES

In this chapter, we will show the DFT results of deoxy and oxy-heme molecules. The DFT calculations are performed by using the Gaussian program (Frisch et al. (2009)). For deoxy and oxy-heme molecules, we will show the results of the singlet-spin state from the DFT calculations in Sections 3.1 and 3.3, respectively. We have explained these calculations in detail in Refs. (Kandemir (2013); Kandemir et al. (2016); Mayda et al. (2017)). In DFT results, we find that the ground state energy of deoxy-heme is the triplet-spin state and the ground state energy of oxy-heme is the open-shell singlet-spin state. We will show the results of these spin state for each heme molecule. In addition, we perform the DFT calculations by using different basis sets for deoxy and oxy-heme. These basis sets are 6-31G(d), 6-31G(d,p), DGDZVP, cc-pVDZ and LanL2DZ+6-31G. In Sections 3.2 and 3.4, we show the results of these basis sets for deoxy and oxy-heme. Although we use different basis sets for deoxy and oxy-heme in our calculations, their results do not change significantly.

3.1. DFT results for deoxy-heme

For deoxy-heme, we perform the DFT calculation by using BP86 exchange correlation energy functional and 6-31G basis set for the singlet-spin state. The parameters of Anderson model: $\varepsilon_{d\nu}$, ε_m and $V_{m\nu}$ are obtained by the DFT calculation. The results of the singlet-spin state of deoxy-heme are used in the DFT+MFA and DFT+QMC methods.

The total density of state is defined by

$$D(\varepsilon) = \sum_{n=1}^{N} \delta(\varepsilon - E_n) \tag{3.1}$$

as a function of ε. E_n is the eigenvalues of Kohn-Sham matrix and N is the number of basis functions. Figure 3.1 (a) shows the total density of states for deoxy-heme. In Fig. 3.1, the vertical black solid and dashes lines denote the values of the HOMO and LUMO, respectively. The HOMO value is located at -3.53 eV and the LUMO value is located at

-3.02 eV. The host density of state is defined by

$$D_h(\varepsilon) = \sum_{m=1}^{N-5} \delta(\varepsilon - \varepsilon_m) \tag{3.2}$$

as a function of ε. ε_m is the eigenvalues of host orbitals and $N - 5$ is the number of host orbitals. In Fig. 3.1 (b), the host density of states is shown without Fe($3d_\nu$) orbitals. The Fe($3d_\nu$) levels have been shifted by the double counting term (Mayda et al. (2017)). The double counting term μ_ν^{DC} is defined by

$$\mu_\nu^{\mathrm{DC}} = U \frac{\langle n_\nu^{\mathrm{DFT}} \rangle}{2} + U' \sum_{\nu' \neq \nu} \frac{\langle n_{\nu'}^{\mathrm{DFT}} \rangle}{2} + (U' - J) \sum_{\nu' \neq \nu} \frac{\langle n_{\nu'}^{\mathrm{DFT}} \rangle}{2} \tag{3.3}$$

including the U, $U'(= U - 2J)$ and $U' - J$ interactions. This term is calculated for Coulomb interaction $U = 4$ eV and Hund's coupling term $J = 0.9$ eV. The new energies $\tilde{\varepsilon}_{d\nu}$ of Fe($3d_\nu$) orbitals are obtained that the bare Fe($3d_\nu$) energy levels $\varepsilon_{d\nu}$ are subtracted from double counting term μ_ν^{DC}. In Fig. 3.1 (b), they are located between -15 eV and -14 eV. The sort of new energies of Fe($3d_\nu$) orbitals is $3d_{yz}$, $3d_{xz}$, $3d_{xy}$, $3d_{3z^2-r^2}$ and $3d_{x^2-y^2}$ after shifting.

From the DFT calculations, the Kohn-Sham matrix have been divided into host and impurity parts. We obtain the eigenvalues ε_m and the eigenvectors u_m of the host matrix after diagonalization. We have explained these calculations in detail in Ref. (Kandemir (2013)). The hybridization matrix element $V_{m\nu}$ is defined by

$$V_{m\nu} = \sum_{i=1}^{N-5} u_{mi} M_{i\nu} \tag{3.4}$$

In Fig. 3.2, the square of the hybridization matrix elements $|V_{m\nu}|^2$ between the m'th host eigenstates and Fe($3d_\nu$) natural atomic orbitals are shown as a function of the m'th host eigenvalues ε_m for deoxy-heme. We observed that the host states $m = 144$th, and 152nd have the highest hybridization matrix elements for $3d_{3z^2-r^2}$ and $3d_{x^2-y^2}$ orbitals. In Fig. 3.2 (a), $3d_{3z^2-r^2}$ orbital has the noticeable hybridization contribution at $m = 145$th, 146th, 153rd and 163rd host states. In Fig. 3.2 (b), the hybridization of xz, yz and xy orbitals are relatively small compared to the hybridization of $x^2 - y^2$ and $3z^2 - r^2$ orbitals. The $m =$
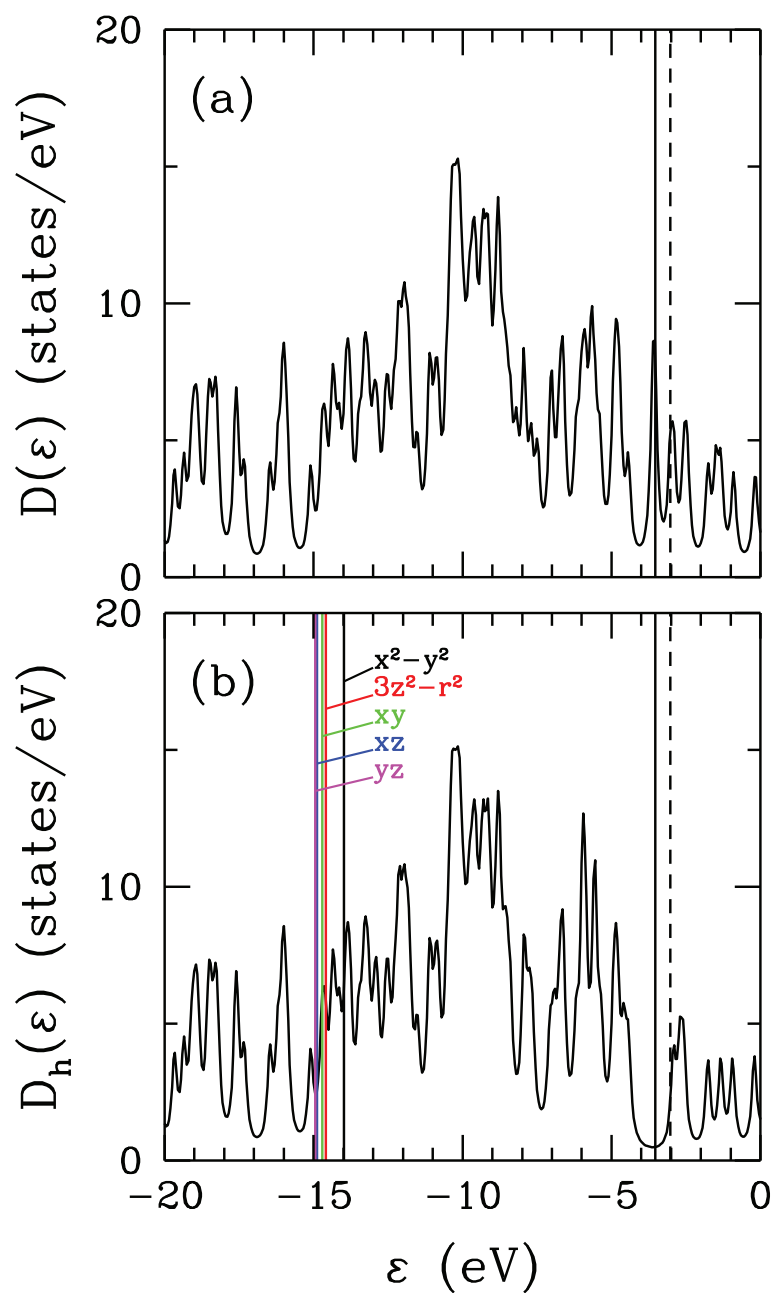
Figure 3.1. (a) For deoxy-heme total density of states $D(\varepsilon)$ versus energy ε, obtained DFT(BP86/6-31G) by using the Gaussian program. (b) For deoxy-heme density of states of the host states $D_h(\varepsilon)$ of the extended Anderson model. The Fe($3d_\nu$) levels have been shifted by the double-counting term. This term is calculated for $U = 4$ eV and $J = 0.9$ eV. Here, the vertical solid and dashed lines denote the HOMO and LUMO levels, respectively. The HOMO and LUMO levels are obtained by the DFT method.

146th and 158th host states have the hybridization with xz and yz orbitals, respectively. The hybridization contributions of $3d$ orbitals are very small for $m = 165$th, 166th and 167th host states in Fig. 3.2. We will show the compositions of these host states in Fig. 3.3. The $m = 165$th host state is near the LUMO level. There is an important detail for the $m = 165$th host state. We will explain this detail in Appendix B.

Figure 3.3 shows the natural atomic orbitals (NAO) (Glendening et al. (2013)) composition of the m'th host eigenstate for deoxy-heme. The Ref. (Kandemir et al. (2016); Kandemir (2013)) was explained more detail for NAO weight of the $|u_{mi}|^2$. The Fe atom is attached to the 10th nitrogen (N) atom of the imidazole part in the first part of Fig. 3.3. In addition, 2nd, 3rd, 4th and 5th N sites are connected to the Fe atom in porphyrin ring. In Figs. 3.3 (a) and 3.3 (b), NAO weights of $2p_z$ orbital of 10th and $2p_x$ orbital of 5th N sites are the largest value for $m = 144$th and 145th host states, respectively. In Figs. 3.3 (c) and 3.3 (d), NAO weights of $2p_x$ and $2p_y$ orbitals of 2nd, 3rd, 4th and 5th N sites are the largest value for $m = 146$th and 152nd. In Figs. 3.3 (e) and 3.3 (f), NAO weights of $2p_z$ orbital of 2nd, 3rd, 4th and 5th N sites and C atoms in the porphyrin ring are the largest value for $m = 153$rd and 163rd. Figures 3.3 (g-i) show that the NAO weights of N and C sites in the porphyrin ring are the largest value at $m = 166$th and 167th. At $m = 165$th host state NAO weights of $2p_x$ and $2p_y$ orbitals of 23rd C and 24th O atoms are the largest value. The $m = 165$th host state is near the LUMO level. There is an important detail for the $m = 165$th host state. We will explain this detail in Appendix B. $m = 144$th and 152nd host states have the highest hybridization matrix elements for $3d_{3z^2-r^2}$ and $3d_{x^2-y^2}$ orbitals. The electron occupation numbers of these orbitals are ≈ 0.5 electrons.

Here, we show the results of the singlet state for the deoxy-heme molecule. The total energies of singlet, triplet and quintuplet states of deoxy-heme are shown in Table 3.1. The triplet state has the lowest energy value, so the ground state energy of deoxy-heme is the triplet state. The results of the triplet ground state of deoxy-heme are explained in Section 3.1.1.

3.1.1. Results of triplet ground state for deoxy-heme

In DFT results, we find that the ground state energy of deoxy-heme is the triplet-spin state. The Gaussian program gives two different electrons as alpha and beta electrons in the triplet-spin state. Alpha (beta) electrons correspond to up-spin (down-spin). We can calculate the electron occupation numbers, magnetic moments and magnetic correlations
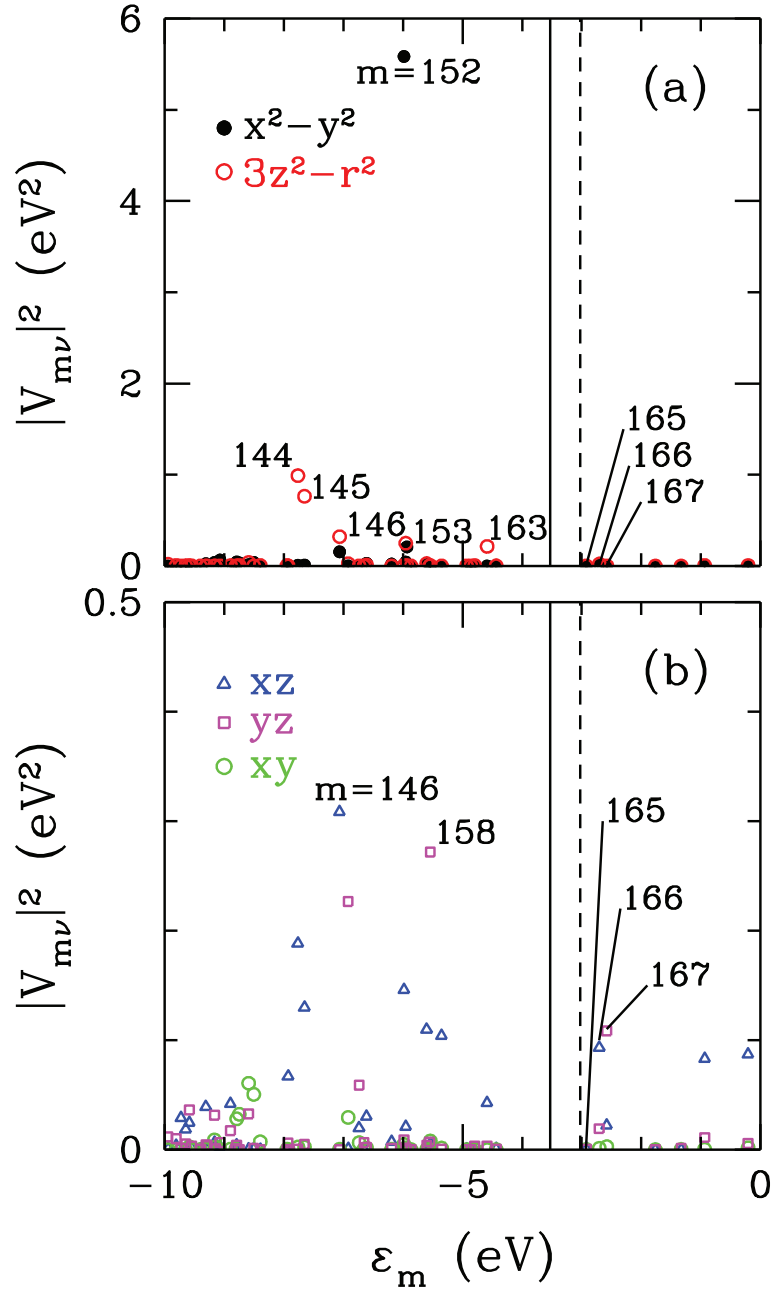
Figure 3.2. For deoxy-heme, DFT(BP86/6-31G) results on the square of hybridization matrix elements $|V_{m\nu}|^2$ between the m'th host eigenstates and Fe($3d_\nu$) natural atomic orbitals as a function of the m'th host eigenvalues ε_m. In (a) results are shown for $3d_{x^2-y^2}$ and $3d_{3z^2-r^2}$ orbitals, and in (b) for $3d_{xz}$, $3d_{yz}$ and $3d_{xy}$ orbitals. Here, the vertical solid and dashed lines denote the values of the HOMO and LUMO, respectively. The HOMO and LUMO levels are obtained by the DFT method. We observe that the $m = 152$nd host state has the highest hybridization matrix elements with $3d_{x^2-y^2}$ orbital.
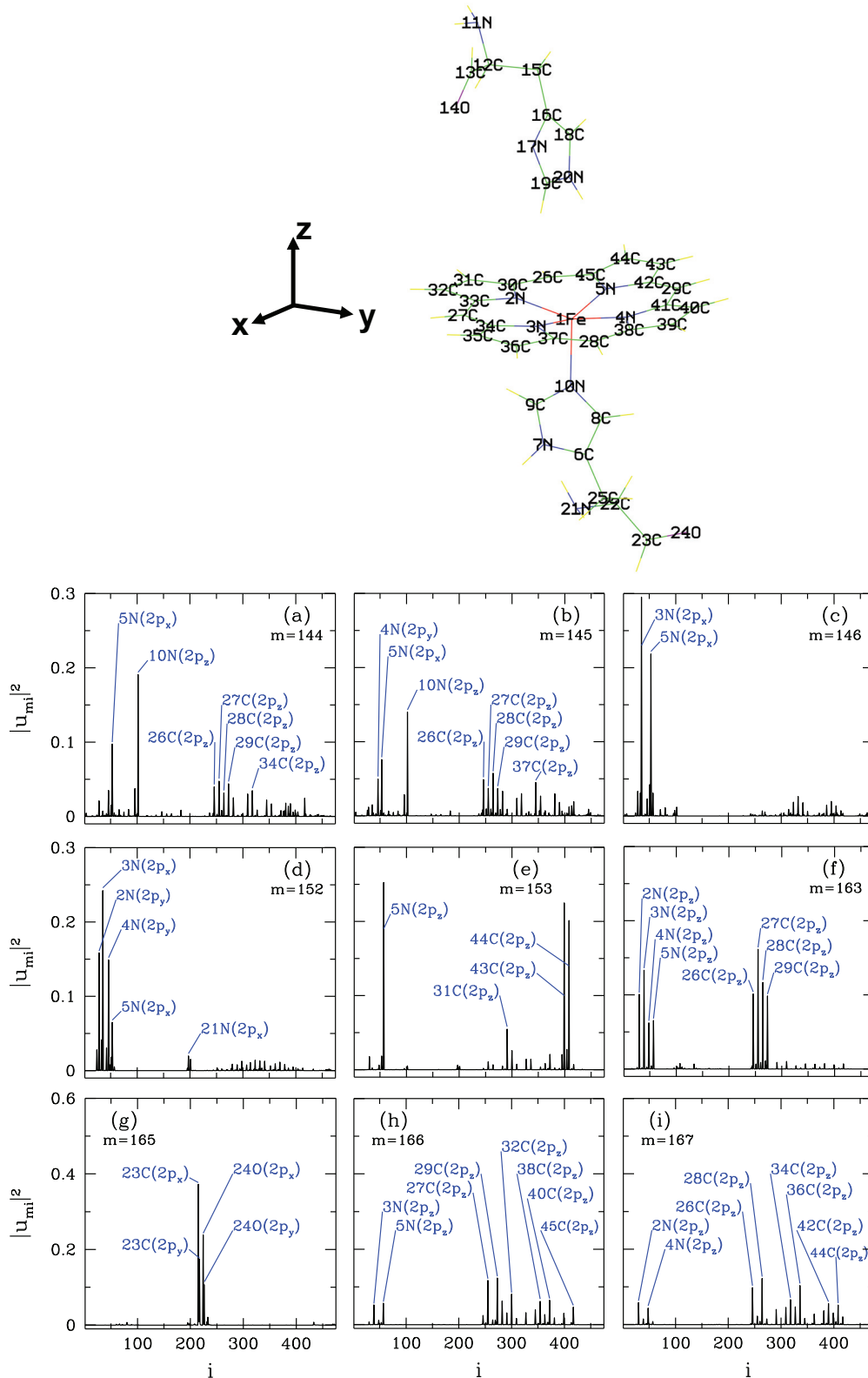
Figure 3.3. For deoxy-heme, schematic plot with label numbers and symbols of atoms. The DFT results on the square of the host eigenstate ($|u_{mi}|^2$) contributions versus the label i for (a) $m = 144$th, (b) 145th, (c) 146th, (d) 152nd, (e) 153rd, (f) 163rd, (g) 165th, (h) 166th and (i) 167th host states.

Table 3.1. DFT results on the total energies of singlet, triplet and quintuplet states of the deoxy-heme molecule. DFT finds that the ground state energy of deoxy-heme is a triplet-spin state. Energies are given in electron volts (eV).

DFT (BP86/6-31G)	
Spin State	Total Energy
Singlet State (S=0)	-87039.75 eV
Quintuplet State (S=2)	-87040.28 eV
Triplet Ground State (S=1)	-87040.34 eV

of Fe($3d$) and the host orbitals. Here, we explain how to obtain the electron occupation number of Fe($3d_\nu$) and host orbitals as a function of chemical potential μ. Then, we will compare these results with the DFT+QMC and DFT+MFA methods in Chapter 6.

For deoxy-heme, n_ν is defined the electron numbers of Fe($3d_\nu$) orbitals as total between up-electrons (alpha) $n_{\nu\uparrow}$ and down-electrons (beta) $n_{\nu\downarrow}$ The magnetic moment of Fe($3d_\nu$) orbitals M_ν^z is defined as differences of them. We first obtain the molecular orbitals (MO) in the natural atomic orbitals (NAO) basis with the Gaussian program. The molecular orbitals $|\psi_n^\sigma\rangle$ can be expressed in terms of NAO basis:

$$|\psi_n^\sigma\rangle = \sum_{n'=1}^{N} \beta_{nn'}^\sigma |\tilde{\phi}_{n'}^\sigma\rangle \qquad (3.5)$$

where $|\tilde{\phi}_{n'}^\sigma\rangle$ is the eigenvectors of NAOs, $\beta_{nn'}^\sigma$ is the coefficients of NAOs and σ denotes alpha and beta spin orbitals. We have explained these calculations in detail in Refs.(Kandemir et al. (2016); Kandemir (2013)). Here, we need to write $|\tilde{\phi}_{n'}^\sigma\rangle$ in terms of the molecular orbitals $|\psi_n^\sigma\rangle$. We get the inverse of $\beta_{nn'}^\sigma$ matrix. Then, we obtain the NAOs in terms of MOs

$$|\tilde{\phi}_{n'}^\sigma\rangle = \sum_{n=1}^{N} B_{n'n}^\sigma |\psi_n^\sigma\rangle \qquad (3.6)$$

where $\tilde{B}^\sigma$ matrix denotes $\left(\tilde{\beta}^\sigma\right)^{-1}$. For Fe($3d$) orbitals, we use the elements of $B_{\nu n}^\sigma$ matrix. Thus, we obtain that the electron occupation numbers of Fe($3d$) orbitals $\langle n_{\nu\sigma}(\mu)\rangle$ as a

function of chemical potential μ

$$\langle n_{\nu\sigma}(\mu)\rangle = \sum_{n=1}^{N} |B_{\nu n}^{\sigma}|^2 f_n^{\sigma}(\mu) \tag{3.7}$$

where the Fermi function $f_n^{\sigma}(\mu)$ is defined by

$$f_n^{\sigma}(\mu) = \frac{1}{e^{\frac{E_n^{\sigma}-\mu}{k_B T}} + 1} \tag{3.8}$$

where E_n^{σ} is the energies of the molecular orbitals for alpha and beta spin orbitals, k_B is the Boltzmann constant and T is temperature. Here, we obtain that the electron numbers of Fe($3d_{\nu}$) orbitals with $\langle n_{\nu}(\mu)\rangle = \langle n_{\nu\uparrow}(\mu)\rangle + \langle n_{\nu\downarrow}(\mu)\rangle$ are shown in Fig. 3.5 (a) and the effective magnetic moment of Fe($3d_{\nu}$) orbitals with $M_{\nu}^{\text{eff}}(\mu) = \langle n_{\nu\uparrow}(\mu)\rangle - \langle n_{\nu\downarrow}(\mu)\rangle$ are shown in Fig. 3.5 (b).

The molecular orbitals $|\psi_n^{\sigma}\rangle$ can be expressed as the impurity and host orbitals:

$$|\psi_n^{\sigma}\rangle = \sum_{\nu=1}^{5} \beta_{n\nu}^{\sigma}|\tilde{\phi}_{d\nu}^{\sigma}\rangle + \sum_{i=1}^{N-5} \beta_{ni}^{\sigma}|\tilde{\phi}_i^{\sigma}\rangle \tag{3.9}$$

where $|\tilde{\phi}_{d\nu}^{\sigma}\rangle$ and $|\tilde{\phi}_i^{\sigma}\rangle$ are the eigenvectors of impurity and host orbitals, $\beta_{n\nu}^{\sigma}$ and β_{ni}^{σ} are the coefficients of their orbitals and σ denotes alpha and beta spin orbitals. From Fock matrix, eigenvectors of host orbitals are obtained as

$$|\phi_m^{\sigma}\rangle = \sum_{i=1}^{N-5} u_{mi}^{\sigma}|\tilde{\phi}_i^{\sigma}\rangle. \tag{3.10}$$

Here, we need to write $|\tilde{\phi}_i^{\sigma}\rangle$ host NAO orbitals in terms of the MOs $|\psi_n^{\sigma}\rangle$. From equation (3.6), we get B_{in}^{σ} matrix for host orbitals. Then, we obtain

$$|\tilde{\phi}_i^{\sigma}\rangle = \sum_{n=1}^{N} B_{in}^{\sigma}|\psi_n^{\sigma}\rangle \tag{3.11}$$

host NAO orbitals in terms of the molecular orbitals and $\tilde{B}^\sigma$ matrix denotes $\left(\tilde{\beta}^\sigma\right)^{-1}$. By substituting equation (3.11) into equation (3.10), the eigenvectors of host orbitals

$$|\phi_m^\sigma\rangle = \sum_{n=1}^{N} W_{mn}^\sigma |\psi_n^\sigma\rangle \tag{3.12}$$

is obtained in terms of the molecular orbitals and where W_{mn}^σ is defined as

$$W_{mn}^\sigma = \sum_{i=1}^{N-5} u_{mi}^\sigma B_{in}^\sigma. \tag{3.13}$$

The electron occupation number of host orbitals is expressed as

$$\langle n_m^\sigma \rangle = \int_{-\infty}^{\infty} d\omega A_m^\sigma(\omega) f^\sigma(\omega) \tag{3.14}$$

where $A_m^\sigma(\omega)$ is spectral weight of host orbitals and $f^\sigma(\omega)$ is the Fermi function. The spectral weight of host orbitals $A_m^\sigma(\omega)$ is defined by using equation (3.13)

$$A_m^\sigma(\omega) = \sum_{n=1}^{N} |W_{mn}^\sigma|^2 \delta(\omega - E_n^\sigma). \tag{3.15}$$

Finally, we obtain the electron occupation number of host orbitals $\langle n_m^\sigma(\mu) \rangle$

$$\langle n_m^\sigma(\mu) \rangle = \sum_{n=1}^{N} |W_{mn}^\sigma|^2 \frac{1}{e^{\frac{E_n^\sigma - \mu}{k_B T}} + 1} \tag{3.16}$$

as a function of chemical potential μ. Here, we obtain that the electron numbers of the m'th host orbitals with $\langle n_m(\mu) \rangle = \langle n_{m\uparrow}(\mu) \rangle + \langle n_{m\downarrow}(\mu) \rangle$ are shown in Figs. 3.6 (a) and 3.7 (a), the effective magnetic moment of the m'th host orbitals with $M_m^{\text{eff}}(\mu) = \langle n_{m\uparrow}(\mu) \rangle - \langle n_{m\downarrow}(\mu) \rangle$ are shown in Figs. 3.6 (b) and 3.7 (b).

In Fig. 3.4, we show the electron occupation number of deoxy-heme for the triplet state. We present the DFT data on the total electron occupation of the Fe($3d$) orbitals $\langle n_d \rangle$ as a function of the chemical potential μ. The total electron number of the host orbitals

$\langle n_h \rangle$ is shown in Fig. 3.4 (b). Figure 3.4 (c) shows the total electron number of the deoxy-heme molecule $\langle n_T \rangle = \langle n_d \rangle + \langle n_h \rangle$ versus μ. The total electron number of deoxy-heme is 334 electrons. We obtain this value at $\mu = -3.1$ eV. Thus, the HOMO levels of the triplet state is $\mu = -3.1$ eV. At this μ value, the electron occupation number of Fe($3d$) orbitals is $\langle n_d \rangle \approx 6.13$ electrons.

For triplet ground state of deoxy-heme, Figures 3.5 (a) and (b) show the electron numbers of Fe($3d_\nu$) orbitals and square of magnetic moment of Fe($3d_\nu$) orbitals as a function of chemical potential μ. In Fig. 3.5 (a), Fe(3d) xz, xy, yz and $3z^2 - r^2$ orbitals become singly occupied in the interval -4.5 eV $\leq \mu \leq -3.5$ eV. When $x^2 - y^2$ orbital becomes singly occupied at $\mu \approx 2.5$ eV, it becomes doubly occupied at -1 eV. In this interval, magnetic moments of Fe($3d_\nu$) orbitals have the highest values in Fig. 3.5 (b). When Fe($3d_\nu$) orbitals become doubly occupied at -2 eV, magnetic moments of them are zero. In Fig. 3.5 (a), the occupation number of $x^2 - y^2$ orbital suddenly increases at $\mu = -2.5$ eV. In the same way, the square of its magnetic moment suddenly increases at the same μ value. This increase can be an impurity bound state (IBS). For this reason, we need to look the occupancy number and magnetic moment of m'th host states.

Figures 3.6 (a) and 3.6 (b) show the electron occupation number $\langle n_m \rangle$ and square of the magnetic moment $\langle (M_m^z)^2 \rangle$ of the m'th host state as a function of μ. $m = 145$th and 146th host state become singly occupied at $\mu = -8$ eV. When $m = 152$nd host state becomes singly occupied at $\mu = -7.5$ eV, this host state has the highest magnetic moment. In Figures 3.6 (a) and 3.7 (a) the electron occupation number of host states for $m = 144$th, 153rd, 163rd 166th and 167th are less than 0.5 electrons along the μ values. In Fig. 3.7 (a) $\langle n_m \rangle$ of host $m = 165$th state is doubly occupied at $\mu = -1$ eV. We observe that the $m = 152$nd host state has the highest hybridization matrix elements with $3d_{x^2 - y^2}$ orbital as shown in Fig. 3.2 (a). In Fig. 3.6 (a), the occupation number of $m = 152$nd host state suddenly increases at $\mu = -2.5$ eV and is nearly doubly occupied. Then, square of magnetic moment of $m = 152$nd host state decreases at $\mu = -2.5$ eV.

Figures 3.8 and 3.9 show the magnetic correlation function $\langle M_\nu^z M_m^z \rangle$ between $m = 144$th, 145th, 146th, 152nd, 163rd, 165th, 166th and 167th host eigenstates and the Fe($3d_\nu$) orbitals. $m = 144$th host state has ferromagnetic correlation in the interval -5 eV $\leq \mu \leq -1$ eV. $m = 145$th, 146th, 152nd, 163rd, 166th and 167th host states have anti-ferromagnetic correlations in the interval -8 eV $\leq \mu \leq -1$ eV. The impurity bound state (IBS) is located the contribution of magnetic correlations between $x^2 - y^2$ orbital and $m = 152$nd host state at $\mu = -2.5$ eV as shown in Fig. 3.8 (d). The IBS is defined as the end of antiferromagnetic correlations. Hence, we find that the spin state of
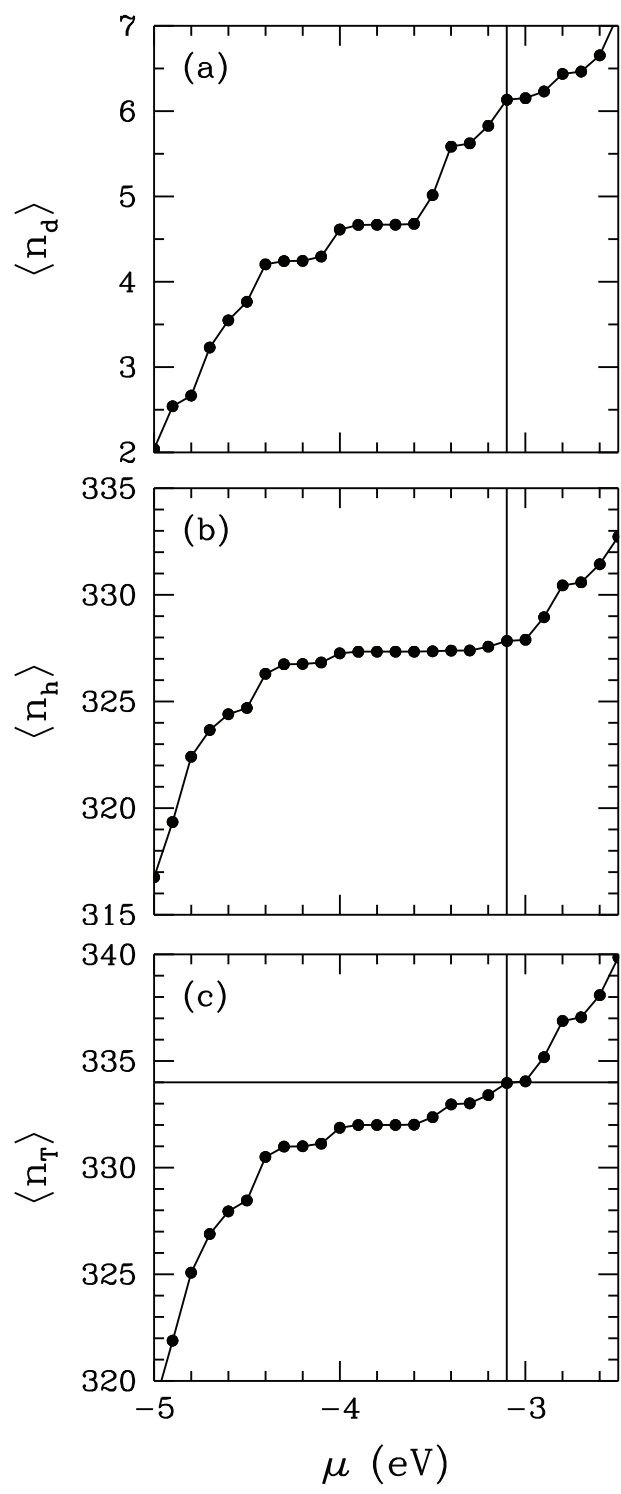
Figure 3.4. For triplet-spin state of deoxy-heme, DFT(BP86/6-31G) results on the electron occupation numbers. (a) Total electron occupation number $\langle n_d \rangle$ of the Fe($3d$) orbitals, (b) total electron number of the host orbitals $\langle n_h \rangle$, (c) total number of electrons $\langle n_T \rangle = \langle n_d \rangle + \langle n_h \rangle$ as a function of the chemical potential μ. Here, the vertical solid line denotes the HOMO level of the triplet-spin state calculated by the DFT method.
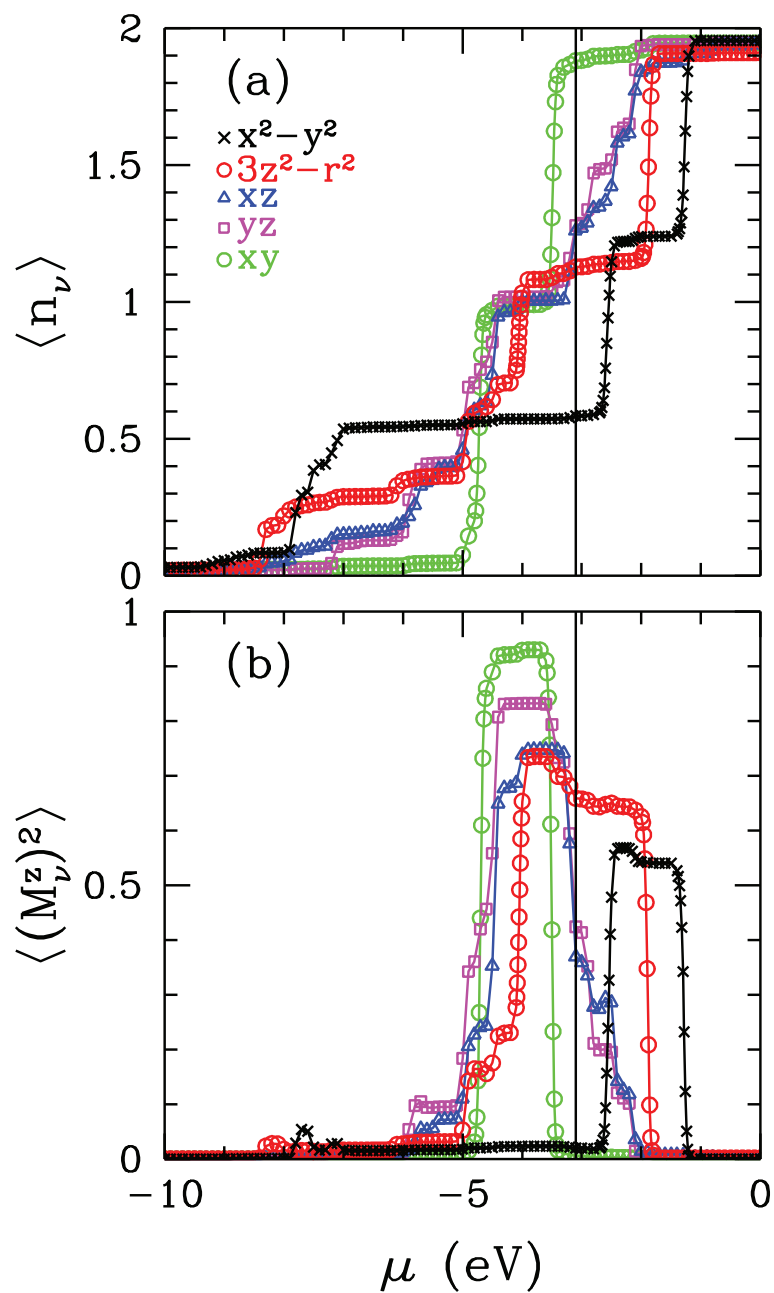
Figure 3.5. For triplet-spin state of deoxy-heme (a) DFT(BP86/6-31G) results on the electron occupation number $\langle n_\nu \rangle$ of the Fe($3d_\nu$) as a function of the chemical potential μ. (b) Square of the magnetic moment $\langle (M_\nu^z)^2 \rangle$ for the Fe($3d_\nu$) orbitals versus the chemical potential μ. Here, the vertical solid denotes the value of the HOMO level and it is calculated by DFT method.
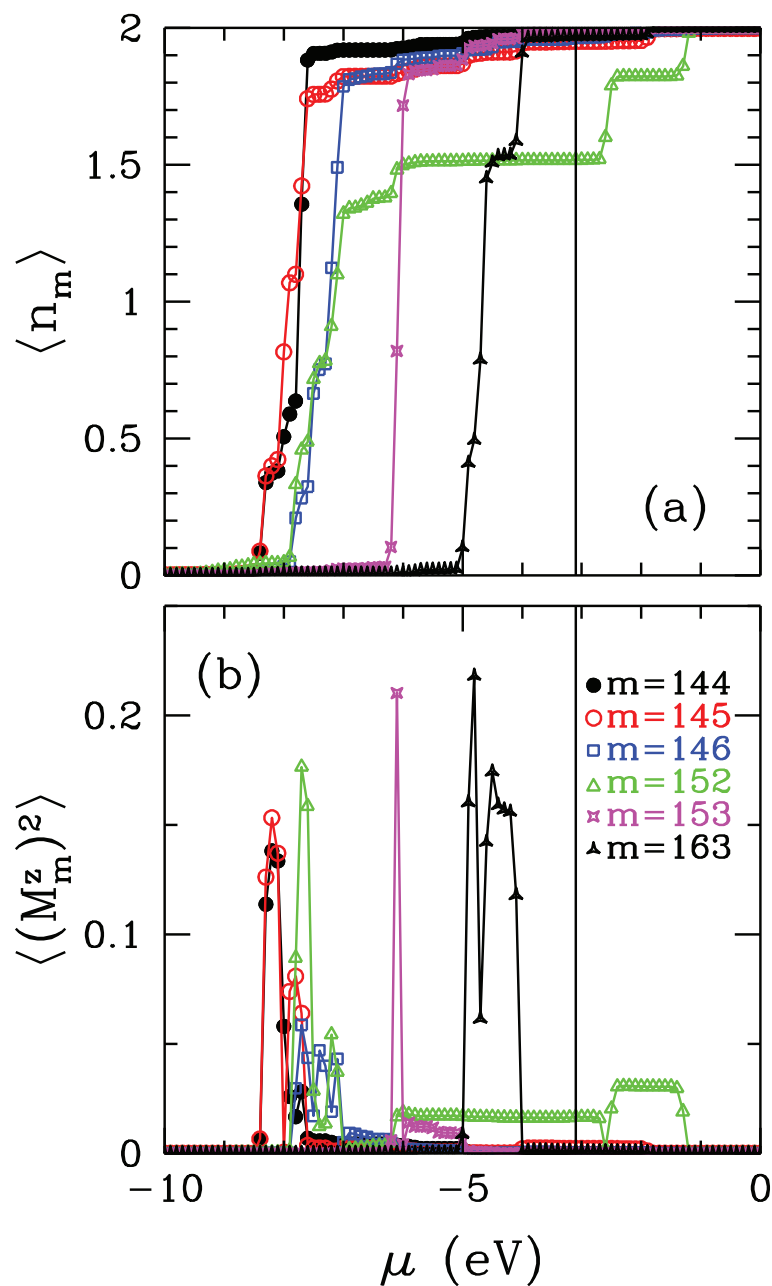
Figure 3.6. For triplet-spin state of deoxy-heme (a) DFT(BP86/6-31G) results on the electron occupation number of the m'th host state n_m versus the chemical potential μ. (b) Square of the magnetic moment of the $m = 144$th, 145th, 146th, 152nd, 153rd and 163rd host states $(M_m^z)^2$ versus μ. Here, the vertical solid denotes the value of the HOMO level and it is calculated by the DFT method.
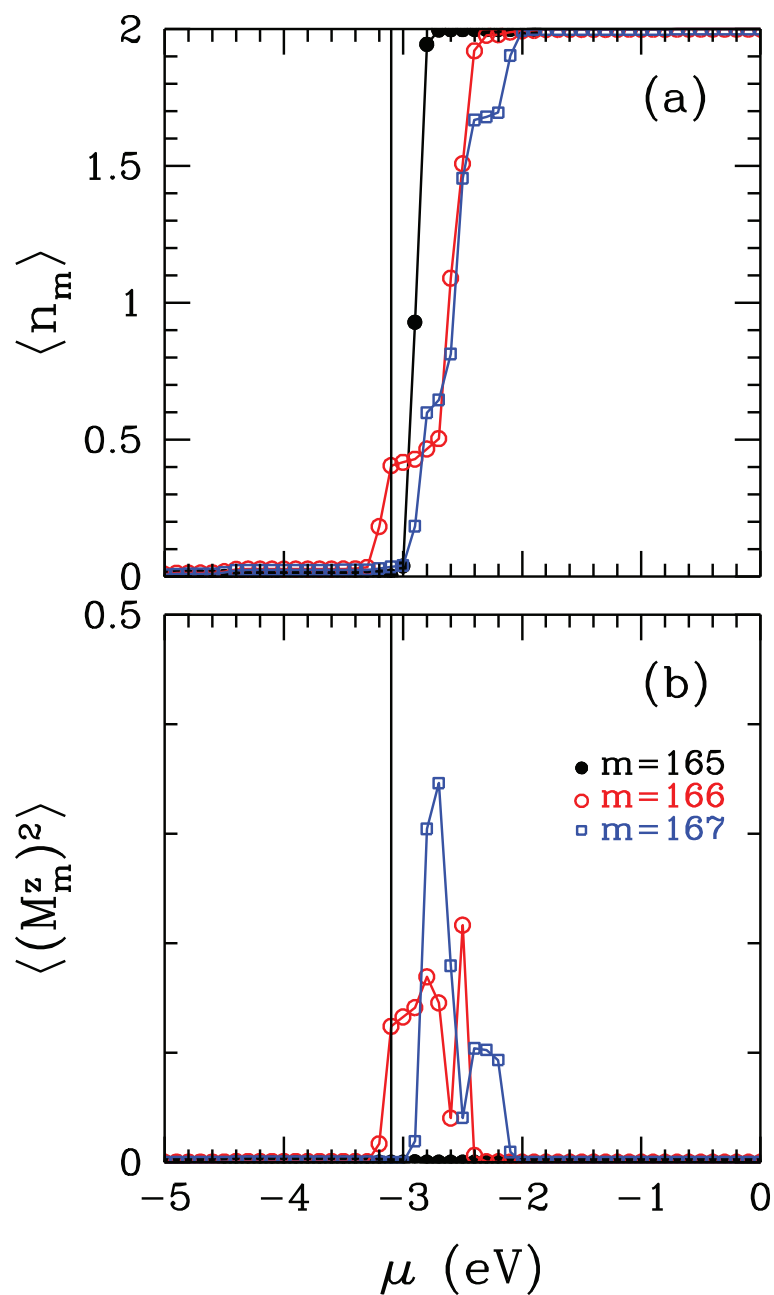
Figure 3.7. For triplet-spin state of deoxy-heme (a) DFT(BP86/6-31G) results on the electron occupation number of the m'th host state n_m versus the chemical potential μ. (b) Square of the magnetic moment of the $m = 165$th, 166th and 167th host states $(M_m^z)^2$ versus μ. Here, the vertical solid denotes the value of the HOMO level and it is calculated by the DFT method.

deoxy-heme is triplet-spin state because the IBS is located above the Fermi level and is unoccupied. For deoxy-heme, DFT method does not find the location of IBS correctly.

For the triplet-spin state, the total energy value of deoxy-heme is -87040.34 eV. For the quintuplet-spin state, the total energy value of deoxy-heme is -87040.28 eV. The difference between their energies is 60 meV. Here, we show the quintuplet-spin state for deoxy-heme. For the quintuplet-spin state of deoxy-heme, DFT finds that the location of IBS is below the Fermi level and IBS is occupied. These results are very similar to DFT+MFA and DFT+QMC results.

For quintuplet-spin state of deoxy-heme, Figures 3.10 (a) and (b) show the electron numbers of Fe($3d_\nu$) orbitals and effective magnetic moment of Fe($3d_\nu$) orbitals as a function of chemical potential μ. In Fig. 3.10 (a), Fe(3d) orbitals become singly occupied at $\mu \approx -3.5$ eV. At this value, effective magnetic moments of Fe($3d_\nu$) orbitals have the highest values in Fig. 3.10 (b). When Fe($3d_\nu$) orbitals become doubly occupied at $\mu = -1$ eV, effective magnetic moments of them are zero. In Fig. 3.10 (a), the occupation number of $x^2 - y^2$ orbital suddenly increases at $\mu = -3.5$ eV. In the same way, its effective magnetic moment suddenly increases at this μ value. This increase is an impurity bound state (IBS). IBS is located below the HOMO level and it is occupied. Here, we show the location of IBS with a light blue vertical ellipse at $\mu = -3.5$ eV. For this reason, we need to look at the occupancy number and effective magnetic moment of m=152nd host state.

We observe that the $m = 152$nd host state has the highest hybridization matrix elements with $3d_{x^2-y^2}$ orbital as shown in Fig. 3.2 (a). In Fig. 3.11 (a), the occupation number of $m = 152$nd host state suddenly increases at $\mu = -3.5$ eV and is nearly doubly occupied. Then, the effective magnetic moment of $m = 152$nd host state decreases at $\mu = -3.5$ eV. At this value, the location of IBS is shown with a black vertical ellipse.

For quintuplet-spin state of deoxy-heme, DFT(BP86/6-31G) results on the magnetic correlation function $\langle M_\nu^z M_m^z \rangle$ between the $m = 152$nd host eigenstate and the Fe($3d_\nu$) orbitals as shown in Fig. 3.12. The location of IBS is shown with a light blue vertical ellipse at $\mu = -3.5$ eV. In Fig. 3.12, $m = 152$nd host state has anti-ferromagnetic correlation in the interval -6 eV $\leq \mu \leq -3.5$ eV. The IBS is located the contribution of magnetic correlations between $x^2 - y^2$ orbital and $m = 152$nd host state at $\mu = -3.5$ eV as shown in Fig. 3.8. The IBS is defined as the end of antiferromagnetic correlation. For quintuplet-spin state of deoxy-heme, the IBS is located below the Fermi level and IBS is occupied.
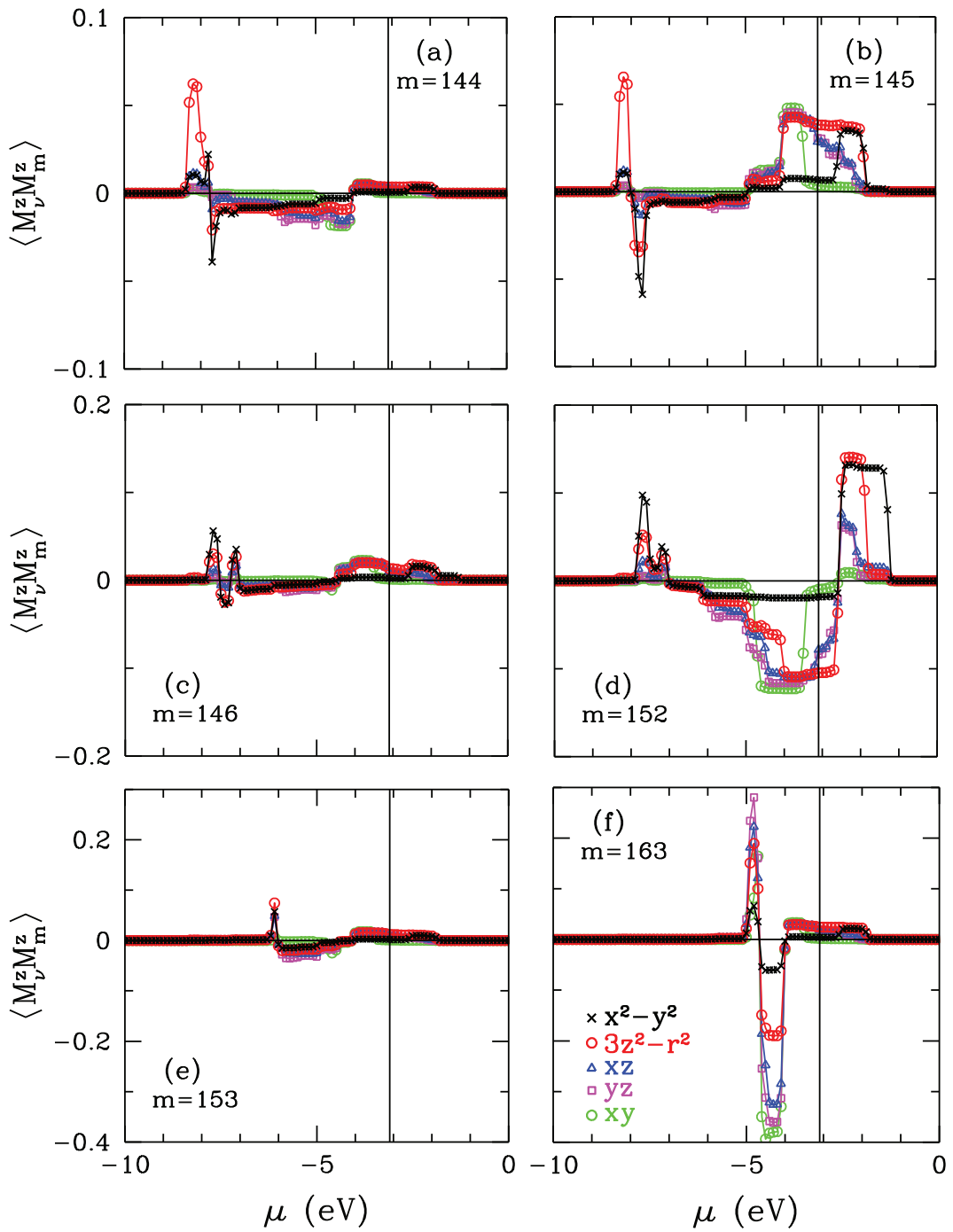
Figure 3.8. For triplet-spin state of deoxy-heme, DFT(BP86/6-31G) results on the magnetic correlation function $\langle M_\nu^z M_m^z \rangle$ between the m'th host eigenstate and the Fe($3d_\nu$) orbitals. Here results are shown for host states (a) $m =$ 144th, (b) 145th, (c) 146th, (d) 152nd, (e) 153rd, and (f) 163rd. Here, the vertical solid denotes the value of the HOMO level and it is calculated by the DFT method.
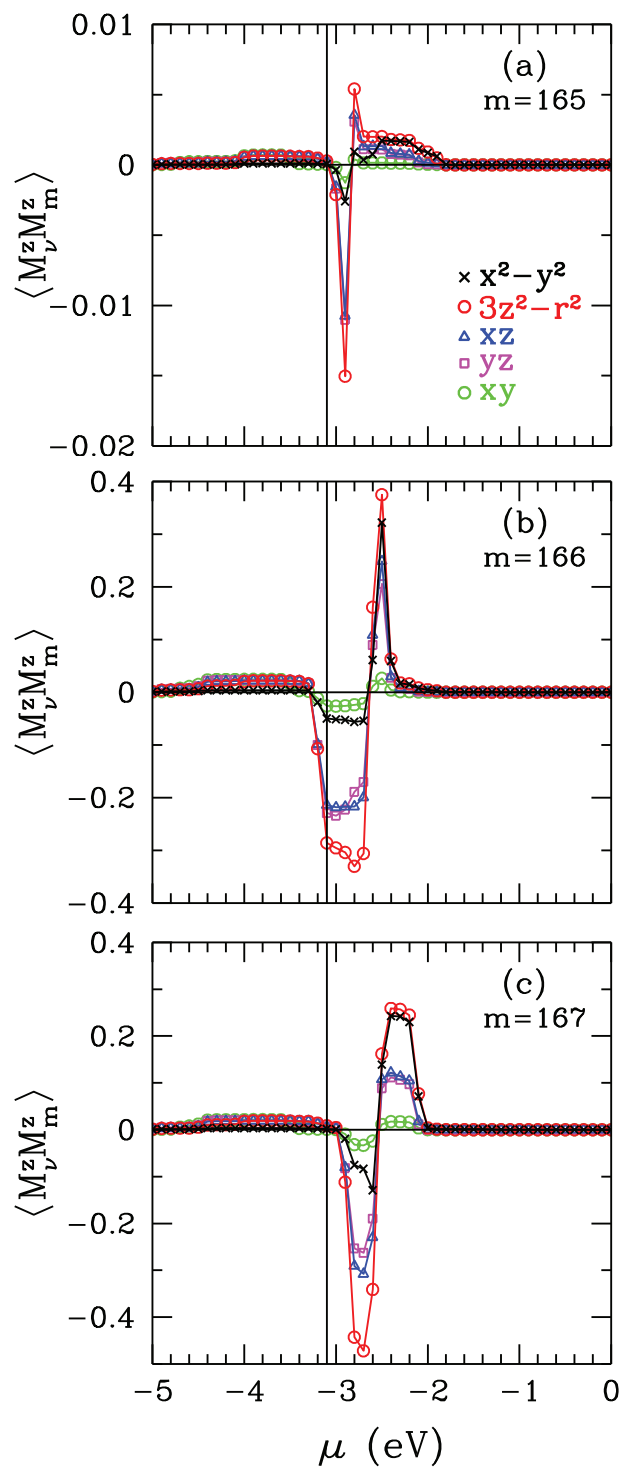
Figure 3.9. For triplet-spin state of deoxy-heme, DFT(BP86/6-31G) results on the magnetic correlation function $\langle M_\nu^z M_m^z \rangle$ between the m'th host eigenstate and the Fe($3d_\nu$) orbitals. Here results are shown for host states (a) $m =$ 165th, (b) 166th, and (c) 167th. Here, the vertical solid denotes the value of the HOMO level and it is calculated by the DFT method.
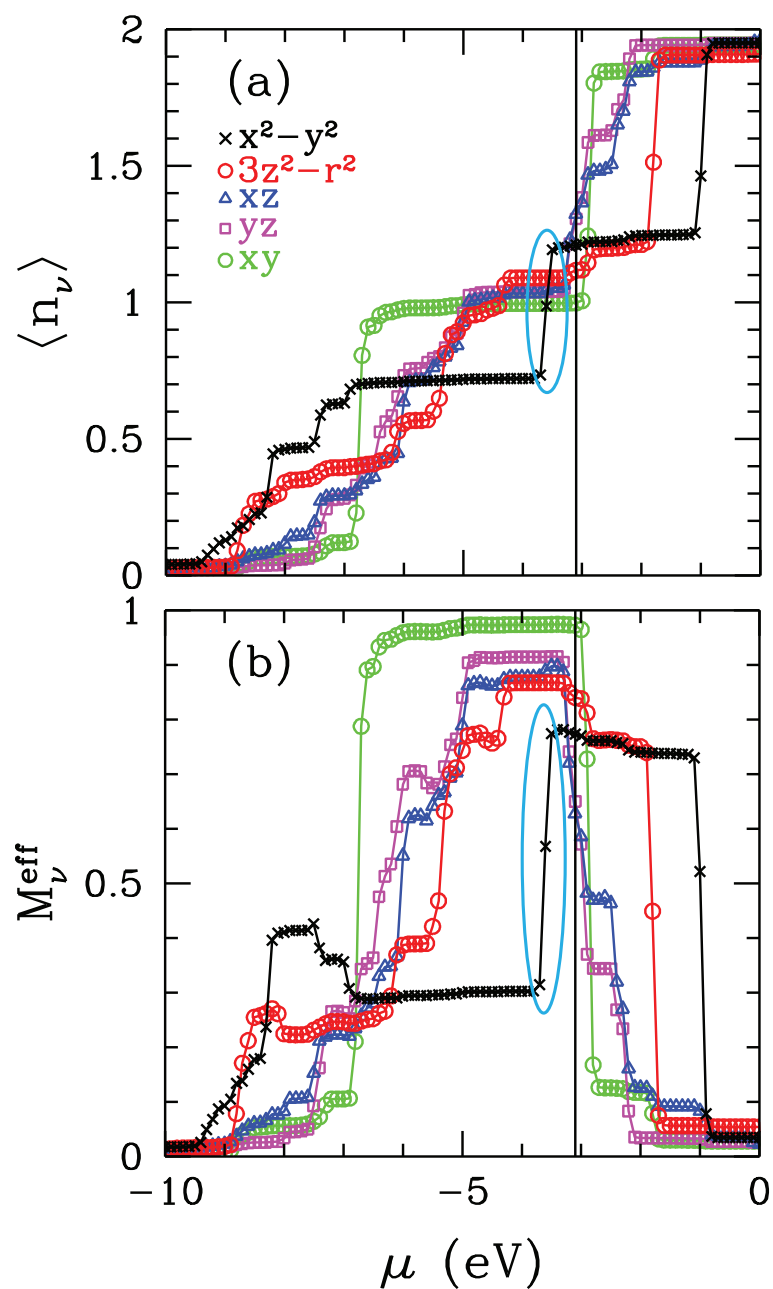
Figure 3.10. For quintuplet-spin state of deoxy-heme (a) DFT(BP86/6-31G) results on the electron occupation number $\langle n_\nu \rangle$ of the Fe($3d_\nu$) as a function of the chemical potential μ. (b) The effective magnetic moment M_ν^{eff} for the Fe($3d_\nu$) orbitals versus the chemical potential μ. Here, the vertical solid denotes the value of the HOMO level and it is calculated by the DFT method. The location of IBS is shown with the light blue vertical ellipse.
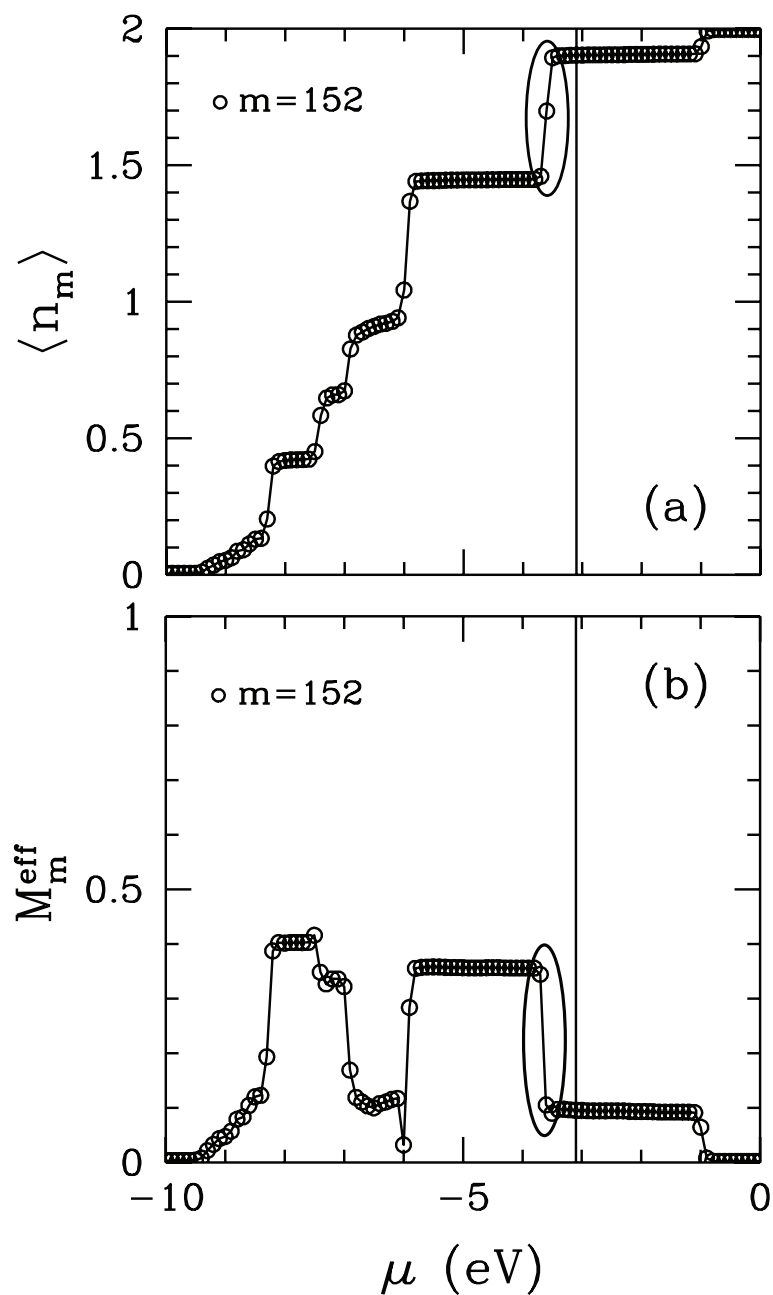
Figure 3.11. For quintuplet-spin state of deoxy-heme (a) DFT(BP86/6-31G) results on the electron occupation number of the $m = 152$nd host state n_m versus the chemical potential μ. The effective magnetic moment of the $m = 152$nd host state M_m^{eff} versus μ. Here, the vertical solid denotes the value of the HOMO level and it is calculated by the DFT method. The location of IBS is shown with the black vertical ellipse.
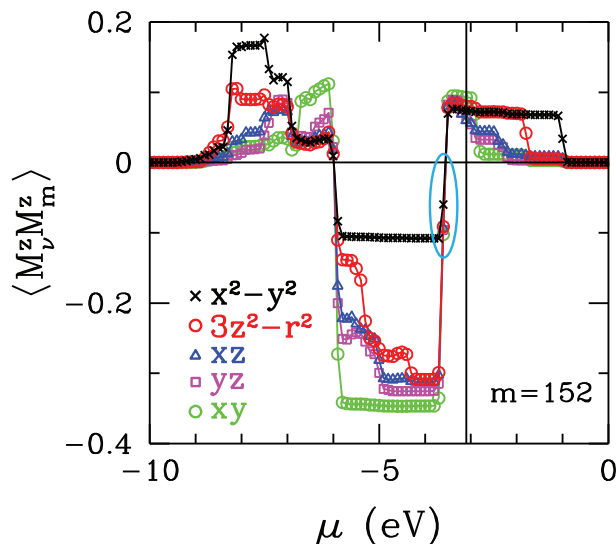
Figure 3.12. For quintuplet-spin state of deoxy-heme, DFT(BP86/6-31G) results on the magnetic correlation function $\langle M_\nu^z M_m^z \rangle$ between the $m = 152$nd host eigenstate and the Fe($3d_\nu$) orbitals. Here, the vertical solid denotes the value of the HOMO level and it is calculated by the DFT method. The location of IBS is shown with the light blue vertical ellipse.

3.2. DFT results of deoxy-heme by using various basis sets

In this section, we will show the DFT results of deoxy-heme by using different basis sets: 6-31G(d), 6-31G(d,p), DGDZVP, cc-pVDZ, and LanL2DZ+6-31G. We choose the same energy functional (BP86) for these basis sets. Here, we show the square of hybridization matrix elements between the Fe($3d$) orbitals and the m'th host states for these basis sets. We increase the size of the 6-31G basis set by adding the d and p polarizations. The DGDZVP basis set is a double zeta valence polarization used in the range between hydrogen and xenon atoms (Godbout et al. (1992); Sosa et al. (1992)). The cc-pVDZ is the Dunning polarized correlation consistent double zeta basis set (Dunning Jr (1989); Woon and Dunning Jr (1993)). The LanL2DZ basis set is Los Alamos effective core potential plus double zeta (Hay and Wadt (1985)). We use the LanL2DZ basis set for the Fe atom and 6-31G basis set for C, N, O and H atoms in the deoxy-heme. Here, we will show the differences between 6-31G basis set and the other basis sets. The results of the NBO analysis are shown the core, valence and rydberg orbital types for the basis sets in Tables 3.2, 3.3 and 3.4. The p and d orbitals consist of p_x, p_y, p_z and $d_{xy}, d_{xz}, d_{yz}, d_{x^2-y^2}, d_{3z^2-r^2}$, respectively.

Table 3.2. For deoxy-heme, the results of the NBO analysis are shown the types of core, valence and rydberg orbitals for the 6-31G basis set. The numbers in parenthesis give the number of atoms for deoxy-heme. The number of basis functions of the deoxy-heme is 483 for the 6-31G basis set. Here, the three p and five d orbitals consist of p_x, p_y, p_z and d_{xy}, d_{xz}, d_{yz}, $d_{x^2-y^2}$, $d_{3z^2-r^2}$, respectively.

BP86/6-31G	Core	Valence	Rydberg	Basis Function
Fe(1)	$1s, 2s, 2p, 3s, 3p$	$4s, 3d$	$4p\ 4d, 5s, 5p$	$27\times(1)=27$
C(32), N(10), O(2)	$1s$	$2s, 2p$	$3s, 3p$	$9\times(32+10+2)=396$
H(30)	-	$1s$	$2s$	$2\times(30)=60$
				Total=483

For deoxy-heme (75 atoms cluster), we perform the DFT calculations by using BP86 exchange-correlation energy functional and various basis sets. These basis sets are 6-31G(d), 6-31G(d,p), DGDZVP, cc-pVDZ, and LanL2DZ+6-31G. For these basis sets, we calculate the square of hybridization matrix elements $|V_{m\nu}|^2$ between the Fe($3d_\nu$) orbitals and m'th host states as a function of the m'th host eigenvalues ε_m. The DFT results on the BP86/6-31G basis set are shown in Section 3.1. In Fig. 3.2, we showed the $|V_{m\nu}|^2$ of the deoxy-heme for 6-31G basis set. Here, the hybridization matrix elements of the 6-31G basis set will be compared with the other basis sets.

In Fig. 3.2, we observed that the $m = 152$nd host state has the highest hybridization matrix elements with $3d_{x^2-y^2}$ orbital. Similarly, it is found that the $m = 152$nd host state has the highest hybridization matrix elements with $3d_{x^2-y^2}$ orbital for 6-31G(d) and 6-31G(d,p) basis sets as shown in Fig. 3.13. The hybridization contributions of other host states have changed little for the $3d$ orbitals. In addition, for 6-31G(d) and 6-31G(d,p) basis sets the $m = 152$nd host state is still composed of the $2p$'s orbitals of 4N's atoms. Here, the vertical solid and dashed lines denote the values of the HOMO and LUMO, respectively. For these basis sets, the values of HOMO and LUMO levels, the energy gap and the total occupation number of Fe($3d$) orbitals are shown in Table 3.5.

For these various basis sets, we find that the ground state energy of deoxy-heme is still the triplet-spin state. We do not show the results of these different basis sets because they are similar to the results of Section 3.1.1.

Table 3.3. For deoxy-heme, the results of the NBO analysis are shown the types of adding rydberg orbitals for the 6-31G(d), 6-31G(d,p) and cc-pVDZ basis sets. The number of basis functions of the deoxy-heme is 710, 800 and 809 for the 6-31G(d), 6-31G(d,p) and cc-pDVZ basis sets, respectively. Here, the three p and five d orbitals consist of p_x, p_y, p_z and d_{xy}, d_{xz}, d_{yz}, $d_{x^2-y^2}$, $d_{3z^2-r^2}$, respectively. There are seven f orbitals: ($f_{y(3z^2-y^2)}$, $f_{z(x^2-y^2)}$, f_{yz^2}, f_{z^3}, f_{xz^2}, f_{xyz} and $f_{x(x^2-3y^2)}$).

For 6-31G(d)	Adding Rydberg	Basis Function
6-31G	-	483
Fe	$4f$	7×(1)=7
C, N, O	$3d$	5×(44)=220
H	-	-
		Total=710
For 6-31G(d,p)		
6-31G(d)	-	710
Fe	-	-
C, N, O	-	-
H	$2p$	3×(30)=90
		Total=800
For cc-pVDZ		
6-31G	-	483
Fe	$6s$, $6p$, $5d$, $4f$	16×(1)=16
C, N, O	$3d$	5×(44)=220
H	$2p$	3×(30)=90
		Total=809

Table 3.4. For deoxy-heme, the results of the NBO analysis are shown the types of removing rydberg orbitals for the DGDZVP and LanL2DZ+6-31G basis sets. The number of basis functions of the deoxy-heme is 700 and 478 for the DGDZVP and LanL2DZ+6-31G basis sets, respectively. Here, the p and d orbitals consist of p_x, p_y, p_z and d_{xy}, d_{xz}, d_{yz}, $d_{x^2-y^2}$, $d_{3z^2-r^2}$, respectively. There are seven f orbitals.

For DGDZVP	Removing Rydberg	Basis Function
6-31G(d)	-	710
Fe	$5p$, $4f$	-(3+7)
C, N, O	-	-
H	-	-
		Total=700
For LanL2DZ+6-31G		
6-31G	-	483
Fe	$1s$, $2s$, $2p$	-5
C, N, O	-	-
H	-	-
		Total=478

Table 3.5. For deoxy-heme, the results of the different basis sets on the total electron numbers of Fe($3d$) orbitals. The HOMO and LUMO levels and the energy gap of deoxy-heme are given for the different basis sets. The HOMO and LUMO energies are given in electron volts.

Basis Sets	$n_{\text{Fe}(3d)}$	E_{HOMO}	E_{LUMO}	E_{gap}
6-31G	6.25	-3.53	-3.02	0.51
6-31G(d)	6.28	-3.56	-3.06	0.50
6-31G(d,p)	6.28	-3.58	-3.07	0.51
DGDZVP	6.78	-4.04	-3.43	0.61
cc-pVDZ	6.78	-3.84	-3.26	0.58
LanL2DZ+6-31G	6.82	-3.80	-2.92	0.88
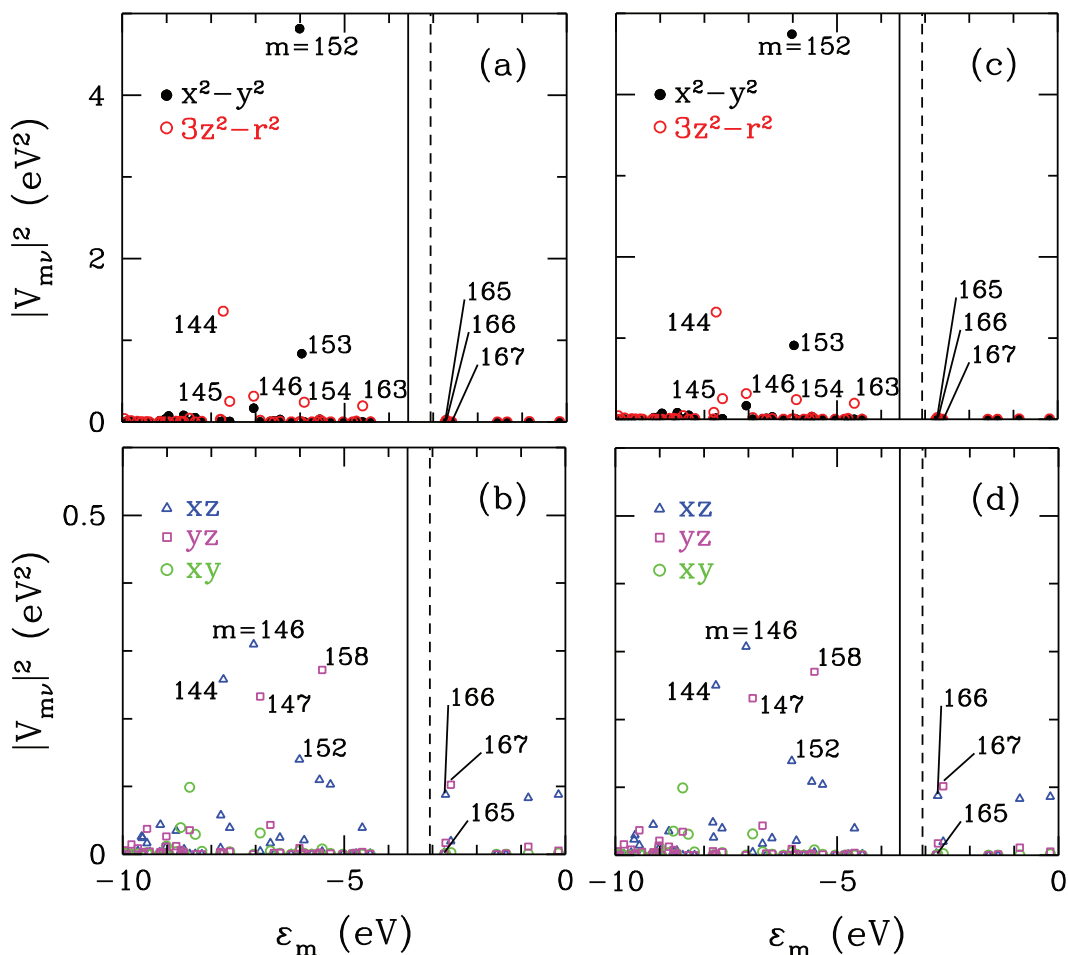
Figure 3.13. For deoxy-heme, (a) and (b) the results of 6-31G(d) basis set, (c) and (d) the results of 6-31G(d,p) basis set on the square of hybridization matrix elements $|V_{m\nu}|^2$ between the m'th host eigenstates and Fe($3d_\nu$) natural atomic orbitals as a function of the m'th host eigenvalues ε_m. We observe that the 152nd host states have the highest hybridization matrix elements with $3d_{x^2-y^2}$ orbital for both basis sets. Here, the vertical solid and dashed lines denote the values of the HOMO and LUMO, respectively. The value of HOMO and LUMO levels are shown in Table 3.5.
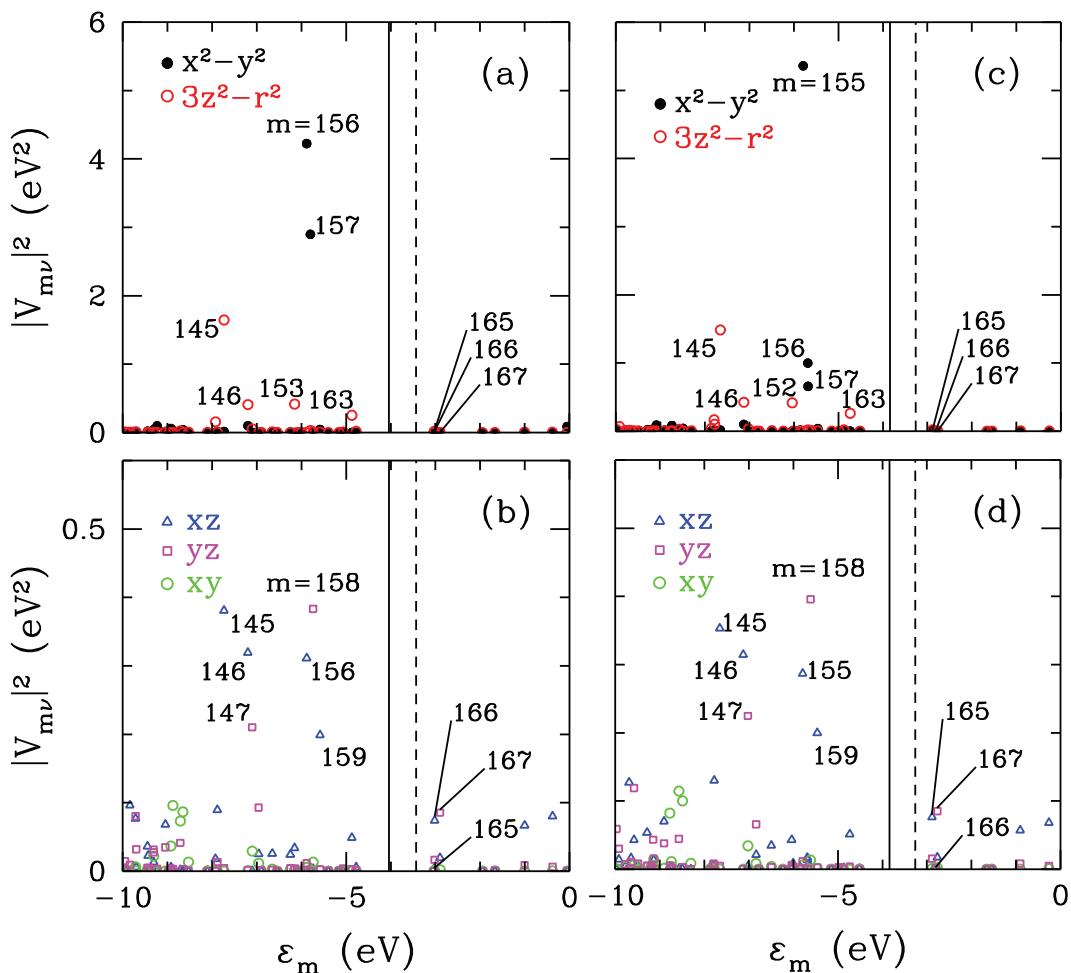
Figure 3.14. For deoxy-heme, (a) and (b) the results of DGDZVP basis set, (c) and (d) the results of cc-pVDZ basis set on the square of hybridization matrix elements $|V_{m\nu}|^2$ between the m'th host eigenstates and Fe($3d_\nu$) natural atomic orbitals as a function of the m'th host eigenvalues ε_m. We observe that for (a) DGDZVP basis set, the $m = 156$th host state and for (c) cc-pVDZ basis set, the $m = 155$th host state have the highest hybridization matrix elements with $3d_{x^2-y^2}$ orbital. Here, the vertical solid and dashed lines denote the values of the HOMO and LUMO, respectively. The value of HOMO and LUMO levels are shown in Table 3.5.
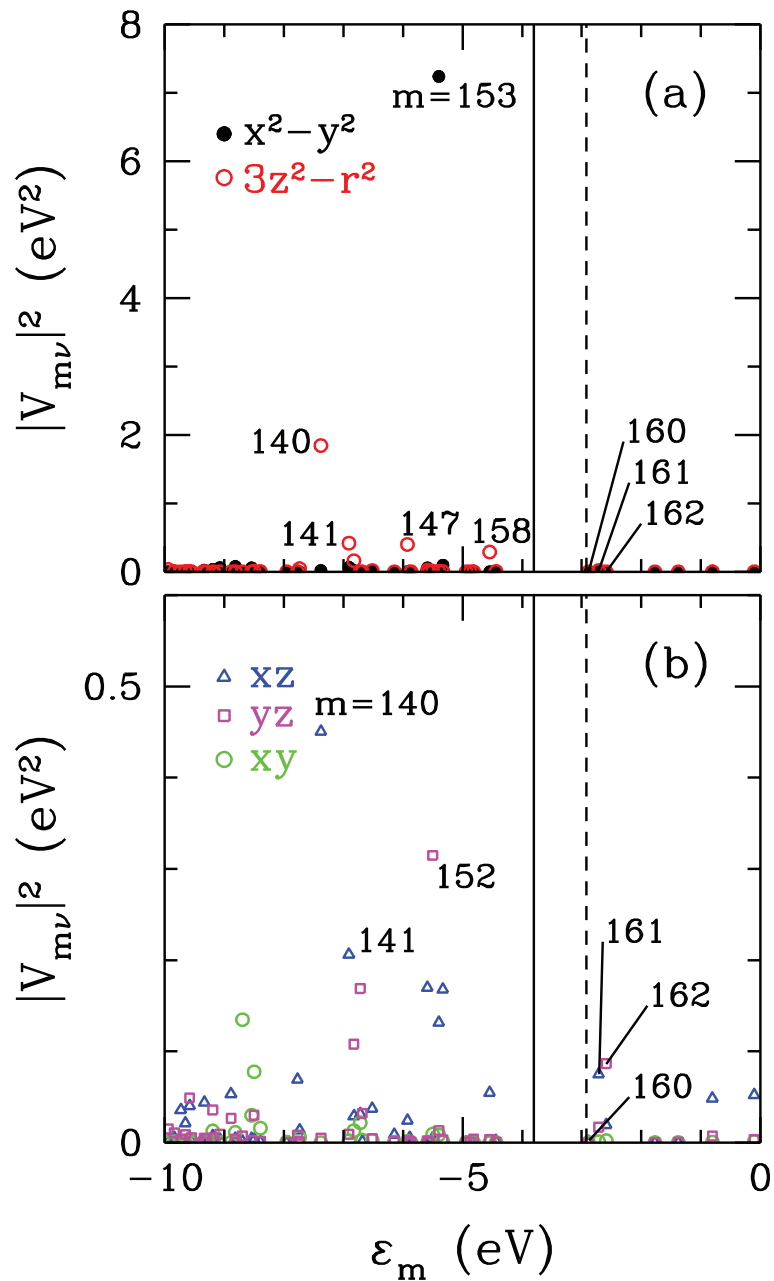
Figure 3.15. For deoxy-heme, DFT(BP86/LanL2DZ+6-31G) results on the square of hybridization matrix elements $|V_{m\nu}|^2$ between the m'th host eigenstates and Fe($3d_\nu$) natural atomic orbitals as a function of the m'th host eigenvalues ε_m. In (a) results are shown for $3d_{x^2-y^2}$ and $3d_{3z^2-r^2}$ orbitals, and in (b) for $3d_{xz}$, $3d_{yz}$ and $3d_{xy}$ orbitals. Here, the vertical solid and dashed lines denote the values of the HOMO and LUMO, respectively. The value of HOMO and LUMO levels are shown in Table 3.5. We observe that the $m = 153$rd host state has the highest hybridization matrix elements with $3d_{x^2-y^2}$ orbital.

3.3. DFT results for oxy-heme

For oxy-heme, we perform the DFT calculation by using BP86 exchange correlation energy functional and 6-31G basis set for singlet state. The results of the singlet state of oxy-heme are used in DFT+MFA and DFT+QMC. Figure 3.16 (a) shows the total density of states $D(\varepsilon)$ as a function of energy ε for oxy-heme. In this figure, the HOMO and LUMO values are located at -4.12 eV and -3.84 eV, respectively. In Fig. 3.16 (b), the host density of states $D_h(\varepsilon)$ is shown without Fe($3d_\nu$) orbitals. The Fe($3d_\nu$) levels have been shifted by the double counting term (Mayda et al. (2017)). This term is calculated for $U = 4$ eV, $J = 0.9$ eV $T = 300$ K. The new energies ($\tilde{\varepsilon}_{d\nu}$) of Fe($3d_\nu$) orbitals are located between -16 eV and -15 eV. The sort of new energies of Fe($3d_\nu$) orbitals is $3d_{yz}$, $3d_{xz}$, $3d_{xy}$, $3d_{3z^2-r^2}$ and $3d_{x^2-y^2}$ after shifting.

In Fig. 3.17, the square of the hybridization matrix elements $|V_{m\nu}|^2$ between the m'th host eigenstates and Fe($3d_\nu$) natural atomic orbitals are shown as a function of the m'th host eigenvalues ε_m for oxy-heme. We observed that the host states $m =$ 153rd, 154th, 158th, 159th and 173rd have the highest hybridization matrix elements. For $3d_{3z^2-r^2}$ orbital, $|V_{m\nu}|^2$ has the largest value at $m =$ 158th and 159th. For $3d_{xz}$ and $3d_{x^2-y^2}$ orbitals, $|V_{m\nu}|^2$ has the largest value for $m =$ 153rd, 154th, 158th, 159th and 173rd. In Fig. 3.17 (a-b), the host states $m =$ 174th, 175th and 176th have small hybridization contributions for the Fe($3d_\nu$) orbitals. These host states will contribute to the reduction of magnetic moment of the oxy-heme molecule. We have also shown them in Fig. 3.17.

Figure 3.18 shows the NAO composition of the m'th host eigenstate for oxy-heme. The Ref. (Kandemir et al. (2016); Kandemir (2013)) was explained more detail for NAO weight of the $|u_{mi}|^2$. The Fe atom is attached to the 11th and 12th oxygen ligand molecule (O$_2$) from above in the first part of Fig. 3.18. The Fe atom is attached to the 10th nitrogen (N) atom of the imidazole part. In addition, 2nd, 3rd, 4th and 5th N sites are connected to the Fe atom in porphyrin ring. In Figs. 3.18 (a) and 3.18 (b), NAO weights of $2p_z$ orbitals of 2nd, 3rd, 4th, 5th and 10th N sites are the largest value for $m =$ 153rd and 154th. Figures 3.18 (c) and 3.18 (d) show that the NAO weights of $2p$ orbitals of N sites in the porphyrin ring and $2p_z$ orbitals of 45th and 46th C atoms have the various values at $m =$ 158th and 159th. In Fig. 3.18 (e), NAO weights of $2p_x$ and $2p_z$ orbitals of 11th and 12th O sites are the largest value for $m =$ 173rd. In porphyrin layer, NAO weights of $2p_z$ orbitals of N and C atoms have the largest value for $m =$ 174th and 176th host states in Fig. 3.18 (f) and 3.18 (h). NAO weights of $2p_x$ and $2p_y$ orbitals of 21st C and 22nd O
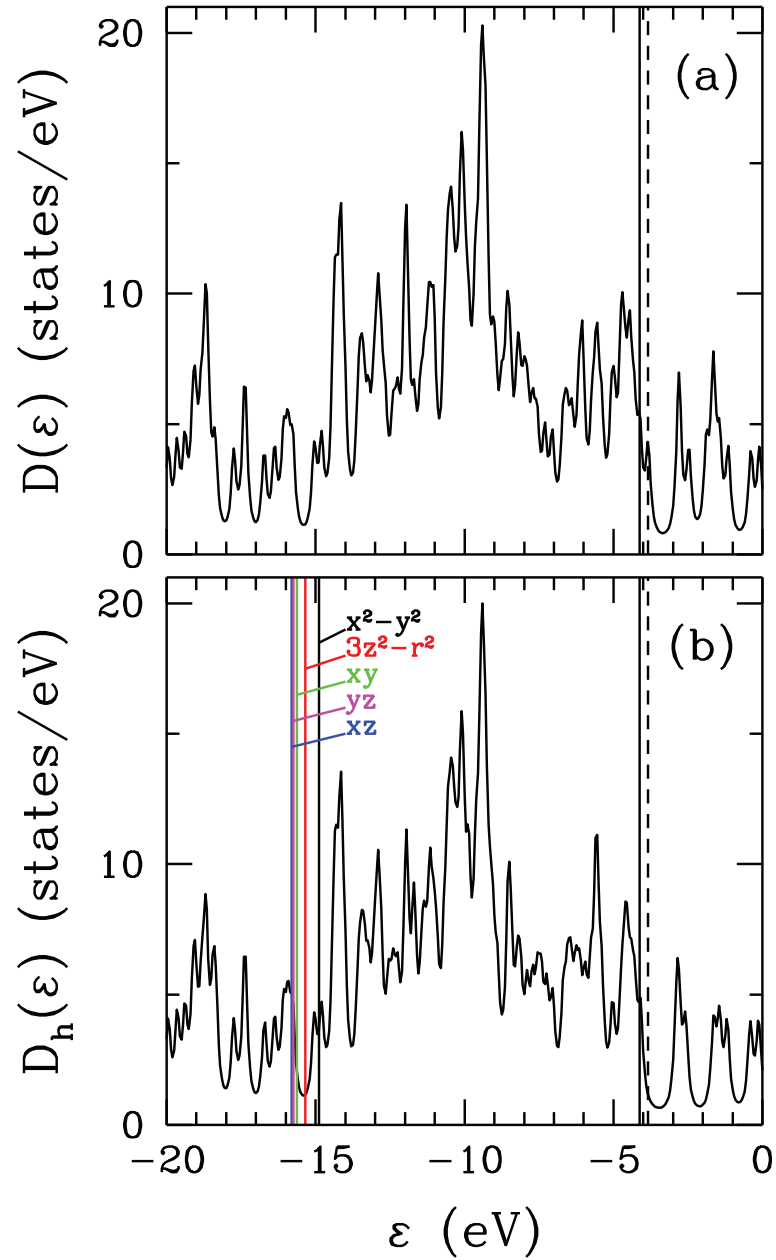
Figure 3.16. (a) For oxy-heme total density of states $D(\varepsilon)$ versus energy ε, obtained DFT(BP86) by using the Gaussian program. (b) For oxy-heme density of states of the host states $D_h(\varepsilon)$ of the extended Haldane-Anderson model. The Fe($3d_\nu$) levels have been shifted by the double counting term. This term is calculated for $U = 4$ eV and $J = 0.9$ eV. Here, the vertical solid and dashed lines denote the HOMO and LUMO levels, respectively.
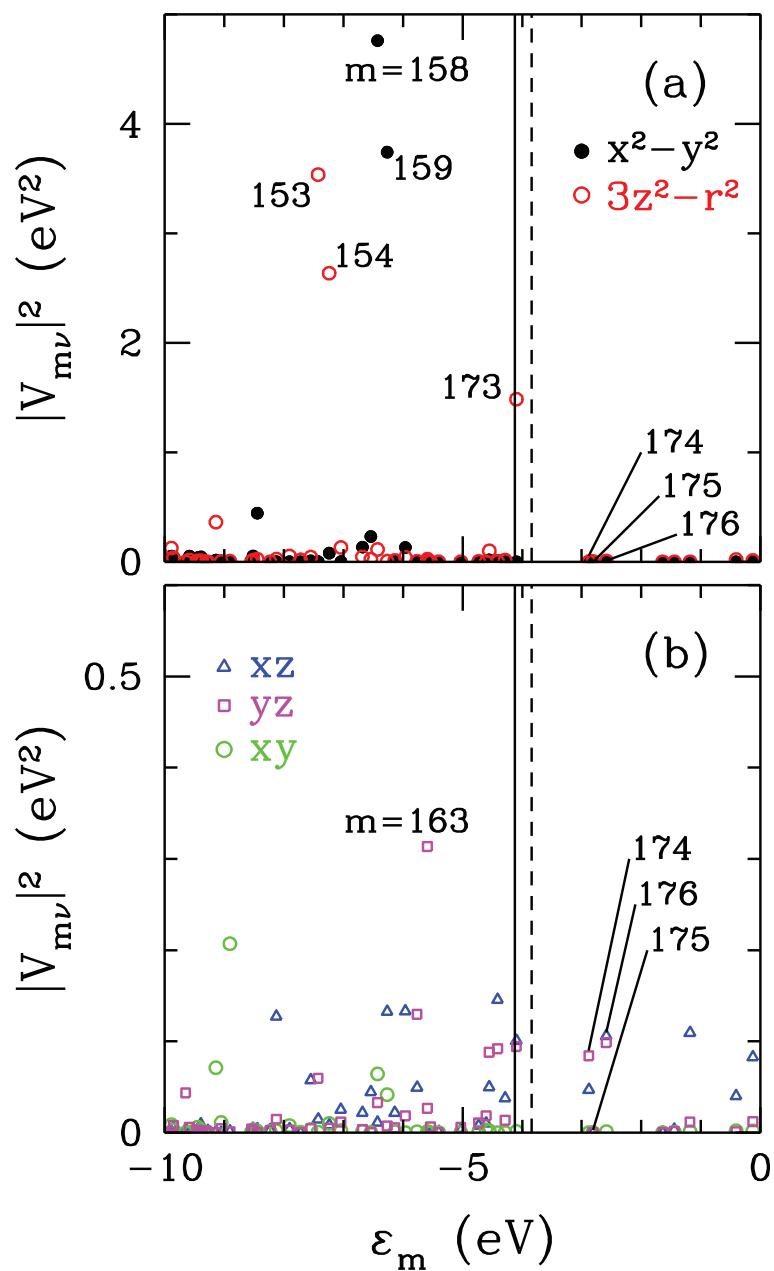
Figure 3.17. For oxy-heme, DFT(BP86) results on the square of hybridization matrix elements $|V_{m\nu}|^2$ between the m'th host eigenstates and Fe($3d_\nu$) natural atomic orbitals as a function of the m'th host eigenvalues ε_m. In (a) results are shown for $3d_{3z^2-r^2}$ and $3d_{xy}$ orbitals, and in (b) for $3d_{xz}$, $3d_{x^2-y^2}$ and $3d_{yz}$ orbitals. Here, the vertical solid and dashed lines denote the values of the HOMO and LUMO, respectively. We observe that the host state $m = 158$th has the highest hybridization matrix elements for $3d_{x^2-y^2}$ orbital. The hybridization contributions of the Fe($3d_\nu$) orbitals are small for the host states $m = 174$th, 175th and 176th.

atoms are high for $m = 175$th host state in Fig. 3.18 (g).

Figure 3.19 (a) shows the energy values of deoxy-heme and oxy-heme $E_n($ eV$)$ denote horizontal black lines for all states, obtained DFT(BP86) by using the Gaussian program. In the left hand side of Fig. 2.6 (a), while $n = 1, \ldots, 165, 166, 167$ states denote the occupied orbitals, $n = 168$ and sequential states indicate the virtual orbitals for deoxy-heme molecule. $n = 167$th and 168th states denote the highest occupied molecular orbital (HOMO) and lowest unoccupied (virtual) molecular orbital (LUMO), respectively. From DFT calculation of deoxy-heme, the energy values of HOMO and LUMO levels are obtained as $E_{\text{HOMO}(167)} = -3.53$ eV and $E_{\text{LUMO}(168)} = -3.02$ eV. In the right hand side of Fig. 3.19 (a), similarly for oxy-heme molecule, up to $n = 175$th state is the occupied orbitals, $n = 176$th and sequential states denote the virtual orbitals. From DFT calculation of oxy-heme, the energy values of HOMO and LUMO levels are obtained as $E_{\text{HOMO}(175)} = -4.12$ eV and $E_{\text{LUMO}(176)} = -3.84$ eV. Here, the horizontal solid line, which is longer than others, denotes the HOMO level.

In Fig. 3.19 (b), we show the energy levels of host and Fe$(3d_\nu)$ orbitals of deoxy-heme and oxy-heme molecules. While the horizontal black lines denote the energy levels of host orbitals ε_m, the color lines indicate the energy levels of Fe$(3d_\nu)$ orbitals $\varepsilon_{d\nu}$. These results are obtained by DFT calculation. Here, the thick solid black and blue lines, which are longer than others, denote the HOMO levels of deoxy and oxy, respectively. The HOMO levels of deoxy and oxy are obtained by DFT+MFA calculation.

Here, we show the results of the singlet state for the oxy-heme molecule. The total energies of open-shell and singlet, triplet and quintuplet states of oxy-heme are shown in Table 3.6. The open-shell singlet-spin state has the lowest energy value, so the ground state energy of oxy-heme is the open-shell singlet state. The results of the open-shell singlet-spin ground state of oxy-heme are explained in Section 3.3.1.

3.3.1. Results for open-shell singlet ground state for oxy-heme

For singlet state (S= 0), the Gaussian program finds equally the occupancies of alpha and beta orbitals. Firstly, we perform the energy calculation of the oxy-heme molecule for triplet state (S= 1). We obtain the checkpoint file of the triplet state for oxy-heme. Then, we start to calculate the energy for the single state of oxy-heme by using the checkpoint file of the triplet state. Thus, we obtain the results of an open-shell singlet state of the oxy-heme molecule. For oxy-heme, the total energy of the open-shell singlet state is less than the total energy of the singlet state.
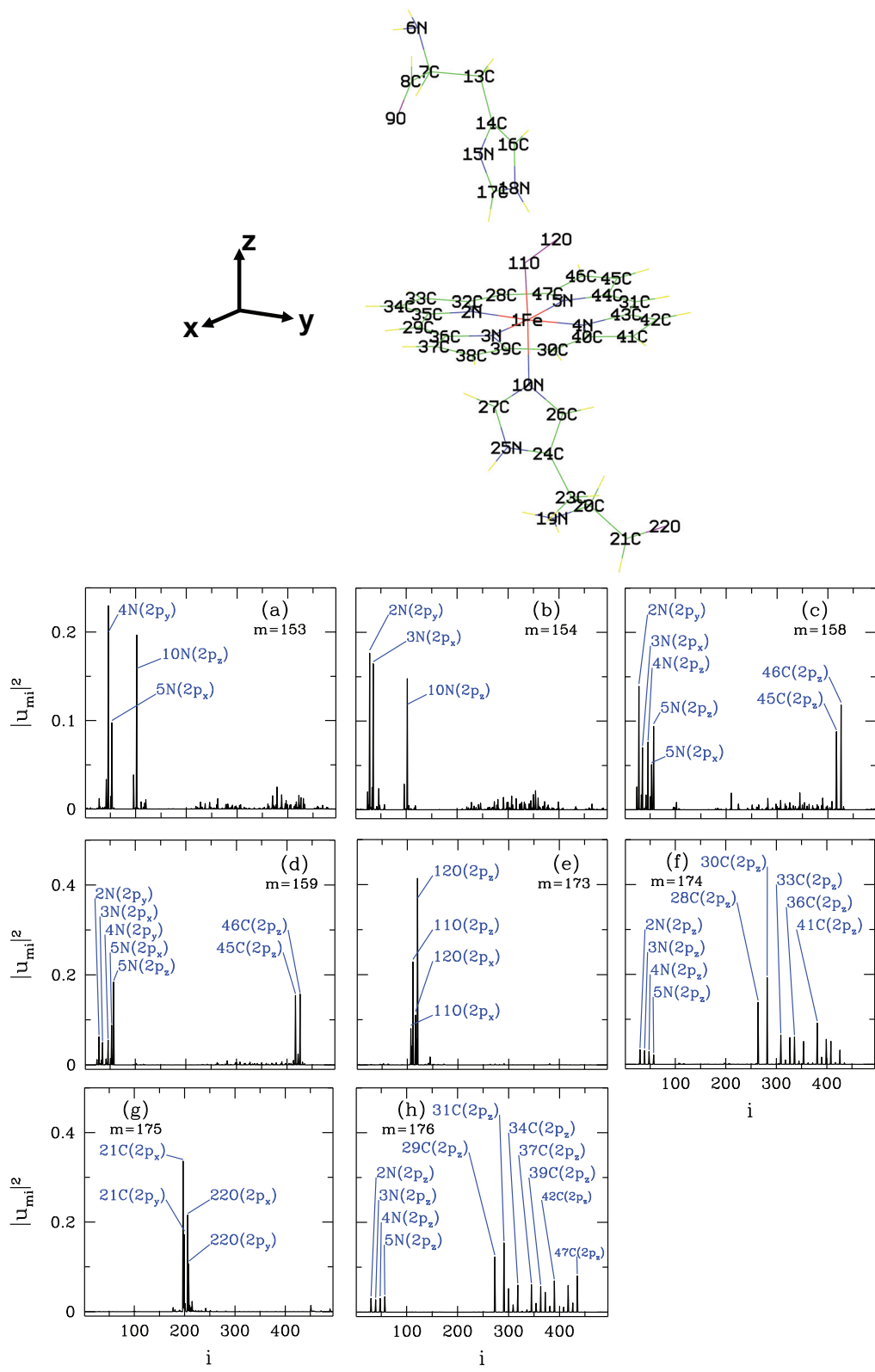
Figure 3.18. For oxy-heme, schematic plot with label numbers and symbols of atoms. The DFT results on the square of the host eigenstate ($|u_{mi}|^2$) contributions versus the label i for (a) $m = 153$rd, (b) 154th, (c) 158th, (d) 159th, (e) 173rd, (f) 174th, (g) 175th and (h) 176th host states.
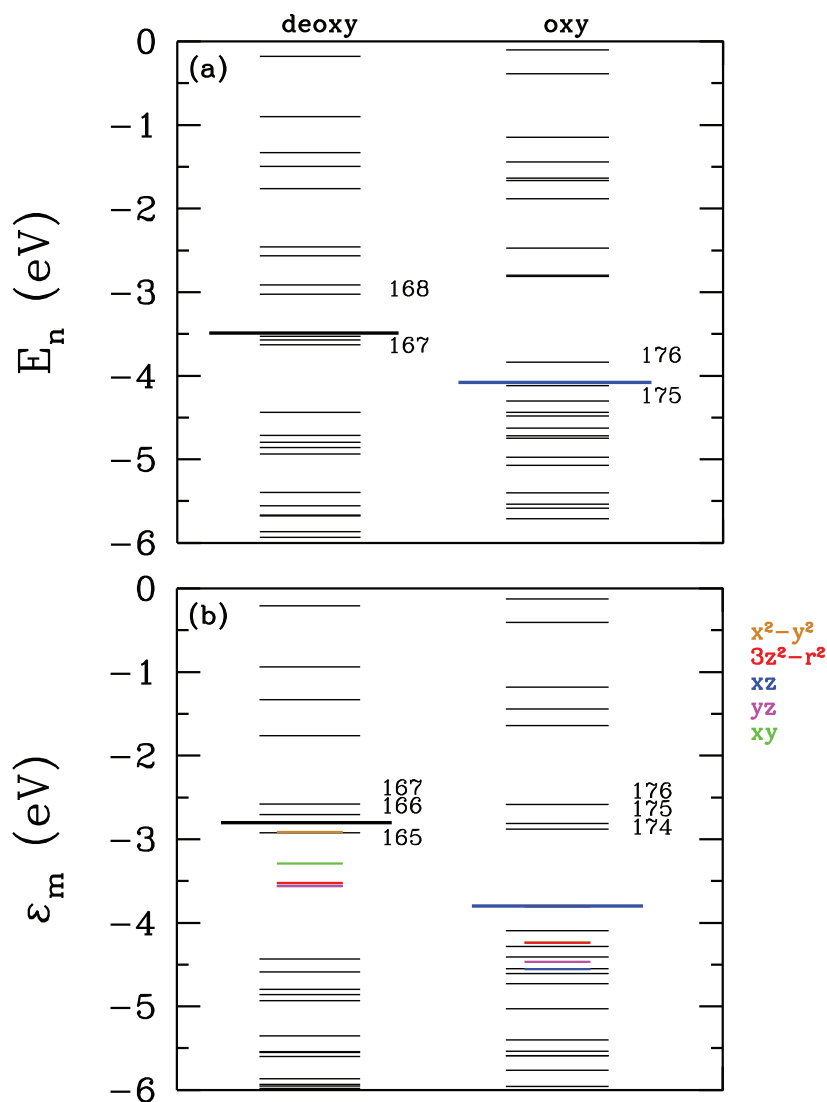
Figure 3.19. (a) For all states, the energy values of deoxy-heme and oxy-heme $E_n(\text{ eV})$ denote horizontal black lines. The thick black solid line denotes the HOMO level of the deoxy and the blue line denotes the HOMO level of oxy. These results are obtained by DFT calculation. (b) The energy values of host states and $Fe(3d_\nu)$ orbitals denote horizontal black lines and color lines, respectively. Here, the thick black solid and blue solid lines, which are longer than others, denote the HOMO levels of deoxy and oxy, respectively. The HOMO levels of deoxy and oxy are obtained by DFT+MFA calculation.

Table 3.6. DFT results on the total energies of open-shell and singlet, triplet and quin-
tuplet states of the oxy-heme molecule. DFT finds that the ground state
energy of oxy-heme is the open-shell singlet-spin state. Energies are given
in electron volts.

DFT (BP86/6-31G)	
Spin State	Total Energy
Quintuplet State (S=2)	-91128.96 eV
Singlet State (S=0)	-91130.09 eV
Triplet State (S=1)	-91130.14 eV
Open-shell Singlet Ground State	-91130.19 eV

In DFT results, we calculate the ground state energy of oxy-heme with the open-shell singlet state. The Gaussian program gives two different electrons as alpha and beta electrons in open-shell singlet state. For oxy-heme, n_ν defines the electron numbers of Fe($3d_\nu$) orbitals as total of up-electrons (alpha) $n_{\nu\uparrow}$ and down-electrons (beta) $n_{\nu\downarrow}$ in the first part of Table 6.5. The magnetic moment of Fe($3d_\nu$) orbitals M_ν^z is defined as differences of them and is given in Table 6.6. Similarly, for oxy-heme, the electron numbers of impurity orbitals $\langle n_{\nu\sigma}(\mu)\rangle$ and m'th host orbitals $\langle n_m^\sigma(\mu)\rangle$ are obtained by using Eq.(3.7) and Eq.(3.16) as a function of μ. For oxy-heme, we obtain that the electron numbers of Fe($3d_\nu$) orbitals with $\langle n_\nu(\mu)\rangle = \langle n_{\nu\uparrow}(\mu)\rangle + \langle n_{\nu\downarrow}(\mu)\rangle$ are shown in Fig. 3.20 (a) and the effective magnetic moment of Fe($3d_\nu$) orbitals with $M_\nu^{\text{eff}}(\mu) = \langle n_{\nu\uparrow}(\mu)\rangle - \langle n_{\nu\downarrow}(\mu)\rangle$ are shown in Fig. 3.20 (b). In addition, we obtain that the electron numbers of the m'th host orbitals with $\langle n_m(\mu)\rangle = \langle n_{m\uparrow}(\mu)\rangle + \langle n_{m\downarrow}(\mu)\rangle$ are shown in Figs. 3.21 (a) and 3.22 (a), the effective magnetic moment of the m'th host orbitals with $M_m^{\text{eff}}(\mu) = \langle n_{m\uparrow}(\mu)\rangle - \langle n_{m\downarrow}(\mu)\rangle$ are shown in Figs. 3.21 (b) and 3.22 (b).

For open-shell singlet ground state of oxy-heme, Fig. 3.20 (a) and Fig. 3.20 (b) are shown the electron numbers of Fe($3d_\nu$) orbitals and square of magnetic moment of Fe($3d_\nu$) orbitals as a function of chemical potential μ. In Fig. 3.20 (a), Fe($3d_\nu$) orbitals become singly occupied in the interval -5 eV $\leq \mu \leq -4$ eV. In this interval, magnetic moments of Fe($3d_\nu$) orbitals have the highest values in Fig. 3.20 (b). When Fe($3d_\nu$) orbitals become doubly occupied at $\mu = -1$ eV, magnetic moments of them are zero.

In Figs. 3.21 and 3.22, the electron occupation numbers and the square of magnetic moments of host states $m = $ 153rd, 154th, 158th, 159th, 173rd, 174th, 175th and 176th. Figure 3.21 (a) shows that the occupation numbers of the host states $m = $ 153rd, 154th, 158th and 159th change from 0.3 to 0.8 electrons. $m = $ 173rd host state is singly
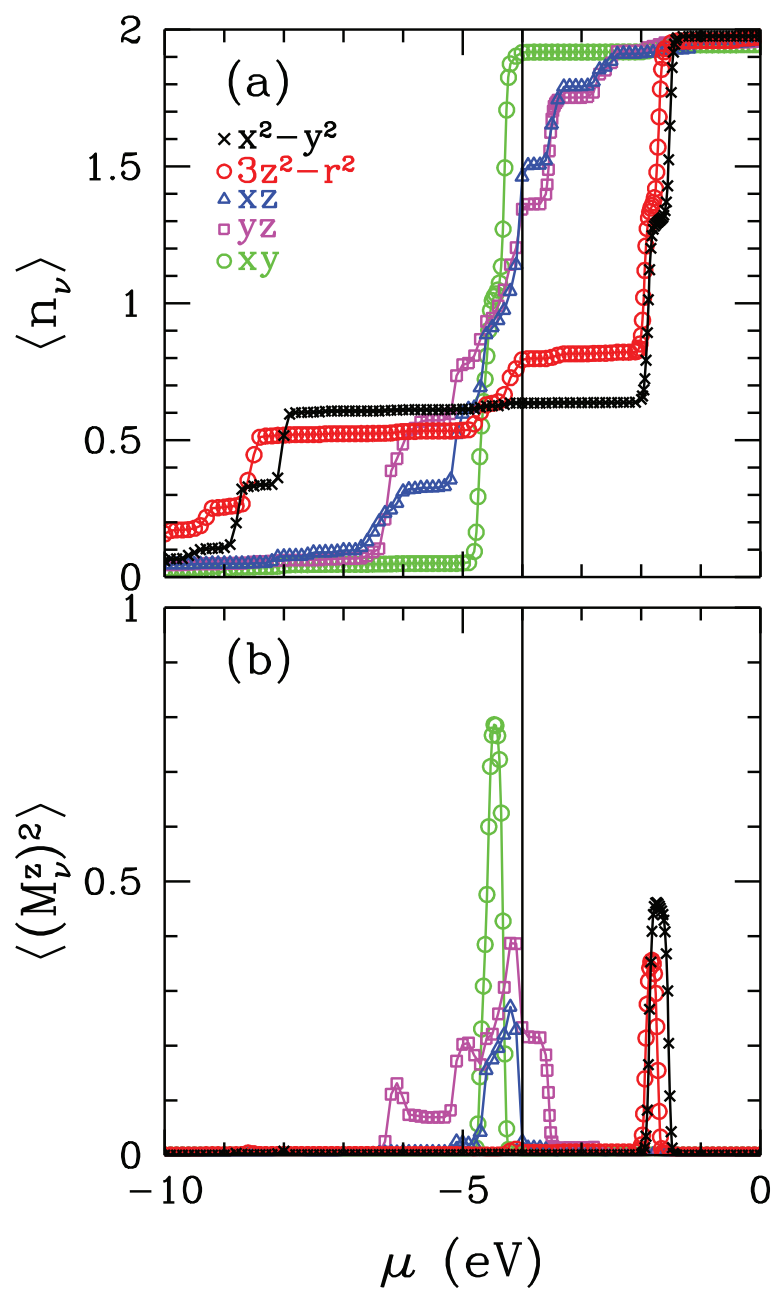
Figure 3.20. For open-shell singlet ground state of oxy-heme (a) DFT results on the electron occupation number $\langle n_\nu \rangle$ of the $Fe(3d_\nu)$ as a function of the chemical potential μ. (b) Square of the magnetic moment $\langle (M_\nu^z)^2 \rangle$ for the $Fe(3d_\nu)$ orbitals versus the chemical potential μ. Here, the vertical solid line denotes the HOMO level of the open-shell singlet-spin state calculated by the DFT method.
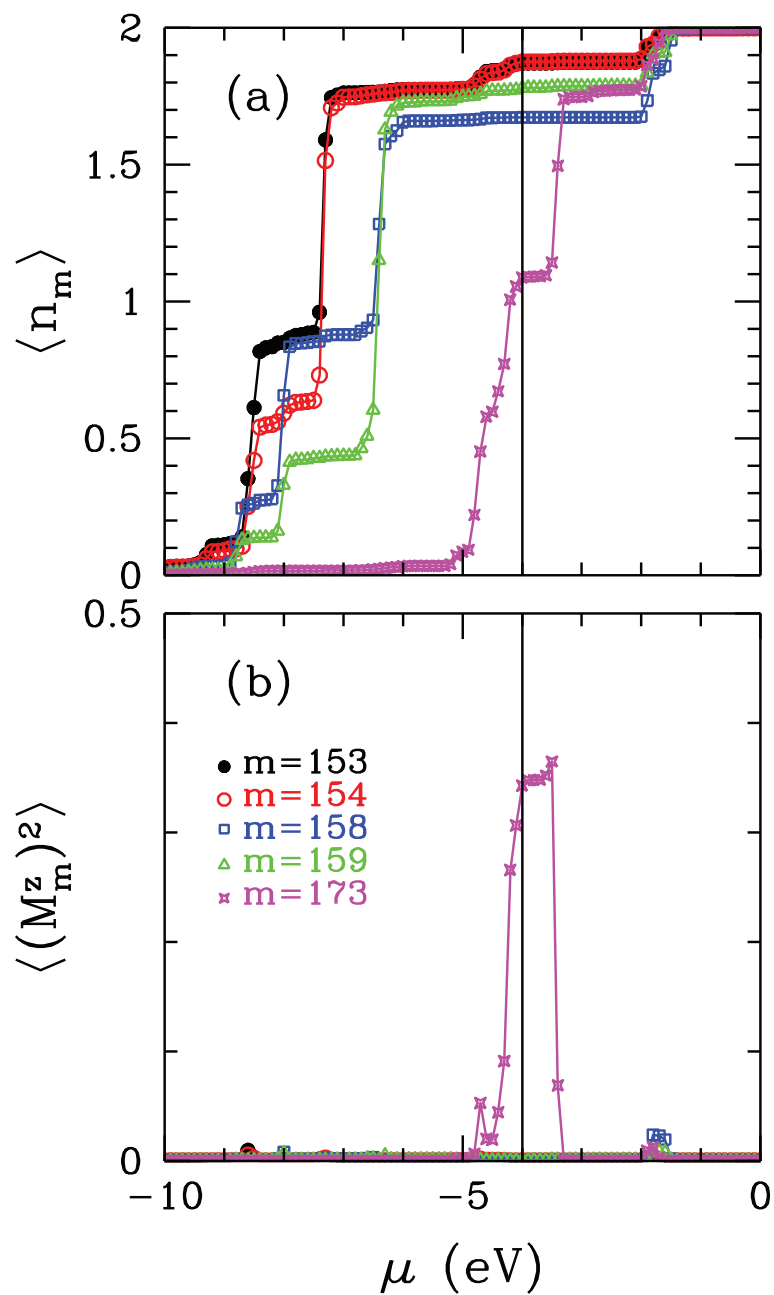
Figure 3.21. For open-shell singlet ground state of oxy-heme (a) DFT results on the electron occupation number of the m'th host state n_m versus the chemical potential μ. (b) Square of the magnetic moment of the $m = 153$rd, 154th, 158th, 159th and 173rd host states $(M_m^z)^2$ versus μ. Here, the vertical solid line denotes the HOMO level of the open-shell singlet-spin state calculated by the DFT method.
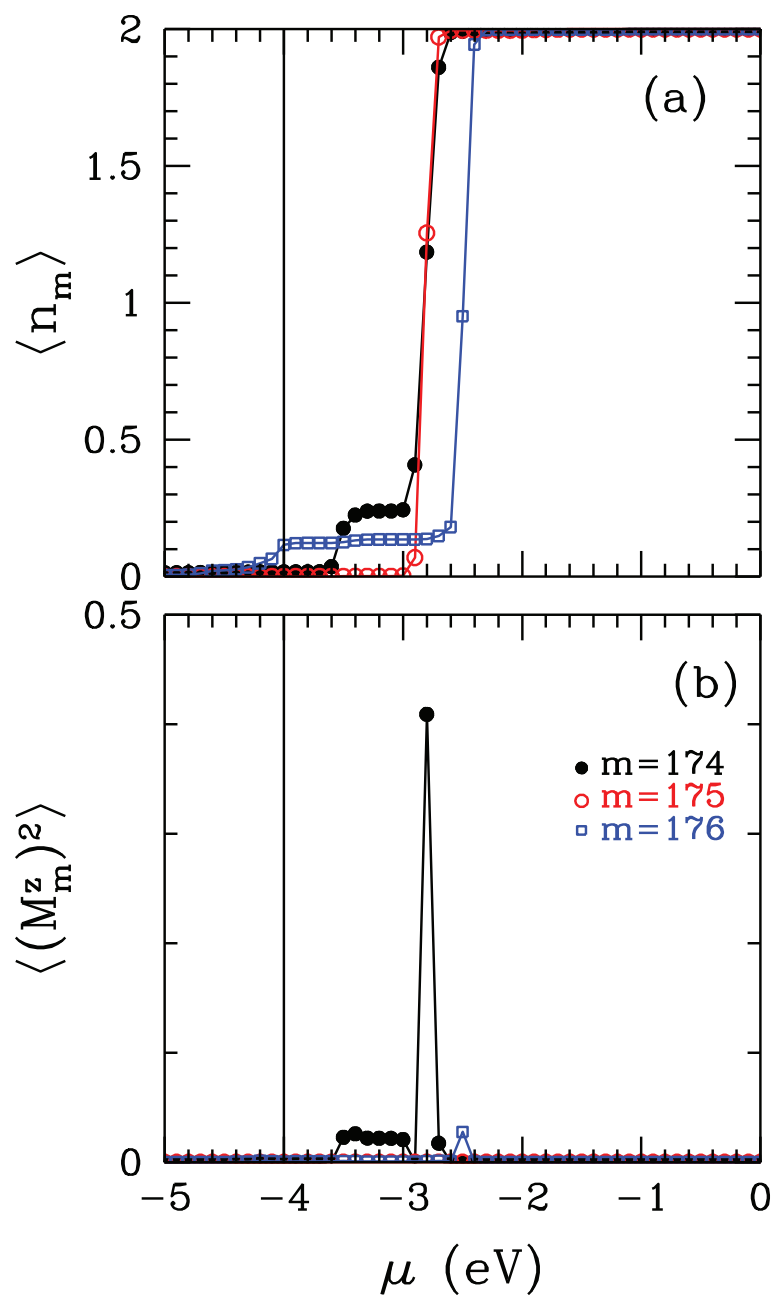
Figure 3.22. For open-shell singlet ground state of oxy-heme (a) DFT results on the electron occupation number of the m'th host state n_m versus the chemical potential μ. (b) Square of the magnetic moment of the $m = 174$th, 175th and 176th host states $(M_m^z)^2$ versus μ. Here, the vertical solid line denotes the HOMO level of the open-shell singlet-spin state calculated by the DFT method.

occupied at $\mu \approx -4.5$ eV and are doubly occupied at $\mu \approx -3$ eV. Figures 3.21 (b) and 3.22 (b) show that square of magnetic moments of host states $m = $ 153rd, 154th, 158th, 159th, 174th, 175th and 176th have small values. $m = $ 173rd host state have obviously magnetic moments at $\mu \approx -4.5$ eV.

Figures 3.23 and 3.24 show that the magnetic correlations between $m = $ 153rd, 154th, 158th, 159th, 173rd, 174th, 175th, 176th host states and the Fe($3d_\nu$) orbitals as a function of μ. All correlation contributions vary in small range. The $m = $ 153th, 154th, 158th, 173rd, 174th, 175th and 176th states $\langle M_\nu^z M_m^z \rangle$ is ferromagnetic at -10 eV $\lesssim \mu \lesssim -1.5$ eV, but it is very small for $m = $ 175th state. For the $m = $ 159th host state the Fe($3d_\nu$) orbitals are antiferromagnetic at -10 eV $\lesssim \mu \lesssim -1.5$ eV. The $m = $ 173rd host state has a higher correlation with the other state.

3.4. DFT results of oxy-heme by using various basis sets

Here, we show the square of hybridization matrix elements between the Fe($3d$) orbitals and the m'th host states for the different basis sets of the oxy-heme molecule. We use these basis sets: 6-31G, 6-31G(d), 6-31G(d,p), DGDZVP, cc-pVDZ and LanL2DZ+6-31G. These basis sets are explained in Subsection 3.2.

For oxy-heme, we perform the DFT calculations by using BP86 exchange correlation energy functional and various basis sets. These basis sets are 6-31G, 6-31G(d), 6-31G(d,p), DGDZVP, cc-pVDZ and LanL2DZ+6-31G. For these basis sets, we calculate the square of hybridization matrix elements $|V_{m\nu}|^2$ between the Fe($3d_\nu$) orbitals and m'th host states as a function of the m'th host eigenvalues ε_m. The DFT results on the BP86/6-31G basis set are shown in Section 3.3. In Fig. 3.17, we showed the $|V_{m\nu}|^2$ of the deoxy-heme for 6-31G basis set. Here, the hybridization matrix elements of the 6-31G basis set will be compared with the other basis sets.

In Fig. 3.17, we observed that the $m = $ 158th host state has the highest hybridization matrix elements with $3d_{x^2-y^2}$ orbital. For 6-31G(d) and 6-31G(d,p) basis sets, the index number of $m = $ 152nd host state has changed as $m = $ 157th. It is found that the $m = $ 157th host states have the highest hybridization matrix elements with $3d_{x^2-y^2}$ orbital for 6-31G(d) and 6-31G(d,p) basis sets as shown in Fig. 3.25. For these basis sets, the $m = $ 157th host state consists of the $2p$'s orbitals of 4N's atoms. We see that the hybridizations of $m = $ 153rd host states increase for both basis sets. The compositions of $m = $ 153rd host state are shown in 3.18 (a). Here, the compositions of $m = $ 153rd host states for both basis sets are the same for the 6-31G set. For the $m = $ 153rd host states
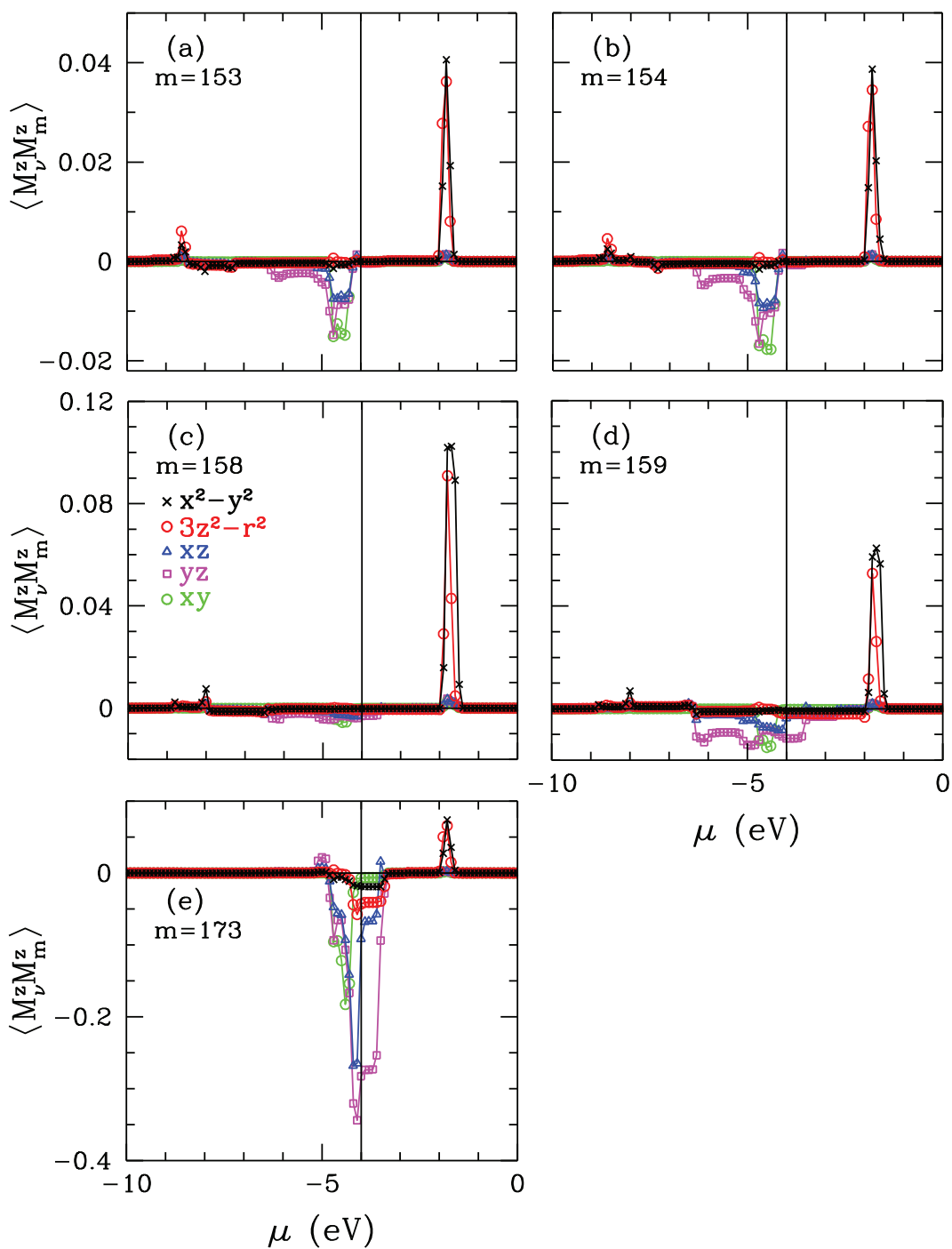
Figure 3.23. For open-shell singlet ground state of oxy-heme, DFT results on the magnetic correlation function $\langle M_\nu^z M_m^z \rangle$ between the m'th host eigenstate and the Fe($3d_\nu$) orbitals. Here results are shown for host states (a) $m = 153$rd, (b) 154th, (c) 158th, (d) 159th and (f) 173rd. Here, the vertical solid line denotes the HOMO level of the open-shell singlet-spin state calculated by the DFT method.
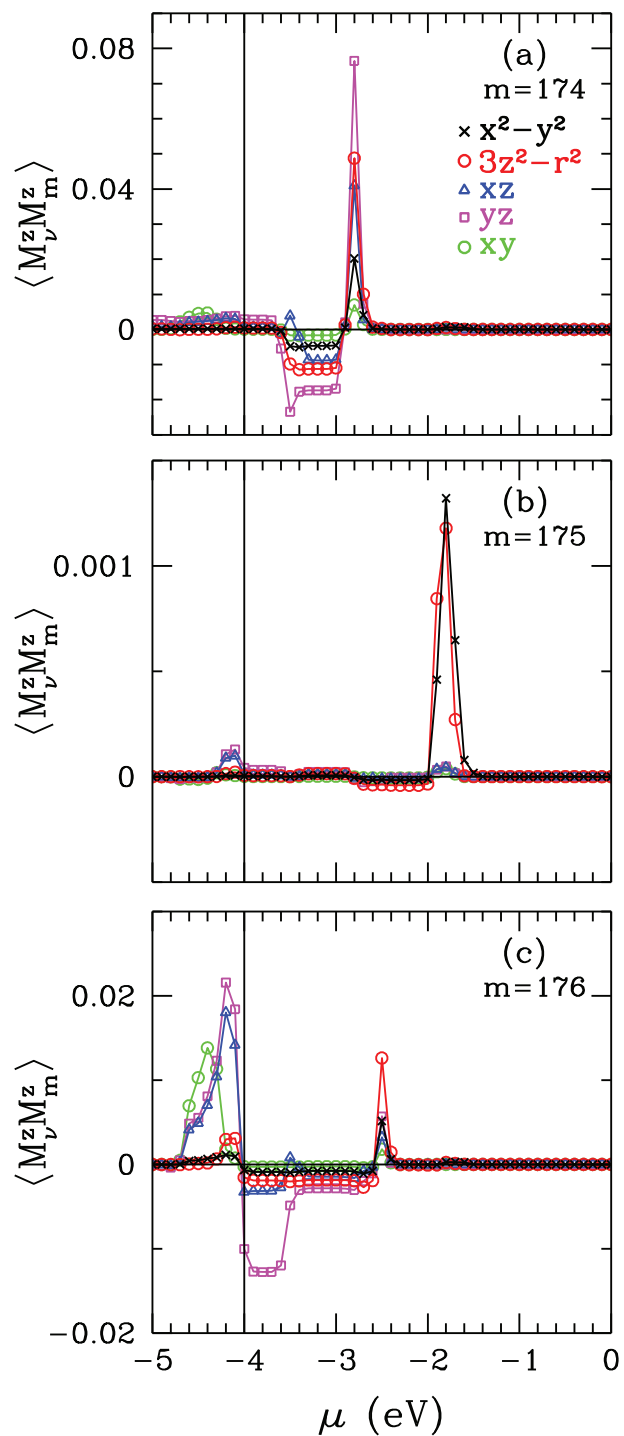
Figure 3.24. For open-shell singlet ground state of oxy-heme, DFT results on the magnetic correlation function $\langle M_\nu^z M_m^z \rangle$ between the m'th host eigenstate and the Fe($3d_\nu$) orbitals. Here results are shown for host states (a) $m = 174$th, (b) 175th and (c) 176th. Here, the vertical solid line denotes the HOMO level of the open-shell singlet-spin state calculated by the DFT method.

the weights of $2p$'s orbitals of 4N, 5N and 10N atoms have increased. The hybridization contributions of other host states have changed little for the $3d$ orbitals. Here, the vertical solid and dashed lines denote the values of the HOMO and LUMO, respectively. For these basis sets, the values of HOMO and LUMO levels, the energy gap and the total occupation number of Fe($3d$) orbitals are shown in Table 3.7.

For these various basis sets, we find that the ground state energy of oxy-heme is still the open-shell singlet-spin state. We do not show the results of these different basis sets because they are similar to the results of Section 3.3.1.

Table 3.7. For oxy-heme, the results of the different basis sets on the total electron numbers of Fe($3d$) orbitals. The HOMO and LUMO levels and the energy gap of oxy-heme are given for the different basis sets. The HOMO and LUMO energies are given in electron volts.

Basis Sets	$n_{\text{Fe}(3d)}$	E_{HOMO}	E_{LUMO}	E_{gap}
6-31G	6.23	-4.12	-3.84	0.28
6-31G(d)	6.27	-4.14	-3.82	0.32
6-31G(d,p)	6.27	-4.16	-3.83	0.33
DGDZVP	6.74	-4.57	-4.23	0.34
cc-pVDZ	6.77	-4.34	-4.01	0.33
LanL2DZ+6-31G	6.96	-4.31	-3.98	0.33

3.5. DFT+U results for deoxy and oxy-heme

The DFT plus Hubbard U potential (DFT+U) calculations of deoxy and oxy-heme molecules are performed with the Vienna Ab-initio Software Package (VASP) (Kresse and Hafner (1994); Kresse and Furthmüller (1996)). We use the Perdew-Burke-Ernzerhof (PBE) exchange correlation functionals as a type for the generalized gradient approximation (GGA) functional (Perdew et al. (1996)). The Fe, C, N, O and H ionic cores are indicated by the projector augmented-wave (PAW) (Kresse and Joubert (1999)) potentials with 8, 4, 5, 6 and 1 valence electrons, respectively. For each molecule, the k-point mesh of $1 \times 1 \times 1$ is used with a cutoff energy of 500 eV. We perform the DFT+U calculations by using the LDAUTYPE=4 (Liechtenstein et al. (1995)) in VASP. In DFT+U method, we choose $U = 4$ eV and $J = 0.9$ eV for the Fe($3d$) orbitals and $U = J = 0$ eV for the remaining orbitals.
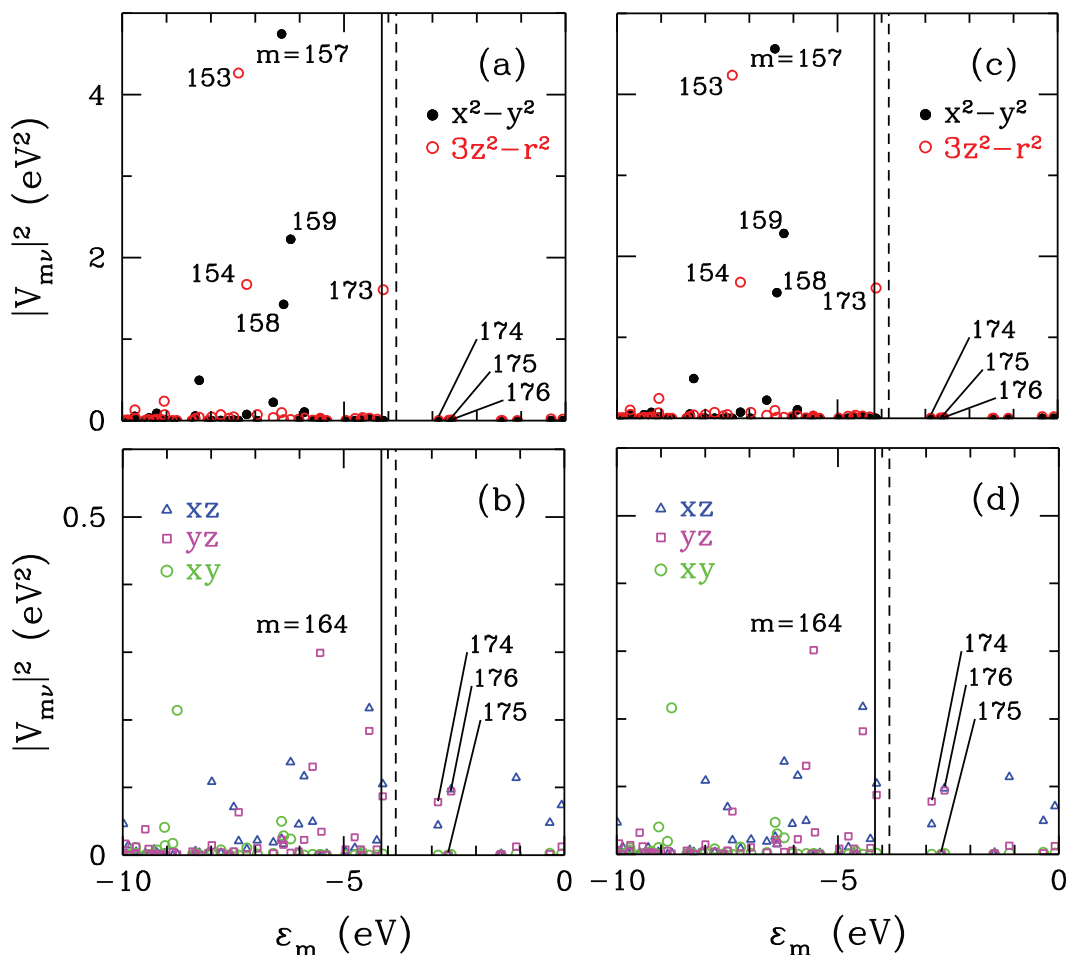
Figure 3.25. For oxy-heme, (a) and (b) the results of 6-31G(d) basis set, (c) and (d) the results of 6-31G(d,p) basis set on the square of hybridization matrix elements $|V_{m\nu}|^2$ between the m'th host eigenstates and Fe($3d_\nu$) natural atomic orbitals as a function of the m'th host eigenvalues ε_m. We observe that the $m = 157$th host states have the highest hybridization matrix elements with $3d_{x^2-y^2}$ orbital for both basis sets. Here, the vertical solid and dashed lines denote the values of the HOMO and LUMO, respectively. The value of HOMO and LUMO levels are shown in Table 3.7.
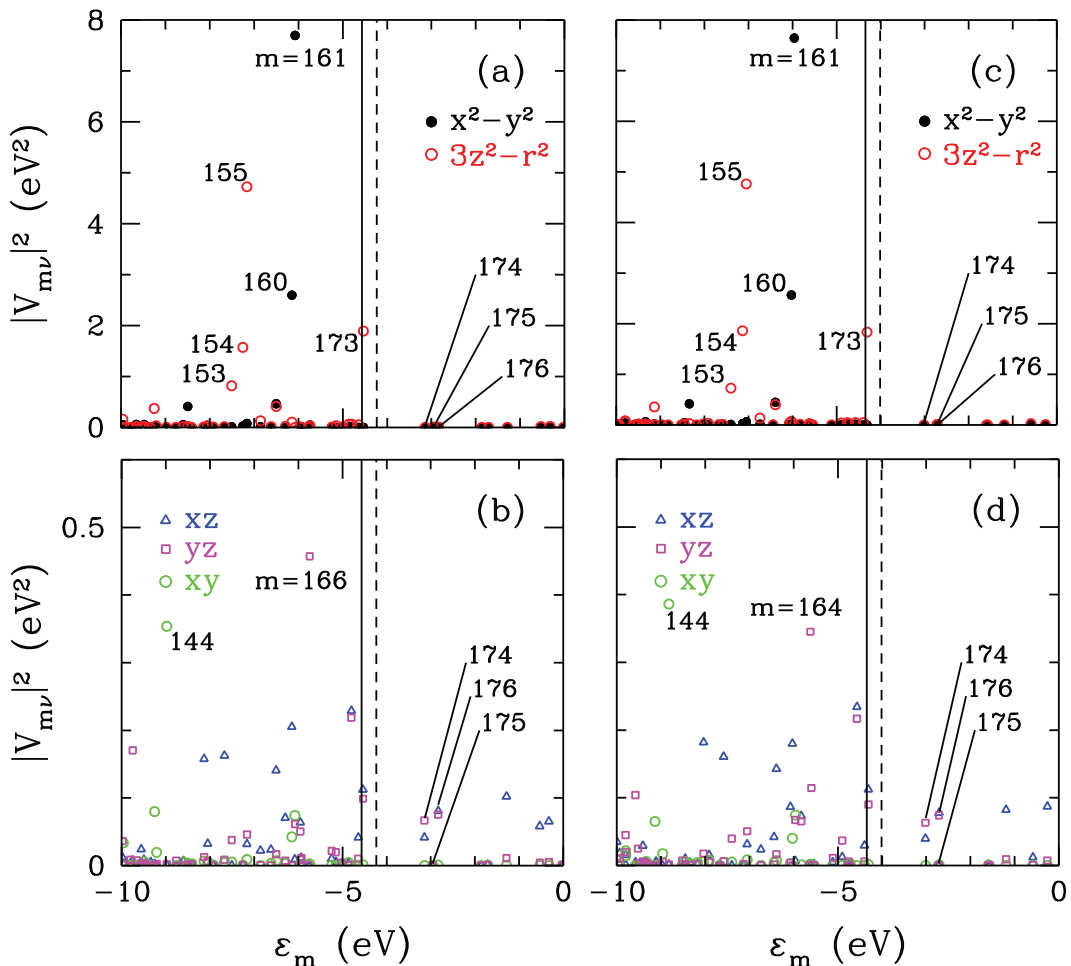
Figure 3.26. For oxy-heme, (a) and (b) the results of DGDZVP basis set, (c) and (d) the results of cc-pVDZ basis set on the square of hybridization matrix elements $|V_{m\nu}|^2$ between the m'th host eigenstates and Fe($3d_\nu$) natural atomic orbitals as a function of the m'th host eigenvalues ε_m. We observe that the $m = 161$st host states have the highest hybridization matrix elements with $3d_{x^2-y^2}$ orbital for both basis sets. Here, the vertical solid and dashed lines denote the values of the HOMO and LUMO, respectively. The value of HOMO and LUMO levels are shown in Table 3.7.
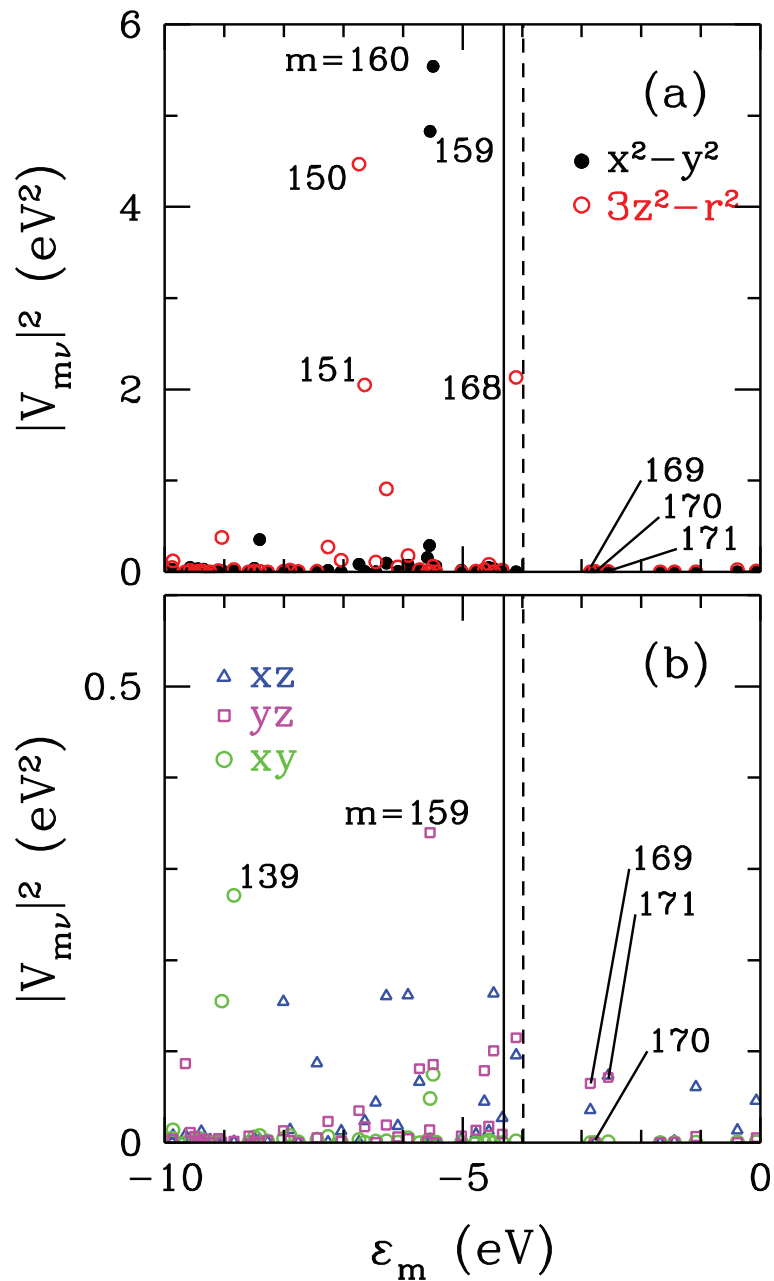
Figure 3.27. For oxy-heme, DFT(BP86/LanL2DZ+6-31G) results on the square of hybridization matrix elements $|V_{m\nu}|^2$ between the m'th host eigenstates and Fe($3d_\nu$) natural atomic orbitals as a function of the m'th host eigenvalues ε_m. In (a) results are shown for $3d_{x^2-y^2}$ and $3d_{3z^2-r^2}$ orbitals, and in (b) for $3d_{xz}$, $3d_{yz}$ and $3d_{xy}$ orbitals. Here, the vertical solid and dashed lines denote the values of the HOMO and LUMO, respectively. The value of HOMO and LUMO levels are shown in Table 3.7. We observe that the $m = 160$th host state has the highest hybridization matrix elements with $3d_{x^2-y^2}$ orbital.

Here, the total energies of different magnetic moments of deoxy-heme are shown in Table 3.8. The total magnetic moment 2.0 μ_B has the lowest energy value, so the ground state energy of deoxy-heme is -496.30 eV.

Table 3.8. For DFT+U results of deoxy-heme, it is shown the total energies of different magnetic moments. DFT+U finds the ground state energy of deoxy-heme at 2.0 μ_B. Energies are given in electron volts.

DFT+U	
Magnetic Moment (μ_B)	Total Energy
1.0	-489.03 eV
0.0	-495.89 eV
0.01	-496.00 eV
3.0	-496.09 eV
4.0	-496.29 eV
2.0	-496.30 eV

Here, the total energies of different magnetic moments of oxy-heme are shown in Table 3.9. The magnetic moment 0.07 μ_B has the lowest energy value, so the ground state energy of oxy-heme is -505.74 eV.

In DFT+U method, the total electron number of Fe($3d$) orbitals of the deoxy-heme is 6.22 electrons for $U = 4$ eV and $J = 0.9$ eV. The total electron number of Fe($3d$) orbitals of the oxy-heme is 6.32 electrons for $U = 4$ eV and $J = 0.9$ eV.

For deoxy-heme, Table 3.10 shows the DFT+U result on the electron numbers of Fe($3d$) orbitals. While $3d_{yz}$, $3d_{xz}$, $3d_{3z^2-r^2}$ and $3d_{x^2-y^2}$ orbitals of deoxy-heme are nearly singly occupied, $3d_{xy}$ orbital are doubly occupied for DFT+U method.

Table 3.9. For DFT+U results of oxy-heme, it is shown the total energies of different magnetic moments. DFT+U finds the ground state energy of oxy-heme at 0.07 μ_B. Energies are given in electron volts.

DFT+U	
Magnetic Moment (μ_B)	Total Energy
4.0	-504.96 eV
2.0	-505.58 eV
1.0	-505.64 eV
0.0	-505.68 eV
0.07	-505.74 eV

Table 3.10. For deoxy-heme, the occupancy numbers of Fe(3d) orbitals are shown as up-electron $n_{\nu\uparrow}$, down-electron $n_{\nu\downarrow}$ and total of up-electron and down-electron n_ν for DFT+U result. Here, we use $U = 4$ eV, $J = 0.9$ eV for the Fe(3d) orbitals and $U = J = 0$ eV for the remaining orbitals.

	ν	$3d_{xz}$	$3d_{yz}$	$3d_{3z^2-r^2}$	$3d_{x^2-y^2}$	$3d_{xy}$
				deoxy-heme		
DFT+U	$n_{\nu\uparrow}$	0.92	0.94	0.97	0.36	0.95
	$n_{\nu\downarrow}$	0.42	0.45	0.16	0.24	0.81
	n_ν	1.34	1.39	1.13	0.60	1.76

Table 3.11. For deoxy-heme, it is shown the effective magnetic moment distributions for DFT+U result. The following values of the effective magnetic moments are calculated in units of Bohr magneton (μ_B). Here, we use $U = 4$ eV, $J = 0.9$ eV for the Fe(3d) orbitals and $U = J = 0$ eV for the remaining orbitals.

deoxy-heme	M_{xz}^{eff}	M_{yz}^{eff}	$M_{3z^2-r^2}^{\text{eff}}$	$M_{x^2-y^2}^{\text{eff}}$	M_{xy}^{eff}	$M_{\text{Fe(3d)}}^{\text{eff}}$	$M_{\text{host}}^{\text{eff}}$	$M_{\text{tot}}^{\text{eff}}$
DFT+U	0.50	0.49	0.81	0.12	0.14	2.06	-0.06	2.0

The effective magnetic moment is defined as $M_\nu^{\text{eff}} = n_{\nu\uparrow} - n_{\nu\downarrow}$ which is the different between spin-up and spin-down electrons. The first five columns of Table 3.11 show the effective magnetic moments of Fe(3d) orbitals of deoxy-heme. The sixth column of Table 3.11 denotes the total effective magnetic moment of Fe(3d) orbitals of deoxy-heme. The last two columns of Table 3.11 denote the total effective magnetic moment of host orbitals and all orbitals of deoxy-heme, respectively. In Table 3.11, the total effective magnetic moment of deoxy-heme is 2.0 μ_B. The ground state energy of deoxy-heme has the triple ground state in the DFT+U result.

In Table 3.12, the occupancy numbers of Fe(3d) orbitals are shown as up-electron $n_{\nu\uparrow}$, down-electron $n_{\nu\downarrow}$ and total of up-electron and down-electron n_ν for DFT+U method. While $3d_{3z^2-r^2}$ and $3d_{x^2-y^2}$ orbitals of oxy-heme are nearly singly occupied, $3d_{xz}$, $3d_{yz}$ and $3d_{xy}$ orbitals are doubly occupied for DFT+U result.

The effective magnetic moment is defined as $M_\nu^{\text{eff}} = n_{\nu\uparrow} - n_{\nu\downarrow}$ which is the different between spin-up and spin-down electrons. The first five columns of Table 3.13 show the effective magnetic moments of Fe(3d) orbitals of oxy-heme. The sixth column

Table 3.12. For oxy-heme, the occupancy numbers of Fe($3d$) orbitals are shown as up-electron $n_{\nu\uparrow}$, down-electron $n_{\nu\downarrow}$ and total of up-electron and down-electron n_ν for DFT+U result. Here, we use $U = 4$ eV, $J = 0.9$ eV for the Fe($3d$) orbitals and $U = J = 0$ eV for the remaining orbitals.

	ν	$3d_{xz}$	$3d_{yz}$	$3d_{3z^2-r^2}$	$3d_{x^2-y^2}$	$3d_{xy}$
				oxy-heme		
	$n_{\nu\uparrow}$	0.86	0.90	0.47	0.35	0.93
DFT+U	$n_{\nu\downarrow}$	0.61	0.55	0.42	0.32	0.91
	n_ν	1.47	1.45	0.89	0.67	1.84

Table 3.13. For oxy-heme, it is shown the effective magnetic moment distributions for DFT+U result. The following values of the effective magnetic moments are calculated in units of Bohr magneton (μ_B). Here, we use $U = 4$ eV, $J = 0.9$ eV for the Fe($3d$) orbitals and $U = J = 0$ eV for the remaining orbitals.

oxy-heme	M_{xz}^{eff}	M_{yz}^{eff}	$M_{3z^2-r^2}^{\text{eff}}$	$M_{x^2-y^2}^{\text{eff}}$	M_{xy}^{eff}	$M_{\text{Fe(3d)}}^{\text{eff}}$	$M_{\text{host}}^{\text{eff}}$	$M_{\text{tot}}^{\text{eff}}$
DFT+U	0.25	0.35	0.05	0.03	0.02	0.70	-0.63	0.07

of Table 3.13 denotes the total effective magnetic moment of Fe($3d$) orbitals of oxy-heme. The last two columns of Table 3.13 denote the total effective magnetic moment of host orbitals and all orbitals of oxy-heme, respectively. In Table 3.13, the total effective magnetic moment of oxy-heme is 0.07 μ_B.

CHAPTER 4

DFT+QMC RESULTS FOR HEME MOLECULES

In this chapter, we show the DFT+QMC results of deoxy and oxy-heme molecules. The DFT+QMC calculations are performed by using the Hirsch-Fye QMC algorithm (Hirsch and Fye (1986)).

We use combined density functional theory plus quantum Monte Carlo (DFT+QMC) results on the extended multi-orbital Anderson model for deoxy-heme and oxy-heme molecules. We first compute the DFT to study the electronic structure of deoxy-heme and oxy-heme molecules within the framework of the extended multi-orbital Anderson model.

Impurity bound state (IBS) knows as correlated electronic states. The IBS plays an important role in determining the magnetic properties of these molecules. Here, we observe that the IBS of deoxy-heme is below the highest occupied molecular orbital (HOMO) level and it is occupied. The spin state of deoxy-heme is a high-spin. The IBS of oxy-heme is above the HOMO level and it is unoccupied. The spin state of oxy-heme is a low-spin. In addition, we obtain the magnetic moment formation and antiferromagnetic correlations for these heme molecules. We will show whether we obtain these results with the DFT+MFA, DFT and DFT+U methods.

4.1. DFT+QMC results for deoxy-heme

In this subsection, we discuss the electron occupation number $\langle n_\nu \rangle$ for Fe($3d_\nu$) orbitals as a function of chemical potential μ for deoxy-heme. Similarly, we show the square of the magnetic moments $\langle (M_\nu^z)^2 \rangle$ at the Fe($3d_\nu$) orbitals as a function of μ. It is possible to obtain information on the single-particle spectral weight distribution and the local moment formation from μ dependence results. In addition, we show the magnetic moments $\langle M_m^z \rangle$ of host states and their magnetic correlations $\langle M_\nu^z M_m^z \rangle$ with Fe(3d) orbitals. These results show that the correlated electronic states known as impurity bound states (IBS's) are formed in deoxy-heme molecule. These electronic states are located below the Fermi-level of the deoxy-heme molecule. In addition, the antiferromagnetic (AF) correlations occur between the Fe(3d) states and host states. These correlations are

disappeared by the electron fillings of IBS. For deoxy-heme molecule, the DFT+QMC results show that when IBS is located below the chemical potential and they are occupied. The deoxy-heme molecule has a high-spin state.

In Fig. 4.1, for deoxy-heme molecule, the DFT+QMC results on the electron occupation number $\langle n_\nu \rangle$ of the Fe($3d_\nu$) as a function of μ. The electron number of $3d_{3z^2-r^2}$ is singly occupied with sudden jump at $\mu \approx -6.5$ eV and the electron number of $3d_{x^2-y^2}$ is also singly occupied with sudden increase at $\mu \approx -4$ eV as shown in Fig. 4.1 (a). The squares of magnetic moment $\langle (M_\nu^z)^2 \rangle$ of the Fe($3d_\nu$) orbitals are shown in Fig. 4.1 (b). The magnetic moments of $3d_{3z^2-r^2}$ and $3d_{x^2-y^2}$ orbitals have a sudden increase at these μ values. We think that the means of these sudden increases are the IBS's located at these energy levels. In Section 5.1, these results will be obtained with the DFT+MFA results in Fig. 5.1. Consequently, we prove the existence of the IBS's with the DFT+MFA from these results. In addition, the DFT+QMC results show that when IBS's are located below the chemical potential and they are occupied. The deoxy-heme molecule has a high-spin state.

In Fig. 4.2 (a), the DFT+QMC data on the host electron number $\langle n_m \rangle$ versus μ are presented for the $m = 144$th, 145th, 146th, 152nd, 153rd, 163rd, 165th, 166th and 167th host eigenstates. In this figure, we see that these host states do not become doubly occupied as μ passes through the ε_m's. At the HOMO level $\mu = -2.8$ eV, calculated by the DFT+QMC, $\langle n_m \rangle = 2$ for $m = 144$th, 145th, 146th and 153rd host states, $\langle n_m \rangle = 1.85$ for $m = 152$nd and $\langle n_m \rangle = 0.01$ for $m = 166$ th and 167th host states. For this reason, these host states have small magnetic moments when $\mu = -2.8$ eV as seen in Figs. 4.2 (b) and 4.3 (b). Figures 4.2 (a) and 4.3 (a) show very similar results with Figs. 5.2 (a) and 5.3 (a). In DFT+QMC result (Figs. 4.2 (b) and 4.3 (b)), the square of host magnetic moments of $m = 144$th, 145th, 146th, 152nd, 153rd, 163rd, 166th and 167th host states are $\approx 0.59(\mu_B)^2$ at $\mu \approx -7.8$ eV, $\approx 0.4(\mu_B)^2$ at $\mu \approx -7.6$ eV, $\approx 0.7(\mu_B)^2$ at $\mu \approx -7$ eV, $\approx 0.6(\mu_B)^2$ in the interval $-7 \leq \mu \leq -6$ eV, $\approx 0.69(\mu_B)^2$ at $\mu \approx -6$ eV, $\approx 0.85(\mu_B)^2$ at $\mu \approx -4.6$ eV, $\approx 0.72(\mu_B)^2$ at $\mu \approx -2.8$ eV and $\approx 0.71(\mu_B)^2$ at $\mu \approx -2.6$ eV, respectively. When the electron occupation number of the $m = 144$th, 145th, 146th, 152nd, 153rd, 163rd, 166th and 167th host states become singly occupied, their magnetic moments are maximum. When the host states become fully occupied, their magnetic moments are zero.

Figure 4.4 (a-f) indicate that Fe($3d_\nu$) NAO's develop AF correlations with the $m = 144$th, 145th, 146th, 152nd, 153rd and 163rd host states below the chemical potential of molecule -2.8 eV. These antiferromagnetic correlations diminish rapidly at
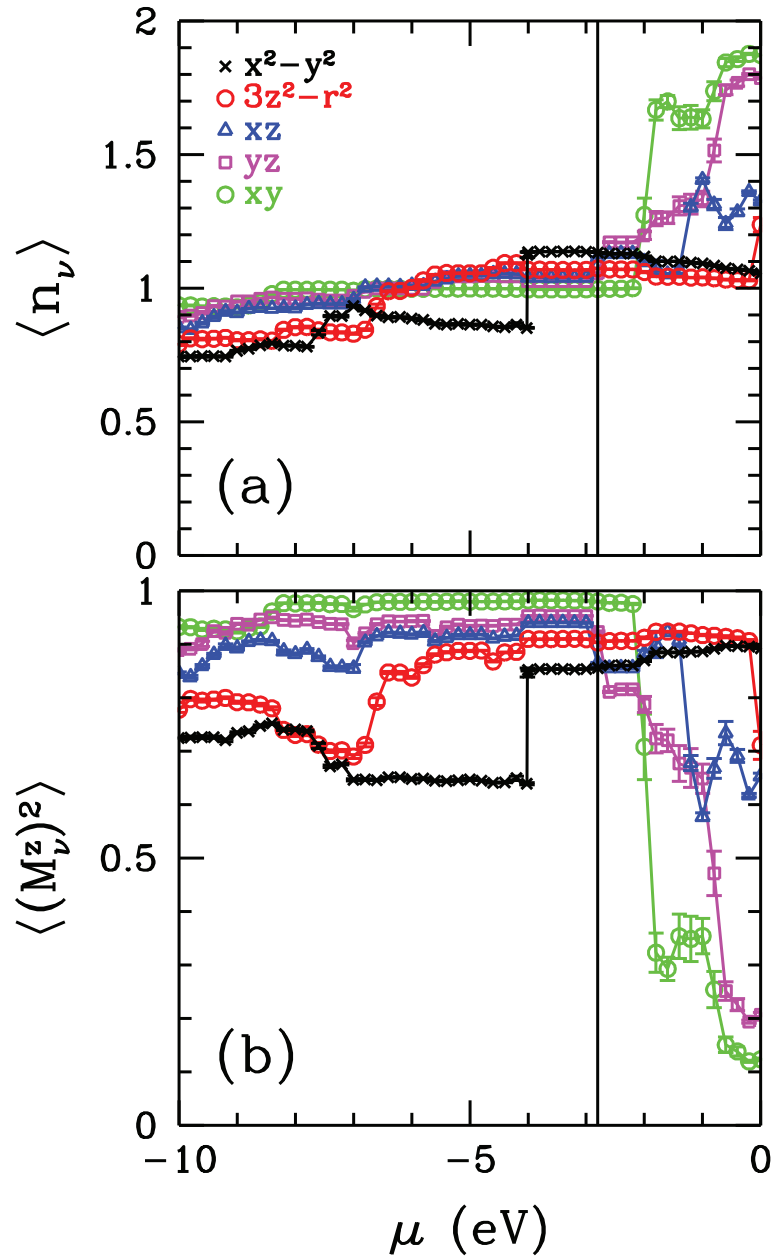
Figure 4.1. For deoxy-heme (a) DFT+QMC results on the electron occupation number $\langle n_\nu \rangle$ of the Fe($3d_\nu$) as a function of the chemical potential μ. (b) Square of the magnetic moment $\langle (M_\nu^z)^2 \rangle$ for Fe($3d_\nu$) orbitals versus μ. The vertical solid denotes the value of the Fermi level and it is calculated by DFT+QMC. These results are for $U = 4$ eV, $J = 0.9$ eV and $T = 300$ K.
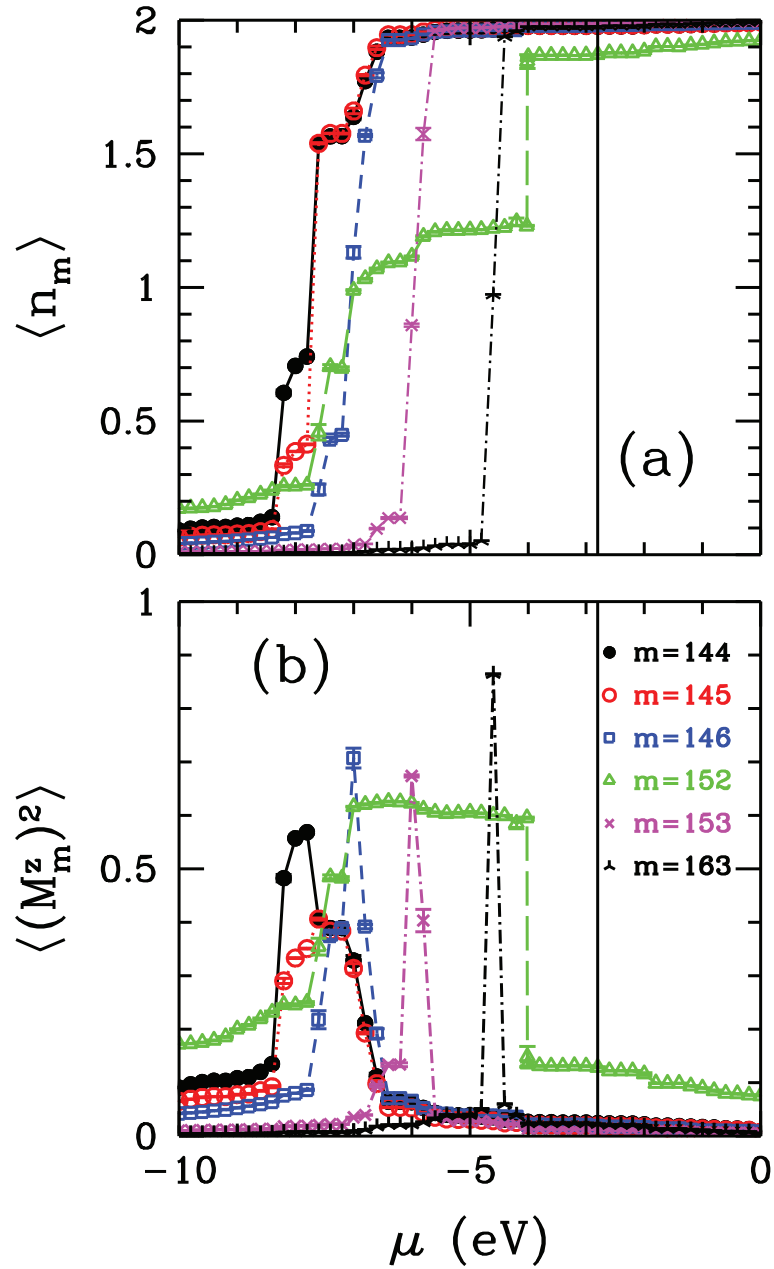
Figure 4.2. For deoxy-heme (a) DFT+QMC results on the electron occupation number $\langle n_m \rangle$ of the m'th host state as a function of the chemical potential μ. (b) Square of the magnetic moment $\langle (M_m^z)^2 \rangle$ of the m'th host state versus μ. The vertical solid denotes the value of the Fermi level and it is calculated by DFT+QMC. These results are for $U = 4$ eV, $J = 0.9$ eV and $T = 300$ K.
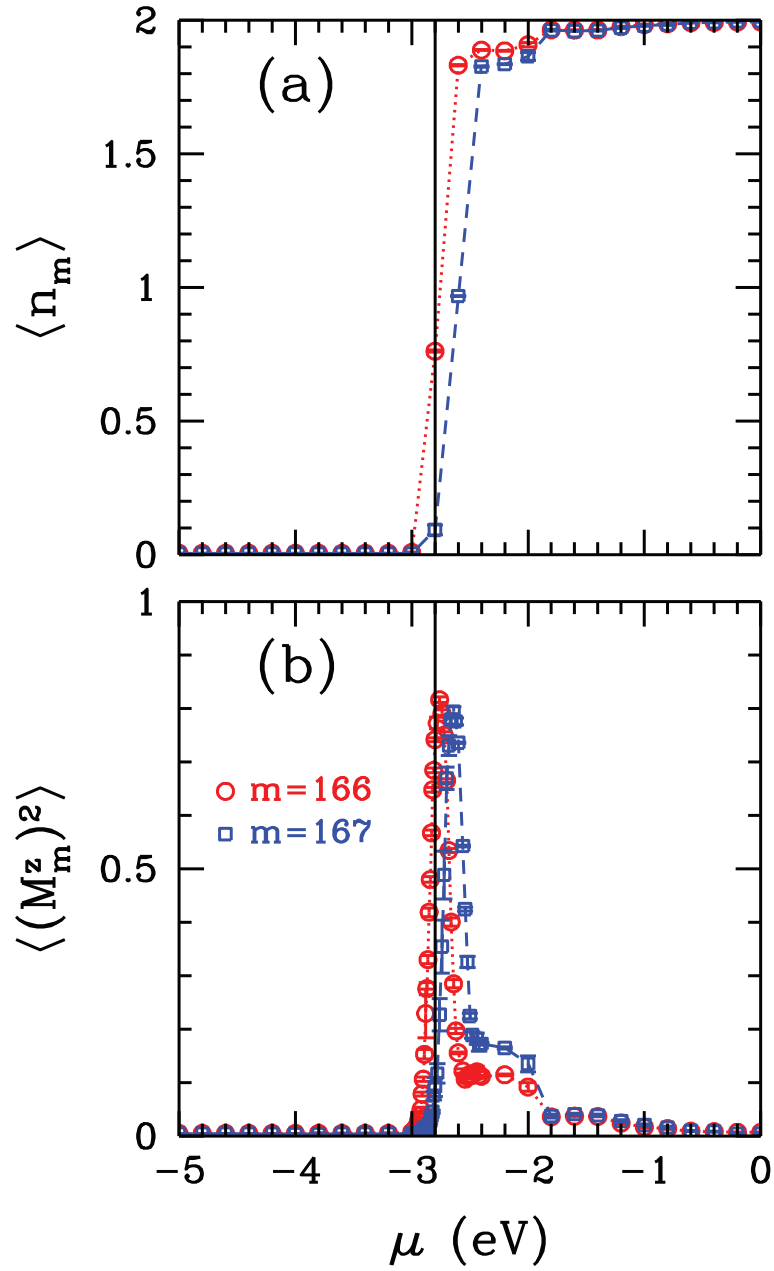
Figure 4.3. For deoxy-heme (a) DFT+QMC results on the electron occupation number $\langle n_m \rangle$ of the m'th host state as a function of the chemical potential μ. (b) Square of the magnetic moment $\langle (M_m^z)^2 \rangle$ of the m'th host state versus μ. The vertical solid denotes the value of the Fermi level and it is calculated by DFT+QMC. These results are for $U = 4$ eV, $J = 0.9$ eV and $T = 300$ K.

$\mu \approx -6.5$ eV for $m = 144$th, 145th and 146th host states, $\mu \approx -4$ eV for $m = 152$nd host state, $\mu \approx -5.5$ eV for $m = 153$rd host state and $\mu \approx -4.5$ eV for $m = 163$rd host state. These host states are doubly occupied at these μ values. When $\mu = -2.80$ eV, $\langle M_\nu^z M_m^z \rangle$ is ferromagnetic, which means that impurity bound states are occupied for deoxy-heme.

We have also studied the $\langle M_\nu^z M_m^z \rangle$ as a function of μ for host states $m = 166$th and 167th. As seen in Fig. 4.5 (a-b), these host states have antiferromagnetic correlations at chemical potential of deoxy molecule $\mu = -2.80$ eV. These antiferromagnetic correlations diminish rapidly when μ equals to bare energy values of these host states.

4.2. DFT+QMC results for oxy-heme

In this subsection, we show the DFT+QMC results on $\langle n_\nu \rangle$ as a function of chemical potential μ and $\langle (M_\nu^z)^2 \rangle$ as a function of μ. In addition, we show the magnetic moments $\langle M_m^z \rangle$ of host states and their magnetic correlations $\langle M_\nu^z M_m^z \rangle$ with Fe(3d) orbitals. The QMC results for oxy-heme molecule indicate that the IBS is located above the chemical potential, and so it is occupied. This causes that the oxy-heme molecule has a low-spin state. Antiferromagnetic (AF) correlations occur between the host and Fe(3d) orbitals. Different from the results for deoxy-heme molecule, these AF correlations disappear above the chemical potential by the fillings of the IBS.

Figure 4.6 is obtained by DFT+QMC result. Figure 4.6a and 4.6b show the electron occupation number $\langle n_\nu \rangle$ and square of the magnetic moment $\langle (M_\nu^z)^2 \rangle$ of the Fe($3d_\nu$) orbitals as a function of μ, respectively. The occupations of $3d_{xz}$ and $3d_{yz}$ orbitals change slightly up to $\mu \approx -6$ eV in Fig. 4.6a. At $\mu \approx -6$ eV, these orbitals become singly occupied. Above this chemical potential, electron number of these Fe($3d_\nu$) orbitals increase continuously and they become doubly occupied at $\mu \approx 2$ eV. Similarly, we see that $\langle n_\nu \rangle$ changes slightly up to $\mu \approx -5.2$ eV for $3d_{3z^2-r^2}$, $3d_{xy}$ and $3d_{x^2-y^2}$ orbitals. At $\mu \approx -5$ eV and $\mu \approx -1$ eV, we see the sharply increase in occupation number of $3d_{3z^2-r^2}$ orbital. In addition, we also see sudden increase in $3d_{xy}$ orbital at $\mu \approx -3.8$ eV and $3d_{x^2-y^2}$ and $3d_{3z^2-r^2}$ orbitals at $\mu \approx -1.2$ eV. We think that these are the energy levels at which IBS's are located. Above $\mu \approx 0$ eV, occupation numbers of Fe($3d_\nu$) orbitals do not change so much for $3d_{xy}$, $3d_{xz}$ and $3d_{yz}$ orbitals. At $\mu = 2$ eV, their electron numbers increase and equal 1.8, 1.95 and 1.85 electrons, respectively. In Fig. 4.6b, we observe that $\langle (M_\nu^z)^2 \rangle$ change continuously for Fe($3d_\nu$) orbitals except for $3d_{xy}$. When the occupations of these orbitals are higher than 1 electron, their magnetic moments start to
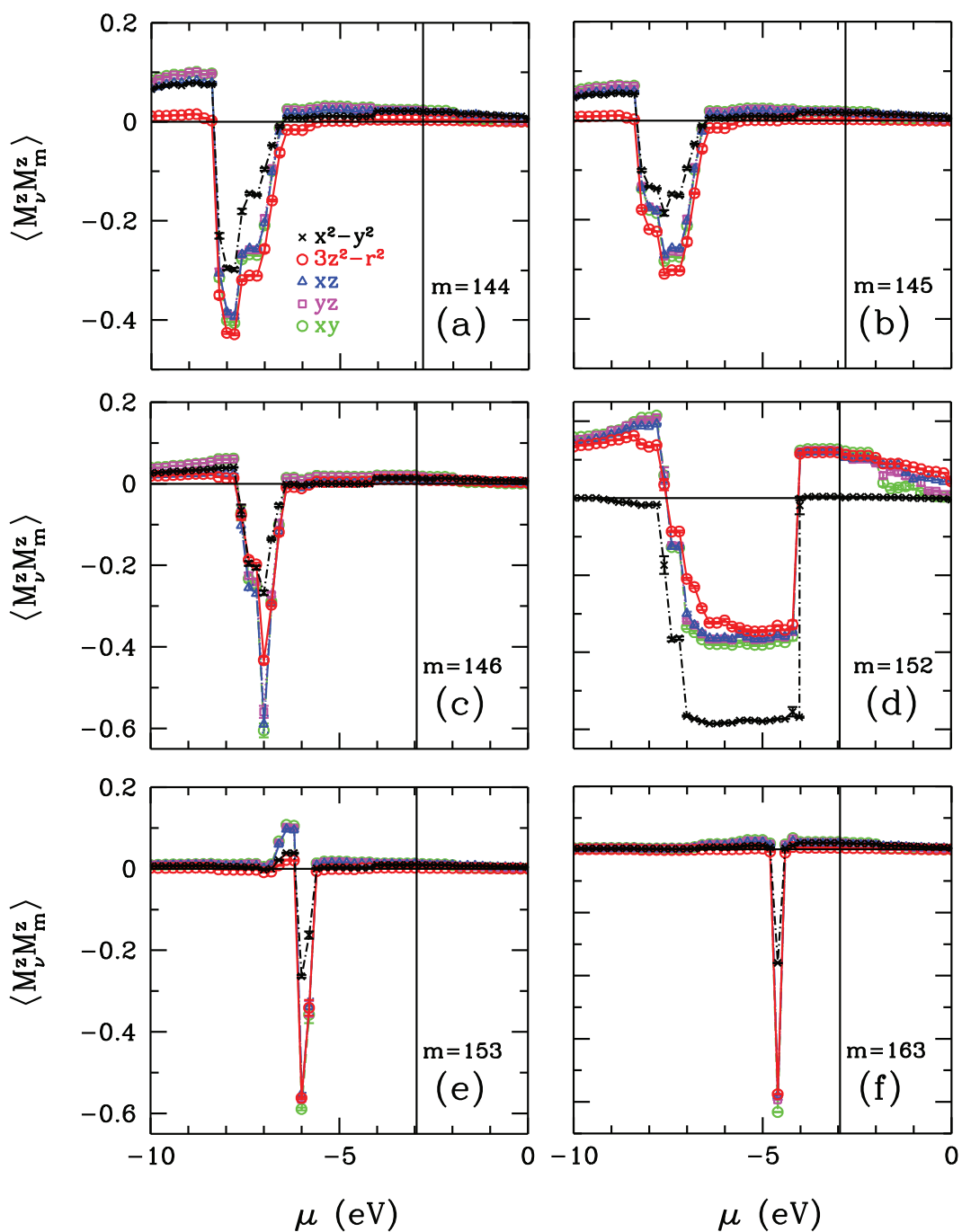
Figure 4.4. For deoxy-heme, DFT+QMC results on the magnetic correlation function $\langle M_\nu^z M_m^z \rangle$ between the m'th host eigenstates and the Fe($3d_\nu$) orbitals. Here results are shown for host states (a) $m = 144$th, (b) 145th, (c) 146th, (d) 152nd, (e) 153rd and (f) 163rd. The vertical solid denotes the value of the HOMO level and it is calculated by DFT+QMC. These results are for $U = 4$ eV, $J = 0.9$ eV and $T = 300$ K.
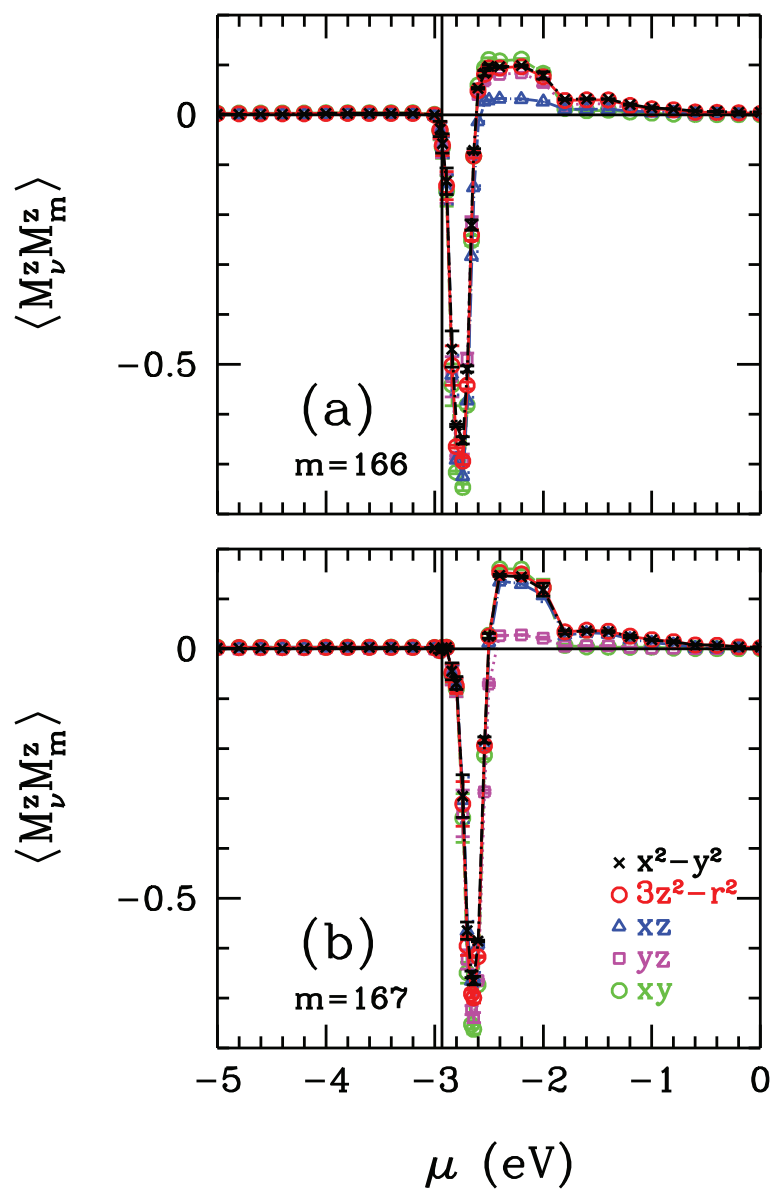
Figure 4.5. For deoxy-heme, DFT+QMC results on the magnetic correlation function $\langle M_\nu^z M_m^z \rangle$ between the m'th host eigenstate and the Fe($3d_\nu$) orbitals. Here results are shown for host states (a) $m = 166$th and (b) 167th. The vertical solid denotes the value of the HOMO level and it is calculated by DFT+QMC. These results are for $U = 4$ eV, $J = 0.9$ eV and $T = 300$ K.

decrease. On the other hand, in Fig. 4.6b, we see the sudden increase in square of magnetic moment of $3d_{3z^2-r^2}$ orbital at $\mu \approx -5.5$ eV and $\mu \approx -1.2$ eV as seen in $3d_{3z^2-r^2}$ orbital. Above $\mu = -1$ eV, the magnetic moment of $3d_{3z^2-r^2}$ orbital change slightly and $\mu = 2$ eV, it equals nearly 1 due to double occupancy.

The DFT+QMC data on the host electron numbers $\langle n_m \rangle$ versus the chemical potential μ are presented for $m = $ 153rd, 154th, 158th, 159th, 173rd, 174th, 175th and 176th host states in figures 4.7a and 4.8a. These results are similar to DFT+MFA results, but the values of magnetic moment of these states are larger. When the electron occupation numbers of the m'th host states are singly occupied for $m = $ 153rd and 154th states at $\mu \approx -7.5$ eV, for $m = $ 158th and 159th states at $\mu \approx -6.5$ eV, for $m = $ 173rd state at $\mu \approx -4.5$ eV, for $m = $ 174th and 175th states at $\mu \approx -2.8$ eV and for $m = $ 176th state at $\mu \approx -2.6$ eV. The magnetic moment of these host states are $\approx 0.4 - 0.6\mu_B$ for $m = $ 153rd, 154th, 158th, 159th and 173rd, $\approx 0.5\mu_B$ for $m = $ 174th, 175th and 176th in Figs. 4.7b and 4.8b.
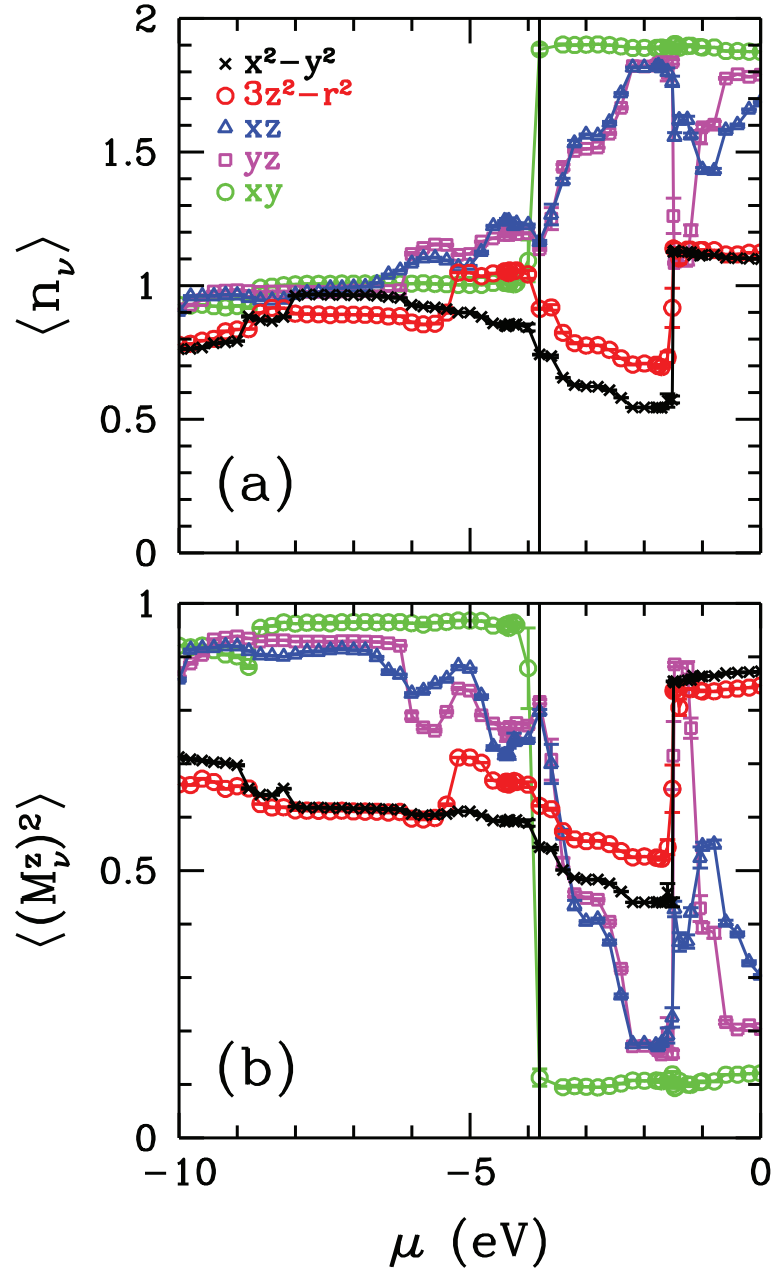
Figure 4.6. For oxy-heme (a) DFT+QMC results on the electron occupation number $\langle n_\nu \rangle$ of the Fe($3d_\nu$) as a function of the chemical potential μ. (b) Square of the magnetic moment $\langle (M^z_\nu)^2 \rangle$ for Fe($3d_\nu$) natural atomic orbitals versus the chemical potential μ. The vertical solid denotes the value of the Fermi level and it is calculated by DFT+QMC. These results are for $U = 4$ eV, $J = 0.9$ eV and $T = 300$ K.
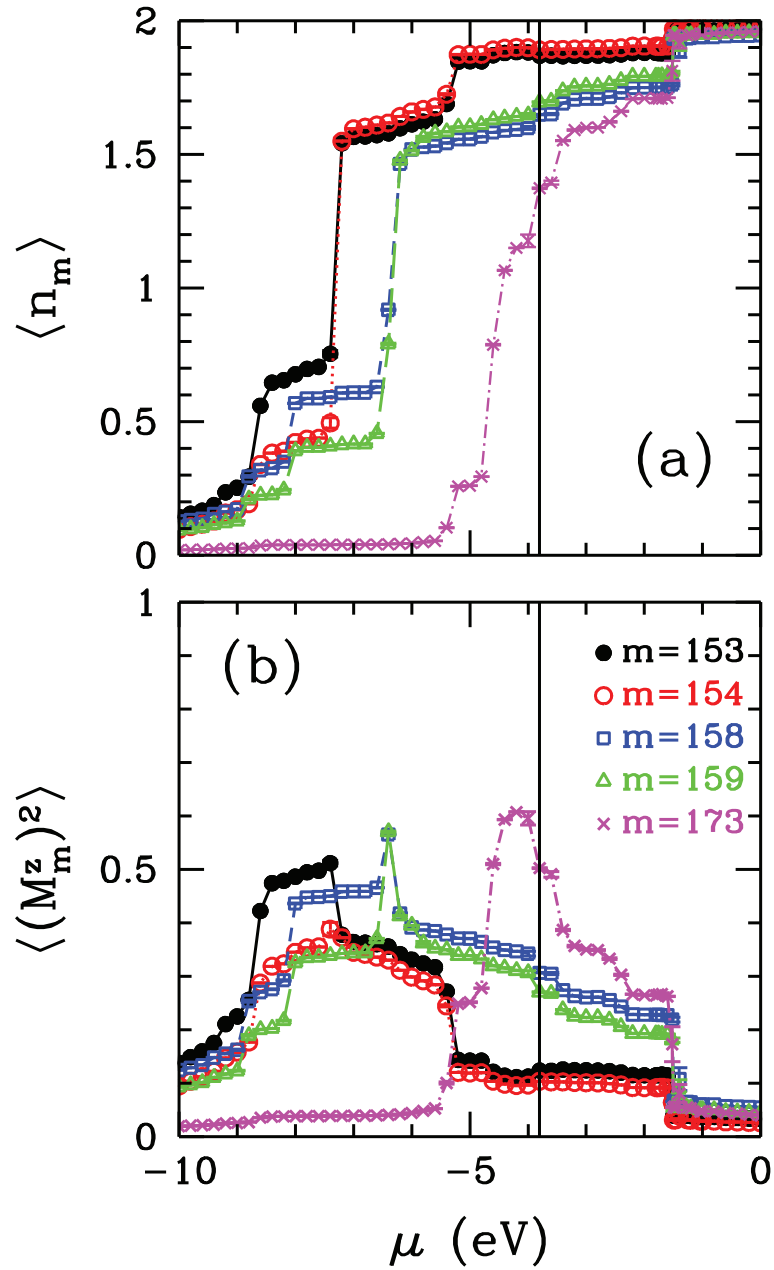
Figure 4.7. For oxy-heme (a) DFT+QMC results on the electron occupation number of the m'th host state $\langle n_m \rangle$ versus the chemical potential μ. (b) Square of the magnetic moment of the m'th host state $\langle (M_m^z)^2 \rangle$ versus μ. The vertical solid denotes the value of the Fermi level and it is calculated by DFT+QMC. These results are for $U = 4$ eV, $J = 0.9$ eV and $T = 300$ K.
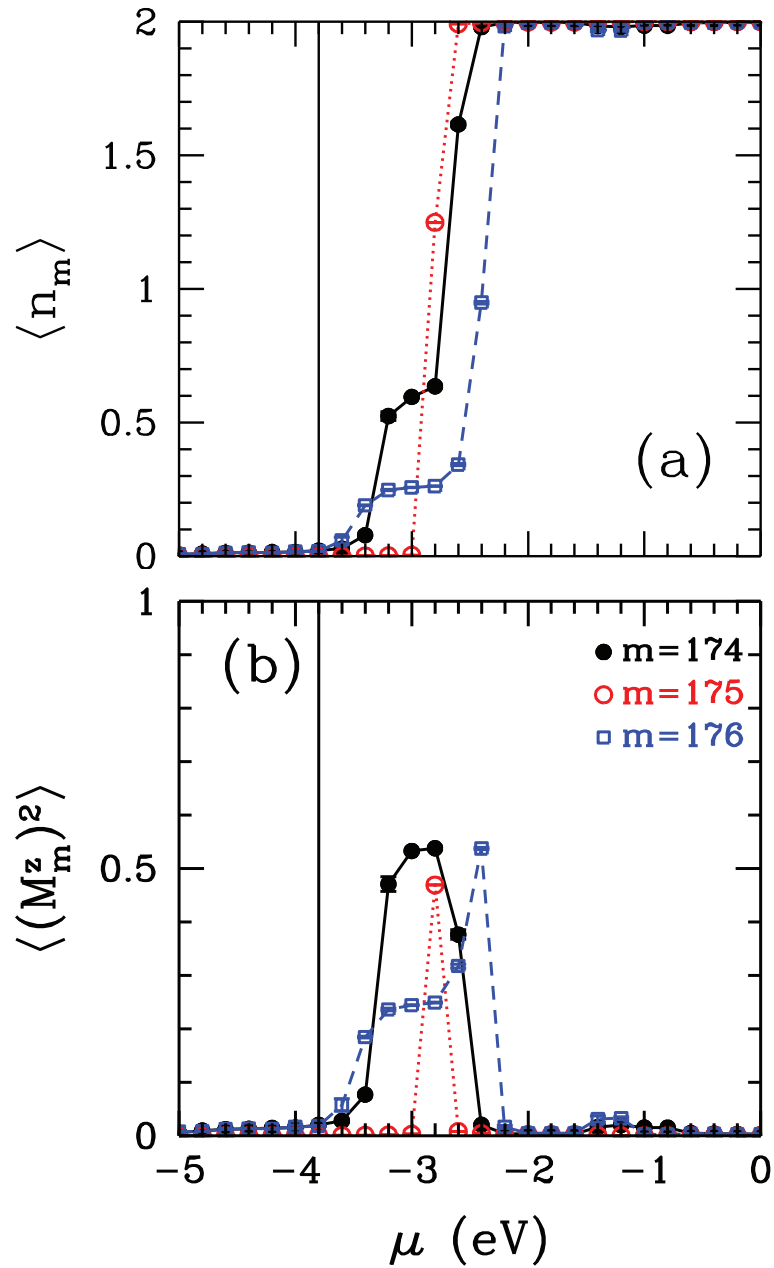
Figure 4.8. For oxy-heme (a) DFT+QMC results on the electron occupation number of the m'th host state $\langle n_m \rangle$ versus the chemical potential μ. (b) Square of the magnetic moment of the m'th host state $\langle (M_m^z)^2 \rangle$ versus μ. The vertical solid denotes the value of the Fermi level and it is calculated by DFT+QMC. These results are for $U = 4$ eV, $J = 0.9$ eV and $T = 300$ K.
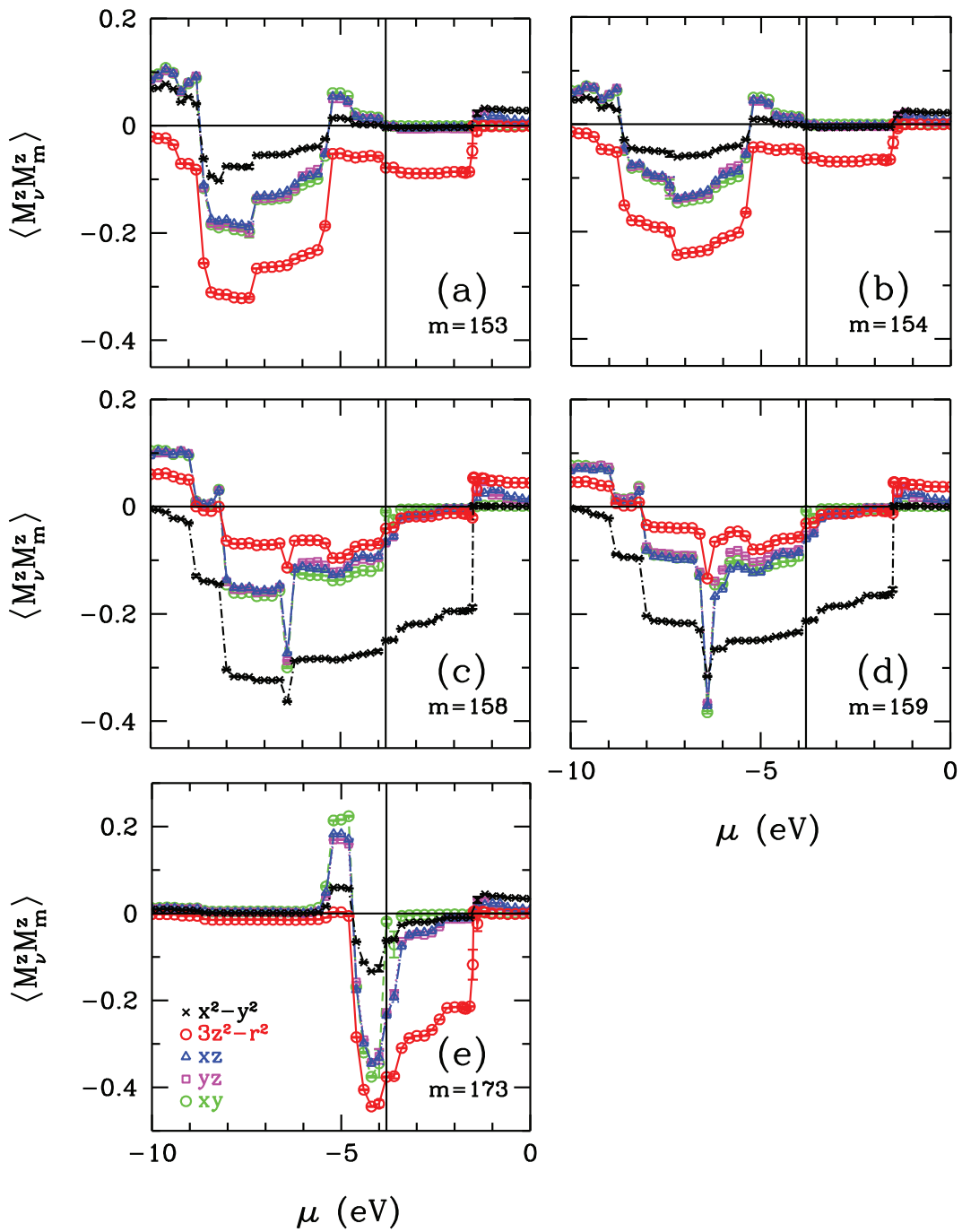
Figure 4.9. For oxy-heme, DFT+QMC results on the magnetic correlation function $\langle M_\nu^z M_m^z \rangle$ between the m'th host eigenstates and the Fe($3d_\nu$) orbitals. Here results are shown for host states (a) $m = 153$rd, (b) 154th, (c) 158th, (d) 159th and (e) 173rd. The vertical solid denotes the value of the Fermi level and it is calculated by DFT+QMC. These results are for $U = 4$ eV, $J = 0.9$ eV and $T = 300$ K.
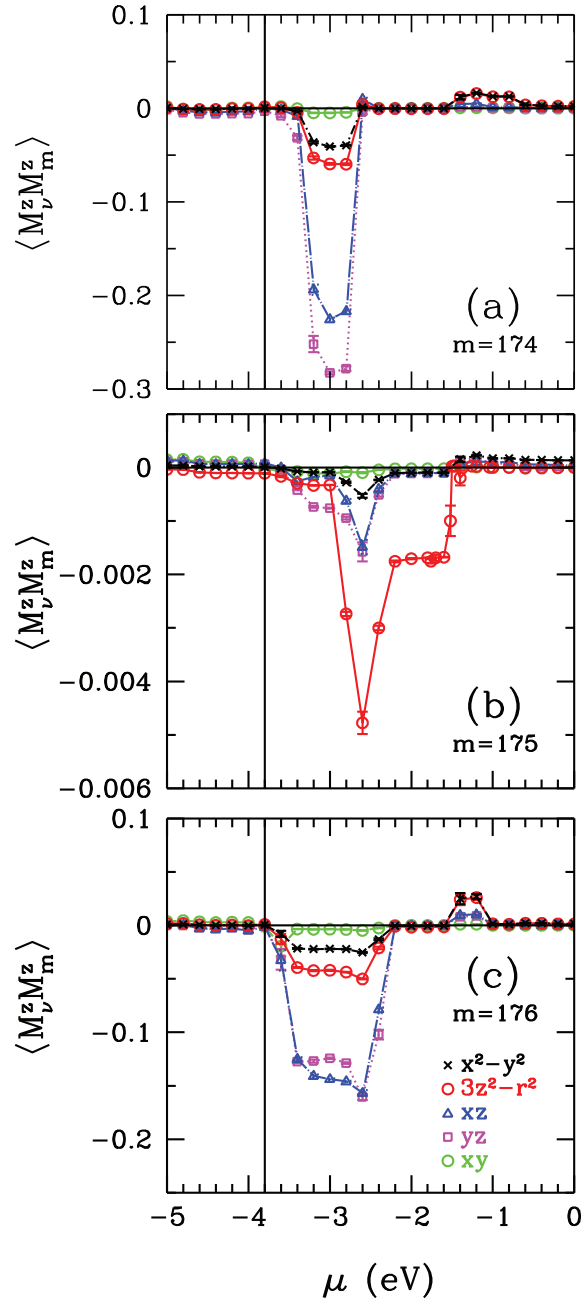
Figure 4.10. For oxy-heme, DFT+QMC results on the magnetic correlation function $\langle M_\nu^z M_m^z \rangle$ between the m'th host eigenstates and the Fe($3d_\nu$) orbitals. Here results are shown for host states (a) $m = 174$th, (b) 175th and (c) 176th. The vertical solid denotes the value of the Fermi level and it is calculated by DFT+QMC. These results are for $U = 4$ eV, $J = 0.9$ eV and $T = 300$ K.

CHAPTER 5

DFT+MFA RESULTS FOR HEME MOLECULES

In this chapter, we show density functional theory plus mean-field approximation (DFT+MFA) results on the extended multi-orbital Anderson model for deoxy-heme and oxy-heme molecules. We have shown the DFT results of these molecules in Chapter 3. We first computed the DFT to study the electronic structure of deoxy-heme and oxy-heme molecules within the framework of the extended multi-orbital Haldane-Anderson model. Then, we solve the extended multi-orbital Anderson model by using DFT+MFA to determine the spin-states and magnetic properties of these molecules. In addition, we explain the mean-field approximation (MFA) technique in detail in Appendix A. For deoxy and oxy-heme molecules, we show the electron occupation number $\langle n_\nu \rangle$ of the Fe($3d_\nu$) orbitals as a function of the chemical potential μ. Here, we observe the sudden increases or discontinuities in occupancy rates and magnetic moments of Fe($3d$) orbitals. These discontinuities are known as impurity bound states (IBS's). We have explained what IBS is in Section 1.4. Locations of IBS's determine the spin-state and effective magnetic moment of molecules. For deoxy-heme, we observe that the location of IBS is below the Fermi level with the DFT+MFA method. The IBS is occupied by electrons. Hence, the effective magnetic moment of deoxy-heme is large and the spin-state of deoxy-heme is a high-spin state. For oxy-heme, we do not find the location of IBS correctly with the DFT+MFA method. IBS is still occupied with DFT+MFA. IBS needs to become unoccupied because oxy-heme has a low-spin state. Thus, the DFT+MFA method does not work well with molecules having a low-spin state.

The electron occupation number $\langle n_\nu \rangle$ and square of the magnetic moment $\langle (M_\nu^z)^2 \rangle$ of the Fe($3d_\nu$) orbitals are shown as a function of the chemical potential μ for deoxy-heme and oxy-heme. In addition, we show DFT+MFA results on the electron occupation number of the m'th host state $\langle n_m \rangle$ and square of the magnetic moment of the m'th host state $\langle (M_m^z)^2 \rangle$ as a function of μ. We also present data on the magnetic correlation function $\langle M_\nu^z M_m^z \rangle$ between the m'th host eigenstate and the Fe($3d_\nu$) orbitals as a function of μ for deoxy-heme and oxy-heme molecules.

A sudden increase (discontinuity) of the electron occupation number can occur at any μ value. This sudden increase refers to the impurity bound state (IBS). At the same time, the presence of IBS corresponds to the end of anti-ferromagnetic contributions at

the magnetic correlation function. We observe the impurity bound state (IBS) for both molecules. The DFT+MFA results are presented for Coulomb interaction $U = 4$ eV, Hund's coupling term $J = 0.9$ eV and temperature $T = 300$ K.

5.1. DFT+MFA results for deoxy-heme

In this part, we present DFT+MFA results on deoxy-heme. Figure 5.1 (a) shows the electron occupation number $\langle n_\nu \rangle$ of the Fe($3d_\nu$) orbitals as a function of the chemical potential μ. In Fig. 5.1 (a), the electron number of $3d_{3z^2-r^2}$, $3d_{xz}$, $3d_{yz}$ and $3d_{xy}$ are singly occupied at $\mu \approx -6.5$ eV. The electron number of $3d_{x^2-y^2}$ is also singly occupied at $\mu \approx -4$ eV. In Figs. 5.1 (a) and 5.1 (b), we observe that the IBS's are seen at $\mu \approx -6.5$ eV for $3d_{3z^2-r^2}$ orbital and at $\mu \approx -4$ eV for $3d_{x^2-y^2}$ orbital. The locations of IBS's are below the Fermi level, so IBS's are occupied by electrons. Here, we will be interested in IBS at $\mu \approx -4$ eV because $x^2 - y^2$ orbital has the strongest hybridization matrix element with $m = 152$nd host state in Fig. 2.9 (b).

Figures 5.2 (a) and 5.3 (a) show the electron occupation number of the m'th host state $\langle n_m \rangle$ as a function of μ. Figures 5.2 (b) and 5.3 (b) show square of the magnetic moment of the m'th host state $\langle (M_m^z)^2 \rangle$ versus μ in DFT+MFA result. In Figs. 5.2 (a) and 5.3 (a) DFT+MFA result of electron numbers of $m = 144$th, 145th, 146th, 152nd, 153rd, 163rd, 166th and 167th host states as a function of μ is similar to DFT+QMC result of them in Figs. 4.2 (a) and 4.3 (a), but the square of host magnetic moments of these results are different. In Figs. 5.2 (a) and 5.3 (a), DFT+MFA data on the host electron number $\langle n_m \rangle$ versus μ are presented for the $m = 144$th, 145th, 146th, 152nd, 153rd, 163rd, 166th and 167th host eigenstates. In DFT results, the bare energy levels ε_m of these states are -7.76 eV, -7.65 eV, -7.06 eV, -5.98 eV, -5.95 eV, -4.59 eV, -2.7 eV and -2.58 eV for $m = 144$th, 145th, 146th, 152nd, 153rd, 163rd, 166th and 167th host states, respectively. In this figure, we see that these m'th host states do not become doubly occupied as μ passes through the ε_m's. At the HOMO level $\mu = -2.78$ eV, calculated by the DFT+MFA, $\langle n_m \rangle = 2$ for $m = 144$th, 145th, 146th and 153rd host states, $\langle n_m \rangle = 1.85$ for $m = 152$nd, $\langle n_m \rangle = 0.8$ for $m = 166$th and $\langle n_m \rangle = 0.12$ for $m = 167$th host states. For this reason, these m'th host states have small magnetic moments when $\mu = -2.78$ eV as seen in Figs. 5.2b and 5.3b. In DFT+MFA result (Figs. 5.2 (b) and 5.3 (b)), the square of host magnetic moments of $m = 144$th, 145th, 146th, 152nd, 153rd, 163rd, 166th and 167th host states are $\approx 0.21(\mu_B)^2$ at $\mu \approx -7.8$ eV, $\approx 0.12(\mu_B)^2$ at $\mu \approx -7.6$ eV, $\approx 0.2(\mu_B)^2$ at $\mu \approx -7$ eV, $\approx 0.18(\mu_B)^2$ in the interval
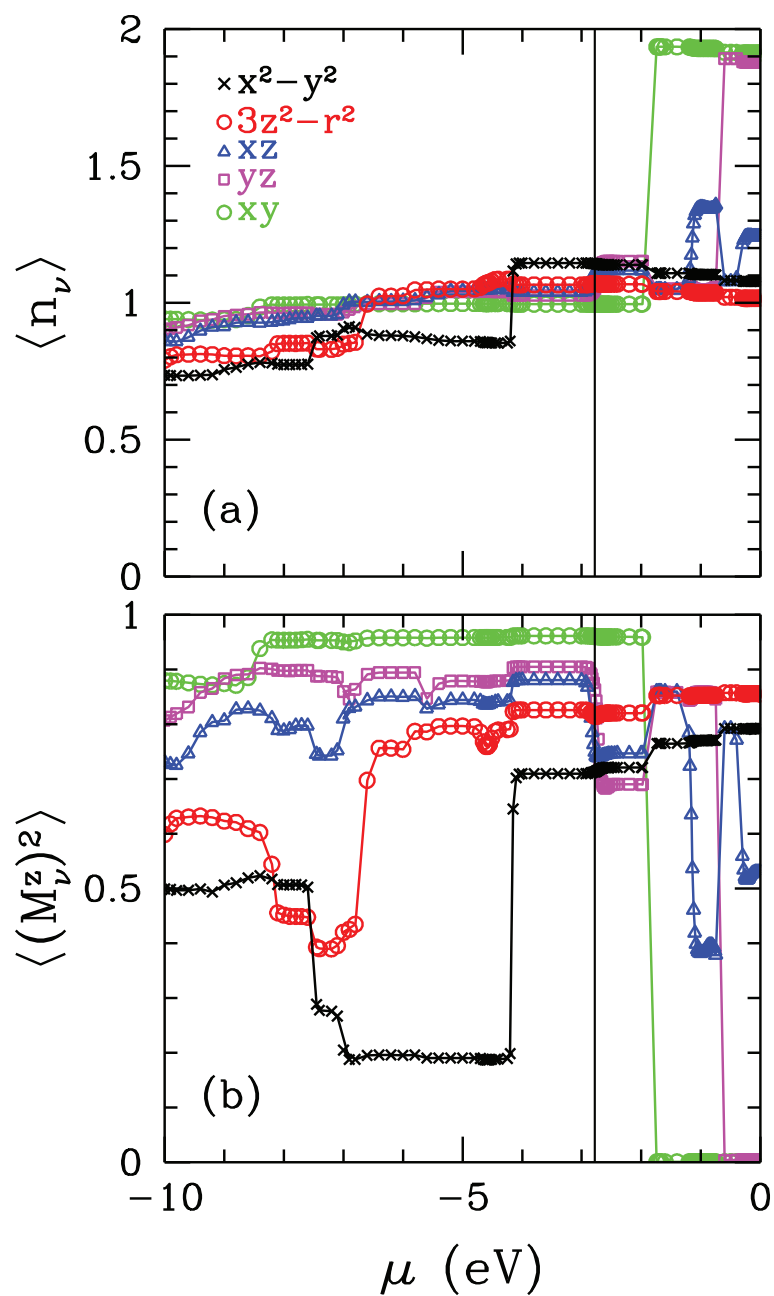
Figure 5.1. For deoxy-heme (a) DFT+MFA results on the electron occupation number $\langle n_\nu \rangle$ of the Fe($3d_\nu$) as a function of the chemical potential μ. (b) Square of the magnetic moment $\langle (M_\nu^z)^2 \rangle$ for the Fe($3d_\nu$) orbitals versus the chemical potential μ. Here, the vertical solid denotes the value of the HOMO level and it is calculated by DFT+MFA. These results are for $U = 4$ eV, $J = 0.9$ eV and $T = 300$ K.

-7 eV $\leq \mu \leq -6$ eV, $\approx 0.33(\mu_B)^2$ at $\mu \approx -6$ eV, $\approx 0.7(\mu_B)^2$ at $\mu \approx -4.6$ eV, $\approx 0.62(\mu_B)^2$ at $\mu \approx -2.76$ eV and $\approx 0.61(\mu_B)^2$ at $\mu \approx -2.64$ eV, respectively.

In Figs. 5.4 and 5.5 DFT+MFA results and in Figs. 4.4 and 4.5 DFT+QMC results show the magnetic correlation functions between $m = $ 144th, 145th, 146th, 152nd, 153rd, 163rd, 166th and 167th host states and the Fe($3d_\nu$) orbitals. In particular, these figures show the impurity-host magnetic correlations $\langle M_\nu^z M_m^z \rangle$ as a function of μ. In both DFT+MFA and DFT+QMC results, $m = $ 144th and 145th host states in the interval -8.5 eV $\lesssim \mu \lesssim -6.5$ eV, $m = $ 146th host state in the interval -7.5 eV $\lesssim \mu \lesssim -6.5$ eV and $m = $ 152nd host state in the interval -7.5 eV $\lesssim \mu \lesssim -4$ eV have antiferromagnetic correlations with Fe($3d_\nu$) orbitals. $m = $ 152nd host state has the strongest hybridization matrix element with $x^2 - y^2$ orbital in Fig. 2.9 (b). In Fig. 5.4 (d), this host state has a wide antiferromagnetic correlation. $m = $ 153rd host state in the interval -6 eV $\lesssim \mu \lesssim -5.6$ eV and $m = $ 163rd host state in the interval -5 eV $\lesssim \mu \lesssim -4.6$ eV have antiferromagnetic correlations with Fe($3d_\nu$) orbitals. For $m = $ 144th, 145th, 146th, 153rd and 163rd host states energy intervals of antiferromagnetic correlation are narrow because their hybridization contributions with $3z^2 - r^2$ orbital are small in Fig. 2.9 (a). $m = $ 166th and 167th host states in the interval -2.8 eV $\lesssim \mu \lesssim -2.6$ eV have antiferromagnetic correlations with Fe($3d_\nu$) orbitals. For these host states energy intervals of antiferromagnetic correlation are narrow and sharp because their hybridization contributions with Fe($3d_\nu$) orbitals are small in Figs. 2.9 (a) and 2.9 (b). In these intervals, magnetic correlation values of Fe($3d_\nu$) orbitals for each the m'th host states are different according to DFT+MFA and DFT+QMC results. Here, we observed that the antiferromagnetic correlation contributions are the same energy intervals for DFT+MFA and DFT+QMC methods. For $m = $ 144th, 145th, 146th, 152nd, 153rd, 163rd, 166th and 167th host states the results of DFT+MFA are similar to the results of DFT+QMC.

As a result, for deoxy-heme molecule DFT+MFA results are very similar to DFT+QMC results. Especially, we observe impurity bound states (IBS) at $\mu \approx -6.5$ eV and $\mu \approx -4$ eV in these results. The locations of IBS's are below the Fermi level, so IBS's are occupied by electrons. IBS's are shown in Fig. 5.1 for DFT+MFA and in Fig. 4.1 for DFT+QMC results. $m = $ 144th, 145th and 146th host eigenstates with the moments at Fe($3d_\nu$) orbitals at $\mu \approx -6.5$ eV are shown in Figs. 5.4 (a-c) and $m = $ 152nd host eigenstate with the moments at Fe($3d_\nu$) orbitals at $\mu \approx -4$ eV are shown in Fig. 5.4 (d) where antiferromagnetic correlations are over refer to the sudden increases of the electron occupation number and magnetic moment at these μ values in Fig. 5.1 in DFT+MFA. They show that these sudden increases become the IBS. For deoxy-heme molecule, the same
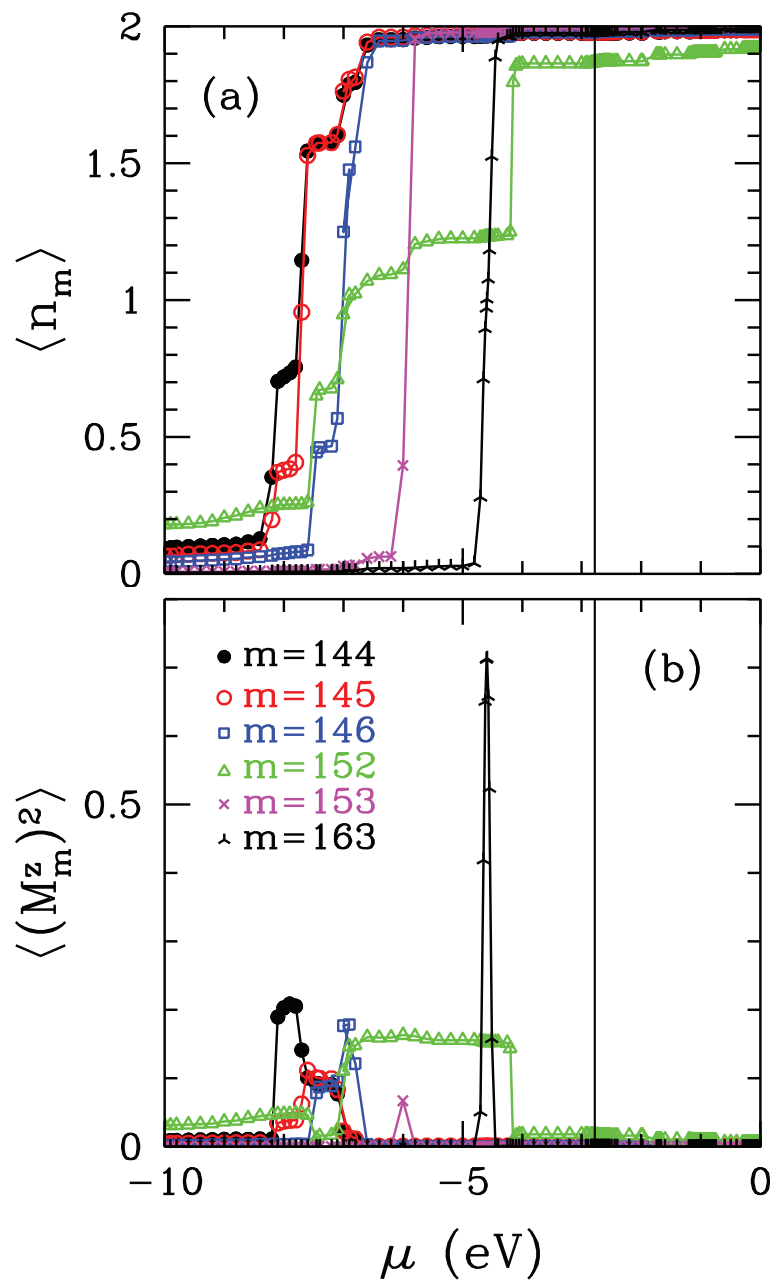
Figure 5.2. For deoxy-heme (a) DFT+MFA results on the electron occupation number of the $m = 144$th, 145th, 146th, 152nd, 153rd and 163rd host states $\langle n_m \rangle$ versus the chemical potential μ. (b) Square of the magnetic moment of the m'th host state $\langle (M_m^z)^2 \rangle$ versus μ. Here, the vertical solid denotes the value of the HOMO level and it is calculated by DFT+MFA. These results are for $U = 4$ eV, $J = 0.9$ eV and $T = 300$ K.
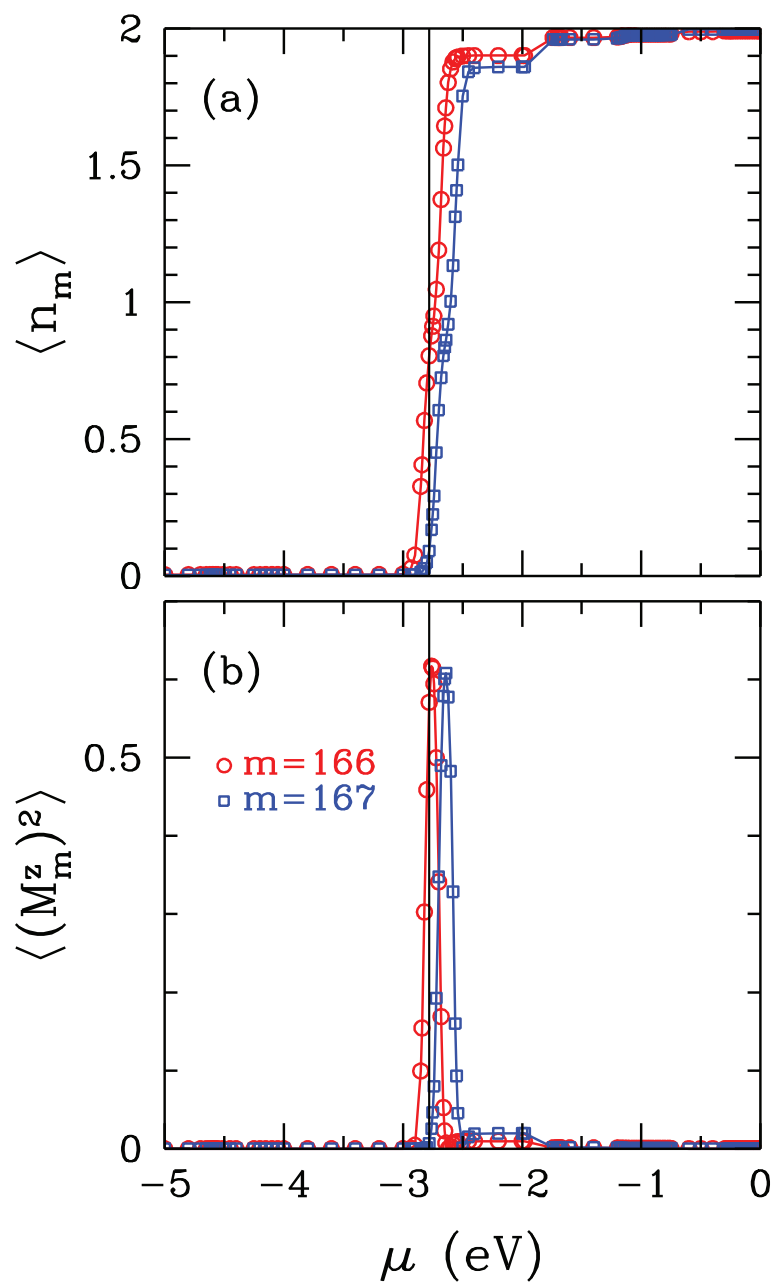
Figure 5.3. For deoxy-heme (a) DFT+MFA results on the electron occupation number of the $m = 166$th and 167th host states $\langle n_m \rangle$ versus the chemical potential μ. (b) Square of the magnetic moment of the m'th host state $\langle (M_m^z)^2 \rangle$ versus μ. Here, the vertical solid denotes the value of the HOMO level and it is calculated by DFT+MFA. These results are for $U = 4$ eV, $J = 0.9$ eV and $T = 300$ K.
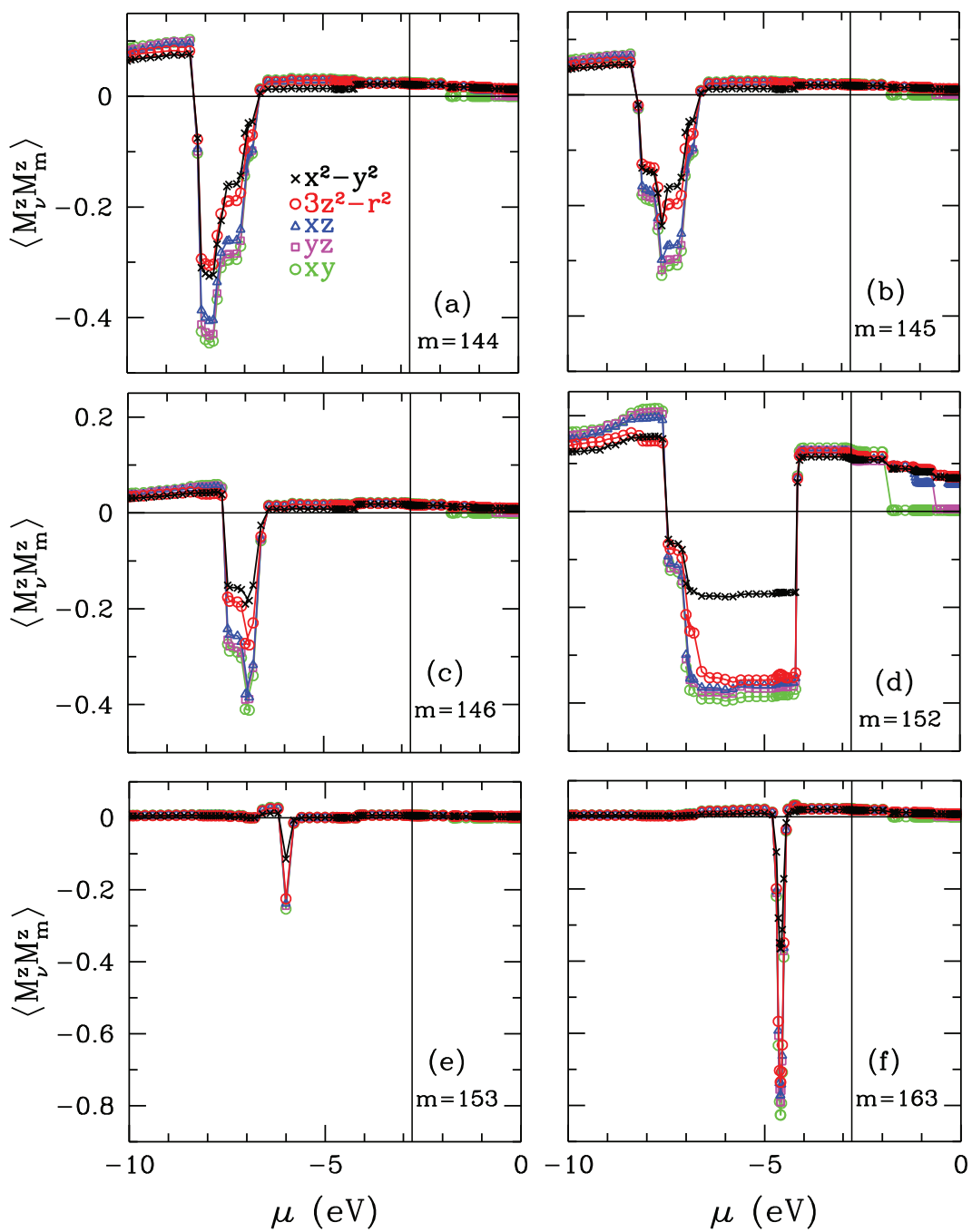
Figure 5.4. For deoxy-heme, DFT+MFA results on the magnetic correlation function $\langle M_\nu^z M_m^z \rangle$ between the m'th host eigenstate and the Fe($3d_\nu$) orbitals. Here results are shown for host states (a) $m = 144$th, (b) 145th, (c) 146th, (d) 152nd, (e) 153rd and (f) 163rd. The vertical solid denotes the value of the HOMO level and it is calculated by DFT+MFA. These results are for $U = 4$ eV, $J = 0.9$ eV and $T = 300$ K.
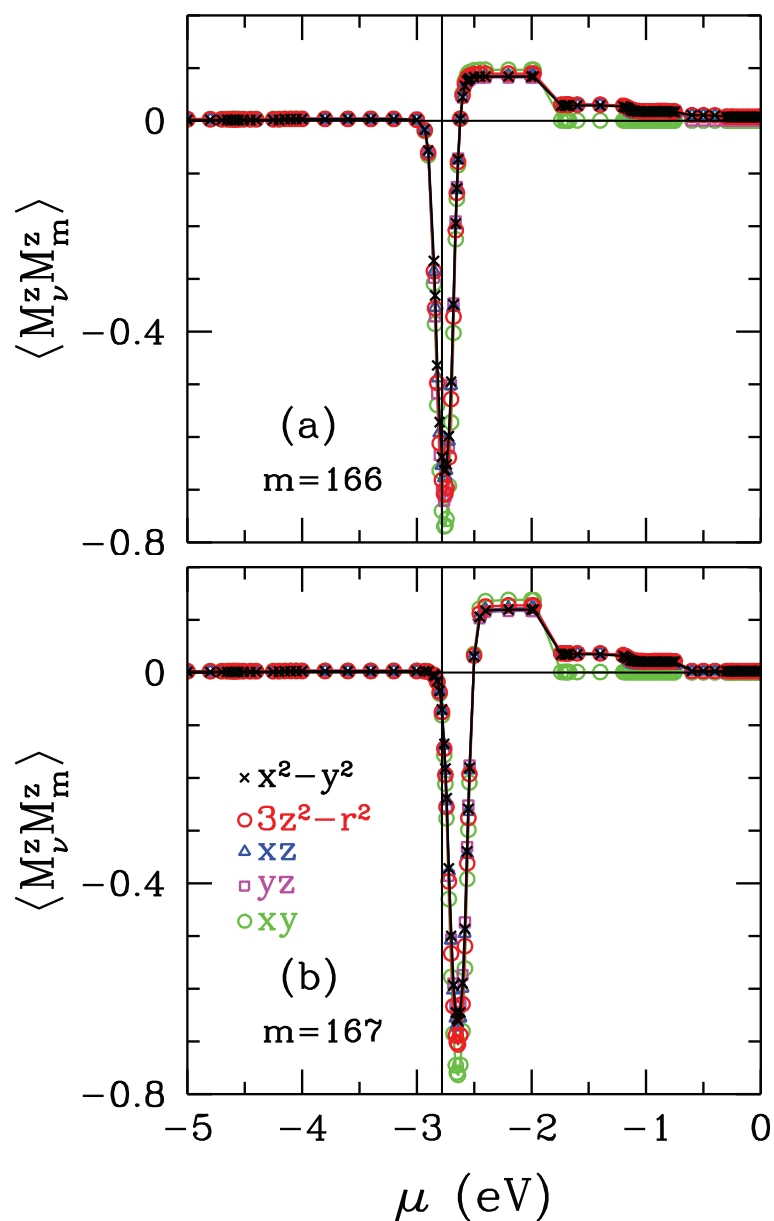
Figure 5.5. For deoxy-heme, DFT+MFA results on the magnetic correlation function $\langle M_\nu^z M_m^z \rangle$ between the m'th host eigenstate and the Fe($3d_\nu$) orbitals. Here results are shown for host states (a) 166th and (b) 167th. The vertical solid denotes the value of the HOMO level and it is calculated by DFT+MFA. These results are for $U = 4$ eV, $J = 0.9$ eV and $T = 300$ K.
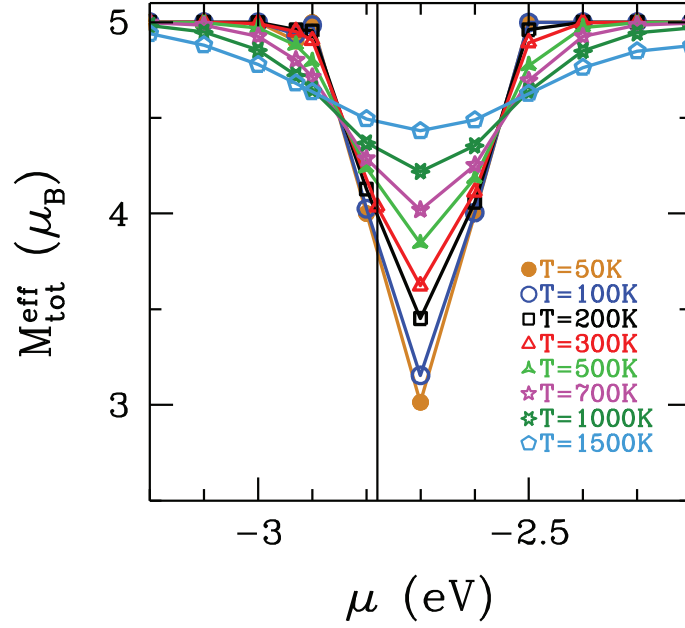
Figure 5.6. For $U = 4$ eV and $J = 0.9$ eV according to different temperatures of deoxy-heme total magnetic moments are shown as a function of the chemical potential μ. Here, the vertical black line denotes the HOMO level $\mu = -2.78$ eV for $T = 300$ K.

results have been achieved with DFT+MFA and DFT+QMC method. Figures 5.4 and 4.4 show that Fe($3d_\nu$) orbitals and host states also have the ferromagnetic correlations at the HOMO levels -2.78 eV and -2.80 eV in DFT+MFA and DFT+QMC, respectively. IBS's are occupied. Hence, the deoxy-heme molecule has a large magnetic moment and a high-spin state.

Figure 5.6 shows total magnetic moments as a function of the chemical potential μ according to different temperatures (50K, 100K, 200K, 300K, 500K, 700K, 1000K and 1500K) of deoxy-heme for $U = 4$ eV and $J = 0.9$ eV. When the temperature decreases, the value of the total magnetic moment decreases. However, this decrease occurs at above the energy level of 334 electrons ($\mu \approx -2.78$ eV) obtained by DFT+MFA. There are no significant changes the value of total magnetic moment between $T = 50$ K and $T = 300$ K. The value of the total magnetic moment is about $\approx 4.0\mu_B$ and deoxy-heme has still high-spin. In addition, we will compare the results of deoxy-heme with oxy-heme about magnetic moments for $T = 300$ K in Fig. 6.1.

5.2. DFT+MFA results for oxy-heme

In this part, we present DFT+MFA results on oxy-heme. Figure 5.7 (a) shows the electron occupation number $\langle n_\nu \rangle$ of the Fe($3d_\nu$) orbitals as a function of the chemical potential μ. In Fig. 5.7 (a), the electron number of $3d_{3z^2-r^2}$, $3d_{xz}$ and $3d_{yz}$ is singly occupied up to $\mu \approx -5.5$ eV. The electron number of $3d_{x^2-y^2}$ is singly occupied up to $\mu \approx -3.8$ eV. The electron number of $3d_{xy}$ is also singly occupied up to $\mu \approx -1.5$ eV. Figure 5.7 (b) shows square of the magnetic moment $\langle (M_\nu^z)^2 \rangle$ of the Fe($3d_\nu$) orbitals as a function of μ. In Figs. 5.7 (a) and 5.7 (b), we observe that the IBS's are seen at $\mu \approx -5.5$ eV for $3d_{3z^2-r^2}$ orbital and at $\mu \approx -3.8$ eV for $3d_{x^2-y^2}$ orbitals. In these figures, solid black vertical line denotes value of chemical potential of oxy-heme at $\mu = -3.84$ eV. Oxy-heme has 350 electrons at this value. This value shows HOMO level.

Figures 5.8 (a) and 5.9 (b) shows the electron occupation number of the m'th host state $\langle n_m \rangle$ as a function of μ. Figures 5.8 (b) and 5.9 (b) show square of the magnetic moment of the m'th host state $\langle (M_m^z)^2 \rangle$ versus μ. The electron occupation numbers of the m'th host states are singly occupied for $m = 153$rd and 154th states at $\mu \approx -7.5$ eV, for $m = 158$th and 159th states at $\mu \approx -6.5$ eV, for $m = 173$rd state at $\mu \approx -4.5$ eV. When these host states become fully occupied, magnetic moments are zero at $\mu \approx -3$ eV. The electron occupation numbers of the m'th host states are singly occupied for $m = 174$th, 175th and 176th states at $\mu \approx -2.7$ eV. The contributions of magnetic moment of $m = 153$rd and 154th states are very small. The value of magnetic moment of $m = 158$th and 159th states is $\approx 0.09\mu_B$ and $\approx 0.12\mu_B$, respectively. The value of magnetic moment of $m = 173$rd state is $\approx 0.3\mu_B$ at $\mu \approx -4.5$ eV. When the electron occupation number of the $m = 174$th, 175th and 176th host states become singly occupied, their magnetic moments are maximum. Although the hybridization contributions of these host states are small as shown in Fig. 3.17, these states have an effect in reducing the magnetic moment of oxy-heme molecule.

Figure 5.10 shows the magnetic correlation function $M_\nu^z M_m^z$ between the $m = 153$rd, 154th, 158th, 159th, 173rd, 174th, 175th and 176th host eigenstates and the Fe($3d_\nu$) orbitals. The magnetic correlations between $m = 153$rd, 154th states and Fe($3d_\nu$) orbitals exhibit ferromagnetic correlations at -10 eV $\lesssim \mu \lesssim -8.5$ eV and antiferromagnetic correlations at -8.5 eV $\lesssim \mu \lesssim -4.5$ eV. For $m = 153$rd and 154th states the antiferromagnetic correlations are over at $\mu \approx -5$ eV. When these antiferromagnetic correlations decrease rapidly at $\mu = -5$ eV for these host states, there are impurity bound states (IBS) for $3d_{3z^2-r^2}$, $3d_{xz}$ and $3d_{yz}$ orbitals. Similarly, for $m = 158$th and 159th host states at
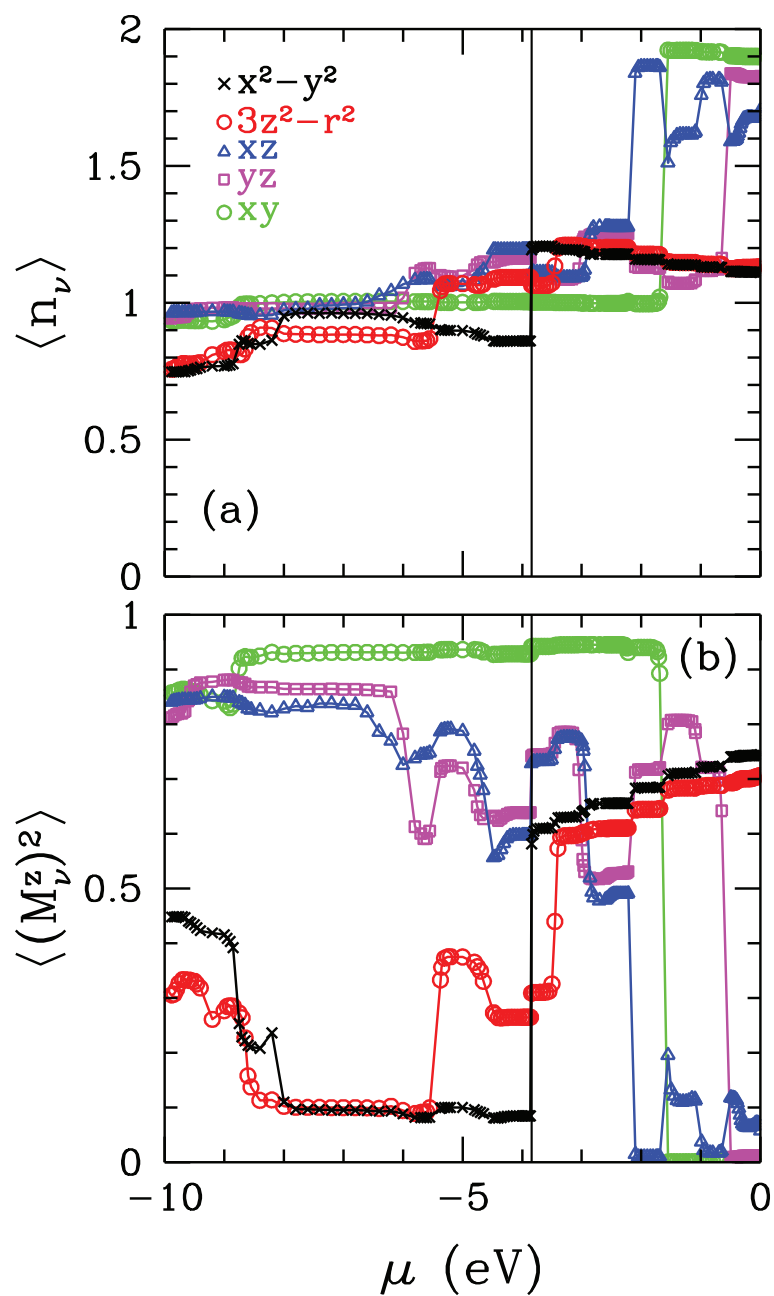
Figure 5.7. For oxy-heme (a) DFT+MFA results on the electron occupation number $\langle n_\nu \rangle$ of the Fe($3d_\nu$) as a function of the chemical potential μ. (b) Square of the magnetic moment $\langle (M_\nu^z)^2 \rangle$ for the Fe($3d_\nu$) orbitals versus the chemical potential μ. The vertical solid denotes the value of the HOMO level and it is calculated by DFT+MFA. These results are for $U = 4$ eV, $J = 0.9$ eV and $T = 300$ K.
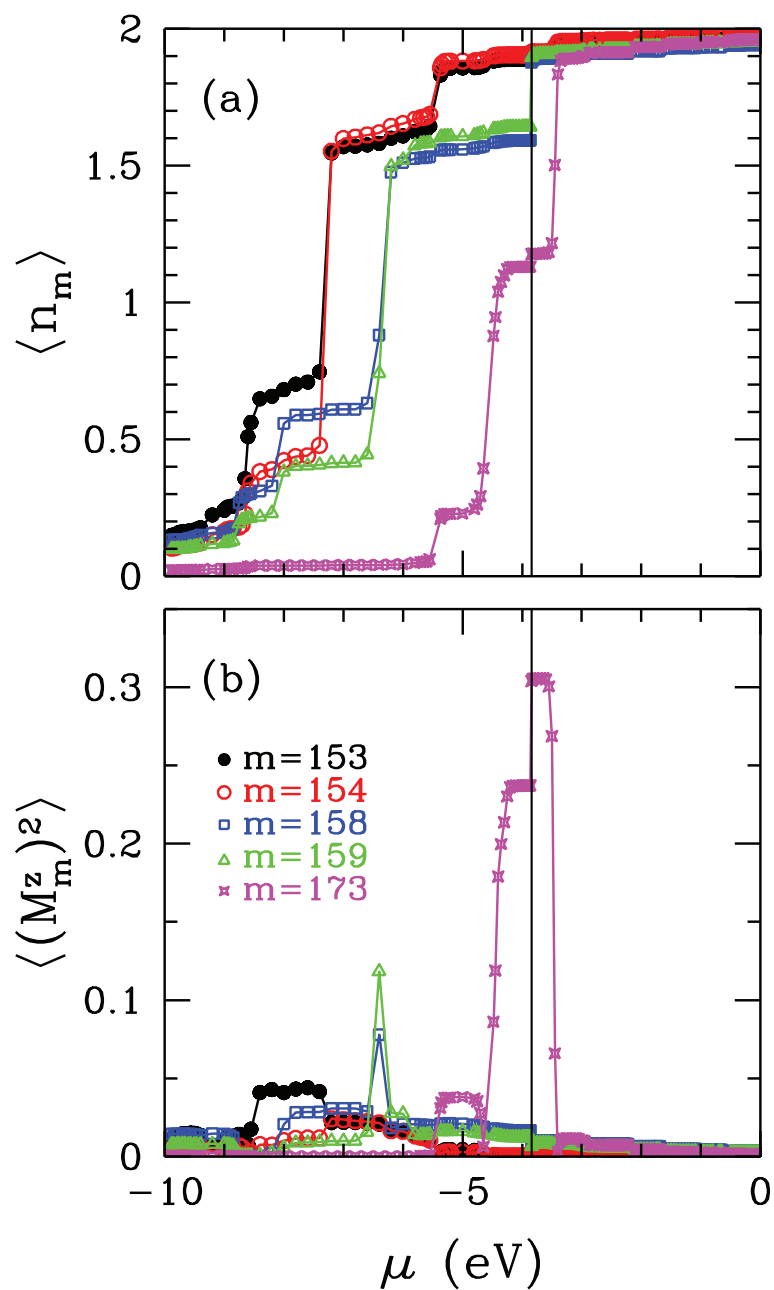
Figure 5.8. For oxy-heme (a) DFT+MFA results on the electron occupation number of the $m = 153$rd, 154th, 158th, 159th and 173rd host states $\langle n_m \rangle$ versus the chemical potential μ. (b) Square of the magnetic moment of the m'th host state $\langle (M_m^z)^2 \rangle$ versus μ. The vertical solid denotes the value of the HOMO level and it is calculated by DFT+MFA. These results are for $U = 4$ eV, $J = 0.9$ eV and $T = 300$ K.
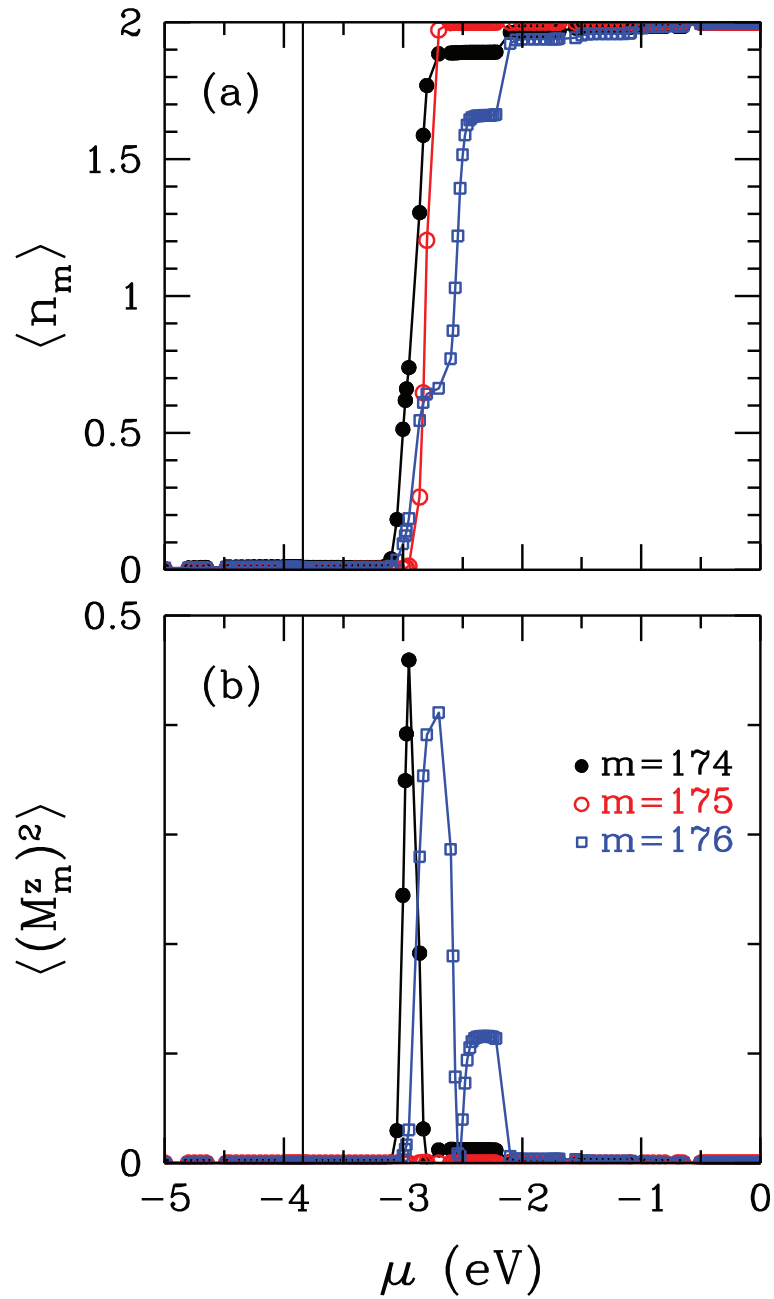
Figure 5.9. For oxy-heme (a) DFT+MFA results on the electron occupation number of $m = 174$th, 175th and 176th host states $\langle n_m \rangle$ versus the chemical potential μ. (b) Square of the magnetic moment of the m'th host state $\langle (M_m^z)^2 \rangle$ versus μ. The vertical solid denotes the value of the HOMO level and it is calculated by DFT+MFA. These results are for $U = 4$ eV, $J = 0.9$ eV and $T = 300$ K.
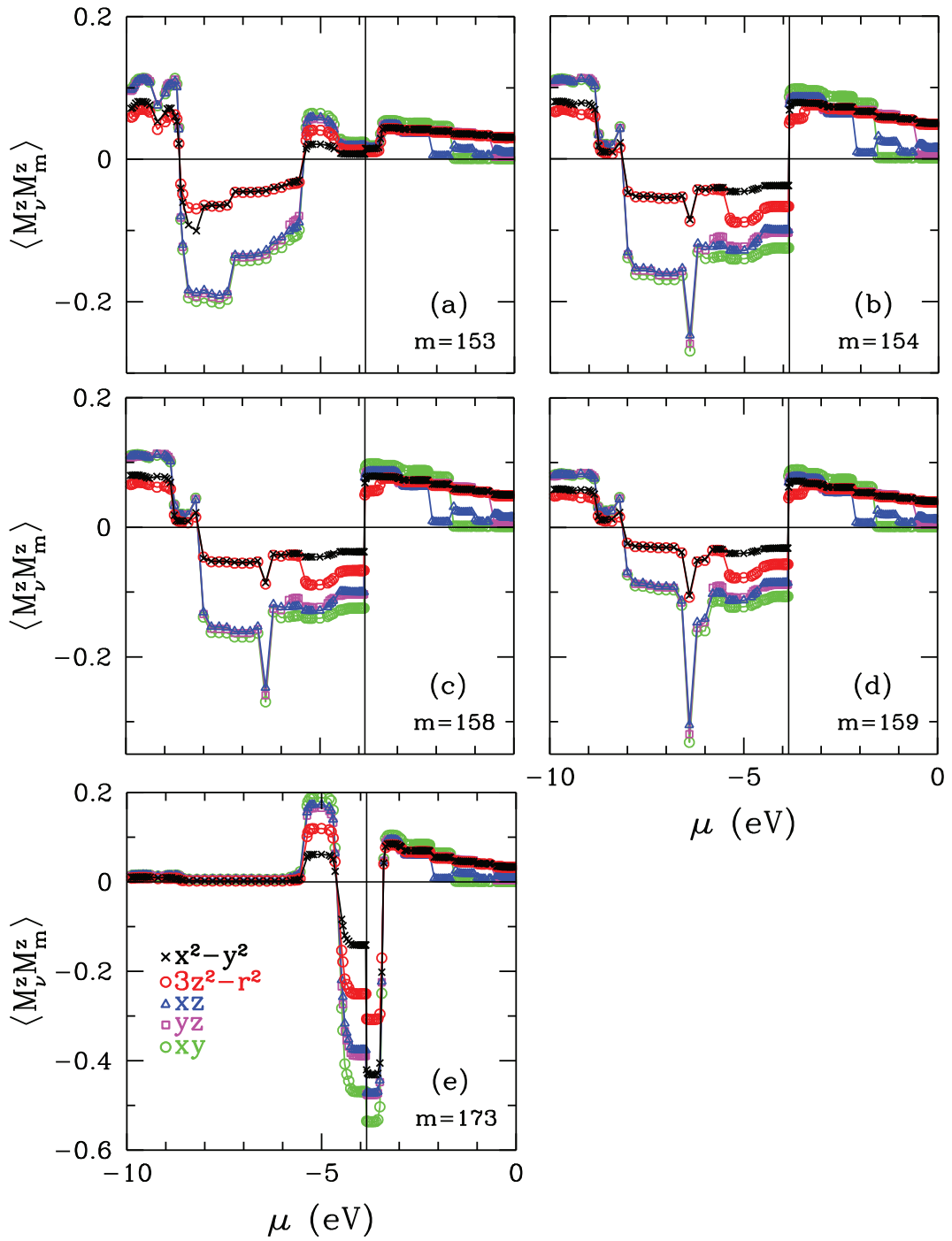
Figure 5.10. For oxy-heme, DFT+MFA results on the magnetic correlation function $\langle M_\nu^z M_m^z \rangle$ between the m'th host eigenstate and the Fe($3d_\nu$) orbitals. Here results are shown for host states (a) $m = 153$rd, (b) 154th, (c) 158th, (d) 159th and (e) 173rd. The vertical solid denotes the value of the HOMO level and it is calculated by DFT+MFA. These results are for $U = 4$ eV, $J = 0.9$ eV and $T = 300$ K.
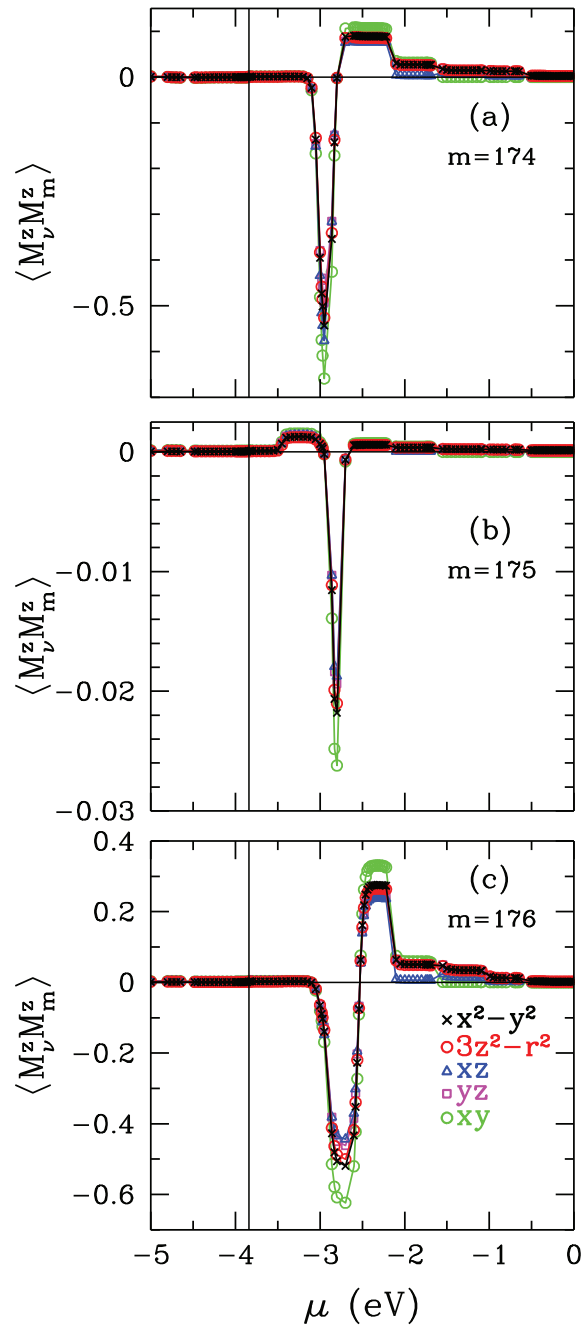
Figure 5.11. For oxy-heme, DFT+MFA results on the magnetic correlation function $\langle M_\nu^z M_m^z \rangle$ between the m'th host eigenstate and the Fe($3d_\nu$) orbitals. Here results are shown for host states (a) $m = 174$th, (g) 175th and (h) 176th. The vertical solid denotes the value of the HOMO level and it is calculated by DFT+MFA. These results are for $U = 4$ eV, $J = 0.9$ eV and $T = 300$ K.

$\mu \approx -4$ eV there are IBS for $3d_{x^2-y^2}$, $3d_{xy}$ and $3d_{yz}$ orbitals. For $m = $ 174th, 175th and 176th host states magnetic correlations are zero up to $\mu \approx -3.5$ eV. For these host states the antiferromagnetic correlations are over at $\mu \approx -4$ eV and $\mu \approx -3$ eV, respectively. At $\mu \approx -3$ eV there are IBS for $3d_{3z^2-r^2}$, $3d_{xz}$ and $3d_{yz}$ orbitals.

As a result, for oxy-heme, we do not find the location of IBS correctly with the DFT+MFA method. IBS is still occupied with DFT+MFA. IBS needs to become unoccupied because oxy-heme has a low-spin state. Thus, the DFT+MFA method does not work well with molecules having a low-spin state.

CHAPTER 6

COMPARISON OF VARIOUS COMPUTATIONAL METHODS FOR HEME MOLECULES

In this section, we use four different methods: DFT, DFT+U, DFT+MFA and DFT+QMC to obtain magnetic properties of deoxy-heme and oxy-heme molecules. We will discuss the results obtained from these methods. Firstly, we carry out the DFT calculations of deoxy-heme and oxy-heme by using Gaussian (Frisch et al. (2009)) program with BP86 exchange-correlation energy functional (Becke (1988); Perdew (1986)) and 6-31G basis set. We obtain parameters of the Anderson model from DFT calculations. We study the DFT+MFA and DFT+QMC methods by using these parameters. We observe that the DFT+MFA results are more reliable than the DFT and DFT+U results. DFT+MFA results are similar to DFT+QMC results. In this chapter, we will compare the results of DFT, DFT+U, DFT+MFA and DFT+QMC with each other and experimental data for deoxy-heme and oxy-heme molecules.

In the DFT+MFA and DFT+QMC results, we use $U = 4$ eV, $J = 0.9$ eV and $T = 300$ K for the deoxy-heme and oxy-heme molecules. DFT result does not depend on these values. We use $U = 4$ eV and $J = 0.9$ eV for DFT+U method. In Chapter 3, we present the DFT and DFT+U results of deoxy and oxy-heme molecules. In Chapter 4, we show the DFT+QMC results of these heme molecules. In addition, we present DFT+MFA results of these heme molecules in Chapter 5. Here, we will compare the charge and effective magnetic moment distributions of Fe($3d$) orbitals for deoxy and oxy-heme. We have showed graphically the DFT, DFT+QMC and DFT+MFA results for deoxy-heme and oxy-heme molecules in Chapters 3, 4 and 5. Here, we discuss the values of total electron numbers of Fe($3d$) orbitals $n_{\text{Fe}(3d)}$ and the effective magnetic moments $M_{\text{Fe}(3d)}^{\text{eff}}$ of deoxy-heme and oxy-heme molecules for $U = 4$ eV, $J = 0.9$ eV and $T = 300$ K.

In the DFT method, we calculate that the ground state energy of deoxy-heme is the triplet-spin state (S=1) and also the ground state energy of oxy-heme is the open-shell singlet-spin state (S=0). The first row of Table 6.1 denotes that the total electron numbers of Fe($3d$) orbitals of deoxy-heme and oxy-heme are shown as 6.14 and 6.20, respectively. Here, the DFT result does not depend on the U and J values.

The second row of Table 6.1 denotes that the total electron numbers of Fe($3d$)

Table 6.1. DFT, DFT+U, DFT+MFA and DFT+QMC results on the total electron numbers of Fe($3d$) orbitals for deoxy-heme and oxy-heme. Here, DFT+U, DFT+MFA and DFT+QMC results are obtained for $U = 4$ eV, $J = 0.9$ eV and $T = 300$ K. DFT result does not depend on the U and J values.

	deoxy-heme $n_{\text{Fe}(3d)}$	oxy-heme $n_{\text{Fe}(3d)}$
DFT	6.14	6.20
DFT+U	6.22	6.32
DFT+MFA	5.37	5.48
DFT+QMC	5.38	5.84
DFT+QMC[a]	5.36	6.07

[a] For $T = 150$ K.

orbitals of deoxy-heme and oxy-heme are obtained by the DFT+U methods. The total electron number of Fe($3d$) orbitals of the deoxy-heme is 6.22 electrons for $U = 4$ eV and $J = 0.9$ eV. The total electron number of Fe($3d$) orbitals of the oxy-heme is 6.32 electrons for $U = 4$ eV and $J = 0.9$ eV.

The third row of Table 6.1 denotes that the total electron numbers of Fe($3d$) orbitals of deoxy-heme and oxy-heme are obtained by the DFT+MFA methods. For $U = 4$ eV, $J = 0.9$ eV and $T = 300$ K, the 334 electrons are achieved at $\mu = -2.78$ eV. The total electron number of Fe($3d$) orbitals of the deoxy-heme is 5.37 electrons at $\mu = -2.78$ eV. For oxy-heme, the 350 electrons are reached at $\mu = -3.84$ eV for the values of $U = 4$ eV, $J = 0.9$ eV and $T = 300$ K. The total electron number of Fe($3d$) orbitals of the oxy-heme is 5.48 electrons at $\mu = -3.84$ eV. In Table 6.1, the total electron numbers of Fe($3d$) orbitals which are obtained by DFT+MFA method are less than their DFT results.

The fourth row of Table 6.1 denotes that the total electron numbers of Fe($3d$) orbitals of deoxy-heme and oxy-heme are obtained by the DFT+QMC methods for $U = 4$ eV, $J = 0.9$ eV and $T = 300$ K. In DFT+QMC results, the total electron numbers of deoxy-heme and oxy-heme, which are 334 and 350 electrons, are achieved at $\mu = -2.8$ eV and $\mu = -3.8$ eV. The total electron numbers of Fe($3d$) orbitals of the deoxy-heme and oxy-heme are 5.38 electrons at $\mu = -2.8$ eV and 5.84 electrons at $\mu = -3.8$ eV, respectively. The last row of Table 6.1 shows the total electron numbers of Fe($3d$) orbitals of deoxy-heme and oxy-heme molecules for $T = 150$ K. The total electron numbers of Fe($3d$) orbitals of the deoxy-heme and oxy-heme are 5.36 electrons at $\mu = -2.81$ eV and 6.07 electrons at $\mu = -3.89$ eV, respectively.

Table 6.1 denotes that DFT+MFA and DFT+QMC results on the total electron numbers of Fe($3d$) orbitals of deoxy-heme and oxy-heme molecules for $U = 4$ eV, $J = 0.9$ eV and $T = 300$ K. We observe that these results are very similar for $n_{\text{Fe}(3d)}$ of deoxy-heme molecule.

From DFT, DFT+U, DFT+MFA and DFT+QMC results, the electron numbers of Fe($3d$) orbitals are shown as up-electron $n_{\nu\uparrow}$, down-electron $n_{\nu\downarrow}$ and total of up-electron and down-electron n_ν in Table 6.2 and 6.5 for deoxy-heme and oxy-heme, respectively.

6.1. Comparison of the DFT, DFT+U, DFT+MFA and DFT+QMC for deoxy-heme

For deoxy-heme, the first two rows of Table 6.2 show DFT and DFT+U results on the electron numbers of Fe($3d$) orbitals. While $3d_{yz}$, $3d_{xz}$, $3d_{3z^2-r^2}$ and $3d_{x^2-y^2}$ orbitals of deoxy-heme are nearly singly occupied, $3d_{xy}$ orbital are doubly occupied for DFT and DFT+U methods. The last two rows of Table 6.2 denote that the occupation numbers of Fe($3d$) orbitals of deoxy-heme are singly occupied in DFT+MFA and DFT+QMC results, respectively. In DFT+MFA results the occupation numbers of Fe($3d$) orbitals of deoxy-heme are very similar to their DFT+QMC results.

The effective magnetic moment is defined as $M_\nu^{\text{eff}} = n_{\nu\uparrow} - n_{\nu\downarrow}$ which is the different between spin-up and spin-down electrons. The first five columns of Table 6.3 show the effective magnetic moments of Fe($3d$) orbitals of deoxy-heme. The sixth column of Table 6.3 denotes the total effective magnetic moment of Fe($3d$) orbitals of deoxy-heme. The last two columns of Table 6.3 denote the total effective magnetic moment of host orbitals and all orbitals of deoxy-heme, respectively. In the first two rows of Table 6.3, DFT and DFT+U give similar results for effective magnetic moments of deoxy-heme. For DFT and DFT+U methods, the total effective magnetic moment of deoxy-heme is 2.0 μ_B. The ground state energy of deoxy-heme has the triple ground state in the DFT and DFT+U results. In the last two rows of Table 6.3, DFT+MFA and DFT+QMC give similar results for effective magnetic moments of deoxy-heme. For DFT+MFA and DFT+QMC methods, the total effective magnetic moment of deoxy-heme is $\approx 4\mu_B$. In the DFT+MFA results, the total effective magnetic moment of Fe($3d$) orbitals is close to DFT+QMC results for $J = 0.9$ eV, but the DFT and DFT+U find almost half. Spin-state of deoxy-heme is found as high-spin from DFT+MFA and DFT+QMC results. These results agree with experimental results.

Table 6.2. For deoxy-heme, the occupancy numbers of Fe($3d$) orbitals are shown as up-electron $n_{\nu\uparrow}$, down-electron $n_{\nu\downarrow}$ and total of up-electron and down-electron n_ν for DFT, DFT+U, DFT+MFA and DFT+QMC results. Here, we use $U = 4$ eV, $J = 0.9$ eV and $T = 300$ K for DFT+U, DFT+MFA and DFT+QMC results. DFT result does not depend on the U and J values.

				deoxy-heme		
	ν	$3d_{xz}$	$3d_{yz}$	$3d_{3z^2-r^2}$	$3d_{x^2-y^2}$	$3d_{xy}$
	$n_{\nu\uparrow}$	0.93	0.97	0.97	0.36	0.98
DFT	$n_{\nu\downarrow}$	0.33	0.32	0.16	0.22	0.90
	n_ν	1.26	1.29	1.13	0.58	1.88
	$n_{\nu\uparrow}$	0.92	0.94	0.97	0.36	0.95
DFT+U	$n_{\nu\downarrow}$	0.42	0.45	0.16	0.24	0.81
	n_ν	1.34	1.39	1.13	0.60	1.76
	$n_{\nu\uparrow}$	0.99	0.99	0.99	0.99	0.99
DFT+MFA	$n_{\nu\downarrow}$	0.12	0.06	0.08	0.15	0.01
	n_ν	1.11	1.05	1.07	1.14	1.0
DFT+QMC	n_ν	1.12	1.06	1.07	1.13	1.0

Table 6.3. For deoxy-heme, it is shown comparison of effective magnetic moment distributions for DFT, DFT+U, DFT+MFA and DFT+QMC results. The DFT result does not depend on the U and J values. The following values of the effective magnetic moments are calculated in units of Bohr magneton (μ_B). Here, we use $U = 4$ eV, $J = 0.9$ eV and $T = 300$ K for DFT+U, DFT+MFA and DFT+QMC results.

deoxy-heme								
	M_{xz}^{eff}	M_{yz}^{eff}	$M_{3z^2-r^2}^{\text{eff}}$	$M_{x^2-y^2}^{\text{eff}}$	M_{xy}^{eff}	$M_{\text{Fe(3d)}}^{\text{eff}}$	$M_{\text{host}}^{\text{eff}}$	$M_{\text{tot}}^{\text{eff}}$
DFT	0.60	0.65	0.81	0.14	0.08	2.28	-0.28	2.0
DFT+U	0.50	0.49	0.81	0.12	0.14	2.06	-0.06	2.0
DFT+MFA	0.87	0.93	0.91	0.84	0.98	4.52	-0.49	4.03
DFT+QMC	0.93	0.96	0.92	0.93	0.99	4.55	1.06	4.08

Table 6.4. For deoxy-heme, it is shown comparison of effective spin moment of Fe($3d$) orbitals, host orbitals and total orbitals for DFT, DFT+U, DFT+MFA and DFT+QMC results. Here, we use $U = 4$ eV, $J = 0.9$ eV and $T = 300$ K for DFT+U, DFT+MFA and DFT+QMC results.

deoxy-heme	$S_{\text{Fe(3d)}}^{\text{eff}}$	$S_{\text{host}}^{\text{eff}}$	$S_{\text{tot}}^{\text{eff}}$
DFT	0.74	0.02	0.62
DFT+U	0.64	0.0	0.62
DFT+MFA	1.81	0.06	1.58
DFT+QMC	1.83	0.23	1.60

In Table 6.4, we show the effective spin of Fe($3d$) orbitals $S_{\text{Fe(3d)}}^{\text{eff}}$, effective spin of the host orbitals $S_{\text{host}}^{\text{eff}}$ and total effective spin of deoxy-heme $S_{\text{tot}}^{\text{eff}}$ for these methods. The effective spin is calculated by using the effective magnetic moment $M_x^{\text{eff}} = 2\sqrt{S_x^{\text{eff}}\left(S_x^{\text{eff}} + 1\right)}$. For DFT and DFT+U methods, the effective spin of $3d$ orbitals and host states are about 0.7 and 0.0, respectively. Total spin of deoxy-heme is 0.62. This means that the deoxy-heme has triplet(intermediate)-spin state for DFT and DFT+U. For DFT+MFA and DFT+QMC methods, the effective spin of $3d$ orbitals is about 1.8. Total spin of deoxy-heme is about 1.6. This means that the deoxy-heme has high-spin state for DFT+MFA and DFT+QMC.

6.2. Comparison of the DFT, DFT+U, DFT+MFA and DFT+QMC for oxy-heme

In Table 6.5, we show the occupancy numbers of Fe($3d$) orbitals for DFT, DFT+U, DFT+MFA and DFT+QMC results of oxy-heme. The occupancy numbers of Fe($3d$) orbitals are shown as up-electron $n_{\nu\uparrow}$, down-electron $n_{\nu\downarrow}$ and total of up-electron and down-electron n_{ν}. The first and second rows of Table 6.5 shows DFT and DFT+U results on the electron numbers of Fe($3d$) orbitals. While $3d_{3z^2-r^2}$ and $3d_{x^2-y^2}$ orbitals of oxy-heme are nearly singly occupied, $3d_{xz}$, $3d_{yz}$ and $3d_{xy}$ orbitals are doubly occupied for DFT and DFT+U results. In Table 6.5, the occupation number of Fe($3d$) orbitals of oxy-heme is obtained with DFT+MFA and also Fe($3d$) orbitals have nearly singly occupied. In the last part of Table 6.5, the electron numbers of Fe($3d$) orbitals are shown from DFT+QMC result for the temperature $T = 300$ K and $^aT = 150$ K. While $3d_{3z^2-r^2}$, $3d_{xz}$, $3d_{yz}$ and

Table 6.5. For oxy-heme, the occupancy numbers of Fe($3d$) orbitals are shown as up-electron $n_{\nu\uparrow}$, down-electron $n_{\nu\downarrow}$ and total of up-electron and down-electron n_ν for DFT, DFT+U, DFT+MFA and DFT+QMC results. Here, we use $U = 4$ eV, $J = 0.9$ eV and $T = 300$ K for DFT+U, DFT+MFA and DFT+QMC results. DFT result does not depend on the U and J values. We use $T = 150$ K for DFT+QMC^a result.

		oxy-heme				
	ν	$3d_{xz}$	$3d_{yz}$	$3d_{3z^2-r^2}$	$3d_{x^2-y^2}$	$3d_{xy}$
DFT	$n_{\nu\uparrow}$	0.81	0.91	0.43	0.33	0.96
	$n_{\nu\downarrow}$	0.70	0.45	0.36	0.30	0.95
	n_ν	1.51	1.36	0.79	0.63	1.91
DFT+U	$n_{\nu\uparrow}$	0.86	0.90	0.47	0.35	0.93
	$n_{\nu\downarrow}$	0.61	0.55	0.42	0.32	0.91
	n_ν	1.47	1.45	0.89	0.67	1.84
DFT+MFA	$n_{\nu\uparrow}$	0.98	0.98	0.81	0.98	0.99
	$n_{\nu\downarrow}$	0.13	0.12	0.25	0.22	0.02
	n_ν	1.11	1.10	1.06	1.20	1.01
DFT+QMC	n_ν	1.18	1.15	0.92	0.75	1.84
DFT+QMC^a	n_ν	1.31	1.34	0.85	0.68	1.88

^{a} For $T = 150$ K.

$3d_{x^2-y^2}$ orbitals of oxy-heme are nearly singly occupied, $3d_{xy}$ orbital is doubly occupied for DFT+QMC result.

The effective magnetic moment is defined as $M_\nu^{\mathrm{eff}} = n_{\nu\uparrow} - n_{\nu\downarrow}$ which is the different between spin-up and spin-down electrons. The first five columns of Table 6.6 show the effective magnetic moments of Fe($3d$) orbitals of oxy-heme. The sixth column of Table 6.6 denotes the total effective magnetic moment of Fe($3d$) orbitals of oxy-heme. The last two columns of Table 6.6 denote the total effective magnetic moment of host orbitals and all orbitals of oxy-heme, respectively. The ground state energy of oxy-heme has the open-shell singlet-spin state in the DFT and DFT+U result. In the first two rows of Table 6.6, DFT and DFT+U give similar results for effective magnetic moments of oxy-heme. For DFT and DFT+U methods, the total effective magnetic moment of oxy-heme is about zero Bohr magneton and oxy-heme has a low-spin state. However, the effective magnetic moments of Fe($3d$) orbitals are very small. We indicate the DFT results in the first row of Table 6.6. Total magnetic moment of Fe($3d$) orbitals and $2p$'s orbitals of dioxygen (O_2) are $0.68\mu_B$ and $-0.68\mu_B$ for the open-shell singlet ground state of oxy-heme, respectively. The magnetic moment of Fe($3d$) orbitals and π^* orbitals of O_2 were

Table 6.6. For oxy-heme, it is shown comparison of effective magnetic moment of Fe($3d$) orbitals for DFT, DFT+U, DFT+MFA and DFT+QMC results. Here, the DFT result does not depend on the U and J values. The following values of the effective magnetic moments calculated in units of Bohr magneton (μ_B). Here, we use $U = 4$ eV, $J = 0.9$ eV and $T = 300$ K for DFT+U, DFT+MFA and DFT+QMC results. We use $T = 150$ K for DFT+QMC^a result.

oxy-heme	M_{xz}^{eff}	M_{yz}^{eff}	$M_{3z^2-r^2}^{\text{eff}}$	$M_{x^2-y^2}^{\text{eff}}$	M_{xy}^{eff}	$M_{\text{Fe(3d)}}^{\text{eff}}$	$M_{\text{host}}^{\text{eff}}$	$M_{\text{tot}}^{\text{eff}}$
DFT	0.11	0.46	0.07	0.03	0.01	0.68	-0.68	0.0
DFT+U	0.25	0.35	0.05	0.03	0.02	0.70	-0.63	0.07
DFT+MFA	0.85	0.86	0.56	0.76	0.97	4.0	-0.05	3.95
DFT+QMC	0.89	0.89	0.79	0.74	0.40	2.50	1.32	2.13
DFT+QMC^a	0.77	0.76	0.77	0.72	0.35	1.65	1.48	0.60

^{a} For $T = 150$ K.

found with DFT calculations in Refs. (Scherlis and Estrin (2002); Scherlis et al. (2007); Rovira et al. (1997)). These values were approximately $-1\mu_B$ and $+1\mu_B$, respectively. In the third row of Table 6.6, the DFT+MFA gives large effective magnetic moments of Fe($3d$) orbitals. For DFT+MFA, the total effective magnetic moment of oxy-heme is $\approx 4\mu_B$. DFT+MFA finds a high-spin state for oxy-heme, which is wrong. In Table 6.5, for DFT+MFA method, $3d_{xy}$ orbital is not doubly occupied, hence it has large effective magnetic moment in Table 6.6. In the DFT+QMC results, the effective magnetic moments of xy orbital is small because it is doubly occupied. The effective magnetic moments of other Fe($3d$) orbitals have strong. DFT+QMC method finds total effective magnetic moment of oxy-heme about 2.1 μ_B at $T = 300$ K and 0.6 μ_B at $T = 150$ K. In the DFT+QMC result, oxy-heme has a small magnetic moment at $T = 150$ K and has a low-spin state.

In Table 6.7, we show the effective spin of Fe($3d$) orbitals $S_{\text{Fe(3d)}}^{\text{eff}}$, effective spin of the host orbitals $S_{\text{host}}^{\text{eff}}$ and total effective spin of oxy-heme $S_{\text{tot}}^{\text{eff}}$ for these methods. The effective spin moment is calculated by $M_x^{\text{eff}} = 2\sqrt{S_x^{\text{eff}}(S_x^{\text{eff}}+1)}$. For DFT and DFT+U methods, the effective spin of $3d$ orbitals and host states are about 0.1. For DFT and DFT+U, oxy-heme has low-spin state but the effective magnetic moments of Fe($3d$) orbitals are very small. For oxy-heme, DFT+MFA finds intermediate-spin (S=1) state, which is wrong. For DFT+QMC results, the effective spin of $3d$ orbitals is about 0.85 at $T = 300$ K and 0.62 at $T = 150$ K. Total spin of oxy-heme is about 0.7 at $T = 300$ K and

Table 6.7. For oxy-heme, it is shown comparison of effective spin moment of Fe(3d) orbital, host orbitals and total orbitals for DFT, DFT+U, DFT+MFA and DFT+QMC results. Here, we use $U = 4$ eV, $J = 0.9$ eV and $T = 300$ K for DFT+U, DFT+MFA and DFT+QMC results. We use $T = 150$ K for DFT+QMC^a result.

oxy-heme	$S_{\text{Fe(3d)}}^{\text{eff}}$	$S_{\text{host}}^{\text{eff}}$	$S_{\text{tot}}^{\text{eff}}$
DFT	0.10	0.10	0.0
DFT+U	0.11	0.09	0.0
DFT+MFA	1.59	0.0	1.04
DFT+QMC	0.85	0.33	0.68
DFT+QMC^a	0.62	0.38	0.33

^{a} For $T = 150$ K.

about 0.3 at $T = 150$ K. This means that the oxy-heme has low-spin state for DFT+QMC results.

In Fig. 6.1, we present DFT+MFA result on the total magnetic moment of Fe(3d) orbitals, host orbitals, between Fe(3d) orbitals and host orbitals, and all orbitals as a function of μ for deoxy-heme and oxy-heme molecules. The vertical blue line denotes the HOMO energy levels of oxy-heme. The vertical black line denotes the HOMO energy level (-2.78 eV) of deoxy-heme. The vertical blue line denotes the HOMO energy level (-3.84 eV) of oxy-heme. For deoxy-heme total magnetic moment of Fe(3d) orbitals $M_{\text{Fe(3d)}}^{\text{eff}}$ is $4.52\mu_B$ at $\mu = -2.78$ eV in Fig. 6.1 (a) and also is shown in the second row of Table 6.3. For oxy-heme total magnetic moment of Fe(3d) orbitals $M_{\text{Fe(3d)}}^{\text{eff}}$ is $4.0\mu_B$ at $\mu = -3.84$ eV in Fig. 6.1 (a) and also is shown in the second row of Table 6.6. Figure 6.1 (b) shows the total magnetic moments of host orbitals for deoxy-heme and oxy-heme. These moments have $-0.49\mu_B$ and $-0.05\mu_B$, respectively. We represent these moments in Tables 6.3 and 6.6 for DFT+MFA results. In Fig. 6.1 (c), the correlations between the $3d$ and host states are antiferromagnetic and $\langle M_{3d}^z M_{\text{host}}^z \rangle$ is -2.20 μ_B^2 for deoxy-heme and -0.19 μ_B^2 for oxy-heme. $M_{\text{tot}}^{\text{eff}}$ of deoxy-heme becomes $4.03\mu_B$ at $\mu = -2.78$ eV in Fig. 6.1 (d) and also it is showed as different temperatures in Fig. 5.6. $M_{\text{tot}}^{\text{eff}}$ of oxy-heme is $\approx 4\mu_B$ at $\mu = -3.84$ eV. DFT+MFA method does not give accurate result for oxy-heme. This technique does not obtain low-spin state because it does not find the location of impurity bound state (IBS) correctly. IBS is at about -3.8 eV which is below the Fermi level. IBS is occupied by electrons.

Fig. 6.2 is shown as DFT+QMC result on the total magnetic moment of Fe(3d)
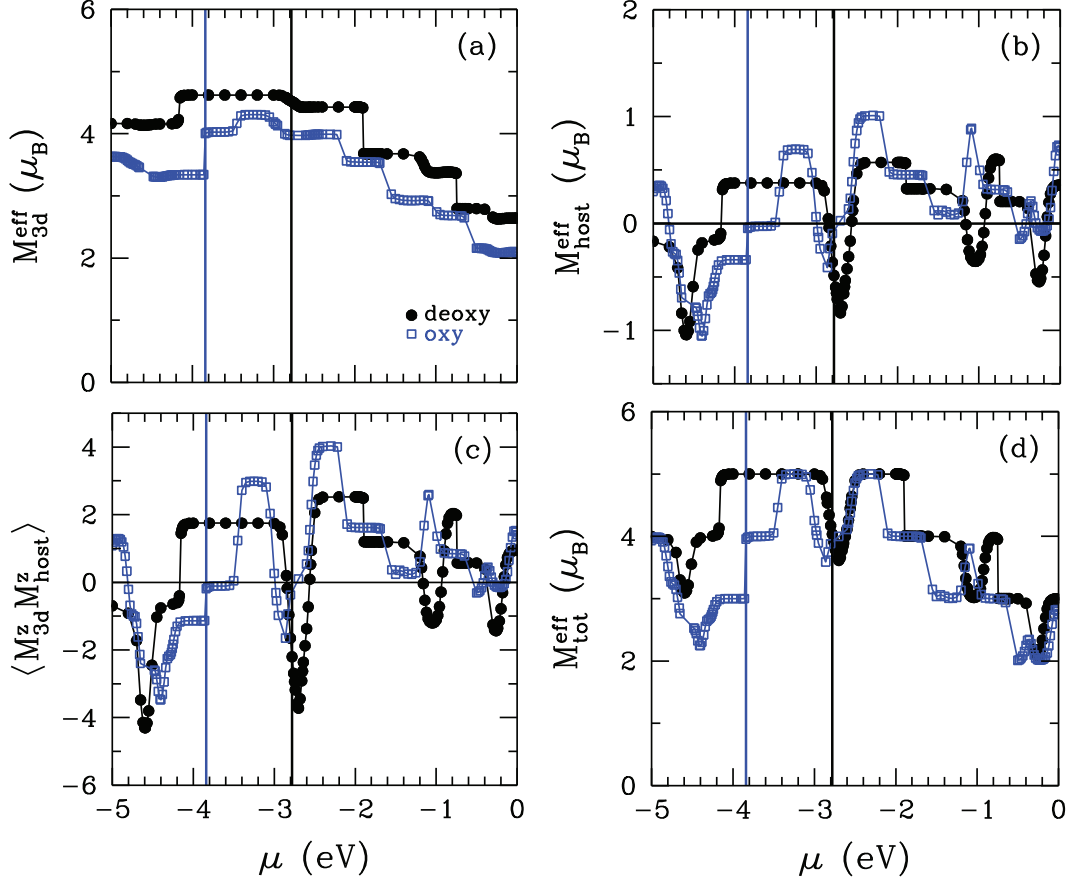
Figure 6.1. For deoxy-heme and oxy-heme molecules, DFT+MFA results on the effective magnetic moments of total of Fe($3d$) orbitals, total of host orbitals, between total of Fe($3d$) orbitals and total of host orbitals, and total of all orbitals. The vertical solid blue and black lines denote the HOMO energy levels of oxy-heme and deoxy-heme, respectively. These values are calculated by DFT+MFA method. These results are for $U = 4$ eV, $J = 0.9$ eV and $T = 300$ K.

orbitals, host orbitals, between Fe($3d$) orbitals and host orbitals, and all orbitals as a function of μ for deoxy-heme and oxy-heme molecules. The HOMO energy level of oxy-heme is $\mu = -3.8$ eV, which denotes the vertical blue line. The HOMO energy level of deoxy-heme is $\mu = -2.8$ eV, which denotes the vertical black line. For deoxy-heme molecule, the DFT+MFA results are similar to the DFT+QMC results in Figs. 6.1 and 6.2. However, for oxy-heme molecule in DFT+QMC results spin state of oxy-heme is closer to the low-spin state. While $M_{\text{tot}}^{\text{eff}}$ of oxy-heme becomes $2.1\mu_B$ at $\mu = -3.8$ eV in Fig. 6.2, $M_{\text{tot}}^{\text{eff}}$ of oxy-heme is $0.6\mu_B$ at $T = 150$ K. Spin-state of oxy-heme has low-spin state in DFT+QMC results.
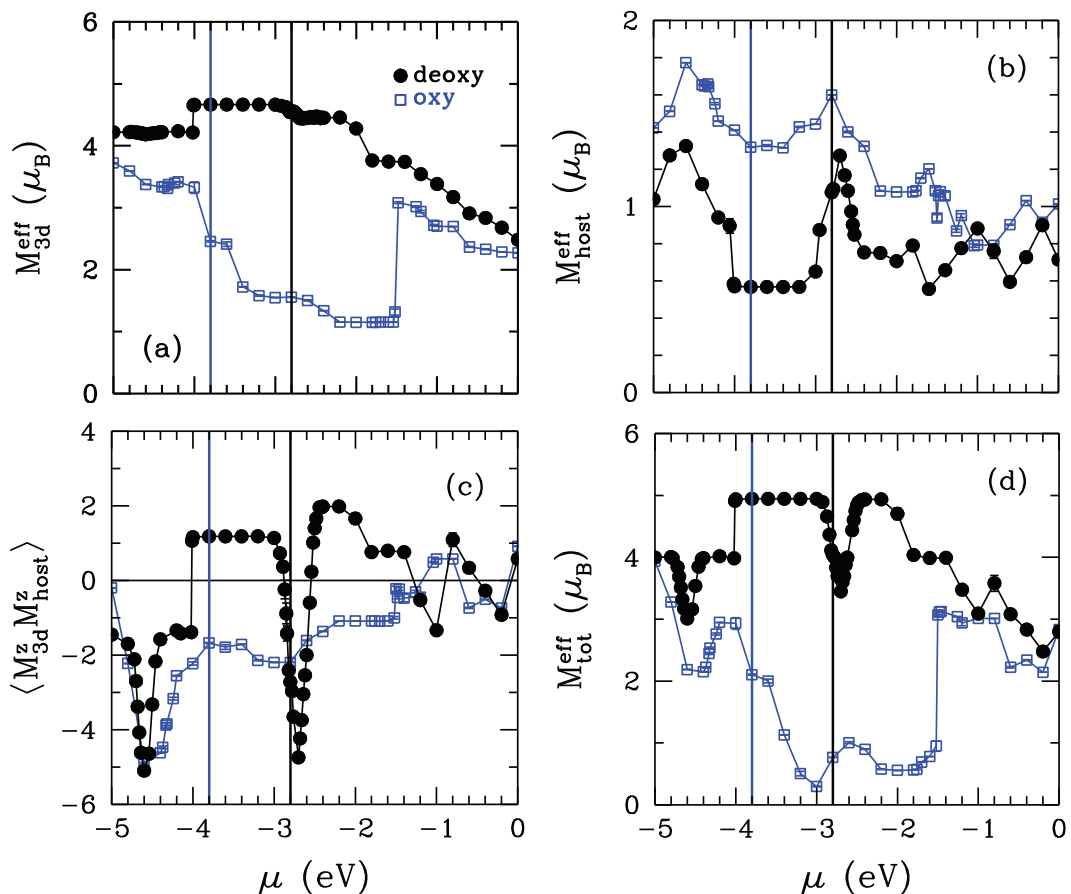
Figure 6.2. For deoxy-heme and oxy-heme molecules, DFT+QMC results on the effective magnetic moments of total of Fe($3d$) orbitals, total of host orbitals, between total of Fe($3d$) orbitals and total of host orbitals, and total of all orbitals. The vertical solid blue and black lines denote the HOMO energy levels of oxy-heme and deoxy-heme, respectively. These values are calculated by DFT+QMC method. These results are for $U = 4$ eV, $J = 0.9$ eV and $T = 300$ K.

CHAPTER 7

DFT+QMC RESULTS OF BIOINORGANIC MOLECULES

In this chapter, we show the DFT+QMC results of deoxy and oxy-heme molecules, cyanocobalamin molecule, N719 and Z907 dye molecules, and platinum, iron and nickel adatoms on a hexagonal graphene nanosheet. The DFT+QMC calculations are performed by using the Hirsch-Fye QMC algorithm (Hirsch and Fye (1986)). In addition, we will show the DFT results of these molecules and structures in Chapter 8.

7.1. For CNCbl molecule

In this subsection, we show the DFT+QMC results of the CNCbl molecule (Mayda et al. (2018)). We start showing the DFT+QMC data with Table 7.1 which shows the electron occupation number $\langle n_\nu \rangle$ of Co($3d_\nu$) orbitals for CNCbl molecule. We observe that the $3z^2 - r^2$ and $x^2 - y^2$ orbitals are single-occupied. On the other hand, xy, xz and yz orbitals are nearly double occupied. In this table, we compare the DFT+QMC results on the $\langle n_\nu \rangle$ values with the experimental results (Mebs et al. (2009)). As seen here, the DFT+QMC results are comparable with the experimental results. For CNCbl molecule, Co($3d$) orbitals have the 7.2 electrons.

Here, we show the DFT+QMC results on the total effective magnetic moments of Co($3d_\nu$) orbitals M_{3d} in μ_B, total effective magnetic moments of the host states M_h, magnetic correlation between the 3d states and host states $\langle M_{3d}^z M_h^z \rangle$, total effective magnetic moment of the CNCbl molecule M_T in Table 7.2. In addition, we also show the effective spin of the 3d orbitals S_{3d}^{eff}, effective spin of the host orbitals S_h^{eff} and the total effective spin of the CNCbl molecule S_T^{eff}. M_{3d} is 1.33 μ_B and M_h equals 1.39 μ_B. The correlations between the 3d states and host states are AF and $\langle M_{3d}^z M_h^z \rangle = -1.61$. The total effective magnetic moment is less than the M_{3d} because of the AF correlations between the 3d and host states. The effective spin of the 3d orbitals and host states are 0.33 and 0.36, respectively. As seen in Table 7.2 that the total spin of CNCbl molecule is 0.11. This means that the CNCbl molecule has the low-spin state.

Figure 7.1 (a) shows DFT+QMC results on the electron occupation number $\langle n_\nu \rangle$ of the Co($3d_\nu$) orbitals as a function of the chemical potential μ. Similarly, the effective

Table 7.1. Electron occupation number $\langle n_\nu \rangle$ of Co($3d_\nu$) orbitals for CNCbl molecule. Here, $U = 4$ eV, $J = 0.7$ eV and $T = 700$ K for DFT+QMC results. For CNCbl molecule, the experimental result is taken from Ref.(Mebs et al. (2009)).

ν	DFT $\langle n_\nu \rangle$	DFT+QMC $\langle n_\nu \rangle$	Experimental result $\langle n_\nu \rangle$
$3z^2 - r^2$	0.92	0.91	1.21
$x^2 - y^2$	0.81	0.81	0.88
xy	1.94	1.92	1.84
xz	1.81	1.77	1.87
yz	1.81	1.76	1.87

Table 7.2. For CNCbl molecule, DFT+QMC results on the total Co($3d$) magnetic moment M_{3d} in μ_B, total effective spin of Co(3d) electrons S_{3d}^{eff}, total host magnetic moment M_h in μ_B, total effective spin of host electrons S_h^{eff}, total Co(3d)-host effective magnetic correlation function $\langle M_{3d}^z M_h^z \rangle$, total effective magnetic moment M_T in μ_B and total effective spin of molecule S_T^{eff}. In addition, total effective spin S_{3d}^{eff} of Fe(3d) is calculated by $M_{3d} = 2\sqrt{S_{3d}^{\mathrm{eff}}(S_{3d}^{\mathrm{eff}} + 1)}$. Total host effective spin S_h^{eff} is calculated by $M_h = 2\sqrt{S_h^{\mathrm{eff}}(S_h^{\mathrm{eff}} + 1)}$ and total molecular effective spin S_T^{eff} is calculate by $M_T = 2\sqrt{S_T^{\mathrm{eff}}(S_T^{\mathrm{eff}} + 1)}$. Here, $U = 4$ eV, $J = 0.7$ eV and $T = 700$ K.

M_{3d}	M_h	$\langle M_{3d}^z M_h^z \rangle$	M_T	S_{3d}^{eff}	S_h^{eff}	S_T^{eff}
1.33	1.39	-1.61	0.71	0.33	0.36	0.11
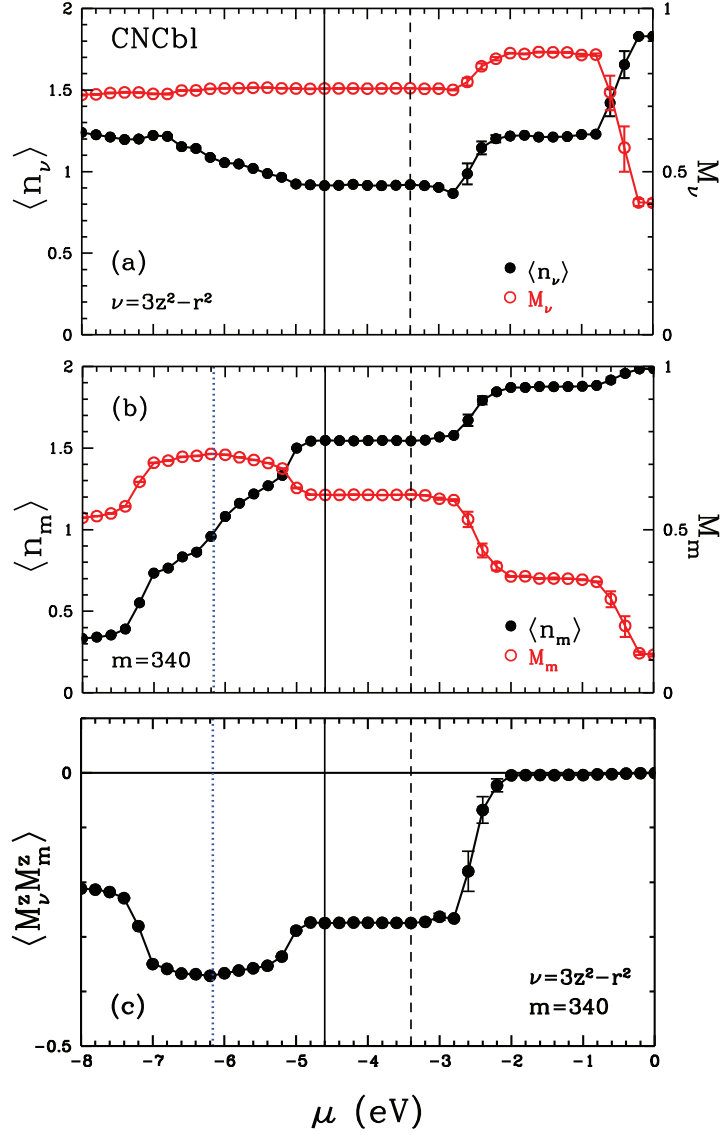
Figure 7.1. For CNCbl molecule, QMC results on the electron occupation number of Co($3d_{3z^2-r^2}$) orbital, the electron occupation number of $m = 340$'th host state, the effective magnetic moments of these orbitals and the magnetic correlation function between the Co($3z^2 - r^2$) and the 340'th host state. In (a), the black circle represents the electron occupation number $\langle n_\nu \rangle$ of the Co($3d_{\nu=3z^2-r^2}$) orbital versus the chemical potential μ, and the red circle represents the effective magnetic moment M_ν of the Co($3d_{\nu=3z^2-r^2}$) orbital versus μ. In (b), the black circle shows the electron occupation number $\langle n_m \rangle$ of the $m = 340$'th host orbital versus μ, and the red circle shows the effective magnetic moment M_m of the 340'th host state versus μ. (c) Magnetic correlation function $\langle M_\nu M_m \rangle$ between the $\nu = 3z^2 - r^2$ and the $m = 340$ orbitals. Here, the vertical solid line denotes the chemical potential of the CNCbl molecule calculated by the QMC. The total electron number does not change up to $\mu = -3.4$ eV shown by the dashed line. The blue dashed lines in (b) and (c) represent the energy level of $m = 340$'th host state. In addition, these results are for $U = 4$ eV, $J = 0.7$ eV and $T = 700$ K.

magnetic moment M_ν of the Co($3d_{3z^2-r^2}$) orbital is shown in Fig.7.1 (a) as a function of μ. Here, we choose the Co($3z^2 - r^2$) orbital because it has the highest hybridization with the host states. In these figures, the solid black and dashed lines denote the highest occupied molecular orbital (HOMO) level and lowest unoccupied molecular orbital (LUMO) level calculated by QMC, respectively.

$\langle n_\nu \rangle$ does not change up to $\mu \approx -2.8$ eV as shown in Fig. 7.1 (a). The occupation number of the $3z^2 - r^2$ orbital exhibits a jump at $\mu \approx -2.8$ eV. Near $\mu = -0.8$ eV, it becomes nearly doubly occupied. We see in Fig. 7.1 (a) that the magnetic moments at $3z^2 - r^2$ orbital remains constant up to $\mu \approx -2.8$ eV. At $\mu = -2.8$ eV, its moment increases suddenly and the magnetic moment of $3z^2 - r^2$ orbital has its maximum value at $\mu \approx -2$ eV. Above $\mu = -1$ eV, (M_ν) decreases rapidly due to double occupancy of the orbital.

We present QMC data on the host electron number $\langle n_m \rangle$ versus μ and the effective magnetic moment M_m versus μ for the $m = 340$'th host state in Fig. 7.1 (b). As seen in Fig. 7.1 that this host orbital consists mainly of the C($2p's$) and N($2p's$) orbitals neighboring the Co atom. Here, we select these host states because they have the highest hybridization values with the Co($3z^2 - r^2$) orbital. In Figure 7.1 (b), the solid and dashed black lines represent the HOMO and LUMO levels, respectively. In addition, the blue dashed line shows the energy level of the $m = 340$'th host state. The $\langle n_m \rangle$ increases up to the energy level of the host state and it equals 1 at $\mu \approx -6.2$ eV. Above this chemical potential, the electron number of the $m = 340$'th host state continues the increase. Between the HOMO and LUMO levels, $\langle n_m \rangle$ remains constant. We observe in Fig. 7.1 (b) that the $\langle n_m \rangle$ has the sudden jump at $\mu \approx -2.8$ eV and it goes double occupancy above the $\mu \approx -2$ eV.

Here we observe that, because of hybridization, this host orbital has partial occupancies and develop magnetic moments. M_m exhibit sudden decreases at $\mu \approx -2.8$ eV due to double occupancy of $\langle n_m \rangle$.

We have also studied the magnetic correlation function $\langle M_\nu^z M_m^z \rangle$ between the Co($3d_{3z^2-r^2}$) electrons and the host state $m = 340$ as a function of the chemical potential μ in Fig. 7.1 (c). Here, we observe that the $3z^2 - r^2$ orbital develops antiferromagnetic (AF) correlations with the $m = 340$'th host state. These AF correlations diminish rapidly at $\mu \approx -2$ eV.

In our calculations, we find that the vanishing of the AF correlations between the $3d$ and the host orbital is the clearest sign for determining the location of the IBS (Kandemir et al. (2016); Mayda et al. (2017)).

7.2. For dye molecules

We use combined density functional theory and quantum Monte Carlo (DFT+ QMC) results on the extended multi-orbital Anderson model for N719 and Z907 molecules. We first compute the DFT to study the electronic structure of N719 and Z907 molecules within the framework of the extended multi-orbital Haldane-Anderson model.

The electron occupation number n_ν and square of the magnetic moment $(M_\nu^z)^2$ of the Ru($4d_\nu$) orbitals are shown as a function of the chemical potential μ for deoxy-heme and oxy-heme. In addition, we show DFT+MFA results on the electron occupation number of the m'th host state n_m and square of the magnetic moment of the m'th host state $(M_m^z)^2$ as a function of μ. We also present data on the magnetic correlation function $M_\nu^z M_m^z$ between the m'th host eigenstate and the Fe($3d_\nu$) orbitals as a function of μ for deoxy-heme and oxy-heme molecules.

In this section also we discuss results on the Ru($4d_\nu$) orbitals and the host orbitals which has the highest hybridization for N719 and Z907 dye molecules.

7.2.1. DFT+QMC results for N719 dye

In this subsection, we present the QMC results on $\langle n_\nu \rangle$ as a function of chemical potential μ and $\langle (M_\nu^z)^2 \rangle$ as a function of μ. In addition, we show the magnetic moments $\langle M_m^z \rangle$ of host states and their magnetic correlations $\langle M_\nu^z M_m^z \rangle$ with Ru($4d$) orbitals. The QMC results for N719 dye molecule indicate that the IBS is located above the chemical potential, and so they are occupied. This causes that the N719 dye molecule has a low-spin state. AF correlations occur between the Ru($4d$) and host states.

Here, we choose the Ru($4d_{3z^2-r^2}$) orbital because this orbital has the highest hybridization with the host state $m = 150$th as shown in Fig. 8.21 (b). As shown in Fig. 7.2 (a), the black circle represents the electron occupation number $\langle n_\nu \rangle$ of the Ru($4d_{3z^2-r^2}$) orbital as a function of the chemical potential μ, and the red circle represents the effective magnetic moment M_ν of the Ru($4d_{3z^2-r^2}$) orbital versus μ. As shown in Fig. 7.2 (b), the black circle shows the electron occupation number $\langle n_m \rangle$ of the $m = 150$th host orbital versus μ, and the red circle shows the effective magnetic moment M_m of the $m = 150$th host state versus μ. Magnetic correlation function $\langle M_\nu M_m \rangle$ between the $\nu = 3z^2 - r^2$ orbital and the $m = 150$tht state is shown in Fig. 7.2 (c). In addition, these results are for $U = 4$ eV, $J = 0.9$ eV and $T = 700$ K. Here, In these figures, the solid black line denotes

the Fermi level of the N719 dye molecule calculated by the DFT+QMC. The value of the Fermi level is $\mu \approx 0.7$ eV. The blue dashed line represents the energy level of $m = 150$th host state. The energy value of this host state is $\varepsilon_m \approx -2.15$ eV

We observe in Fig. 7.2 (a) that $\langle n_{3z^2-r^2} \rangle$ gradually change in the interval -1 eV $\lesssim \mu \lesssim 1$ eV. The occupation number of the $3z^2 - r^2$ orbital exhibits a jump at $\mu \approx 3.2$ eV. Near $\mu = 3$ eV, it becomes nearly doubly occupied. As shown in Fig. 7.2 (a) the magnetic moment of the $3z^2 - r^2$ orbital remains constant in the interval -5 eV $\lesssim \mu \lesssim 3$ eV. The electron occupation number of $3z^2 - r^2$ orbital decreases gradually from $\mu = -2$ eV to $\mu = 3$ eV and increases suddenly at $\mu \approx 3.2$ eV.

We present the DFT+QMC results on the host electron number $\langle n_m \rangle$ versus μ and the effective magnetic moment M_m versus μ for the $m = 150$th host state in Fig. 7.2 (b). As seen in Fig. 8.22 (b) that this host orbital consists mainly of the N(2s) and N(2p) orbitals neighboring the Ru atom. Here, we choose this host state because it has the highest hybridization value with the Ru($4d_{3z^2-r^2}$) orbital. In Figure 7.2 (b), the solid black line represents the Fermi level of the N719 dye molecule. In addition, the blue dashed line shows the energy level of the $m = 150$th host state. The $\langle n_m \rangle$ increases up to energy level of the host state and it equals 1 at $\mu \approx -2.15$ eV. Above this chemical potential, the electron number of the $m = 150$th host state continues the increase. Between $\mu \approx 0.7$ eV and $\mu \approx 3$ eV , $\langle n_m \rangle$ remains constant. We see in Fig. 7.2 (b) that the $\langle n_m \rangle$ has the sudden jump at $\mu \approx 3.2$ eV and it goes double occupancy above the $\mu \approx 5$ eV. Here we observe that, because of hybridization, this host orbital has partial occupancies and develop magnetic moments. M_m exhibit sudden decreases at $\mu \approx 3.2$ eV due to double occupancy of $\langle n_m \rangle$.

We have also studied the magnetic correlation function $\langle M_\nu^z M_m^z \rangle$ between the Ru($4d_{3z^2-r^2}$) electrons and the host state $m = 150$th as a function of the chemical potential μ in Fig. 7.2 (c). Here, we observe that the $3z^2 - r^2$ orbital develops antiferromagnetic (AF) correlations with the $m = 150$th host state. These AF correlations diminish rapidly at $\mu \approx 3.2$ eV.

7.2.2. DFT+QMC results for Z907 dye

In this subsection, we present the DFT+QMC results on $\langle n_\nu \rangle$ as a function of chemical potential μ and $\langle (M_\nu^z)^2 \rangle$ as a function of μ. In addition, we show the magnetic moments $\langle M_m^z \rangle$ of host states and their magnetic correlations $\langle M_\nu^z M_m^z \rangle$ with Ru($4d$) orbitals. The DFT+QMC results for the Z907 dye molecule indicate that the IBS is located
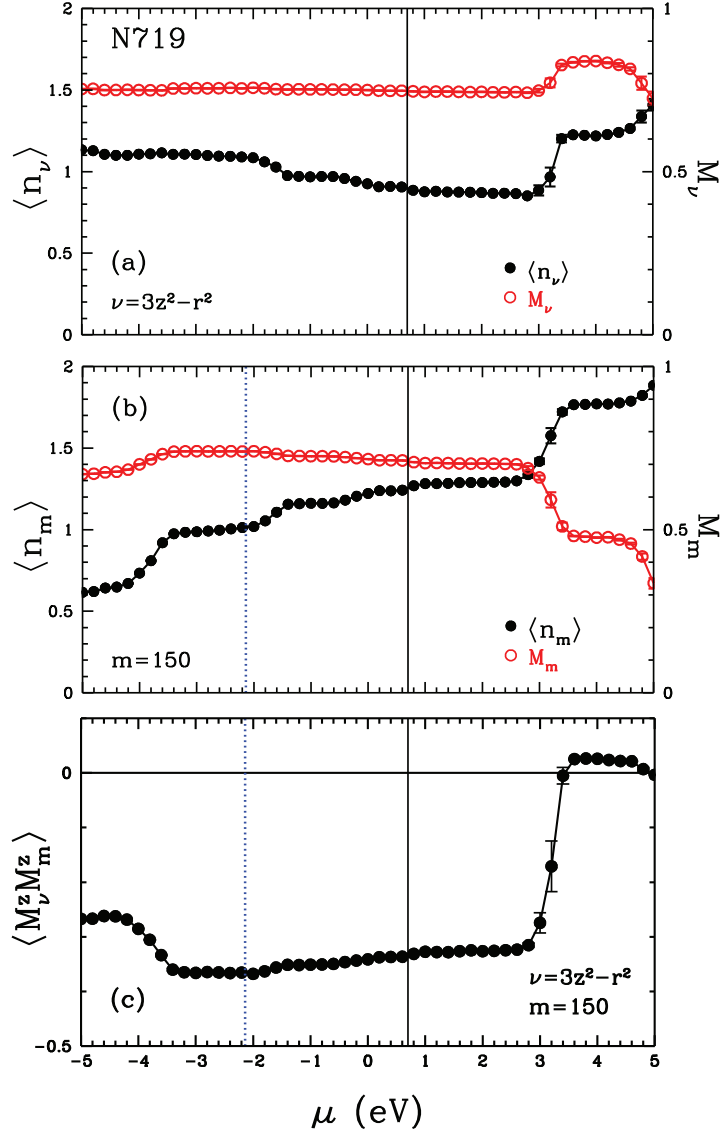
Figure 7.2. For N719 dye molecule, DFT+QMC results on the electron occupation number of Ru($4d_{3z^2-r^2}$) orbital, the electron occupation number of $m = 150$'th host state, the effective magnetic moments of these orbitals and the magnetic correlation function between the Ru($3z^2 - r^2$) and the 150'th host state. In (a), the black circle represents the electron occupation number $\langle n_\nu \rangle$ of the Ru($4d_{\nu=3z^2-r^2}$) orbital versus the chemical potential μ, and the red circle represents the effective magnetic moment M_ν of the Ru($4d_{\nu=3z^2-r^2}$) orbital versus μ. In (b), the black circle shows the electron occupation number $\langle n_m \rangle$ of the $m = 150$'th host orbital versus μ, and the red circle shows the effective magnetic moment M_m of the 150'th host state versus μ. (c) Magnetic correlation function $\langle M_\nu M_m \rangle$ between the $\nu = 3z^2 - r^2$ and the $m = 150$ orbitals. Here, the vertical solid line denotes the chemical potential of the N719 dye molecule calculated by the DFT+QMC. The blue dashed lines in (b) and (c) represent the energy level of $m = 150$'th host state. In addition, these results are for $U = 4$ eV, $J = 0.9$ eV and $T = 700$ K.

above the chemical potential, and so they are occupied. This causes that the Z907 dye molecule has low-spin state. AF correlations occur between the Ru(4d) and host states.

Figure 7.3 show the electronic and magnetic properties of the Ru($3z^2 - r^2$) and $m = 205$'th host state for Z907 dye molecule.

We observe in Fig. 7.3 (a) that $\langle n_\nu \rangle$ does not change up to $\mu \approx -1.5$ eV. The occupation number of the $3z^2 - r^2$ orbital exhibits a jump at $\mu \approx -1.4$ eV. Near $\mu = -1$ eV, it becomes nearly doubly occupied. Similarly, we see in Fig. 7.3 (a) that the magnetic moments at $3z^2 - r^2$ orbital remains constant up to $\mu \approx -1.5$ eV. At $\mu = -1.4$ eV, its moment increases suddenly and the magnetic moment of $3z^2 - r^2$ orbital. Above $\mu = -1$ eV, (M_ν) decreases rapidly due to double occupancy of the orbital.

We present QMC data on the host electron number $\langle n_m \rangle$ versus μ and the effective magnetic moment M_m versus μ for the $m = 205$'th host state in Fig. 7.3 (b). As seen in Fig. 8.25 that this host orbital consists mainly of the C(2p) and N(2p) orbitals neighboring the Ru atom. Here, we choose these host states because they have the highest hybridization values with the Ru($3z^2 - r^2$) orbital. In Figure 7.3 (b), the solid line represents the chemical potential calculated by DFT+QMC. Here, we see that $\langle n_m \rangle$ and M_m do not change up to $\mu \approx -1.5$ eV. At $\mu \approx -1.4$ eV, the electron occupation of $m = 205$'th host state has a sudden increase, on the other hand, M_m exhibit sudden decreases.

Figure 7.3 (c) shows the $\langle M_\nu^z M_m^z \rangle$ between the Ru($4d_{3z^2-r^2}$) electrons and the host state $m = 205$ as a function of the chemical potential μ. Here, we observe that the $3z^2 - r^2$ orbital develops antiferromagnetic (AF) correlations with the $m = 205$'th host state. These AF correlations diminish rapidly at $\mu \approx -1$ eV at which IBS is located.

Z907 and N719 dye molecules are similar structures with the CNCbl molecule. All of these molecules have the transition metal at their active site. Our DFT+QMC results show that CNCbl molecule and Ru-based dye molecules have IBS. We think that the IBS found in these calculations might be important for the functioning of these molecules.

7.3. For graphene catalysts

For Fe/3A-HGNS, Ni/3A-HGNS and Pt/3A-HGNS molecules, the height above graphene is shown in the first column and the site of transition metal atom is shown in the second column of Table 7.3. The Fe and Ni atoms are located at the hollow site and 1.56 Å and 1.66 Å above the current layer, respectively. The Pt atom is located at the bridge site and 2.04 Å above the current layer. In the third and the fourth columns of Table 7.3, QMC results on the total magnetic moment of $3d$ orbitals for Fe and Ni atoms, $5d$ orbitals for
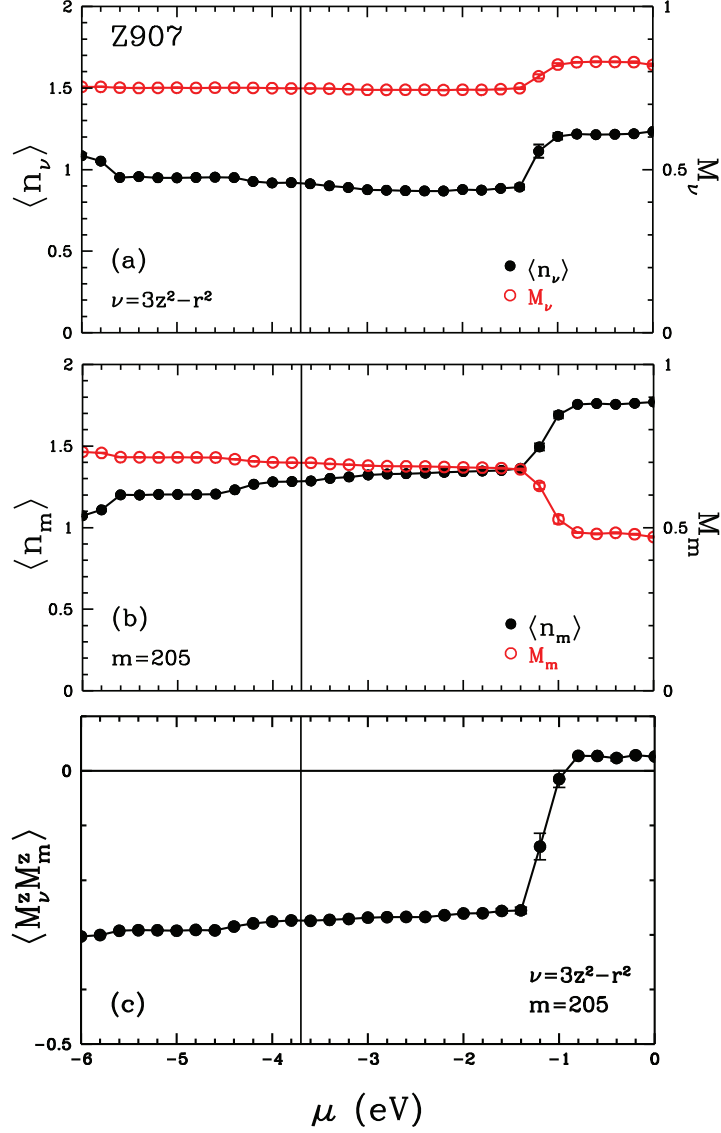
Figure 7.3. For Z907 molecule, QMC results on the electron occupation number of Ru($4d_{3z^2-r^2}$) orbital, the electron occupation number of $m = 205$'th host state, the effective magnetic moments of these orbitals and the magnetic correlation function between the Ru($3z^2 - r^2$) and the 205'th host state. We choose the Ru($4d_{3z^2-r^2}$) orbital and host state $m = 205$ because these orbitals have the highest hybridization as seen in Fig. 8.24. In (a), the black circle represents the electron occupation number $\langle n_\nu \rangle$ of the Ru($4d_{\nu=3z^2-r^2}$) orbital versus the chemical potential μ, and the red circle represents the effective magnetic moment M_ν of the Ru($4d_{\nu=3z^2-r^2}$) orbital versus μ. In (b), the black circle shows the electron occupation number $\langle n_m \rangle$ of the $m = 205$'th host orbital versus μ, and the red circle shows the effective magnetic moment M_m of the 205'th host state versus μ. (c) Magnetic correlation function $\langle M_\nu M_m \rangle$ between the $\nu = 3z^2 - r^2$ and the $m = 205$ orbitals. Here, the vertical solid line denotes the chemical potential of the Z907 molecule calculated by the DFT+QMC. In addition, these results are for $U = 4$ eV, $J = 0.9$ eV and $T = 700$ K.

Table 7.3. For Fe/3A-HGNS, Ni/3A-HGNS and Pt/3A-HGNS molecules, the height
above the graphene layer is shown in the first column and the site of tran-
sition metal atom is shown in the second column. The Fe and Ni atoms are
located at the hollow site and 1.56 Å and 1.66 Å above the current layer,
respectively. The Pt atom is located at the bridge site and 2.04 Å above the
current layer. In the third and the fourth column, DFT+QMC results on
the total magnetic moment of $3d$ orbitals for Fe and Ni atoms, $5d$ orbitals
for Pt atom and the total magnetic moments of the systems are written,
respectively. Here, for DFT+QMC calculations we use $U = 4$ eV, $J = 0.9$
eV and $T = 700$ K.

Molecules	Height (Å)	Site	M_d (μ_B)	M_T (μ_B)
Fe/3A-HGNS	1.56	hollow	1.08	0.16
Ni/3A-HGNS	1.66	hollow	0.82	0.19
Pt/3A-HGNS	2.04	bridge	0.85	0.36

Pt atom and the total magnetic moments of the systems are written, respectively. Here,
$U = 4$ eV, $J = 0.9$ eV and $T = 700$ K. In addition, Hu et. al. (Hu et al. (2010))
calculated the magnetic moment per adatom of graphene system. They found that the
magnetic moment of Fe adatom is 2 μ_B for the hollow site, the magnetic moment of Ni
adatom is 0 μ_B for the hollow site and the magnetic moment of Pt adatom is 0 μ_B for the
bridge site (Hu et al. (2010)).

7.3.1. DFT+QMC results for Pt/3A-HGNS

In this subsection, we present the QMC results on $\langle n_\nu \rangle$ as a function of chemical
potential μ and $\langle (M_\nu^z)^2 \rangle$ as a function of μ. In addition, we show the magnetic moments
$\langle M_m^z \rangle$ of host states and their magnetic correlations $\langle M_\nu^z M_m^z \rangle$ with Pt($5d$) orbitals. The
DFT+QMC results for Pt/3A-HGNS (or Pt/graphene) indicate that the IBS is located
above the Fermi level, and so they are occupied. This causes that the Pt/3A-HGNS has a
low-spin state. AF correlations occur between the Pt($5d$) and host states.

Here, we choose the Pt($5d_{yz}$) orbital because this orbital has the highest hybridiza-
tion with the host state $m = 141$st as shown in Fig. 8.27 (b). As shown in Fig. 7.4 (a),
the black circle represents the electron occupation number $\langle n_\nu \rangle$ of the Pt($5d_{\nu=yz}$) orbital
as a function of the chemical potential μ, and the red circle represents the effective mag-
netic moment M_ν of the Pt($5d_{\nu=yz}$) orbital versus μ. As shown in Fig. 7.4 (b), the black

circle shows the electron occupation number $\langle n_m \rangle$ of the $m = 141$st host orbital versus μ, and the red circle shows the effective magnetic moment M_m of the $m = 141$st host state versus μ. Magnetic correlation function $\langle M_\nu M_m \rangle$ between the $\nu = yz$ orbital and the $m = 141$st state is shown in Fig. 7.4 (c). In addition, these results are for $U = 4$ eV, $J = 0.9$ eV and $T = 700$ K. Here, In these figures, the solid black line denotes the Fermi level of the Pt/graphene calculated by the DFT+QMC. The value of the Fermi level is $\mu = -4.6$ eV. The blue dashed line represents the energy level of $m = 141$st host state. The energy value of this host state is $\varepsilon_m \approx -2.0$ eV

We observe in Fig. 7.4 (a) that $\langle n_{yz} \rangle$ does not change in the interval -4.6 eV $\lesssim \mu \lesssim -2$ eV. The occupation number of the yz orbital exhibits a jump at $\mu \approx -1.5$ eV. Near $\mu = 3$ eV, it becomes nearly doubly occupied. As shown in Fig. 7.4 (a) the magnetic moment of the yz orbital remains constant in the interval -4.6 eV $\lesssim \mu \lesssim -2$ eV. While the electron occupation number of yz orbital increases gradually from $\mu = -1.5$ eV to $\mu = 3$ eV, its the magnetic moment decreases. Above $\mu = 0$ eV, (M_ν) decreases gradually due to double occupancy of the $\nu = yz$ orbital.

We present the DFT+QMC results on the host electron number $\langle n_m \rangle$ versus μ and the effective magnetic moment M_m versus μ for the $m = 141$st host state in Fig. 7.4 (b). As seen in Fig. 8.28 that this host orbital consists mainly of the C(2p) orbitals neighbouring the Pt atom. Here, we choose this host state because it has the highest hybridization value with the Pt($5d_{yz}$) orbital. In Figure 7.4 (b), the solid black line represents the Fermi level of the Pt/graphene. In addition, the blue dashed line shows the energy level of the $m = 141$st host state. The $\langle n_m \rangle$ increases up to energy level of the host state and it equals 0.3 at $\mu \approx -4.6$ eV. Above this chemical potential, the electron number of the $m = 141$st host state continues the increase. Between $\mu \approx -4.6$ eV and $\mu \approx -2$ eV , $\langle n_m \rangle$ remains constant. We see in Fig. 7.4 (b) that the $\langle n_m \rangle$ has the sudden jump at $\mu \approx -1.5$ eV and it goes double occupancy above the $\mu \approx -0.5$ eV. Here we observe that, because of hybridization, this host orbital has partial occupancies and develop magnetic moments. M_m exhibit sudden decreases at $\mu \approx -1.5$ eV due to double occupancy of $\langle n_m \rangle$.

We have also studied the magnetic correlation function $\langle M_\nu^z M_m^z \rangle$ between the Pt($5d_{yz}$) electrons and the host state $m = 141$st as a function of the chemical potential μ in Fig. 7.4 (c). Here, we observe that the yz orbital develops antiferromagnetic (AF) correlations with the $m = 141$st host state. These AF correlations diminish rapidly at $\mu \approx -1.5$ eV.

7.3.2. DFT+QMC results for Fe/3A-HGNS

In this subsection, we present the DFT+QMC results on $\langle n_\nu \rangle$ as a function of chemical potential μ and $\langle (M_\nu^z)^2 \rangle$ as a function of μ. In addition, we show the magnetic moments $\langle M_m^z \rangle$ of host states and their magnetic correlations $\langle M_\nu^z M_m^z \rangle$ with Fe($3d$) orbitals. The DFT+QMC results for Fe/3A-HGNS (or Fe/graphene) indicate that the IBS is located above the chemical potential, and so they are occupied. This causes that the Fe/3A-HGNS has low-spin state. AF correlations occur between the Fe($3d$) and host states.

Here, we choose the Fe($3d_{x^2-y^2}$) orbital because this orbital has the highest hybridization with the host state $m = 140$th as shown in Fig. 8.30 (b). As shown in Fig. 7.5 (a), the black circle represents the electron occupation number $\langle n_\nu \rangle$ of the Fe($3d_{\nu=x^2-y^2}$) orbital as a function of the chemical potential μ, and the red circle represents the effective magnetic moment M_ν of the Fe($3d_{\nu=x^2-y^2}$) orbital versus μ. As shown in Fig. 7.5 (b), the black circle shows the electron occupation number $\langle n_m \rangle$ of the $m = 140$th host orbital versus μ, and the red circle shows the effective magnetic moment M_m of the $m = 140$th host state versus μ. Magnetic correlation function $\langle M_\nu M_m \rangle$ between the $\nu = x^2 - y^2$ orbital and the $m = 140$th state is shown in Fig. 7.5 (c). In addition, these results are for $U = 4$ eV, $J = 0.9$ eV and $T = 700$ K. In these figures, the solid black line denotes the Fermi level of the Fe/graphene calculated by the DFT+QMC. The value of the Fermi level is $\mu = -3.4$ eV. The blue dashed line represents the energy level of $m = 140$th host state. The energy value of this host state is $\varepsilon_m \approx -1.9$ eV

We observe in Fig. 7.5 (a) that $\langle n_{x^2-y^2} \rangle$ does not change in the interval -3.4 eV $\lesssim \mu \lesssim -1.9$ eV. The occupation number of the $x^2 - y^2$ orbital exhibits a jump at $\mu \approx -1.9$ eV. Near $\mu = 3$ eV, it becomes nearly doubly occupied. As shown in Fig. 7.5 (a) the magnetic moment of the yz orbital remains constant in the interval -3.4 eV $\lesssim \mu \lesssim -1.9$ eV. While the electron occupation number of $x^2 - y^2$ orbital increases gradually from $\mu = -1.9$ eV to $\mu = 3$ eV, its the magnetic moment decreases. Above $\mu = 0$ eV, (M_ν) decreases gradually due to double occupancy of the $\nu = x^2 - y^2$ orbital.

We present the DFT+QMC results on the host electron number $\langle n_m \rangle$ versus μ and the effective magnetic moment M_m versus μ for the $m = 140$th host state in Fig. 7.5 (b). As seen in Fig. 8.31 that this host orbital consists mainly of the C($2p$) orbitals neighbouring the Fe atom. Here, we choose this host state because it has the highest hybridization value with the Fe($3d_{x^2-y^2}$) orbital. In Figure 7.5 (b), the solid black line represents the Fermi level of the Fe/graphene. In addition, the blue dashed line shows the

energy level of the $m = 140$th host state. The $\langle n_m \rangle$ increases up to energy level of the host state and it equals 0.4 at $\mu \approx -3.4$ eV. Above this chemical potential, the electron number of the $m = 140$th host state continues the increase. Between $\mu \approx -3.4$ eV and $\mu \approx -1.9$ eV , $\langle n_m \rangle$ remains constant. We see in Fig. 7.5 (b) that the $\langle n_m \rangle$ has the sudden jump at $\mu \approx -1.5$ eV and it goes double occupancy above the $\mu \approx 0$ eV. Here we observe that, because of hybridization, this host orbital has partial occupancies and develop magnetic moments. M_m exhibit sudden decreases at $\mu \approx -1.5$ eV due to double occupancy of $\langle n_m \rangle$.

We have also studied the magnetic correlation function $\langle M_\nu^z M_m^z \rangle$ between the Fe($3d_{x^2-y^2}$) electrons and the host state $m = 140$th as a function of the chemical potential μ in Fig. 7.5 (c). Here, we observe that the $x^2 - y^2$ orbital develops antiferromagnetic (AF) correlations with the $m = 140$th host state. These AF correlations diminish rapidly at $\mu \approx -1.5$ eV.

7.3.3. DFT+QMC results for Ni/3A-HGNS

In this subsection, we present the DFT+QMC results on $\langle n_\nu \rangle$ as a function of chemical potential μ and $\langle (M_\nu^z)^2 \rangle$ as a function of μ. In addition, we show the magnetic moments $\langle M_m^z \rangle$ of host states and their magnetic correlations $\langle M_\nu^z M_m^z \rangle$ with Ni($3d$) orbitals. The DFT+QMC results for Ni/3A-HGNS (or Ni/graphene) indicate that the IBS are located above the chemical potential, and so they are occupied. This causes that the Ni/3A-HGNS has low-spin state. AF correlations occur between the Ni($3d$) and host states.

Here, we choose the Ni($3d_{x^2-y^2}$) orbital because this orbital has the highest hybridization with the host state $m = 141$st as shown in Fig. 8.33 (b). As shown in Fig. 7.6 (a), the black circle represents the electron occupation number $\langle n_\nu \rangle$ of the Ni($3d_{\nu=x^2-y^2}$) orbital as a function of the chemical potential μ, and the red circle represents the effective magnetic moment M_ν of the Ni($3d_{\nu=x^2-y^2}$) orbital versus μ. As shown in Fig. 7.6 (b), the black circle shows the electron occupation number $\langle n_m \rangle$ of the $m = 141$st host orbital versus μ, and the red circle shows the effective magnetic moment M_m of the $m = 141$st host state versus μ. Magnetic correlation function $\langle M_\nu M_m \rangle$ between the $\nu = x^2 - y^2$ orbital and the $m = 141$st state is shown in Fig. 7.6 (c). In addition, these results are for $U = 4$ eV, $J = 0.9$ eV and $T = 700$ K. Here, In these figure, the solid black line denotes the Fermi level of the Fe/graphene calculated by the DFT+QMC. The value of the Fermi level is $\mu = -4.0$ eV. The blue dashed line represents the energy level of $m = 141$st host

state. The energy value of this host state is $\varepsilon_m \approx -1.8$ eV

We observe in Fig. 7.6 (a) that $\langle n_{x^2-y^2} \rangle$ does not change in the interval -4.0 eV $\lesssim$ $\mu \lesssim -1.8$ eV. The occupation number of the $x^2 - y^2$ orbital exhibits a jump at $\mu \approx -1.8$ eV. Near $\mu = 3$ eV, it becomes nearly doubly occupied. As shown in Fig. 7.6 (a) the magnetic moment of the yz orbital remains constant in the interval -4.0 eV $\lesssim \mu \lesssim$ -1.8 eV. While the electron occupation number of $x^2 - y^2$ orbital increases gradually from $\mu = -1.8$ eV to $\mu = 3$ eV, its the magnetic moment decreases. Above $\mu = 0$ eV, (M_ν) decreases gradually due to double occupancy of the $\nu = x^2 - y^2$ orbital.

We present the DFT+QMC results on the host electron number $\langle n_m \rangle$ versus μ and the effective magnetic moment M_m versus μ for the $m = 141$st host state in Fig. 7.6 (b). As seen in Fig. 8.34 that this host orbital consists mainly of the C(2p) orbitals neighbouring the Ni atom. Here, we choose this host state because it has the highest hybridization value with the Ni($3d_{x^2-y^2}$) orbital. In Figure 7.6 (b), the solid black line represents the Fermi level of the Ni/graphene. In addition, the blue dashed line shows the energy level of the $m = 141$st host state. The $\langle n_m \rangle$ increases up to energy level of the host state and it equals 0.2 at $\mu \approx -4.0$ eV. Above this chemical potential, the electron number of the $m = 141$st host state continues the increase. Between $\mu \approx -4.0$ eV and $\mu \approx -1.8$ eV , $\langle n_m \rangle$ remains constant. We see in Fig. 7.6 (b) that the $\langle n_m \rangle$ has the sudden jump at $\mu \approx -1.5$ eV and it goes double occupancy above the $\mu \approx 0$ eV. Here we observe that, because of hybridization, this host orbital has partial occupancies and develop magnetic moments. M_m exhibit sudden decreases at $\mu \approx -1.5$ eV due to double occupancy of $\langle n_m \rangle$.

We have also studied the magnetic correlation function $\langle M_\nu^z M_m^z \rangle$ between the Ni($3d_{x^2-y^2}$) electrons and the host state $m = 141$st as a function of the chemical potential μ in Fig. 7.6 (c). Here, we observe that the $x^2 - y^2$ orbital develops antiferromagnetic (AF) correlations with the $m = 141$st host state. These AF correlations diminish rapidly at $\mu \approx -1.5$ eV.
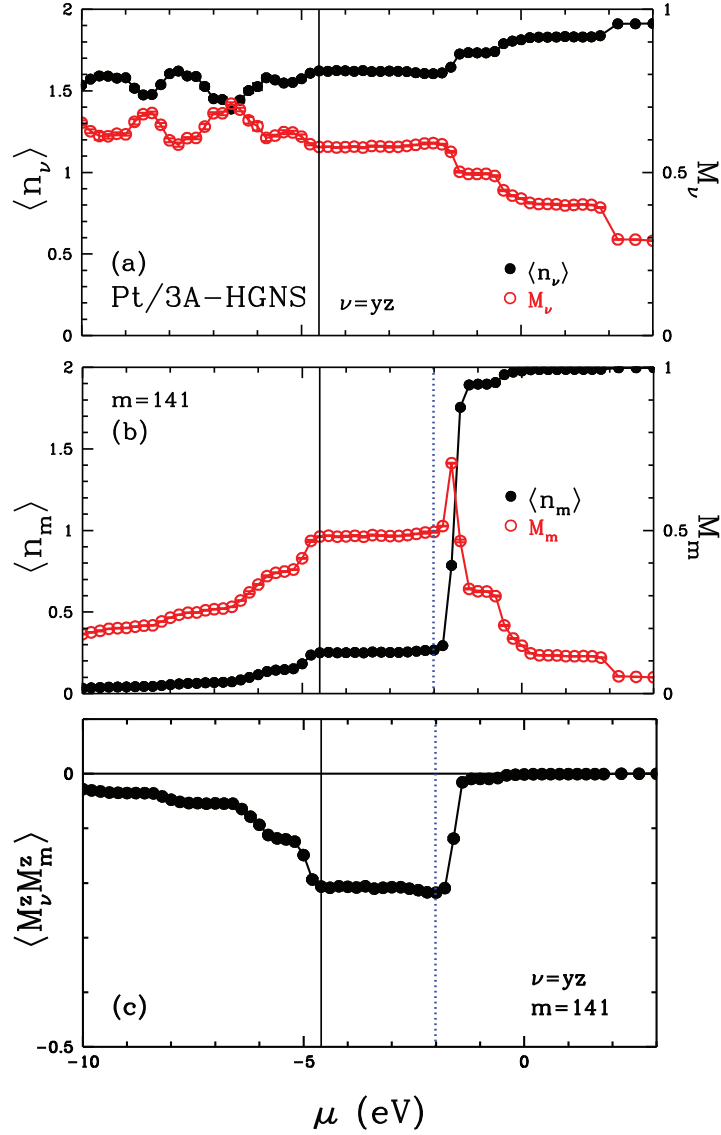
Figure 7.4. For Pt on graphene, DFT+QMC results on the electron occupation number of Pt($5d_{yz}$) orbital, the electron occupation number of $m = 141$'st host state, the effective magnetic moments of these orbitals and the magnetic correlation function between the Pt($5d_{yz}$) and the $m = 141$st host state. In (a), the black circle represents the electron occupation number $\langle n_\nu \rangle$ of the Pt($5d_{\nu=yz}$) orbital versus the chemical potential μ, and the red circle represents the effective magnetic moment M_ν of the Pt($5d_{\nu=yz}$) orbital versus μ. In (b), the black circle shows the electron occupation number $\langle n_m \rangle$ of the $m = 141$st host orbital versus μ, and the red circle shows the effective magnetic moment M_m of the $m = 141$st host state versus μ. (c) Magnetic correlation function $\langle M_\nu M_m \rangle$ between the $\nu = yz$ and the $m = 141$st state. Here, the vertical solid line denotes the chemical potential of the Pt/graphene calculated by the DFT+QMC. The blue dashed lines in (b) and (c) represent the energy level of $m = 141$st host state. In addition, these results are for $U = 4$ eV, $J = 0.9$ eV and $T = 700$ K.
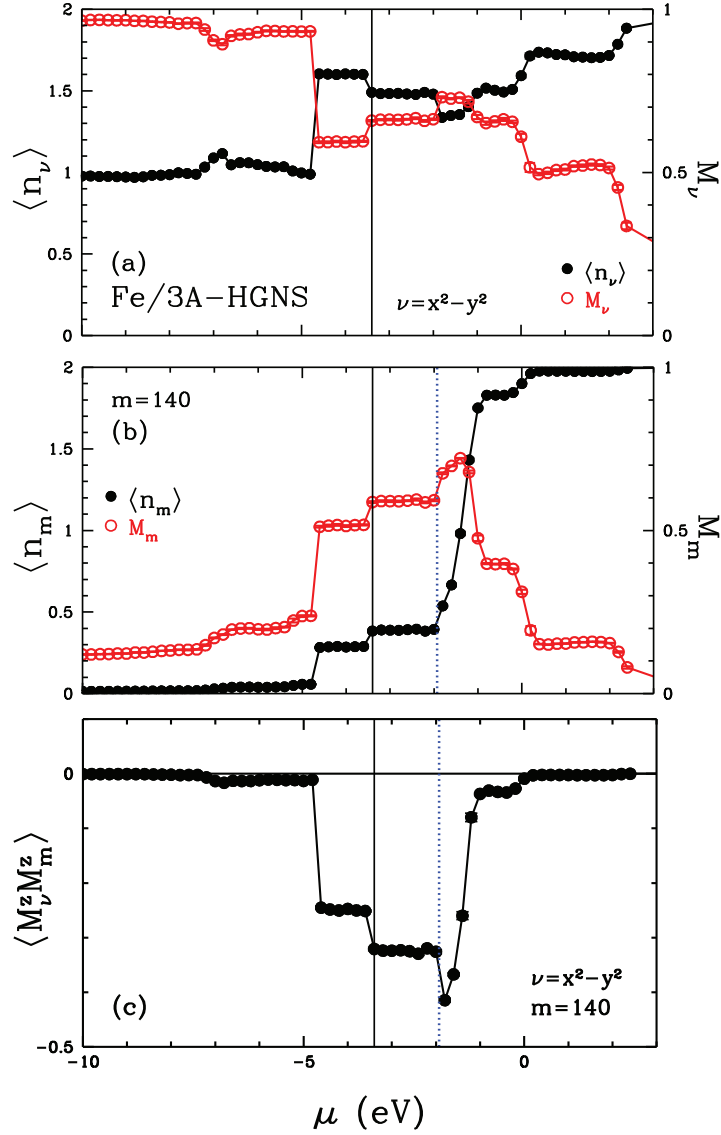
Figure 7.5. For Fe on graphene, DFT+QMC results on the electron occupation number of Fe($3d_{x^2-y^2}$) orbital, the electron occupation number of $m = 140$th host state, the effective magnetic moments of these orbitals and the magnetic correlation function between the Fe($x^2 - y^2$) and the 140th host state. In (a), the black circle represents the electron occupation number $\langle n_\nu \rangle$ of the Fe($3d_{\nu=x^2-y^2}$) orbital versus the chemical potential μ, and the red circle represents the effective magnetic moment M_ν of the Fe($3d_{\nu=x^2-y^2}$) orbital versus μ. In (b), the black circle shows the electron occupation number $\langle n_m \rangle$ of the $m = 140$th host orbital versus μ, and the red circle shows the effective magnetic moment M_m of the 140th host state versus μ. (c) Magnetic correlation function $\langle M_\nu M_m \rangle$ between the $\nu = x^2 - y^2$ and the $m = 140$th state. Here, the vertical solid line denotes the chemical potential of the Fe/graphene calculated by the DFT+QMC. The blue dashed lines in (b) and (c) represent the energy level of $m = 140$th host state. In addition, these results are for $U = 4$ eV, $J = 0.9$ eV and $T = 700$ K.
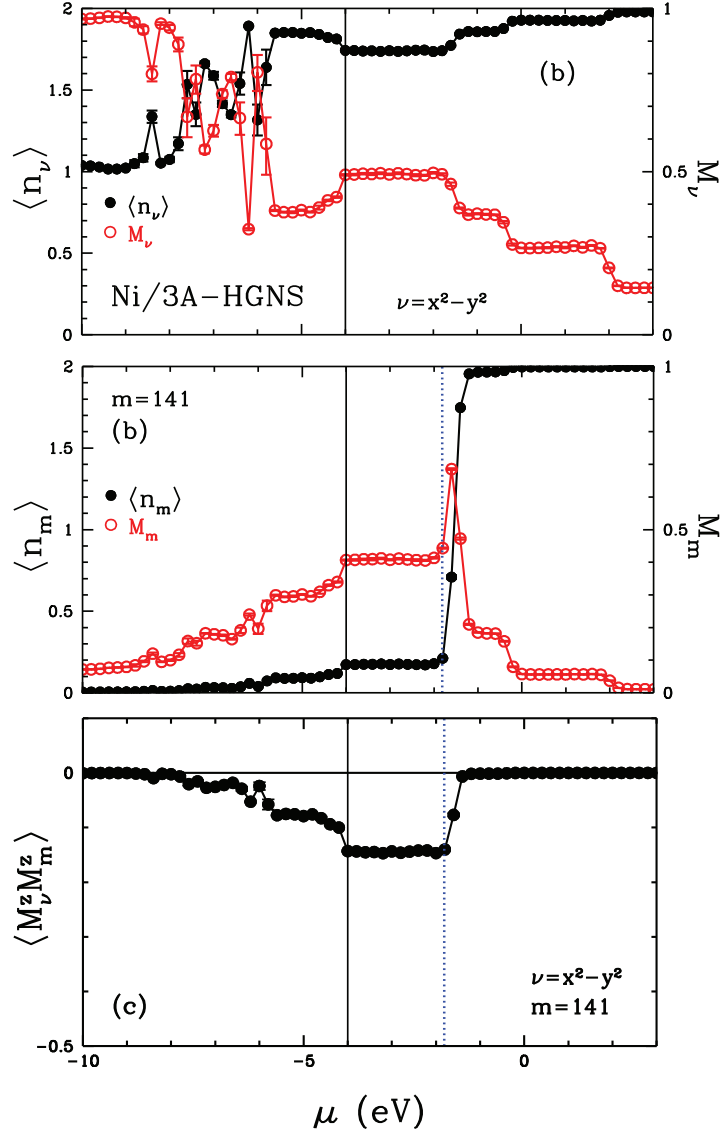
Figure 7.6. For Ni on graphene, DFT+QMC results on the electron occupation number of Ni($3d_{x^2-y^2}$) orbital, the electron occupation number of $m = 141$st host state, the effective magnetic moments of these orbitals and the magnetic correlation function between the Ni($3d_{x^2-y^2}$) and the $m = 141$st host state. In (a), the black circle represents the electron occupation number $\langle n_\nu \rangle$ of the Ni($3d_{\nu=x^2-y^2}$) orbital versus the chemical potential μ, and the red circle represents the effective magnetic moment M_ν of the Ni($3d_{\nu=x^2-y^2}$) orbital versus μ. In (b), the black circle shows the electron occupation number $\langle n_m \rangle$ of the $m = 141$st host orbital versus μ, and the red circle shows the effective magnetic moment M_m of the $m = 141$st host state versus μ. (c) Magnetic correlation function $\langle M_\nu M_m \rangle$ between the $\nu = x^2 - y^2$ orbital and the $m = 141$st state. Here, the vertical solid line denotes the chemical potential of the Ni/graphene calculated by the DFT+QMC. The blue dashed lines in (b) and (c) represent the energy level of $m = 141$st host state. In addition, these results are for $U = 4$ eV, $J = 0.9$ eV and $T = 700$ K.

CHAPTER 8

DFT RESULTS FOR BIOINORGANIC MOLECULES

The DFT calculations are performed by using the Gaussian program (Frisch et al. (2009)). We first compute DFT to study the electronic structure of hemoglobin and myoglobin derivatives, cyanocobalamin (CNCbl), ruthenium based dye molecules and transition-metal adatoms on a hexagonal graphene nanosheet within the framework of extended multi-orbital Haldane-Anderson model. Then, the parameters of Anderson model: $\varepsilon_{d\nu}$, ε_m and $V_{m\nu}$ are obtained by the DFT calculations for each molecule. For these molecules, we will show the results of the singlet state from the DFT calculations. We have explained these calculations in detail in Refs. (Kandemir (2013); Kandemir et al. (2016); Mayda et al. (2017)).

8.1. DFT results for carbonmonoxy-heme

The carbonmonoxy-heme (CO-heme) molecule is shown in Fig. 2.3 (a) and it has 77 atoms. We take the human carbonmonoxy hemoglobin (COHbA) molecule from the PDB with key 2DN3 (Park et al. (2006)). In the COHbA, α_1 heme group is used for CO-heme molecule. For our works, we add proximal and distal histidine parts in the CO-heme.

For carbonmonoxy-heme, we perform the DFT calculation by using BP86 exchange-correlation energy functional and 6-31G basis set for singlet state. Figure 8.1 (a) shows the total density of states $D(\varepsilon) = \sum_{n=1}^{N} \delta(\varepsilon - E_n)$ for carbonmonoxy-heme. E_n is the eigenvalues of Kohn-Sham matrix. The HOMO and LUMO values are located at -3.98 eV and -2.74 eV, respectively. In Fig. 8.1 (b), the host density of states $D_h(\varepsilon) = \sum_{m=1}^{N-5} \delta(\varepsilon - \varepsilon_m)$ is shown without Fe($3d_\nu$) orbitals. The Fe($3d_\nu$) levels have been shifted by the double counting term (Mayda et al. (2017)). The double counting term μ_ν^{DC} includes U, $U'(= U - 2J)$ and $U' - J$ interactions. This term is calculated for Coulomb interaction $U = 4$ eV and Hund's coupling term $J = 0.9$ eV. The new energies $\tilde{\varepsilon}_{d\nu}$ of Fe($3d_\nu$) orbitals are obtained that the bare Fe($3d_\nu$) energy levels $\varepsilon_{d\nu}$ are subtracted from double counting term μ_ν^{DC}. In Fig. 8.1 (b), they are located between -15 eV and -14 eV. The sort of new energies of Fe($3d_\nu$) orbitals is $3d_{yz}$, $3d_{xz}$, $3d_{xy}$, $3d_{3z^2-r^2}$ and

Figure 8.1. (a) For carbonmonoxy-heme total density of states $D(\varepsilon)$ versus energy ε, obtained DFT(BP86) by using the Gaussian program. (b) For carbonmonoxy-heme density of states of the host states $D_h(\varepsilon)$ of the extended Haldane-Anderson model. The Fe($3d_\nu$) levels have been shifted by the double counting term. This term is calculated for $U = 4$ eV and $J = 0.9$ eV. Here, the vertical solid and dashed lines denote the HOMO and LUMO levels, respectively.

$3d_{x^2-y^2}$ after shifting.

In Fig. 8.2, the square of the hybridization matrix elements $|V_{m\nu}|^2$ between the m'th host eigenstates and Fe($3d_\nu$) natural atomic orbitals as a function of the m'th host eigenvalues ε_m for carbonmonoxy-heme. We observed that the host states $m = 157$th, and 159th have the highest hybridization matrix elements for $3d_{3z^2-r^2}$ and $3d_{x^2-y^2}$ orbitals. In Fig. 8.2 (b), $3d_{yz}$ and $3d_{xz}$ orbitals have the noticeable hybridization contribution at $m = 160$th, 177th and 178th host states. Hybridization contributions of $3d$ orbitals are very small for $m = 172$nd, 173rd and 174th host states in Fig. 8.2.

Figure 8.3 shows the NAO (Glendening et al. (2013)) composition of the m'th host eigenstate for carbonmonoxy-heme. The Ref.(Kandemir et al. (2016); Kandemir (2013)) was explained more detail for NAO weight of the $|u_{mi}|^2$. The Fe atom is attached to the 10th nitrogen (N) atom of the imidazole part in the first part of Fig. 8.3. The Fe atom is attached to the 11th carbon and 12th oxygen ligand molecule (CO) from above in the first part of Fig. 8.3. In addition, 2nd, 3rd, 4th and 5th N sites are connected to the Fe atom in porphyrin ring. In Fig. 8.3 (a) and (b), NAO weights of $2p_z$ orbital of 10th and $2p_x$ orbital of 5th N sites are the largest value for $m = 157$th and 159th host states, respectively. In addition, there are NAO weights of $2p$'s orbitals of 4N's atoms and $2s$ orbitals 11th carbon atom which bind to Fe atom. In Figs. 8.3 (c), (d) and (e), NAO weights of $2p_z$ orbital of 4N's and carbon atoms in porphyrin layer are the largest values for $m = 160$th, 172nd and 174th. In Fig. 8.3 (f), NAO weights of $2p_x$ and $2p_y$ orbitals of 21st C and 22nd O atoms in distal histidine are the largest value due to finite size effects for $m = 173$rd host state. Figures 8.3 (g) and (h) show that the NAO weights of $2p_x$ and $2p_y$ orbitals of 11th C and 12th O atoms for CN ligand are the largest value at $m = 177$th and 178th.

8.2. DFT results for cyanomet-heme

We take human cyanomet hemoglobin (CNHbA) molecule from the PDB with key 1ABY (Kroeger and Kundrot (1997)). In the CNHbA, α_1 heme group is used for cyanomet-heme (CN-heme) molecule as shown in Fig. 2.3 (b). This molecule contains 77 atoms. The total number of electrons of the CN-heme molecule is 347 electrons. If the total number of electrons is odd, the DFT calculations become doublet state. The DFT results are divided into alpha and beta orbitals in the doublet state. We bring singlet state to pass by adding one electron to the [CN-heme]$^-$ because we use the singlet state in the DFT calculations.

For cyanomet-heme, we perform the DFT calculation by using BP86 exchange-

Figure 8.2. For carbonmonoxy-heme, DFT(BP86) results on the square of hybridization matrix elements $|V_{m\nu}|^2$ between the m'th host eigenstates and Fe($3d_\nu$) natural atomic orbitals as a function of the m'th host eigenvalues ε_m. In (a) results are shown for $3d_{x^2-y^2}$ and $3d_{3z^2-r^2}$ orbitals, and in (b) for $3d_{xz}$, $3d_{yz}$ and $3d_{xy}$ orbitals. Here, the vertical solid and dashed lines denote the values of the HOMO and LUMO, respectively. We observe that the host states $m = 157$th and 159th have the highest hybridization matrix elements with $3z^2 - r^2$ and $x^2 - y^2$ orbitals.
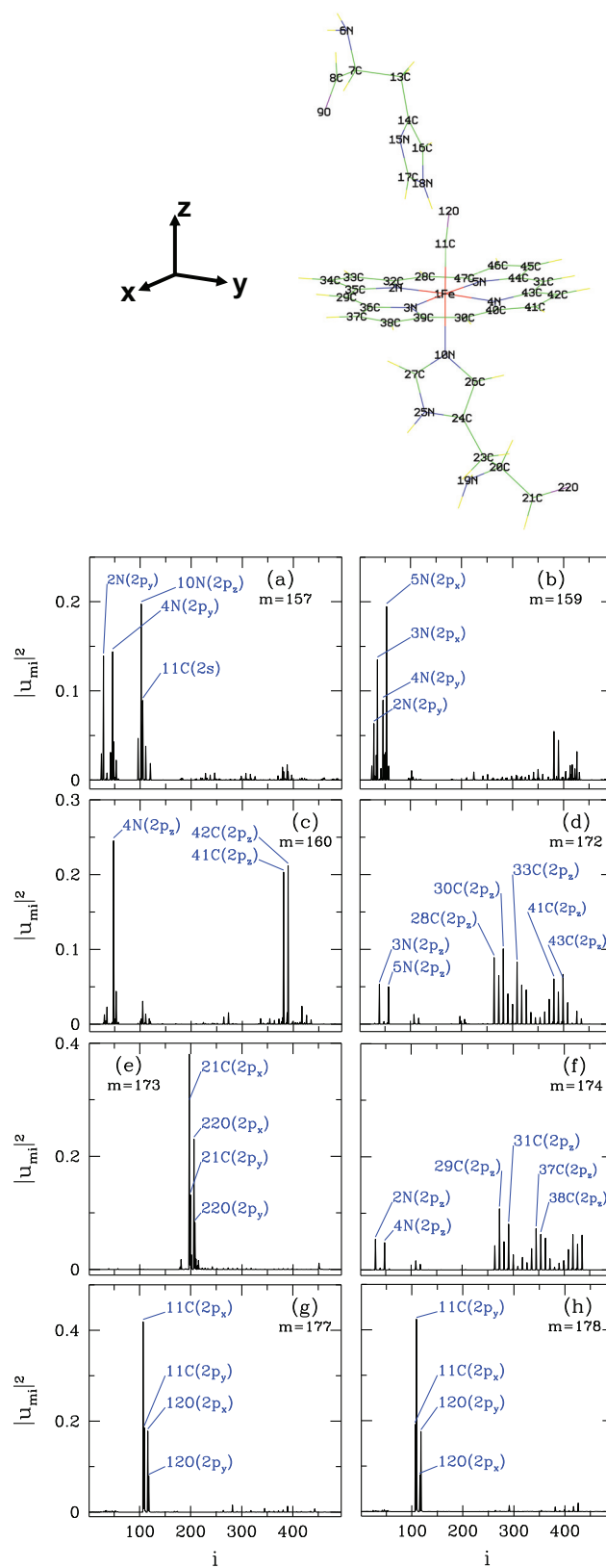
Figure 8.3. For carbonmonoxy-heme, schematic plot with label numbers and symbols of atoms. The DFT results on the square of the host eigenstate ($|u_{mi}|^2$) contributions versus the label i for (a) $m = 157$th, (b) 159th, (c) 160th, (d) 172nd, (e) 173rd, (f) 174th, (g) 177th and (h) 178th host states.

correlation energy functional and 6-31G basis set for the singlet-spin state. Figure 8.4 (a) shows the total density of states $D(\varepsilon) = \sum_{n=1}^{N} \delta(\varepsilon - E_n)$ for cyanomet-heme. E_n is the eigenvalues of Kohn-Sham matrix. The HOMO and LUMO values are located at -0.54 eV and -0.42 eV, respectively. In Fig. 8.4 (b), the host density of states $D_h(\varepsilon) = \sum_{m=1}^{N-5} \delta(\varepsilon - \varepsilon_m)$ is shown without Fe($3d_\nu$) orbitals. The Fe($3d_\nu$) levels have been shifted by the double counting term (Mayda et al. (2017)). The double counting term μ_ν^{DC} includes U, $U'(= U - 2J)$ and $U' - J$ interactions. This term is calculated for Coulomb interaction $U = 4$ eV and Hund's coupling term $J = 0.9$ eV. The new energies $\tilde{\varepsilon}_{d\nu}$ of Fe($3d_\nu$) orbitals are obtained that the bare Fe($3d_\nu$) energy levels $\varepsilon_{d\nu}$ are subtracted from double counting term μ_ν^{DC}. In Fig. 8.4 (b), they are located between -12 eV and -11 eV. The sort of new energies of Fe($3d_\nu$) orbitals is $3d_{yz}$, $3d_{xz}$, $3d_{xy}$, $3d_{3z^2-r^2}$ and $3d_{x^2-y^2}$ after shifting.

In Fig. 8.5, the square of the hybridization matrix elements $|V_{m\nu}|^2$ between the m'th host eigenstates and Fe($3d_\nu$) natural atomic orbitals as a function of the m'th host eigenvalues ε_m for cyanomet-heme. We observed that the host states $m = 158$th, and 162nd have the highest hybridization matrix elements for $3d_{3z^2-r^2}$ and $3d_{x^2-y^2}$ orbitals, respectively. Hybridization contributions of $3d$ orbitals are very small for $m = 142$nd, 146th, 147th, 151st, 161st, 164th, 174th and 175th host states as shown in Fig. 8.5.

Figure 8.6 shows the NAO (Glendening et al. (2013)) composition of the m'th host eigenstate for cyanomet-heme. The Ref.(Kandemir et al. (2016); Kandemir (2013)) was explained more detail for NAO weight of the $|u_{mi}|^2$. The Fe atom is attached to the 10th nitrogen (N) atom of the imidazole part in the first part of Fig. 8.6. The Fe atom is attached to the 11th carbon and 12th nitrogen ligand molecule (CN) from above in the first part of Fig. 8.6. In addition, 2nd, 3rd, 4th and 5th N sites are connected to the Fe atom in porphyrin ring. In Figs. 8.6 (a) and 8.6 (b), NAO weights of $2p_z$ orbital of 10th nitrogen atom is the largest value for $m = 146$th and 147th host states. In Figs. 8.6 (c) and 8.6 (d), NAO weights of $2p_x$ and $2p_y$ orbitals of 2nd, 3rd, 4th and 5th N sites are the largest value for $m = 158$th and 162nd states. We see that $m = 164$th state has large weight from $2p_z$ orbitals of 5th N, 45th C and 46th C atoms as shown in Fig. 8.6 (e). In Fig. 8.6 (f), NAO weights of $2p_x$ and $2p_y$ orbitals of 21st C and 22nd O atoms in distal histidine are the largest value due to finite size effects for $m = 172$nd host state. Figures 8.6 (g) and (h) show that the NAO weights of $2p_z$ orbitals of N and C sites in the porphyrin ring are the largest value at $m = 174$th and 175th.

Figure 8.4. (a) For cyanomet-heme total density of states $D(\varepsilon)$ versus energy ε, obtained DFT(BP86) by using the Gaussian program. (b) For cyanomet-heme density of states of the host states $D_h(\varepsilon)$ of the extended Haldane-Anderson model. The Fe($3d_\nu$) levels have been shifted by the double counting term. This term is calculated for $U = 4$ eV and $J = 0.9$ eV. Here, the vertical solid and dashed lines denote the HOMO and LUMO levels, respectively.
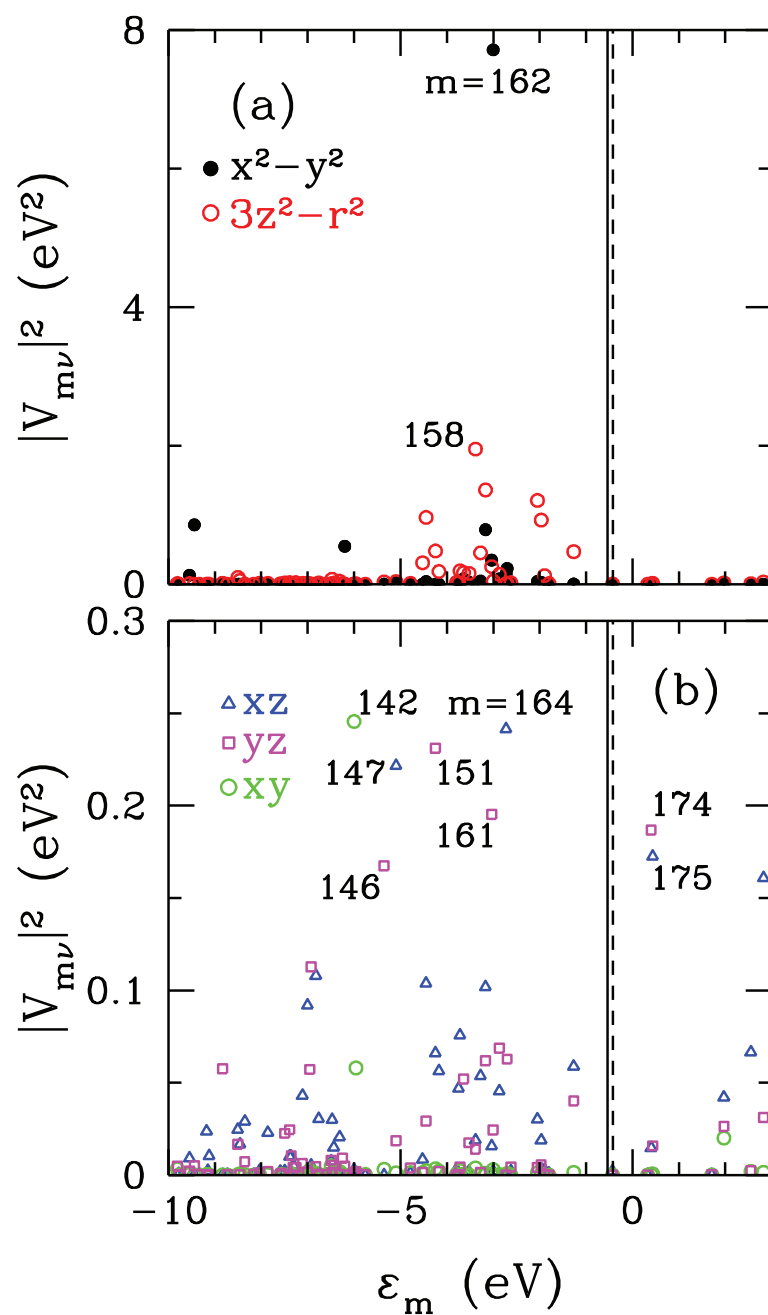
Figure 8.5. For cyanomet-heme, DFT(BP86) results on the square of hybridization matrix elements $|V_{m\nu}|^2$ between the m'th host eigenstates and Fe($3d_\nu$) natural atomic orbitals as a function of the m'th host eigenvalues ε_m. In (a) results are shown for $3d_{x^2-y^2}$ and $3d_{3z^2-r^2}$ orbitals, and in (b) for $3d_{xz}$, $3d_{yz}$ and $3d_{xy}$ orbitals. Here, the vertical solid and dashed lines denote the values of the HOMO and LUMO, respectively. We observe that the host states $m = 158$th and 162nd have the highest hybridization matrix elements.
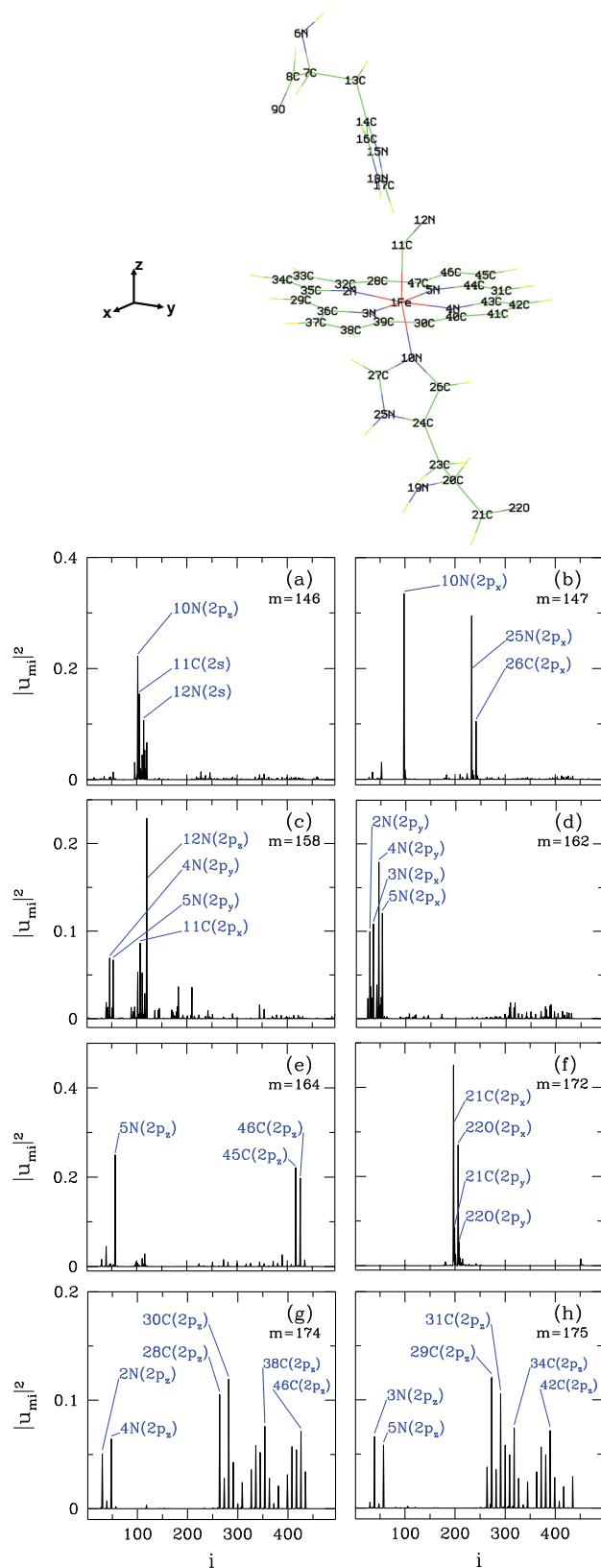
Figure 8.6. For cyanomet-heme, schematic plot with label numbers and symbols of atoms. The DFT results on the square of the host eigenstate ($|u_{mi}|^2$) contributions versus the label i for (a) $m = 146$th, (b) 147th, (c) 158th, (d) 162th, (e) 164th, (f) 172nd, (g) 174th and (h) 175th host states.

8.3. DFT results for myoglobin molecules

In this section, we show the DFT results for myoglobin molecules. We examine the horse heart deoxymyoglobin (deoxyMb) and carbonmonoxy myoglobin (MbCO) and sperm whale cyanomet myoglobin (MbCN) molecules (Tsukahara (1986)). We get these myoglobin molecules from the Protein Data Bank (PDB) with key 5D5R (Barends et al. (2015)), 1DWR (Chu et al. (2000)) and 2JHO (Arcovito et al. (2007)), respectively. In addition, Badaut et. al. (Badaut et al. (2012)) studied the high-spin to low-spin states due to O_2 binding in myoglobin molecule by using mean-field approximation (MFA) for the Haldane-Anderson model. However, this Anderson model Hamiltonian is not similar to our Hamiltonian.

For our works, we add proximal and distal histidine parts in myoglobin derivatives. The deoxyMb molecule is shown in Fig. 2.4 and it has 75 atoms. The deoxyMb molecule is similar to the deoxy-heme molecule. For the deoxyMb molecule, the second column of Table 2.2 shows the distances of N atoms that bind to the Fe atom. The structure of the MbCO and MbCN are similar to the CO-heme and CN-heme molecules. Fig. 2.4 (b) and Fig. 2.4 (c) show the structures of the MbCO and MbCN molecules, respectively. The charge of the MbCN molecule has minus 1. In the MbCO and MbCN molecules, the Fe atom binds to CO and CN ligands, respectively. The third and fourth columns of Table 2.2 show the distances of C and N atoms which bind to the Fe atom.

8.3.1. Deoxymyoglobin

For deoxymyoglobin (deoxyMb), we perform the DFT calculation by using BP86 exchange-correlation energy functional and 6-31G basis set for singlet state. The deoxyMb molecule is shown in Fig. 2.4 (a) and it has 75 atoms. The deoxyMb molecule is similar to the deoxy-heme molecule. Figure 8.7 (a) shows the total density of states $D(\varepsilon) = \sum_{n=1}^{N} \delta(\varepsilon - E_n)$ for deoxyMb. E_n is the eigenvalues of Kohn-Sham matrix. The HOMO and LUMO values are located at -3.44 eV and -2.96 eV, respectively. In Fig. 8.7 (b), the host density of states $D_h(\varepsilon) = \sum_{m=1}^{N-5} \delta(\varepsilon - \varepsilon_m)$ is shown without Fe($3d_\nu$) orbitals. The Fe($3d_\nu$) levels have been shifted by the double counting term (Mayda et al. (2017)). The double counting term μ_ν^{DC} includes U, $U'(= U - 2J)$ and $U' - J$ interactions. This term is calculated for Coulomb interaction $U = 4$ eV and Hund's coupling term $J = 0.9$ eV. The new energies $\tilde{\varepsilon}_{d\nu}$ of Fe($3d_\nu$) orbitals are obtained that the bare
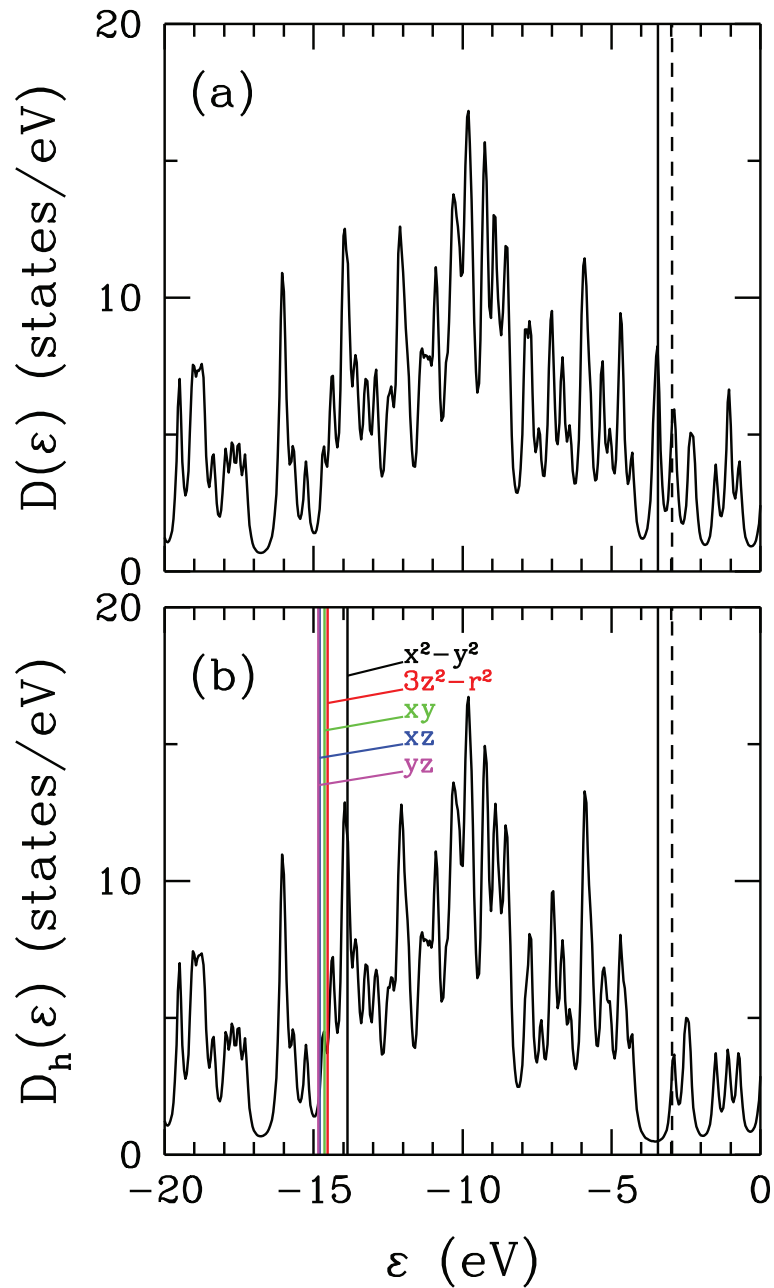
Figure 8.7. (a) For deoxyMb, total density of states $D(\varepsilon)$ versus energy ε, obtained DFT(BP86) by using the Gaussian program. (b) For deoxyMb, density of states of the host states $D_h(\varepsilon)$ of the extended Haldane-Anderson model. The Fe($3d_\nu$) levels have been shifted by the double counting term. This term is calculated for $U = 4$ eV and $J = 0.9$ eV. Here, the vertical solid and dashed lines denote the HOMO and LUMO levels, respectively.

Fe($3d_\nu$) energy levels $\varepsilon_{d\nu}$ are subtracted from double counting term μ_ν^{DC}. In Fig. 8.7 (b), they are located between -15 eV and -14 eV. The sort of new energies of Fe($3d_\nu$) orbitals is $3d_{yz}$, $3d_{xz}$, $3d_{xy}$, $3d_{3z^2-r^2}$ and $3d_{x^2-y^2}$ after shifting.

In Fig. 8.8, the square of the hybridization matrix elements $|V_{m\nu}|^2$ between the m'th host eigenstates and Fe($3d_\nu$) natural atomic orbitals as a function of the m'th host eigenvalues ε_m for deoxyMb. We observed that the host states $m = 154$th, 153rd and 145th have the highest hybridization matrix elements for $3d_{x^2-y^2}$ and $3d_{3z^2-r^2}$ orbitals. In Fig. 8.8 (b), $3d_{yz}$ and $3d_{xz}$ orbitals have small hybridization contribution at $m = 156$th and 154th host states. Hybridization contributions of $3d$ orbitals are very small for $m = 165$th, 166th and 167th host states as shown in Fig. 8.8.

Figure 8.9 shows the NAO (Glendening et al. (2013)) composition of the $m = 145$th, 153rd, 154th, 156th, 165th, 166th and 167th host eigenstates for deoxyMb. The Ref.(Kandemir et al. (2016); Kandemir (2013)) was explained more detail for NAO weight of the $|u_{mi}|^2$. The Fe atom is attached to the 10th nitrogen (N) atom of the imidazole part in the first part of Fig. 8.9. In addition, 2nd, 3rd, 4th and 5th N sites are connected to the Fe atom in porphyrin ring. Here, we show the highest NAO weights with blue colors.

8.3.2. Carbonmonoxy myoglobin

For carbonmonoxy myoglobin (MbCO), we perform the DFT calculation by using BP86 exchange-correlation energy functional and 6-31G basis set for singlet state. The structure of the MbCO is similar to the CO-heme molecule. Fig. 2.4 (b) shows the structure of the MbCO molecule. Figure 8.10 (a) shows the total density of states $D(\varepsilon) = \sum_{n=1}^{N} \delta(\varepsilon - E_n)$ for MbCO. E_n is the eigenvalues of Kohn-Sham matrix. The HOMO and LUMO values are located at -3.77 eV and -2.85 eV, respectively. In Fig. 8.10 (b), the host density of states $D_h(\varepsilon) = \sum_{m=1}^{N-5} \delta(\varepsilon - \varepsilon_m)$ is shown without Fe($3d_\nu$) orbitals. The Fe($3d_\nu$) levels have been shifted by the double counting term (Mayda et al. (2017)). The double counting term μ_ν^{DC} includes U, $U'(= U - 2J)$ and $U' - J$ interactions. This term is calculated for Coulomb interaction $U = 4$ eV and Hund's coupling term $J = 0.9$ eV. The new energies $\tilde{\varepsilon}_{d\nu}$ of Fe($3d_\nu$) orbitals are obtained that the bare Fe($3d_\nu$) energy levels $\varepsilon_{d\nu}$ are subtracted from double counting term μ_ν^{DC}. In Fig. 8.10 (b), they are located between -15.5 eV and -14.5 eV. The sort of new energies of Fe($3d_\nu$) orbitals is $3d_{yz}$, $3d_{xz}$, $3d_{xy}$, $3d_{3z^2-r^2}$ and $3d_{x^2-y^2}$ and after shifting.

In Fig. 8.11, the square of the hybridization matrix elements $|V_{m\nu}|^2$ between the m'th host eigenstates and Fe($3d_\nu$) natural atomic orbitals as a function of the m'th host

Figure 8.8. For deoxyMb, DFT(BP86) results on the square of hybridization matrix elements $|V_{m\nu}|^2$ between the m'th host eigenstates and Fe($3d_\nu$) natural atomic orbitals as a function of the m'th host eigenvalues ε_m. In (a) results are shown for $3d_{x^2-y^2}$ and $3d_{3z^2-r^2}$ orbitals, and in (b) for $3d_{xz}$, $3d_{yz}$ and $3d_{xy}$ orbitals. Here, the vertical solid and dashed lines denote the values of the HOMO and LUMO, respectively. We observe that the host state $m = 154$th has the highest hybridization matrix element with $x^2 - y^2$ orbital.

```
For m = 145th          εm = -7.37 eV
   i   host orbitals    |umi|²
--------------------------------
   28     N 2( 2py)     0.053
   35     N 3( 2px)     0.033
   46     N 4( 2py)     0.043
   53     N 5( 2px)     0.043
   96     N10( 2s )     0.078
   98     N10( 2px)     0.049
  102     N10( 2pz)     0.409

For m = 153rd          εm = -5.91 eV
   i   host orbitals    |umi|²
--------------------------------
   28     N 2( 2py)     0.032
   30     N 2( 2pz)     0.126
   35     N 3( 2px)     0.039
   46     N 4( 2py)     0.080
   53     N 5( 2px)     0.049
  291     C31( 2pz)     0.106
  300     C32( 2pz)     0.118

For m = 154th          εm = -5.49 eV
   i   host orbitals    |umi|²
--------------------------------
   28     N 2( 2py)     0.108
   30     N 2( 2pz)     0.039
   35     N 3( 2px)     0.112
   46     N 4( 2py)     0.097
   53     N 5( 2px)     0.118
  291     C31( 2pz)     0.054
  300     C32( 2pz)     0.071

For m = 156th          εm = -5.75 eV
   i   host orbitals    |umi|²
--------------------------------
   30     N 2( 2pz)     0.129
   39     N 3( 2pz)     0.036
   48     N 4( 2pz)     0.201
  291     C31( 2pz)     0.072
  300     C32( 2pz)     0.065
  336     C36( 2pz)     0.051
  363     C39( 2pz)     0.160
  372     C40( 2pz)     0.140

For m = 165th          εm = -2.92 eV
   i   host orbitals    |umi|²
--------------------------------
  215     C23( 2px)     0.436
  217     C23( 2py)     0.118
  224     O24( 2px)     0.266
  226     O24( 2py)     0.074

For m = 166th          εm = -2.52 eV
   i   host orbitals    |umi|²
--------------------------------
   30     N 2( 2pz)     0.059
   48     N 4( 2pz)     0.060
  246     C26( 2pz)     0.081
  255     C27( 2pz)     0.053
  264     C28( 2pz)     0.065
  273     C29( 2pz)     0.078
  318     C34( 2pz)     0.054
  327     C35( 2pz)     0.051
  336     C36( 2pz)     0.056
  345     C37( 2pz)     0.048
  399     C43( 2pz)     0.076
  408     C44( 2pz)     0.080

For m = 167th          εm = -2.40 eV
   i   host orbitals    |umi|²
--------------------------------
   39     N 3( 2pz)     0.062
   57     N 5( 2pz)     0.050
  246     C26( 2pz)     0.063
  255     C27( 2pz)     0.073
  264     C28( 2pz)     0.067
  273     C29( 2pz)     0.077
  282     C30( 2pz)     0.051
  291     C31( 2pz)     0.057
  300     C32( 2pz)     0.062
  354     C38( 2pz)     0.051
  363     C39( 2pz)     0.062
  372     C40( 2pz)     0.063
```

Figure 8.9. For deoxyMb, schematic plot with label numbers and symbols of atoms. The DFT results on the square of the host eigenstate ($|u_{mi}|^2$) contributions and eigenvalues (ε_m) of the $m = $ 145th, 153rd, 154th, 156th, 165th, 166th and 167th host states.

Figure 8.10. (a) For MbCO, total density of states $D(\varepsilon)$ versus energy ε, obtained DFT(BP86) by using the Gaussian program. (b) For MbCO, density of states of the host states $D_h(\varepsilon)$ of the extended Haldane-Anderson model. The Fe($3d_\nu$) levels have been shifted by the double counting term. This term is calculated for $U = 4$ eV and $J = 0.9$ eV. Here, the vertical solid and dashed lines denote the HOMO and LUMO levels, respectively.

eigenvalues ε_m for MbCO. We observed that the host states $m = 157$th, and 161st have the highest hybridization matrix elements for $3d_{3z^2-r^2}$ and $3d_{x^2-y^2}$ orbitals, respectively. Hybridization contributions of $3d$ orbitals are very small for $m = 172$nd, 173rd, 174th, 177th and 178th host states in Fig. 8.11 (a) and (b).

Figure 8.12 shows the NAO (Glendening et al. (2013)) composition of the $m = 157$th, 161st, 162nd, 172nd, 173rd, 174th, 177th and 178th host eigenstates for MbCO. The Ref.(Kandemir et al. (2016); Kandemir (2013)) was explained more detail for NAO weight of the $|u_{mi}|^2$. The Fe atom is attached to the 10th nitrogen (N) atom of the imidazole part in the first part of Fig. 8.12. In addition, 2nd, 3rd, 4th and 5th N sites are connected to the Fe atom in the porphyrin ring. Here, we show the highest NAO weights with blue colors. Figures 8.12 (a-h) show that the NAO weights of $2p_z$ orbitals of N and C sites in the porphyrin ring are the largest value at mth host states.

8.3.3. Cyanomet myoglobin

For cyanomet myoglobin (MbCN), we perform the DFT calculation by using BP86 exchange-correlation energy functional and 6-31G basis set for singlet state. The structure of the MbCN is similar to the CN-heme molecule. Figure 2.4 (c) shows the structure of the MbCN molecule. The charge of the MbCN molecule has minus 1. Figure 8.13 (a) shows the total density of states $D(\varepsilon) = \sum_{n=1}^{N} \delta(\varepsilon - E_n)$ for MbCN. E_n is the eigenvalues of Kohn-Sham matrix. The HOMO and LUMO values are located at -0.53 eV and -0.52 eV, respectively. In Fig. 8.13 (b), the host density of states $D_h(\varepsilon) = \sum_{m=1}^{N-5} \delta(\varepsilon - \varepsilon_m)$ is shown without Fe($3d_\nu$) orbitals. The Fe($3d_\nu$) levels have been shifted by the double counting term (Mayda et al. (2017)). The double counting term μ_ν^{DC} includes U, $U'(= U - 2J)$ and $U' - J$ interactions. This term is calculated for Coulomb interaction $U = 4$ eV and Hund's coupling term $J = 0.9$ eV. The new energies $\tilde{\varepsilon}_{d\nu}$ of Fe($3d_\nu$) orbitals are obtained that the bare Fe($3d_\nu$) energy levels $\varepsilon_{d\nu}$ are subtracted from double counting term μ_ν^{DC}. In Fig. 8.13 (b), they are located between -12 eV and -11 eV. The sort of new energies of Fe($3d_\nu$) orbitals is $3d_{yz}$, $3d_{xz}$, $3d_{xy}$, $3d_{3z^2-r^2}$ and $3d_{x^2-y^2}$ and after shifting.
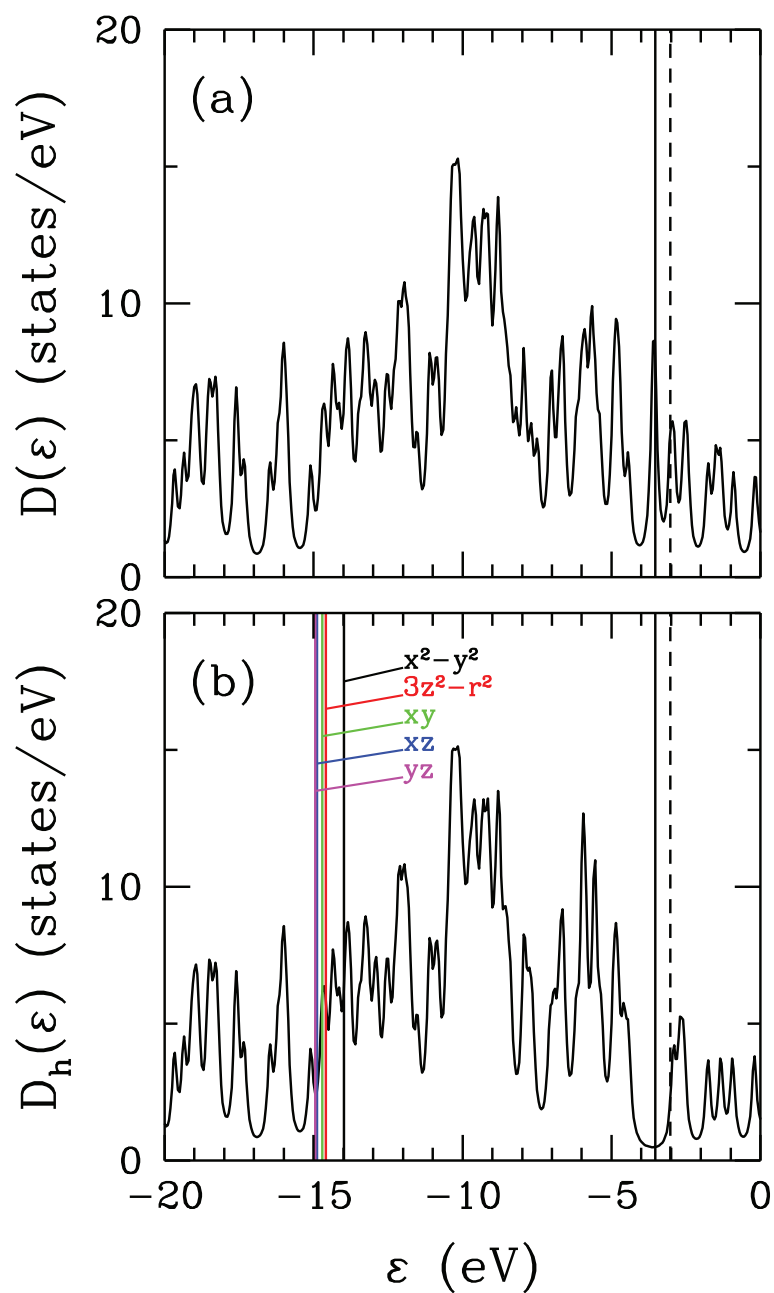
In Fig. 8.14, the square of the hybridization matrix elements $|V_{m\nu}|^2$ between the m'th host eigenstates and Fe($3d_\nu$) natural atomic orbitals as a function of the m'th host eigenvalues ε_m for MbCO. We observed that the host states $m = 162$nd, and 169th have the highest hybridization matrix elements for $3d_{3z^2-r^2}$ and $3d_{x^2-y^2}$ orbitals, respectively. Hybridization contributions of $3d$ orbitals are very small for $m = 172$nd, 173rd and 174th

Figure 8.11. For MbCO, DFT(BP86) results on the square of hybridization matrix elements $|V_{m\nu}|^2$ between the m'th host eigenstates and $Fe(3d_\nu)$ natural atomic orbitals as a function of the m'th host eigenvalues ε_m. In (a) results are shown for $3d_{x^2-y^2}$ and $3d_{3z^2-r^2}$ orbitals, and in (b) for $3d_{xz}$, $3d_{yz}$ and $3d_{xy}$ orbitals. Here, the vertical solid and dashed lines denote the values of the HOMO and LUMO, respectively. We observe that the host states $m = 157$st and 161st have the highest hybridization matrix elements for $3d_{3z^2-r^2}$ and $3d_{x^2-y^2}$ orbitals.
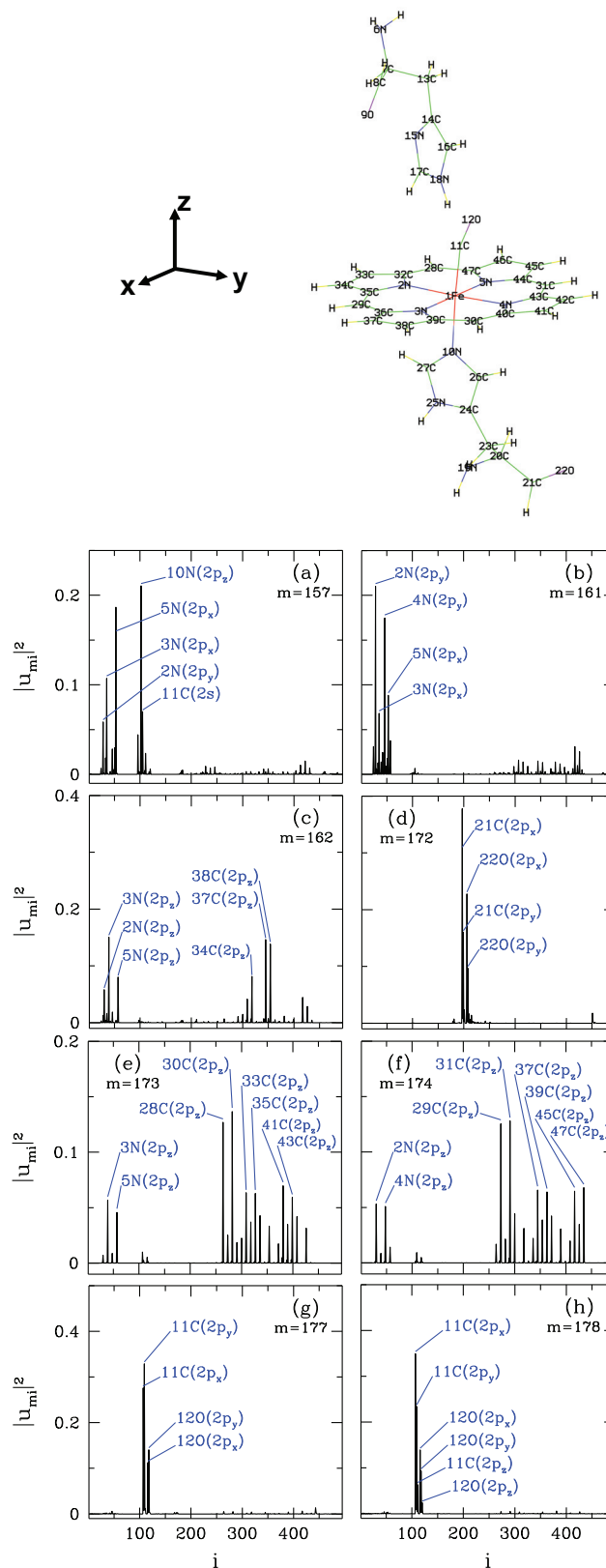
Figure 8.12. For MbCO, schematic plot with label numbers and symbols of atoms. The DFT results on the square of the host eigenstate ($|u_{mi}|^2$) contributions versus the label i for (a) $m = 157$th, (b) 161st, (c) 162nd, (d) 172nd, (e) 173rd, (f) 174th, (g) 177th and (h) 178th host states.
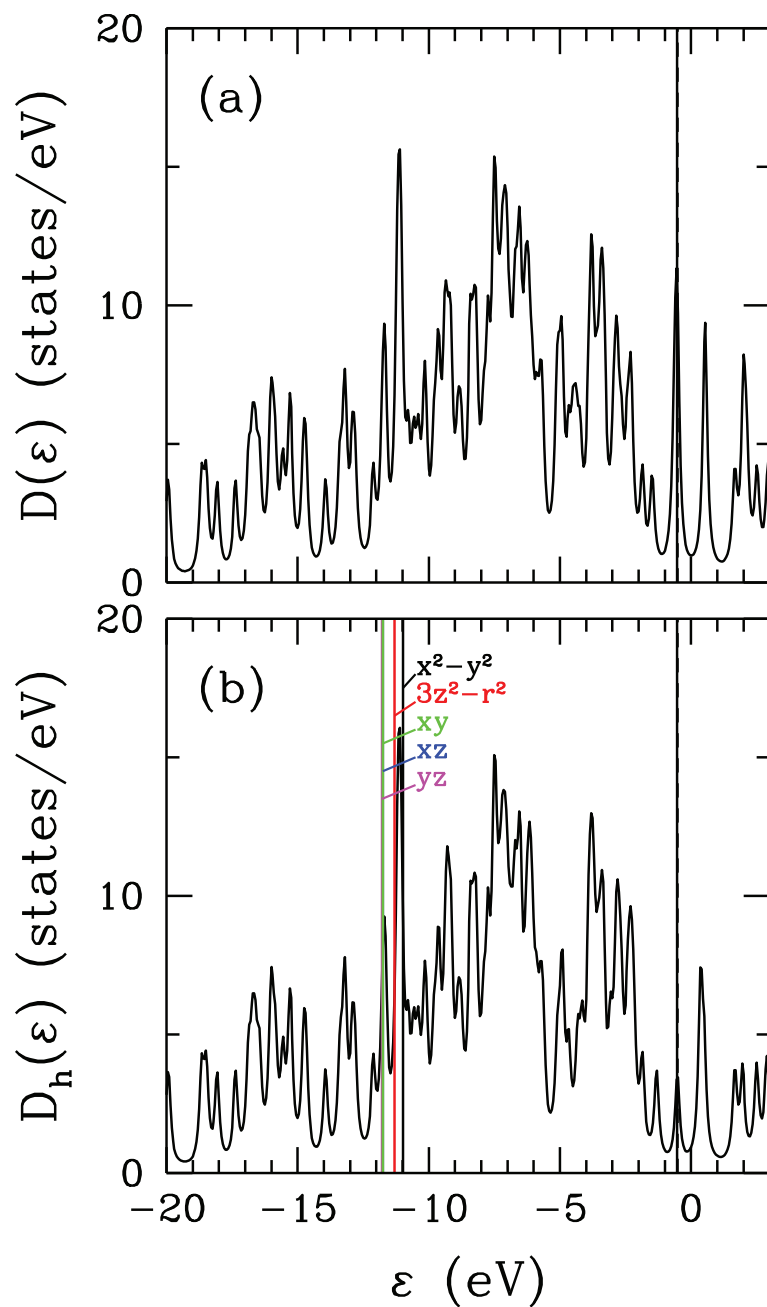
Figure 8.13. (a) For MbCN, total density of states $D(\varepsilon)$ versus energy ε, obtained DFT(BP86) by using the Gaussian program. (b) For MbCN, density of states of the host states $D_h(\varepsilon)$ of the extended Haldane-Anderson model. The Fe($3d_\nu$) levels have been shifted by the double counting term. This term is calculated for $U = 4$ eV and $J = 0.9$ eV. Here, the vertical solid and dashed lines denote the HOMO and LUMO levels, respectively.

host states in Fig. 8.14 (a) and (b).

Figures 8.15 and 8.16 show the NAO (Glendening et al. (2013)) composition of the $m = 150$th, 151st, 153rd, 156th, 172nd, 163rd, 166th, 169th, 173rd and 174th host eigenstates for MbCN. The Ref.(Kandemir et al. (2016); Kandemir (2013)) was explained more detail for NAO weight of the $|u_{mi}|^2$. The Fe atom is attached to the 10th nitrogen (N) atom of the imidazole part in the first part of Fig. 8.15. In addition, 2nd, 3rd, 4th and 5th N sites are connected to the Fe atom in the porphyrin ring. Figures 8.15 (a-f) show that the NAO weights of $2p_z$ orbitals of N and C sites in the porphyrin ring are the largest value at mth host states.

8.4. DFT results for CNCbl

For cyanocobalamin (CNCbl) molecule, we perform the DFT calculation by using BP86 exchange-correlation energy functional and 6-31G basis set for singlet state. The molecular structure of CNCbl molecule with the chemical formula $C_{63}H_{88}Co\,N_{14}O_{14}P$ is shown in Fig. 2.5. This molecule consists of a cobalt atom at the center and four nitrogen atoms attached to Co atom in the corrin ring. A ligand and a nucleotide are attached to the corrin ring as shown in Fig. 2.5. The neutral CNCbl molecule has 718 electrons. Figure 8.17 (a) shows the total density of states $D(\varepsilon) = \sum_{n=1}^{N} \delta(\varepsilon - E_n)$ for CNCbl. E_n is the eigenvalues of Kohn-Sham matrix. The HOMO and LUMO values are located at -4.91 eV and -3.15 eV, respectively. In Fig. 8.17 (b), the host density of states $D_h(\varepsilon) = \sum_{m=1}^{N-5} \delta(\varepsilon - \varepsilon_m)$ is shown without Co($3d_\nu$) orbitals. The Co($3d_\nu$) levels have been shifted by the double counting term (Mayda et al. (2017)). The double counting term μ_ν^{DC} includes U, $U'(= U - 2J)$ and $U' - J$ interactions. This term is calculated for Coulomb interaction $U = 4$ eV and Hund's coupling term $J = 0.7$ eV. The new energies $\tilde{\varepsilon}_{d\nu}$ of Co($3d_\nu$) orbitals are obtained that the bare Co($3d_\nu$) energy levels $\varepsilon_{d\nu}$ are subtracted from double counting term μ_ν^{DC}. In Fig. 8.17 (b), they are located between -22 eV and -20 eV. The sort of new energies of Co($3d_\nu$) orbitals is $3d_{yz}$, $3d_{xz}$, $3d_{xy}$, $3d_{3z^2-r^2}$ and $3d_{x^2-y^2}$ after shifting.

In Fig. 8.18, the square of the hybridization matrix elements $|V_{m\nu}|^2$ between the m'th host eigenstates and Co($3d_\nu$) natural atomic orbitals as a function of the m'th host eigenvalues ε_m for CNCbl molecule. We observe that the host state $m = 340$th has the highest hybridization matrix element for $3d_{3z^2-r^2}$ orbital. We also see that the host states $m = 336$th and 337th have the highest hybridization matrix elements for $3d_{x^2-y^2}$ orbital. In Fig. 8.18 (a), $3d_{3z^2-r^2}$ orbital has the noticeable hybridization contribution
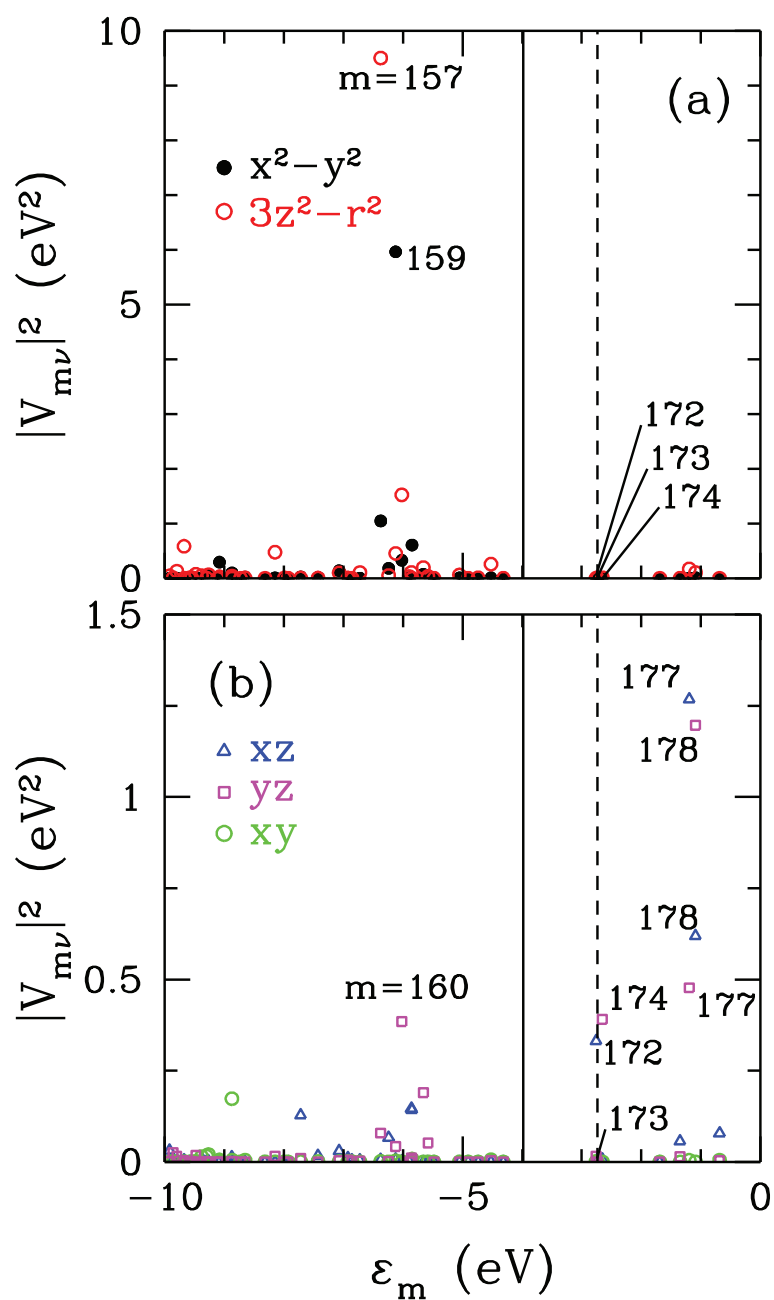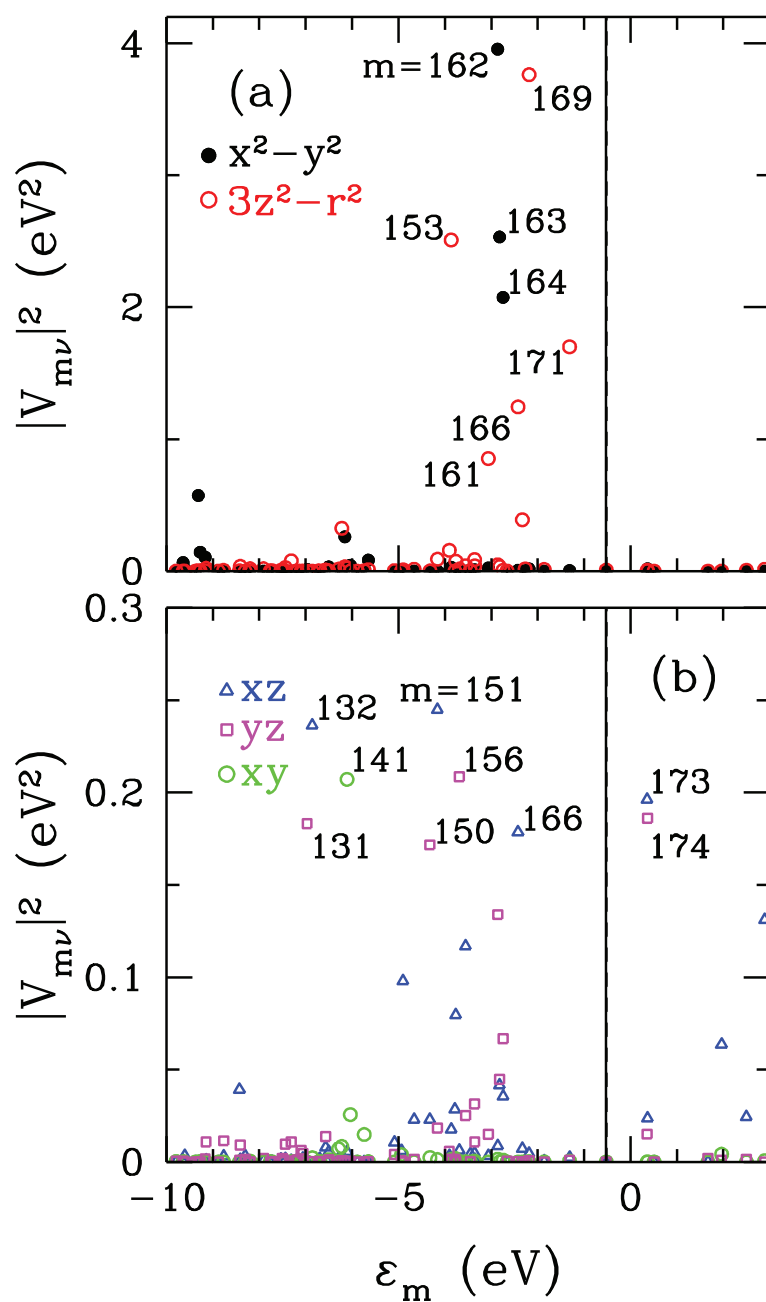
Figure 8.14. For MbCN, DFT(BP86) results on the square of hybridization matrix elements $|V_{m\nu}|^2$ between the m'th host eigenstates and Fe($3d_\nu$) natural atomic orbitals as a function of the m'th host eigenvalues ε_m. In (a) results are shown for $3d_{x^2-y^2}$ and $3d_{3z^2-r^2}$ orbitals, and in (b) for $3d_{xz}$, $3d_{yz}$ and $3d_{xy}$ orbitals. Here, the vertical solid and dashed lines denote the values of the HOMO and LUMO, respectively. We observe that the host states $m = 162$nd, and 169th have the highest hybridization matrix elements for $3d_{3z^2-r^2}$ and $3d_{x^2-y^2}$ orbitals.
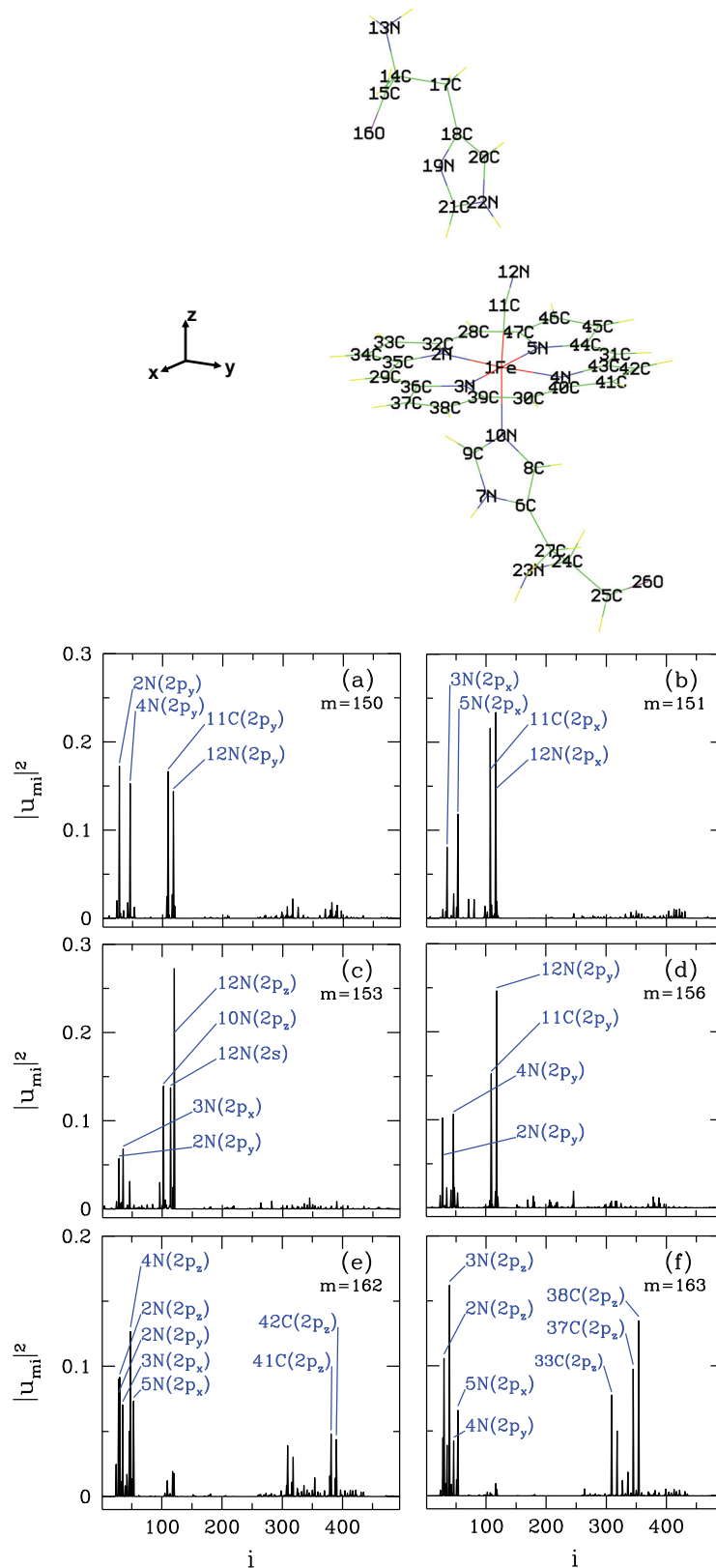
Figure 8.15. For MbCN, schematic plot with label numbers and symbols of atoms. The DFT results on the square of the host eigenstate ($|u_{mi}|^2$) contributions versus the label i for (a) $m = 150$th, (b) 151st, (c) 153rd, (d) 156th, (e) 172nd and (f) 163rd host states.
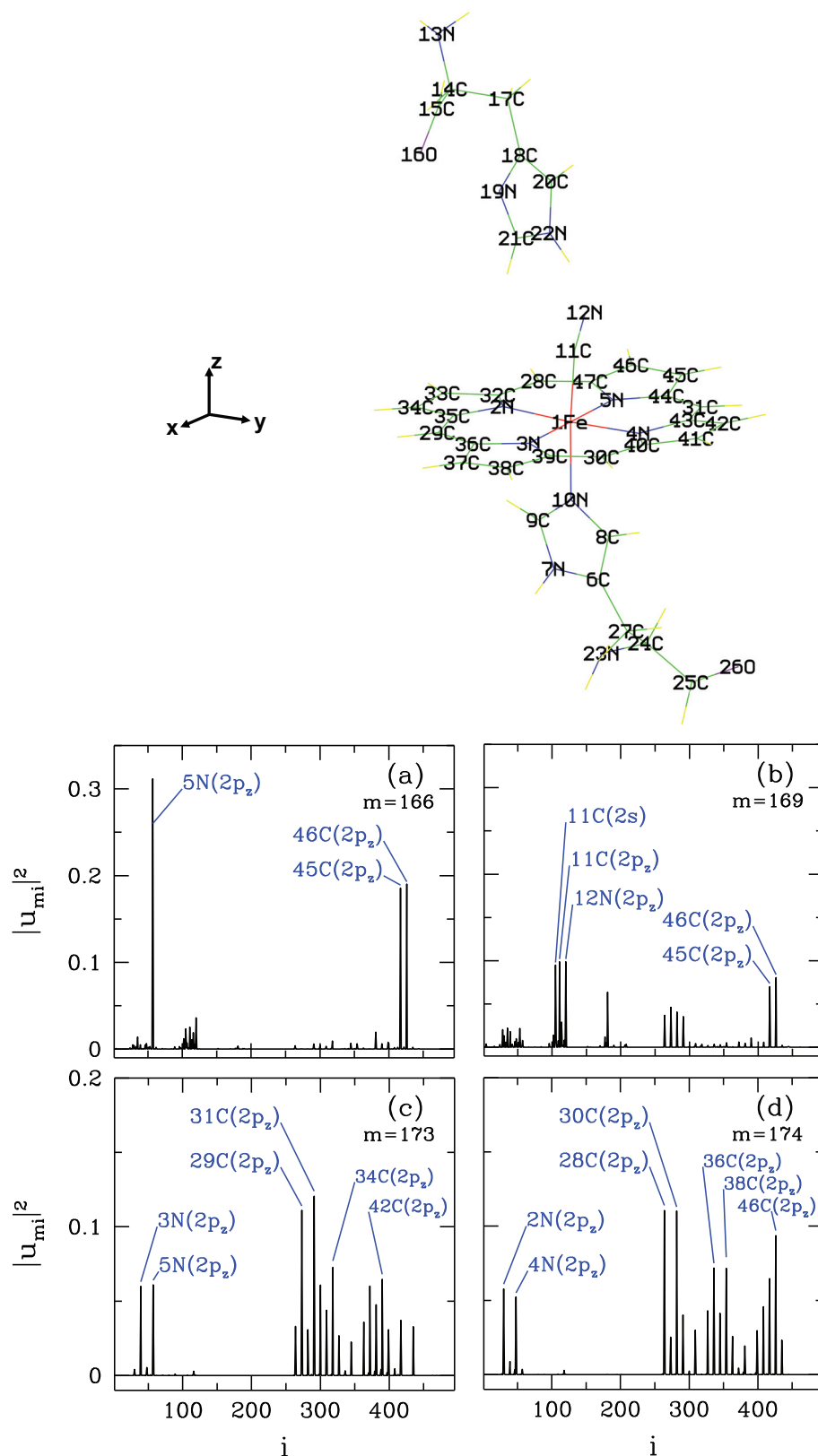
Figure 8.16. For MbCN, schematic plot with label numbers and symbols of atoms. The DFT results on the square of the host eigenstate ($|u_{mi}|^2$) contributions versus the label i for (a) $m = 166$th, (b) 169th, (c) 173rd and (d) 174th host states.
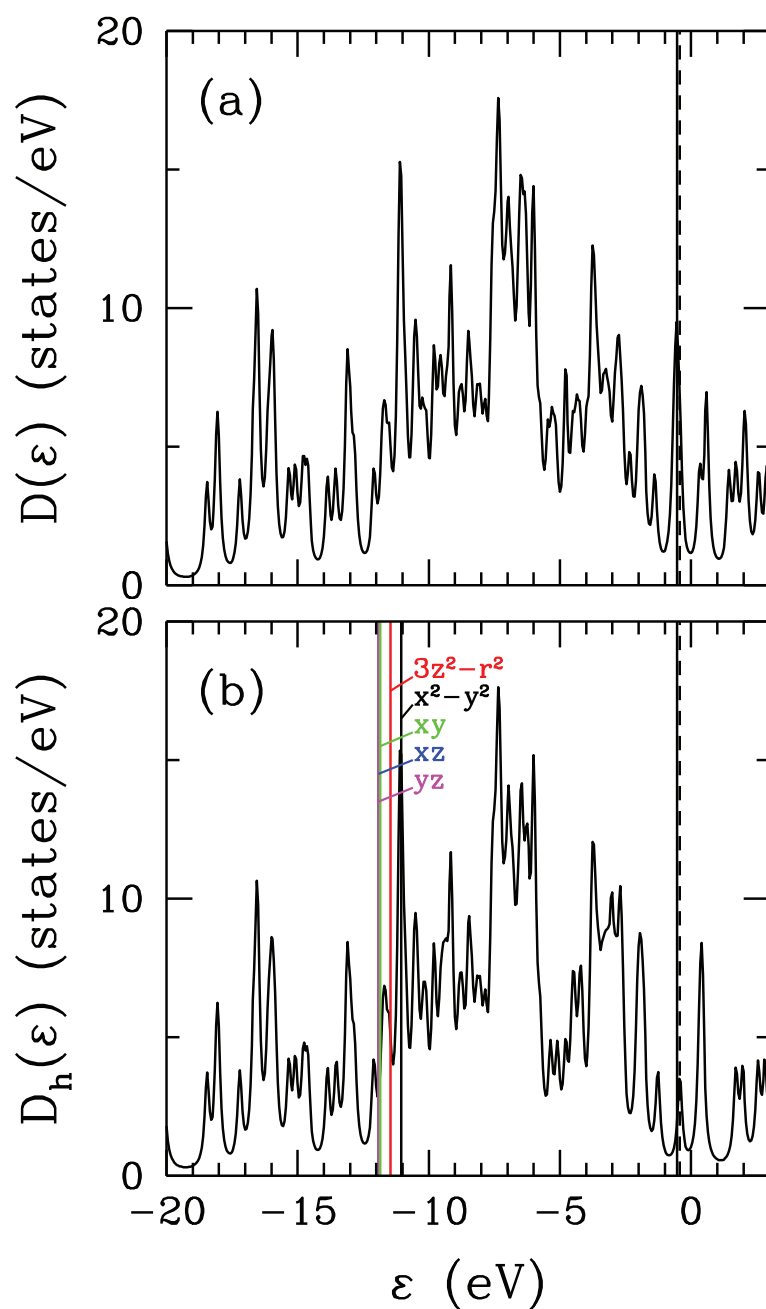
Figure 8.17. (a) For CNCbl, total density of states $D(\varepsilon)$ versus energy ε, obtained DFT(BP86) by using the Gaussian program. (b) For CNCbl, density of states of the host states $D_h(\varepsilon)$ of the extended Haldane-Anderson model. The Co($3d_\nu$) levels have been shifted by the double counting term. This term is calculated for $U = 4$ eV and $J = 0.7$ eV. Here, the vertical solid and dashed lines denote the HOMO and LUMO levels, respectively.

at $m = 322$nd host state. Hybridization contributions of $3d_{xz}$ and $3d_{yz}$ orbitals are very small for $m = 357$th, 358th, 373rd and 375th host states as shown in Fig. 8.18 (b).

Figure 8.19 shows the NAO (Glendening et al. (2013)) composition of the $m = 322$nd, 336th, 337th and 340th host eigenstates for CNCbl. The Ref.(Kandemir et al. (2016); Kandemir (2013)) was explained more detail for NAO weight of the $|u_{mi}|^2$. The Co atom is attached to the 10th nitrogen (N) atom of the imidazole part in the first part of Fig. 8.19. In addition, 2nd, 3rd, 4th and 5th N sites are connected to the Co atom in corrin ring. In Figs. 8.19 (a) and 8.19 (d), NAO weights of $2s$ and $2p$'s orbitals of 10th N, 11th C and 12th C atoms are the largest values for $m = 322$nd and 340th host states, respectively. In Figs. 8.19 (b) and 8.19 (c), NAO weights of $2p_z$ orbitals of 2nd, 3rd, 4th and 5th N atoms, 50th O and 51st N atoms are the largest values for $m = 336$th and 337th.

8.5. DFT results for Ru-based dye molecules

In this section, we show the DFT results of N719 and Z907 molecules. They are Ru-based dye molecules. The DFT calculations of N719 and Z907 dye molecules are used BP86 exchange-correlation energy functional and two basis sets. These basis sets are LanL2DZ and 6-31G(d). We will explain these basis sets as follows. Ruthenium (Ru) atom is the 5th row of the element in the periodic table. The 6-31G basis set does not work for this atom, so we use the LanL2DZ basis set. The LanL2DZ basis set is used with between sodium and bismuth (Na-Bi) elements. This basis set is double zeta effective core potential (ECP). We use the LanL2DZ basis set for Ru atom and 6-31G(d) basis set for C, H, O, N, and S atoms in dye molecules. There is only one difference between 6-31G(d) and 6-31G basis sets. The 6-31G(d) basis set contains the contributions of 3d orbitals in addition to the 6-31G set for C, N, O and S atoms.

8.5.1. N719 dye

For N719 dye, we perform the DFT calculation by using BP86 exchange-correlation energy functional and the LanL2DZ basis set for Ru atom and 6-31G(d) basis set for C, H, O, N, and S atoms in the singlet-spin state. Figure 8.20 (a) shows the total density of states $D(\varepsilon) = \sum_{n=1}^{N} \delta(\varepsilon - E_n)$ for N719 dye. E_n is the eigenvalues of Kohn-Sham matrix. The HOMO and LUMO values are located at $+0.54$ eV and $+0.70$ eV,
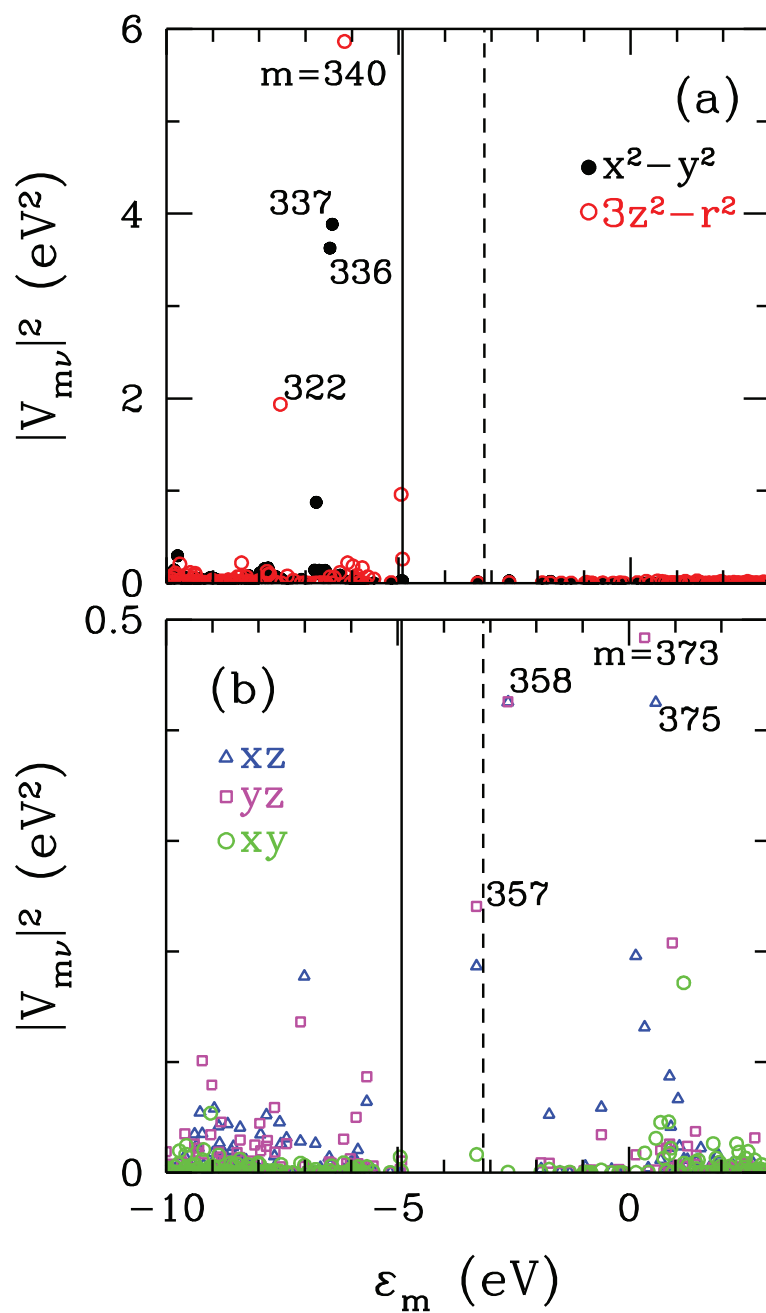
Figure 8.18. For CNCbl, DFT(BP86) results on the square of hybridization matrix elements $|V_{m\nu}|^2$ between the m'th host eigenstates and Co($3d_\nu$) natural atomic orbitals as a function of the m'th host eigenvalues ε_m. In (a) results are shown for $3d_{x^2-y^2}$ and $3d_{3z^2-r^2}$ orbitals, and in (b) for $3d_{xz}$, $3d_{yz}$ and $3d_{xy}$ orbitals. Here, the vertical solid and dashed lines denote the values of the HOMO and LUMO, respectively. We observe that the host states $m = 340$th has the highest hybridization matrix element with $3z^2 - r^2$ orbital.
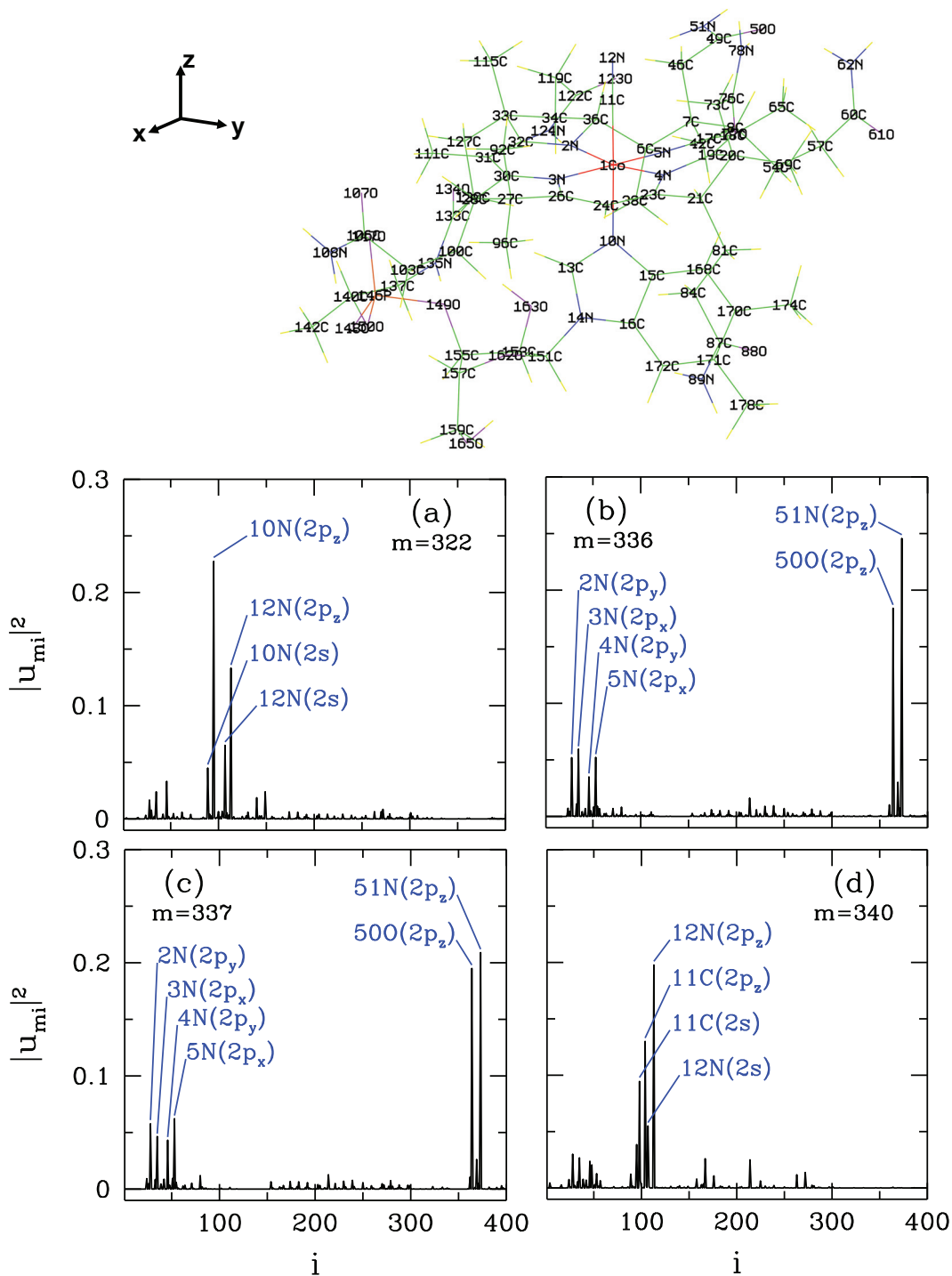
Figure 8.19. For CNCbl, schematic plot with label numbers and symbols of atoms. The DFT results on the square of the host eigenstate ($|u_{mi}|^2$) contributions versus the label i for (a) $m = 322$nd, (b) 336th, (c) 337th and (d) 340th host states.
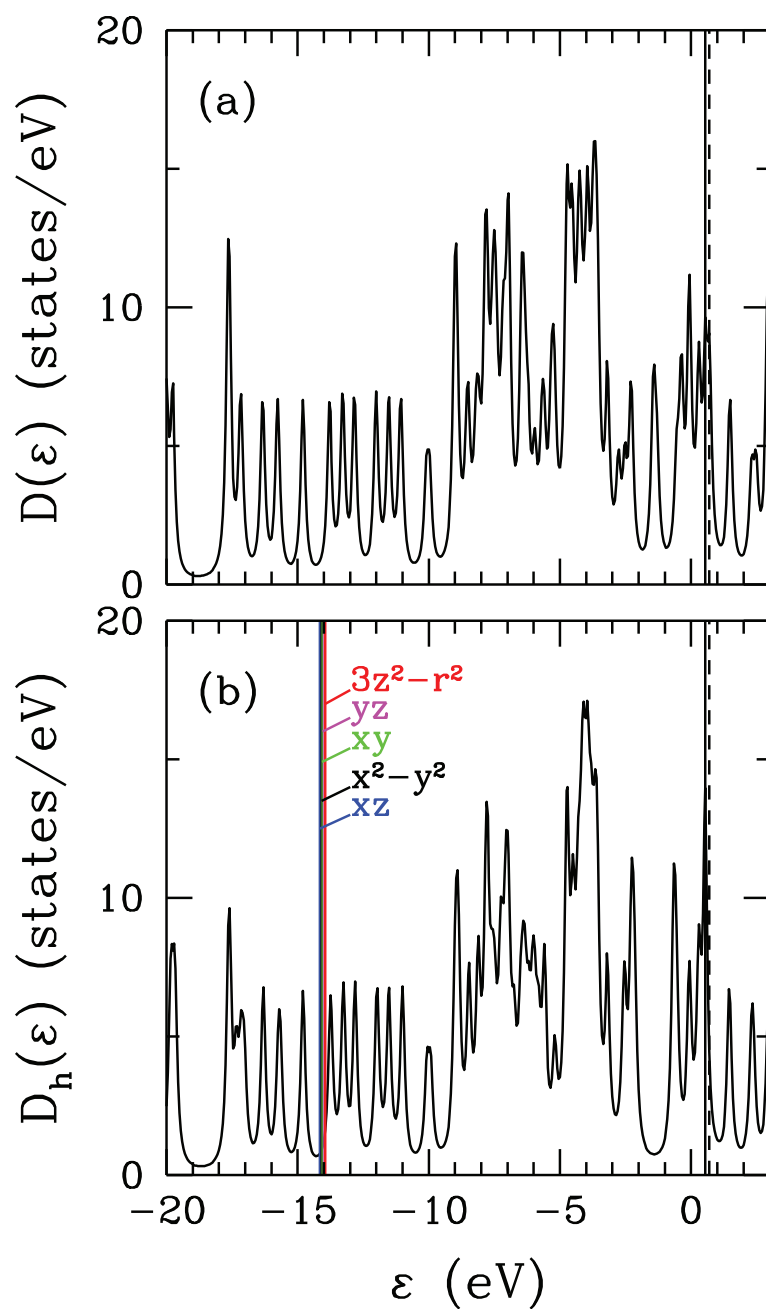
Figure 8.20. (a) For N719 dye, total density of states $D(\varepsilon)$ versus energy ε, obtained DFT(BP86) by using the Gaussian program. (b) For N719 dye, density of states of the host states $D_h(\varepsilon)$ of the extended Haldane-Anderson model. The Ru($4d_\nu$) levels have been shifted by the double counting term. This term is calculated for $U = 4$ eV and $J = 0.9$ eV. Here, the vertical solid and dashed lines denote the HOMO and LUMO levels, respectively.

respectively. In Fig. 8.20 (b), the host density of states $D_h(\varepsilon) = \sum_{m=1}^{N-5} \delta(\varepsilon - \varepsilon_m)$ is shown without Ru($4d_\nu$) orbitals. The Ru($4d_\nu$) levels have been shifted by the double counting term (Mayda et al. (2017)). The double counting term μ_ν^{DC} includes U, $U'(= U - 2J)$ and $U' - J$ interactions. This term is calculated for Coulomb interaction $U = 4$ eV and Hund's coupling term $J = 0.9$ eV. The new energies $\tilde{\varepsilon}_{d\nu}$ of Ru($4d_\nu$) orbitals are obtained that the bare Ru($4d_\nu$) energy levels $\varepsilon_{d\nu}$ are subtracted from double counting term μ_ν^{DC}. In Fig. 8.20 (b), they are located between -15 eV and -13 eV. The sort of new energies of Ru($4d_\nu$) orbitals is $4d_{yz}$, $4d_{xz}$, $4d_{xy}$, $4d_{3z^2-r^2}$ and $4d_{x^2-y^2}$ after shifting.

In Fig. 8.21, the square of the hybridization matrix elements $|V_{m\nu}|^2$ between the m'th host eigenstates and Ru($4d_\nu$) natural atomic orbitals as a function of the m'th host eigenvalues ε_m for N719 dye. We observed that the host states $m = 149$th, and 150th have the highest hybridization matrix elements for $4d_{3z^2-r^2}$ and $4d_{x^2-y^2}$ orbitals. Hybridization contributions of $4d_{xz}$, $4d_{yz}$ and $4d_{xy}$ orbitals are small for $m = 116$th, 131st and 150th host states as shown in Fig. 8.21.

Figure 8.22 shows the NAO (Glendening et al. (2013)) composition of the m'th host eigenstate for N719 dye molecule. The Ref.(Kandemir et al. (2016); Kandemir (2013)) was explained more detail for NAO weight of the $|u_{mi}|^2$. The Ru atom is attached to the 2nd, 3rd, 4th, 5th, 6th and 7th nitrogen (N) atoms in the first part of Fig. 8.22. In Figs. 8.22 (a) and (b), NAO weights of $2s$, $2p_x$, $2p_y$ and $2p_z$ orbitals of the 2nd, 3rd, 4th, 5th, 6th and 7th N sites are the largest value for $m = 149$th and 150th host states. In Figs. 8.22 (c) and (d), NAO weights of $2p_x$ and $2p_z$ orbitals of the 2nd, 3rd, 4th, 5th, 6th and 7th N sites are the largest value for $m = 116$th and 131st host states. For 131st host state, NAO weights of $2p_x$ and $2p_z$ orbitals of the 31st and 33rd C atoms and 32nd and 34th S atoms are the largest value as shown in Fig. 8.22 (d) $m = 149$th and 150th host states have the highest hybridization matrix elements for $4d_{3z^2-r^2}$ and $4d_{x^2-y^2}$ orbitals.

8.5.2. Z907 dye

For Z907 dye, we perform the DFT calculation by using BP86 exchange-correlation energy functional and the LanL2DZ basis set for Ru atom and 6-31G(d) basis set for C, H, O, N, and S atoms in the singlet-spin state. Figure 8.23 (a) shows the total density of states $D(\varepsilon) = \sum_{n=1}^{N} \delta(\varepsilon - E_n)$ for Z907 dye. E_n is the eigenvalues of Kohn-Sham matrix. The HOMO and LUMO values are located at -4.1 eV and -3.5 eV, respectively. In Fig. 8.23 (b), the host density of states $D_h(\varepsilon) = \sum_{m=1}^{N-5} \delta(\varepsilon - \varepsilon_m)$ is shown without Ru($4d_\nu$) orbitals. The Ru($4d_\nu$) levels have been shifted by the double counting term (Mayda et al.
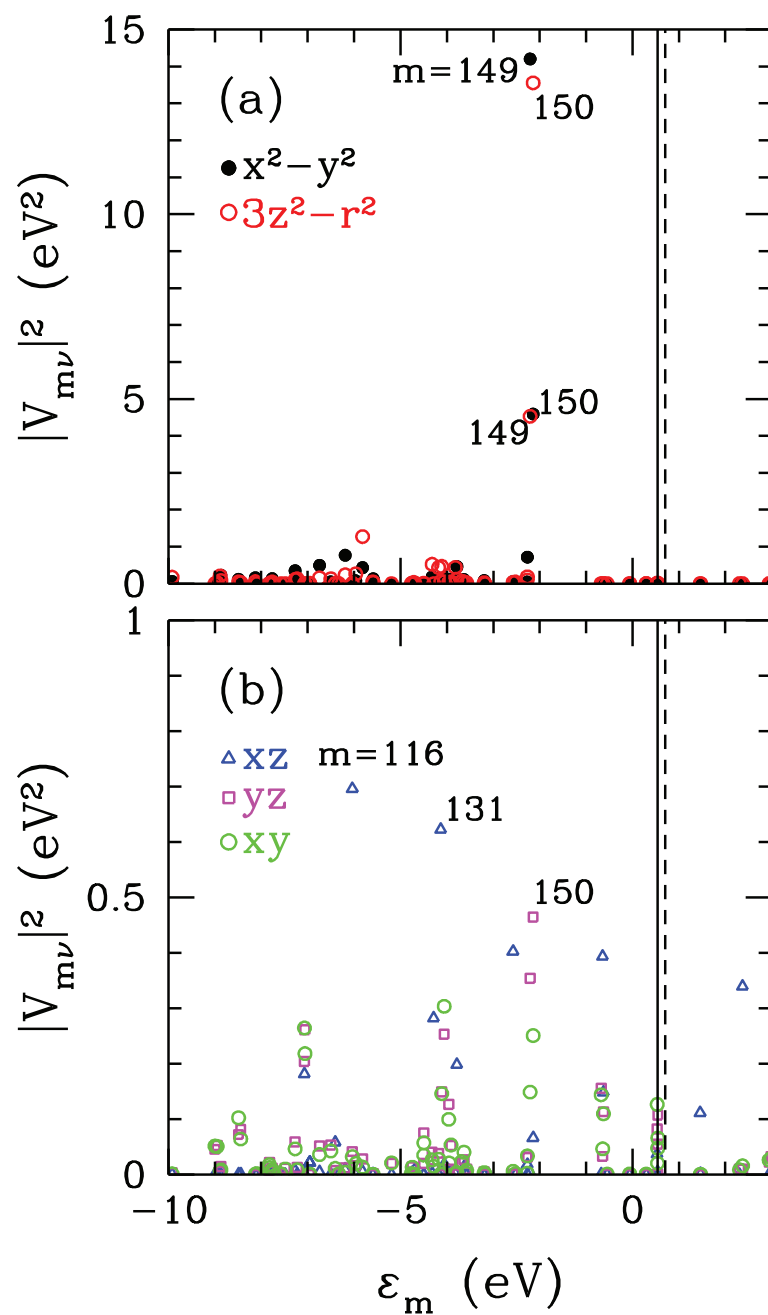
Figure 8.21. For N719 dye, DFT(BP86) results on the square of hybridization matrix elements $|V_{m\nu}|^2$ between the m'th host eigenstates and Ru($4d_\nu$) nat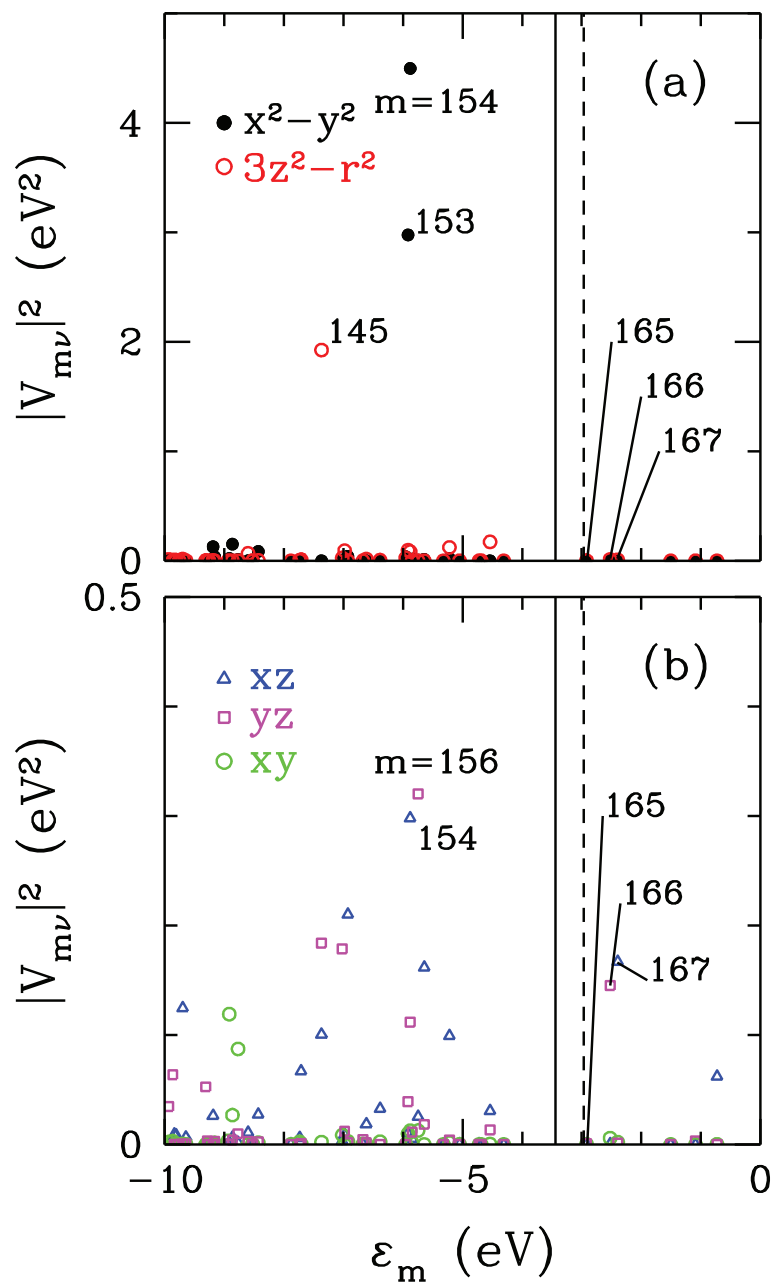ural atomic orbitals as a function of the m'th host eigenvalues ε_m. In (a) results are shown for $4d_{x^2-y^2}$ and $4d_{3z^2-r^2}$ orbitals, and in (b) for $4d_{xz}$, $4d_{yz}$ and $4d_{xy}$ orbitals. Here, the vertical solid and dashed lines denote the values of the HOMO and LUMO, respectively. We observe that the host states $m = 149$th and 150th have the highest hybridization matrix elements with $4d_{x^2-y^2}$ and $4d_{3z^2-r^2}$ orbitals.
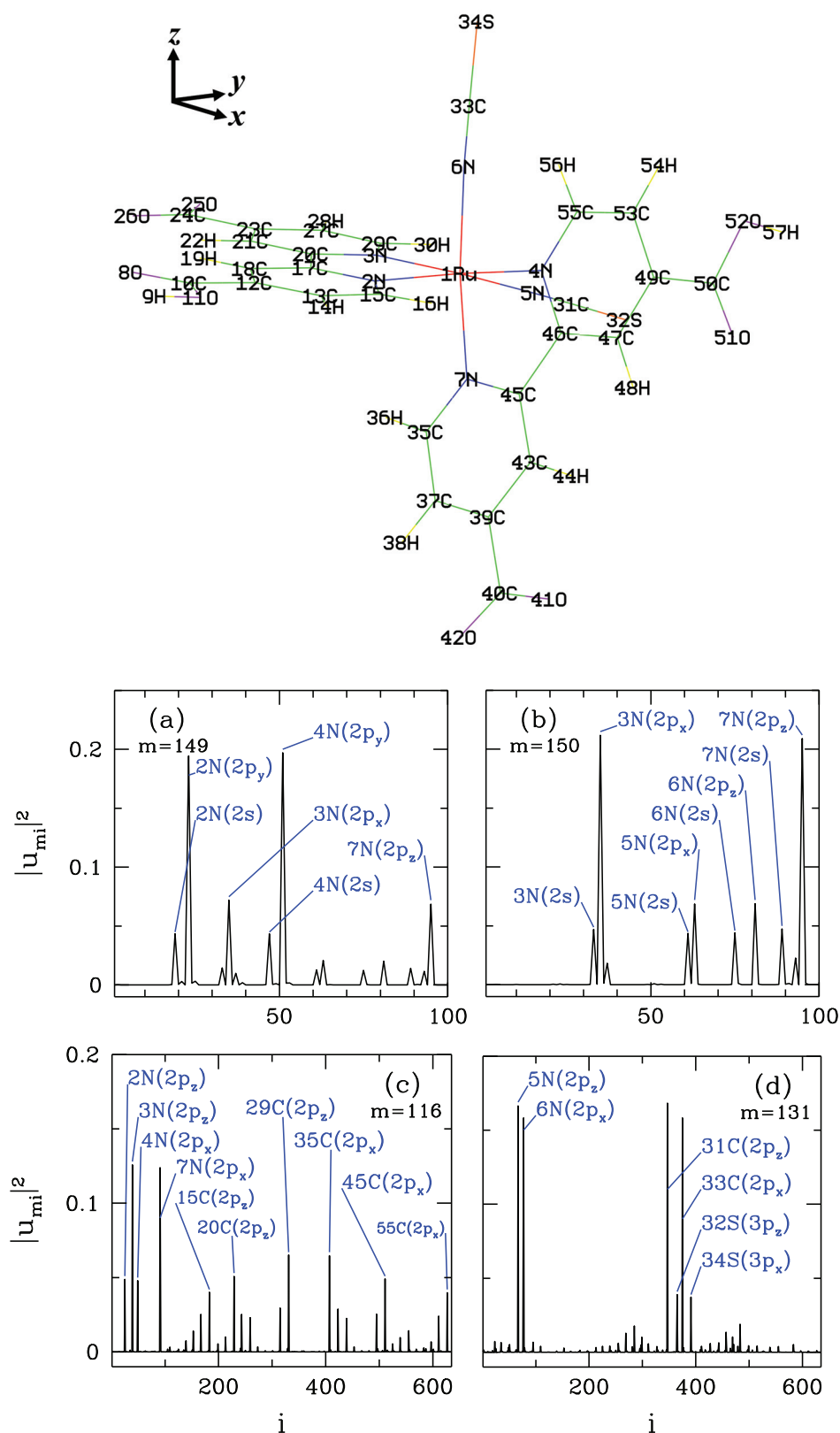
Figure 8.22. For N719 dye, schematic plot with label numbers and symbols of atoms. The DFT results on the square of the host eigenstate ($|u_{mi}|^2$) contributions versus the label i for (a) $m = 149$th, (b) 150th, (c) 116th and (d) 131st host states.
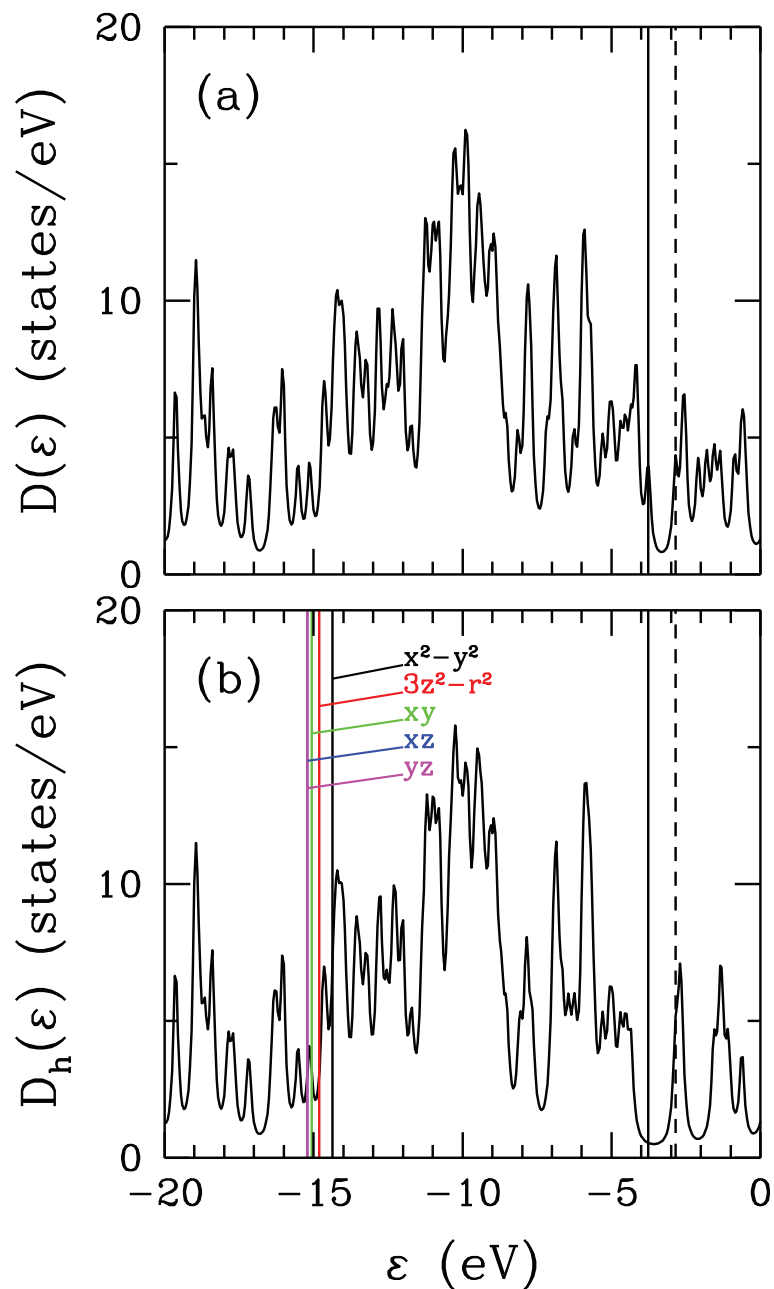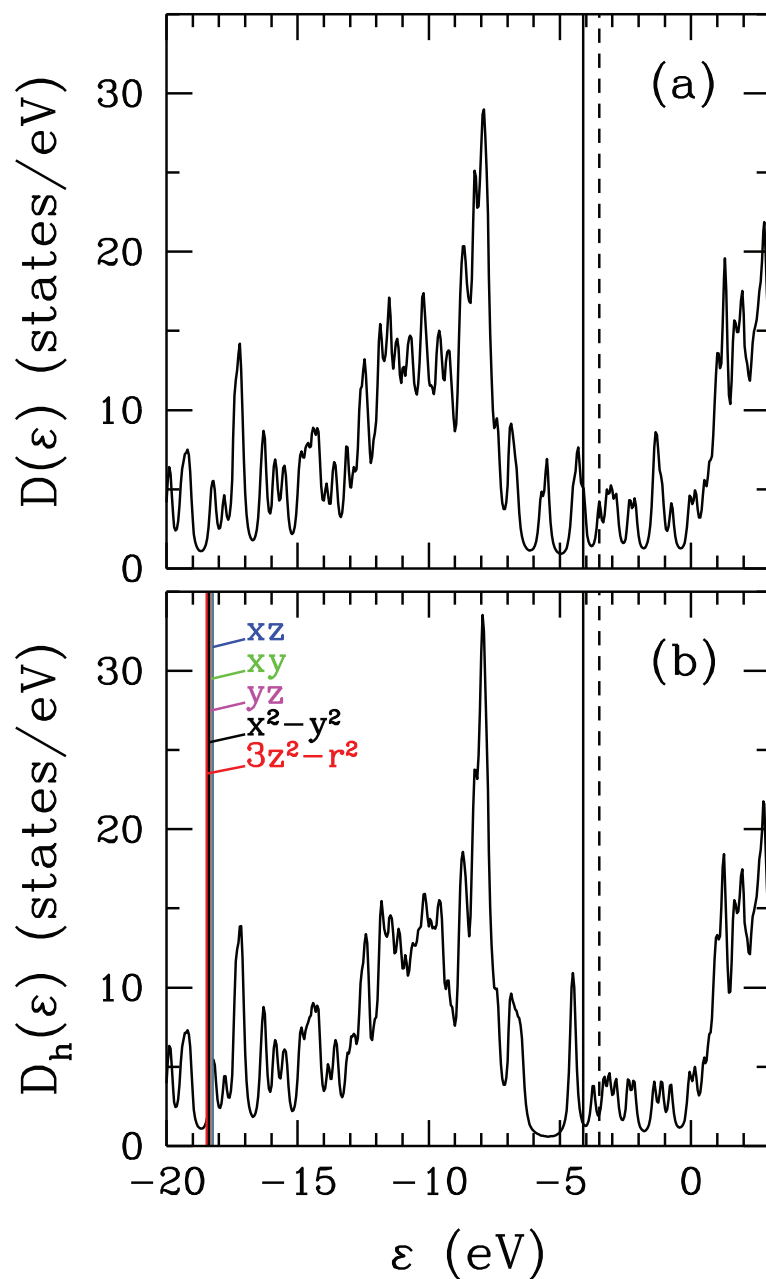
Figure 8.23. (a) For Z907 dye, total density of states $D(\varepsilon)$ versus energy ε, obtained DFT(BP86) by using the Gaussian program. (b) For Z907 dye, density of states of the host states $D_h(\varepsilon)$ of the extended Haldane-Anderson model. The Ru($4d_\nu$) levels have been shifted by the double counting term. This term is calculated for $U = 4$ eV and $J = 0.9$ eV. Here, the vertical solid and dashed lines denote the HOMO and LUMO levels, respectively.

(2017)). The double counting term μ_ν^{DC} includes U, $U'(= U - 2J)$ and $U' - J$ interactions. This term is calculated for Coulomb interaction $U = 4$ eV and Hund's coupling term $J = 0.9$ eV. The new energies $\tilde{\varepsilon}_{d\nu}$ of Ru($4d_\nu$) orbitals are obtained that the bare Ru($4d_\nu$) energy levels $\varepsilon_{d\nu}$ are subtracted from double counting term μ_ν^{DC}. In Fig. 8.23 (b), they are located between -19 eV and -18 eV. The sort of new energies of Ru($4d_\nu$) orbitals is $4d_{yz}$, $4d_{xz}$, $4d_{xy}$, $4d_{3z^2-r^2}$ and $4d_{x^2-y^2}$ after shifting.

In Fig. 8.24, the square of the hybridization matrix elements $|V_{m\nu}|^2$ between the m'th host eigenstates and Ru($4d_\nu$) natural atomic orbitals as a function of the m'th host eigenvalues ε_m for Z907 dye. We observed that the host states $m = 205$th and 206th have the highest hybridization matrix elements for $4d_{3z^2-r^2}$ and $4d_{x^2-y^2}$ orbitals.

Figure 8.25 shows the NAO (Glendening et al. (2013)) composition of the m'th host eigenstate for Z907 dye. The Ref.(Kandemir et al. (2016); Kandemir (2013)) was explained more detail for NAO weight of the $|u_{mi}|^2$. The Ru atom is attached to the 2nd, 3rd, 4th, 5th, 6th and 7th nitrogen (N) atoms in the first part of Fig. 8.25. In Figs. 8.25 (a) and (b), NAO weights of $2s$, $2p_x$, $2p_y$ and $2p_z$ orbitals of the 2nd, 11th, 20th, 29th, 46th and 48th N sites are the largest value for $m = 205$th and 206th host states. In Figs. 8.25 (c) and (d), NAO weights of $2s$, $2p_x$, $2p_y$ and $2p_z$ orbitals of these N sites are the largest value for $m = 205$th and 206th host states. $m = 205$th and 206th host states have the highest hybridization matrix elements for $4d_{3z^2-r^2}$ and $4d_{x^2-y^2}$ orbitals as shown in Fig. 8.24.

8.6. DFT results for graphene catalysts

In this section, we show the DFT results of three graphene catalysts. They are platinum, iron and nickel adatoms on a hexagonal graphene nanosheet. The DFT calculations of these graphene catalysts are used B3LYP hybrid functional and two basis sets. These basis sets are LanL2DZ and 6-31G. For the calculation of graphene catalysts, we use the structure of hexagonal graphene nanosheet with an armchair edge (A-HGNS). n-A-HGNS layer has a low effect of the magnetic moment. n refers to the number of peripheral rings (Deng et al. (2014)). We choose $n = 3$ (3A-HGNS) layer with enough size for us. In addition, we hydrogenated the edges of the 3A-HGNS layer. In this layer, the total number of carbon atoms is 42 and the total number of hydrogen atoms is 18. We use the transition metal atoms as Fe, Ni and Pt, which are located different distances and positions on the 3A-HGNS layer. Figure 2.7, 2.8 and 2.9 show the structure of Pt/3A-HGNS ($C_{42}H_{18}Pt$), Fe/3A-HGNS ($C_{42}H_{18}Fe$) and Ni/3A-HGNS ($C_{42}H_{18}Ni$), respectively and they have 61
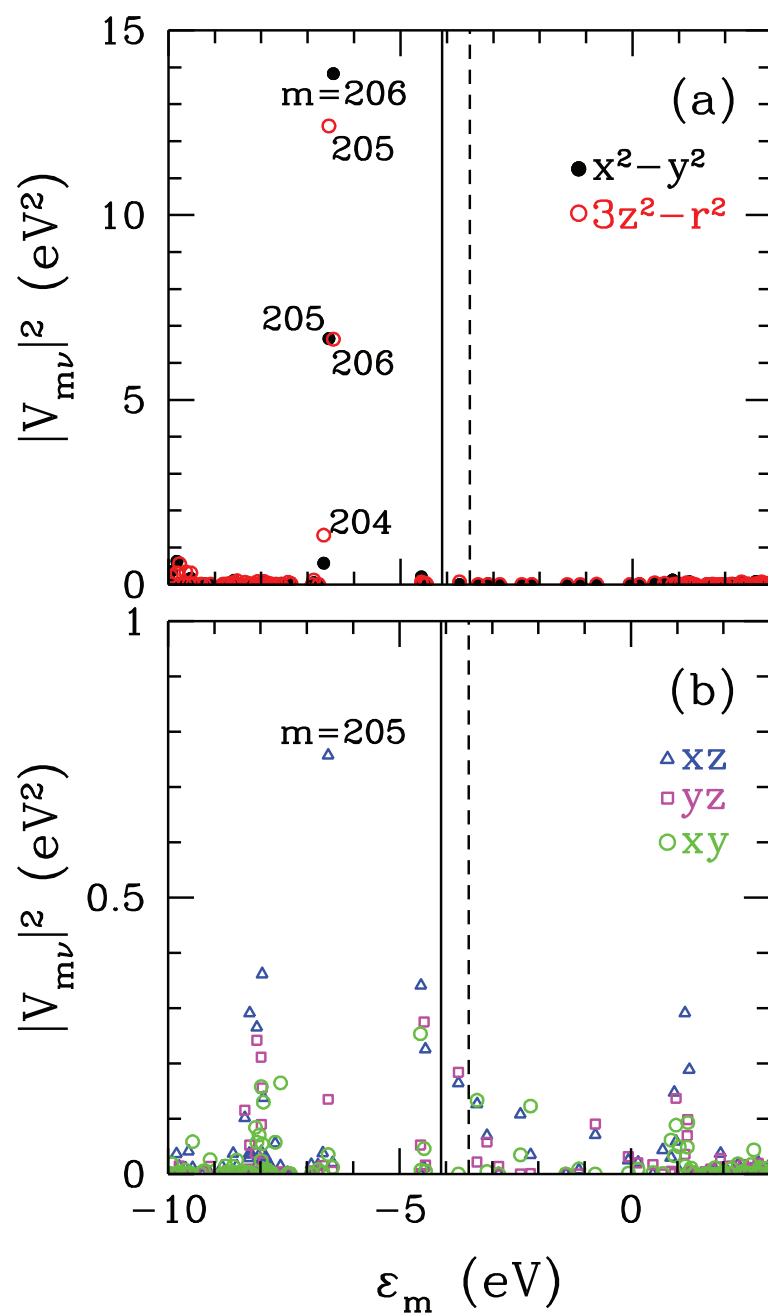
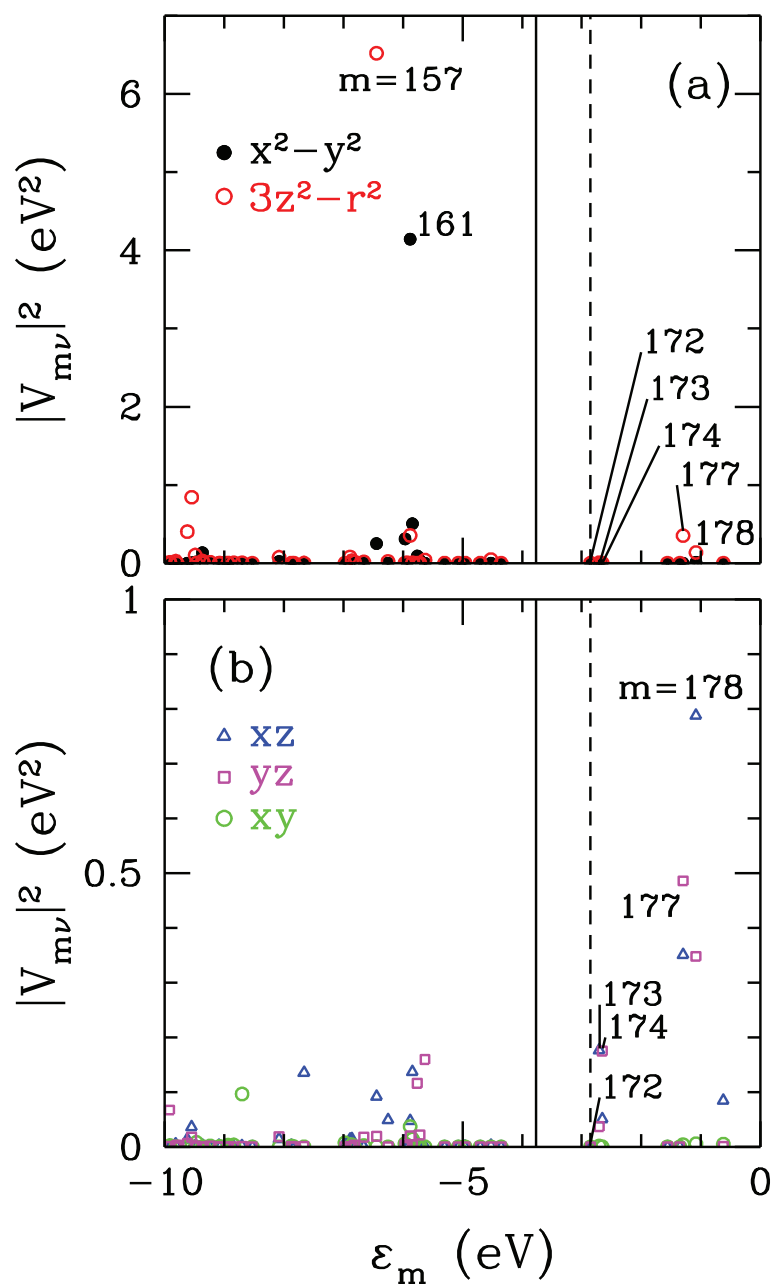Figure 8.24. For Z907 dye, DFT(BP86) results on the square of hybridization matrix elements $|V_{m\nu}|^2$ between the m'th host eigenstates and Ru($4d_\nu$) natural atomic orbitals as a function of the m'th host eigenvalues ε_m. In (a) results are shown for $4d_{x^2-y^2}$ and $4d_{3z^2-r^2}$ orbitals, and in (b) for $4d_{xz}$, $4d_{yz}$ and $4d_{xy}$ orbitals. Here, the vertical solid and dashed lines denote the values of the HOMO and LUMO, respectively. We observe that the host states $m = 205$th and 206th have the highest hybridization matrix elements for $4d_{x^2-y^2}$ and $4d_{3z^2-r^2}$ orbitals.
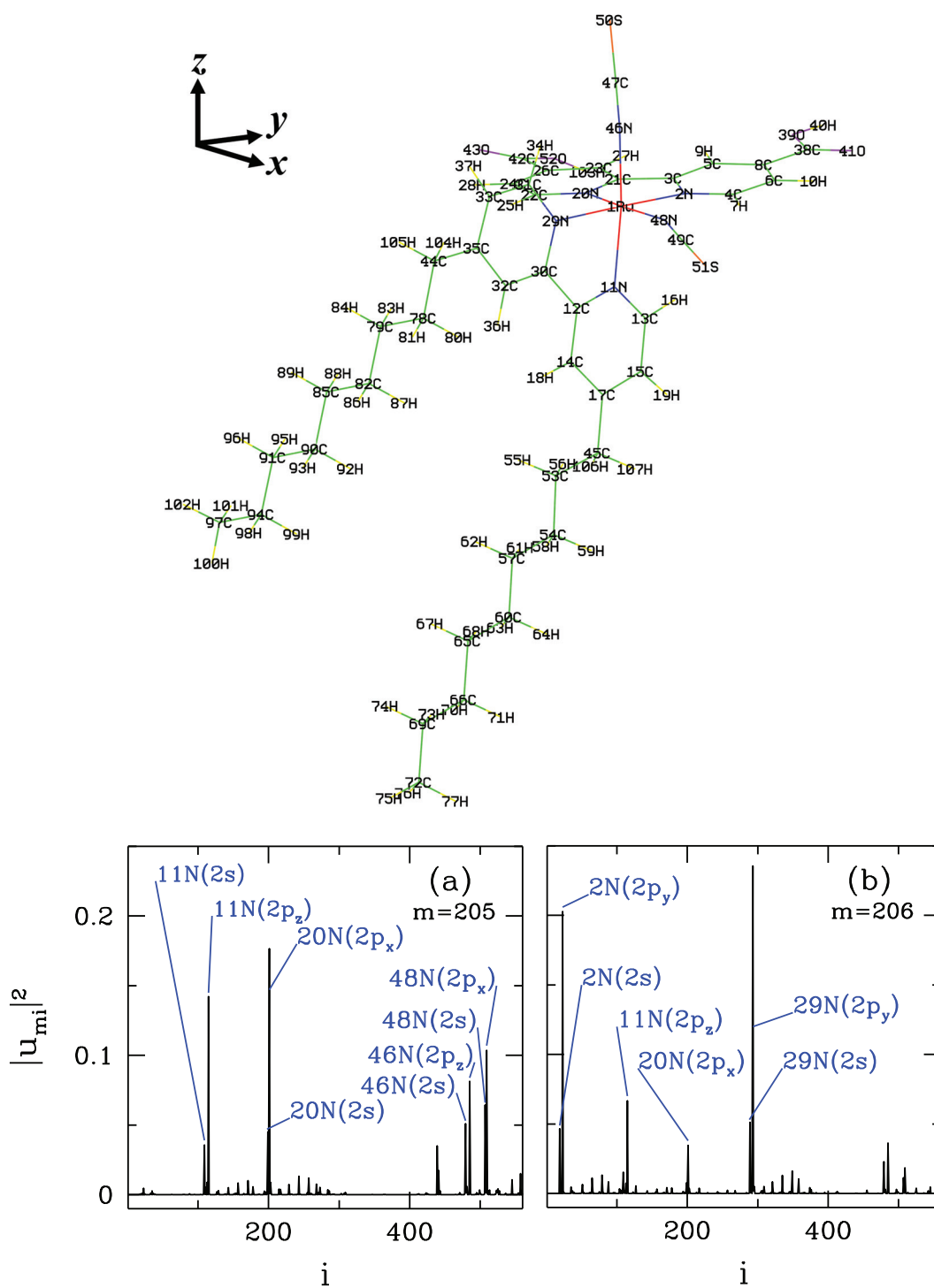
Figure 8.25. For Z907 dye, schematic plot with label numbers and symbols of atoms. The DFT results on the square of the host eigenstate ($|u_{mi}|^2$) contributions versus the label i for (a) $m = 205$th and (b) 206th host states.

atoms. As seen in Fig. 2.8 and 2.9, Fe and Ni atoms are located at the hollow site. On the other hand, Figure 2.7 shows that the Pt atom is located at the bridge site. We choose these locations for the transition metal atoms because transition metal/graphene systems have the minimum energy at these sites. The structures of Pt/3A-HGNS, Fe/3A-HGNS and Ni/3A-HGNS have 348, 296 and 298 electrons, respectively. The number of basis functions is 436 for each structures.

8.6.1. Pt/3A-HGNS

For Pt/3A-HGNS (or Pt/graphene), we perform the DFT calculation by using B3LYP hybrid functional and the LanL2DZ basis set for Pt atom and 6-31G basis set for C and H in a singlet-spin state. Figure 8.26 (a) shows the total density of states $D(\varepsilon) = \sum_{n=1}^{N} \delta(\varepsilon - E_n)$ for Pt/3A-HGNS. E_n is the eigenvalues of Kohn-Sham matrix. The HOMO and LUMO values are located at -4.94 eV and -2.55 eV, respectively. In Fig. 8.26 (b), the host density of states $D_h(\varepsilon) = \sum_{m=1}^{N-5} \delta(\varepsilon - \varepsilon_m)$ is shown without Pt($5d_\nu$) orbitals. The Pt($5d_\nu$) levels have been shifted by the double counting term (Mayda et al. (2017)). The double counting term μ_ν^{DC} includes U, $U'(= U - 2J)$ and $U' - J$ interactions. This term is calculated for Coulomb interaction $U = 4$ eV and Hund's coupling term $J = 0.9$ eV. The new energies $\tilde{\varepsilon}_{d\nu}$ of Pt($5d_\nu$) orbitals are obtained that the bare Pt($5d_\nu$) energy levels $\varepsilon_{d\nu}$ are subtracted from double counting term μ_ν^{DC}. In Fig. 8.26 (b), they are located between -23 eV and -22 eV. The sort of new energies of Pt($5d_\nu$) orbitals is $5d_{yz}$, $5d_{xz}$, $5d_{xy}$, $5d_{3z^2-r^2}$ and $5d_{x^2-y^2}$ after shifting.

In Fig. 8.27, the square of the hybridization matrix elements $|V_{m\nu}|^2$ between the m'th host eigenstates and Pt($5d_\nu$) NAO's as a function of the m'th host eigenvalues ε_m for Pt/3A-HGNS. We observed that the host states $m = 140$th and 141st have the highest hybridization matrix elements for $5d_{3z^2-r^2}$ and $5d_{yz}$ orbitals. In Fig. 8.27 (a), $5d_{3z^2-r^2}$ orbital has the noticeable hybridization contribution at $m = 124$th, 142nd and 156th host states. Hybridization contributions of $5d_{yz}$ orbital is small for $m = 155$th host state as shown in Fig. 8.27 (b).

Figure 8.28 shows the NAO's(Glendening et al. (2013)) composition of the m'th host eigenstate for deoxy-heme. The Ref.(Kandemir et al. (2016); Kandemir (2013)) was explained more detail for NAO weight of the $|u_{mi}|^2$. The Pt atom is attached to the 2nd and 3rd carbon (C) atoms in the first part of Fig. 8.28. In Fig. 8.28 (a), NAO weight of Pt6s orbital is the largest value and NAO weights of the 2nd, 3rd, 4th and 5th C sites is small for $m = 140$th host state. In Fig. 8.28 (b), NAO weights of $2p_z$ orbitals of the 2nd,
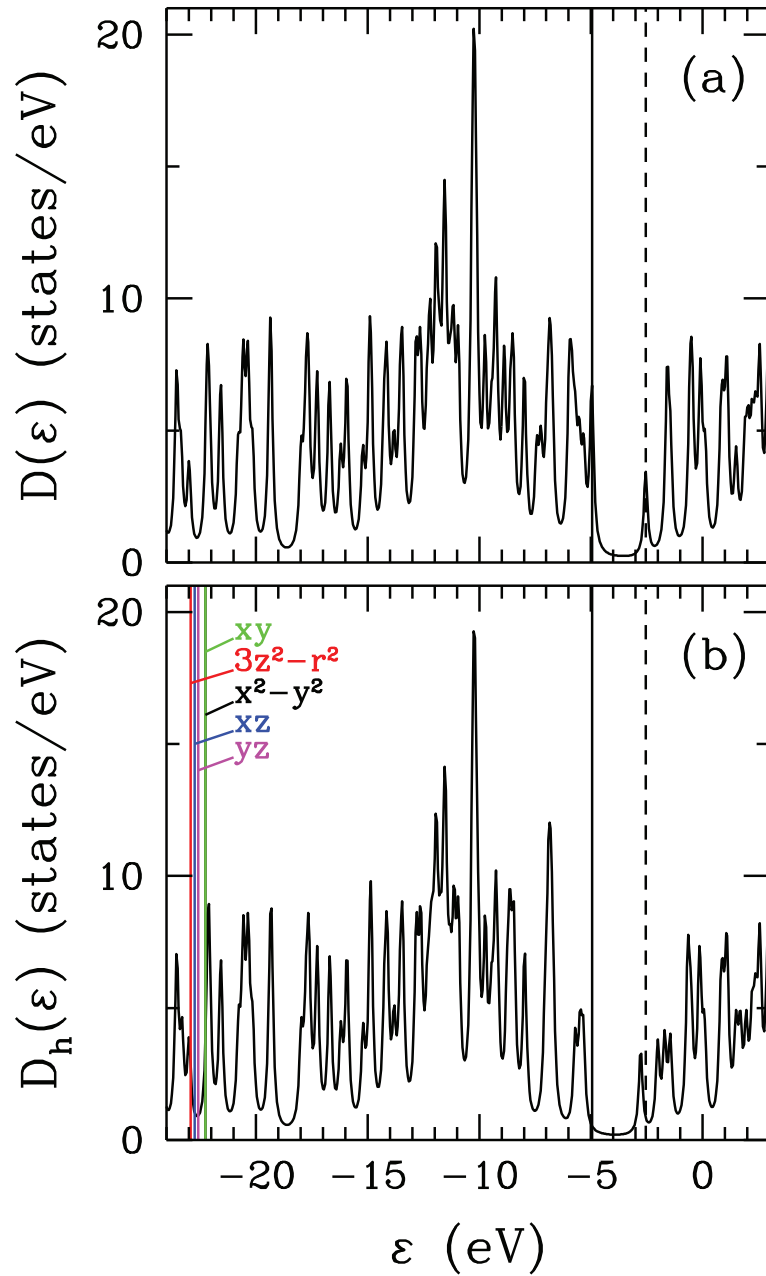
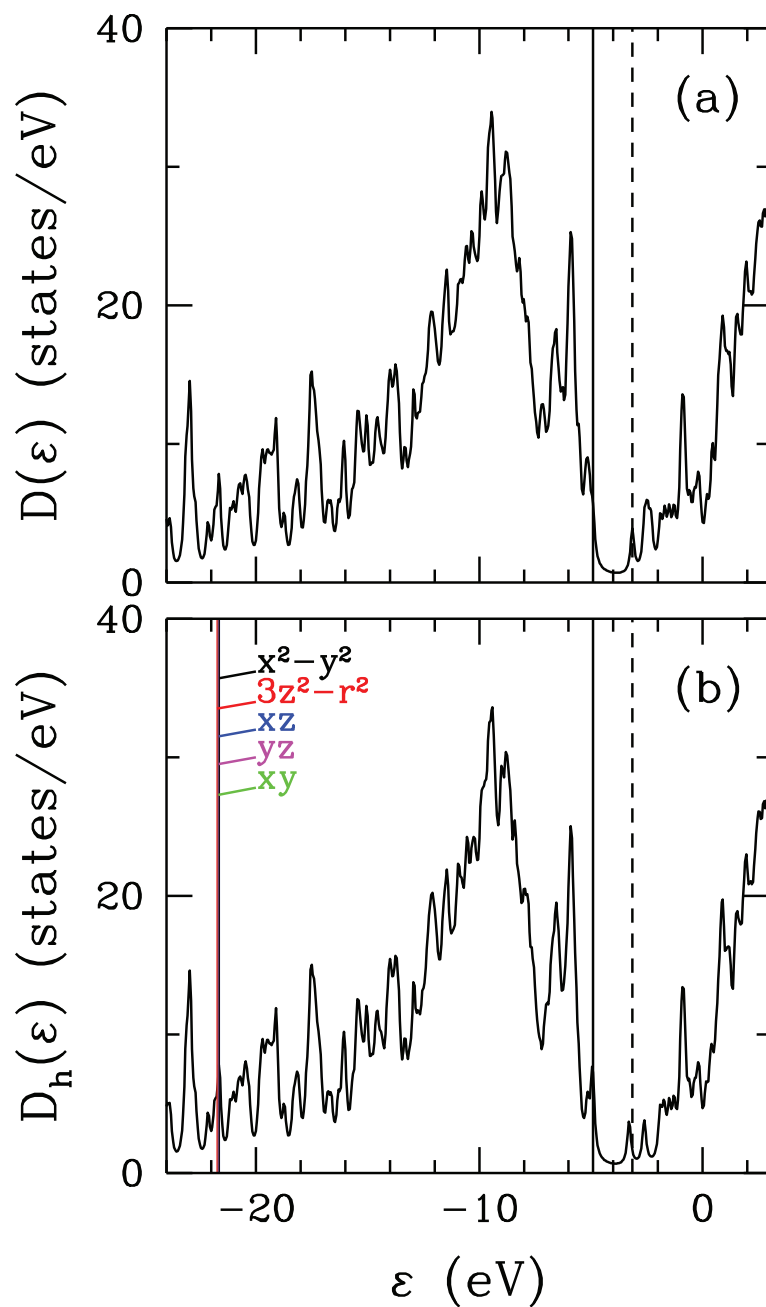Figure 8.26. (a) For Pt/3A-HGNS, total density of states $D(\varepsilon)$ versus energy ε, obtained DFT(BP86) by using the Gaussian program. (b) For Pt/3A-HGNS, density of states of the host states $D_h(\varepsilon)$ of the extended Haldane-Anderson model. The Pt($5d_\nu$) levels have been shifted by the double counting term. This term is calculated for $U = 4$ eV and $J = 0.9$ eV. Here, the vertical solid and dashed lines denote the HOMO and LUMO levels, respectively.

Figure 8.27. For Pt/3A-HGNS, DFT(BP86) results on the square of hybridization matrix elements $|V_{m\nu}|^2$ between the m'th host eigenstates and Pt($5d_\nu$) natural atomic orbitals as a function of the m'th host eigenvalues ε_m. In (a) results are shown for $5d_{x^2-y^2}$ and $5d_{3z^2-r^2}$ orbitals, and in (b) for $5d_{xz}$, $5d_{yz}$ and $5d_{xy}$ orbitals. Here, the vertical solid and dashed lines denote the values of the HOMO and LUMO, respectively. We observe that the host states $m = 140$th and 141st have the highest hybridization matrix elements.

(a)

For m = 140th		$\varepsilon_m = -2.77$ eV
i	host orbitals	$\|u_{mi}\|^2$
2	Pt 1(6s)	0.824
25	C 2(2pz)	0.015
34	C 3(2pz)	0.015
43	C 4(2pz)	0.015
52	C 5(2pz)	0.015

(b)

For m = 141st		$\varepsilon_m = -2.01$ eV
i	host orbitals	$\|u_{mi}\|^2$
25	C 2(2pz)	0.119
34	C 3(2pz)	0.119
61	C 6(2pz)	0.071
70	C 7(2pz)	0.071
160	C17(2pz)	0.030
178	C19(2pz)	0.030
205	C22(2pz)	0.037
214	C23(2pz)	0.037
241	C26(2pz)	0.035

Figure 8.28. For Pt/3A-HGNS, schematic plot with label numbers and symbols of atoms. The DFT results on the square of the host eigenstate ($|u_{mi}|^2$) contributions versus the label i for (a) $m = 140$th and (b) 141st host states.

3rd, 6th and 7th C sites are the largest value and other C sites are small for $m = 141$st host state. $m = 140$th and 141st host states have the highest hybridization matrix elements for $5d_{3z^2-r^2}$ and $5d_{yz}$ orbitals.

8.6.2. Fe/3A-HGNS

For Fe/3A-HGNS (or Fe/graphene), we perform the DFT calculation by using B3LYP hybrid functional and the LanL2DZ basis set for Fe atom and 6-31G basis set for C and H in a singlet-spin state. Figure 8.29 (a) shows the total density of states $D(\varepsilon) = \sum_{n=1}^{N} \delta(\varepsilon - E_n)$ for Fe/3A-HGNS. E_n is the eigenvalues of Kohn-Sham matrix. The HOMO and LUMO values are located at -3.93 eV and -1.59 eV, respectively. In Fig. 8.29 (b), the host density of states $D_h(\varepsilon) = \sum_{m=1}^{N-5} \delta(\varepsilon - \varepsilon_m)$ is shown without Fe($3d_\nu$)
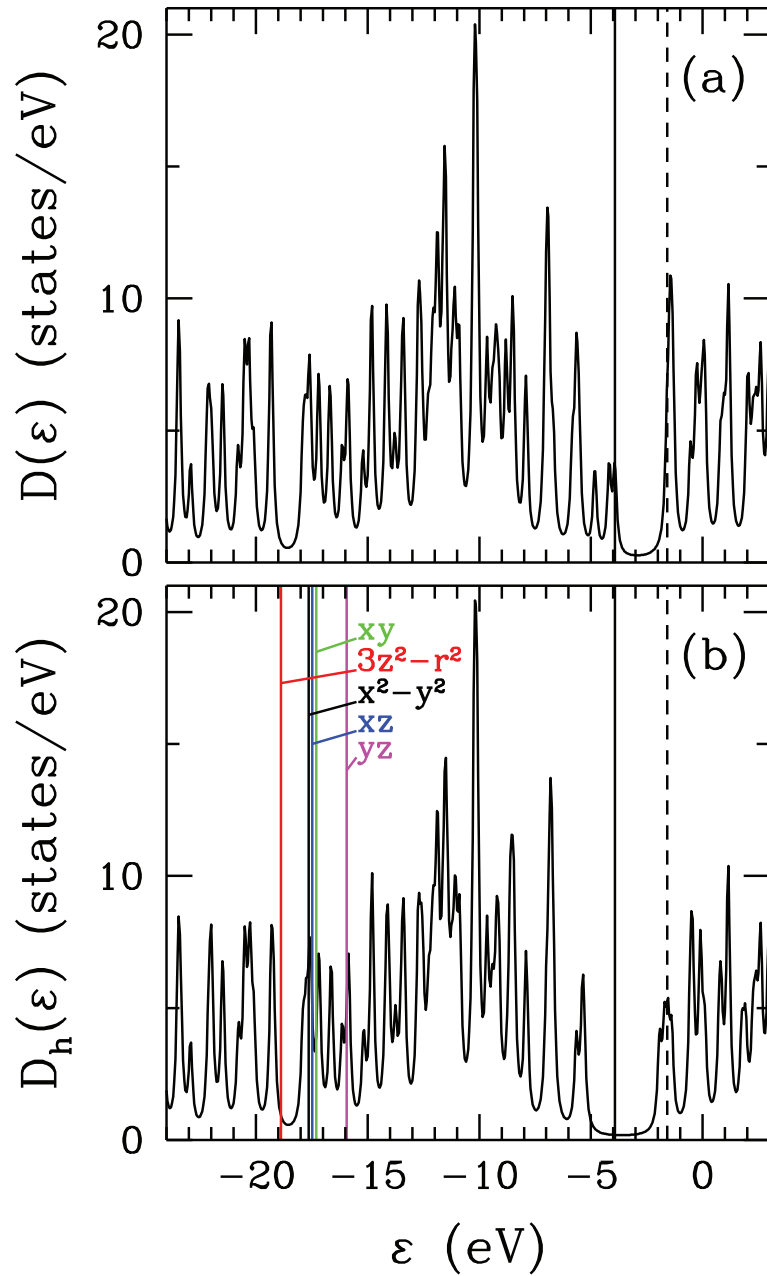
Figure 8.29. (a) For Fe/3A-HGNS, total density of states $D(\varepsilon)$ versus energy ε, obtained DFT(BP86) by using the Gaussian program. (b) For Fe/3A-HGNS, density of states of the host states $D_h(\varepsilon)$ of the extended Haldane-Anderson model. The Fe($3d_\nu$) levels have been shifted by the double counting term. This term is calculated for $U = 4$ eV and $J = 0.9$ eV. Here, the vertical solid and dashed lines denote the HOMO and LUMO levels, respectively.

orbitals. The Fe($3d_\nu$) levels have been shifted by the double counting term (Mayda et al. (2017)). The double counting term μ_ν^{DC} includes U, $U'(=U-2J)$ and $U'-J$ interactions. This term is calculated for Coulomb interaction $U = 4$ eV and Hund's coupling term $J = 0.9$ eV. The new energies $\tilde{\varepsilon}_{d\nu}$ of Fe($3d_\nu$) orbitals are obtained that the bare Fe($3d_\nu$) energy levels $\varepsilon_{d\nu}$ are subtracted from double counting term μ_ν^{DC}. In Fig. 8.29 (b), they are located between -20 eV and -15 eV. The sort of new energies of Fe($3d_\nu$) orbitals is $3d_{3z^2-r^2}$, $3d_{x^2-y^2}$, $3d_{xz}$, $3d_{xy}$ and $3d_{yz}$ after shifting.

In Fig. 8.30, the square of the hybridization matrix elements $|V_{m\nu}|^2$ between the m'th host eigenstates and Fe($3d_\nu$) natural atomic orbitals as a function of the m'th host eigenvalues ε_m for Fe/3A-HGNS. We observed that the host states $m = 140$th and 141st have the highest hybridization matrix elements for $3d_{x^2-y^2}$ and $3d_{xy}$ orbitals. In Fig. 8.30 (a), $3d_{x^2-y^2}$ orbital has the noticeable hybridization contribution at $m = 140$th and 156th host states. Hybridization contributions of $3d_{yz}$ and $3d_{xy}$ orbitals are noticeable at $m = 125$th, 139th and 155th host states as shown in Fig. 8.30 (b).

Figure 8.31 shows the NAO (Glendening et al. (2013)) composition of the m'th host eigenstate for deoxy-heme. The Ref.(Kandemir et al. (2016); Kandemir (2013)) was explained more detail for NAO weight of the $|u_{mi}|^2$. The Fe atom is attached to the 2nd, 3rd, 4th, 5th, 6th and 7th carbon (C) atoms in the first part of Fig. 8.31. In Fig. 8.31 (a), NAO weight of Fe4s orbital is the largest value and NAO weights of the 2nd and 6th C2p_z sites is small for $m = 140$th host state. In Fig. 8.31 (b), NAO weights of $2p_z$ orbitals of the 3rd, 4th, 5th and 7th C sites are the largest value and other C sites are small for $m = 141$st host state. $m = 140$th and 141st host states have the highest hybridization matrix elements for $3d_{x^2-y^2}$ and $3d_{xy}$ orbitals.

8.6.3. Ni/3A-HGNS

For Ni/3A-HGNS (or Ni/graphene), we perform the DFT calculation by using B3LYP hybrid functional and the LanL2DZ basis set for Ni atom and 6-31G basis set for C and H in a singlet-spin state. Figure 8.32 (a) shows the total density of states $D(\varepsilon) = \sum_{n=1}^{N} \delta(\varepsilon - E_n)$ for Ni/3A-HGNS. E_n is the eigenvalues of Kohn-Sham matrix. The HOMO and LUMO values are located at -4.2 eV and -1.56 eV, respectively. In Fig. 8.32 (b), the host density of states $D_h(\varepsilon) = \sum_{m=1}^{N-5} \delta(\varepsilon - \varepsilon_m)$ is shown without Ni($3d_\nu$) orbitals. The Ni($3d_\nu$) levels have been shifted by the double counting term (Mayda et al. (2017)). The double counting term μ_ν^{DC} includes U, $U'(=U-2J)$ and $U'-J$ interactions. This term is calculated for Coulomb interaction $U = 4$ eV and Hund's coupling term
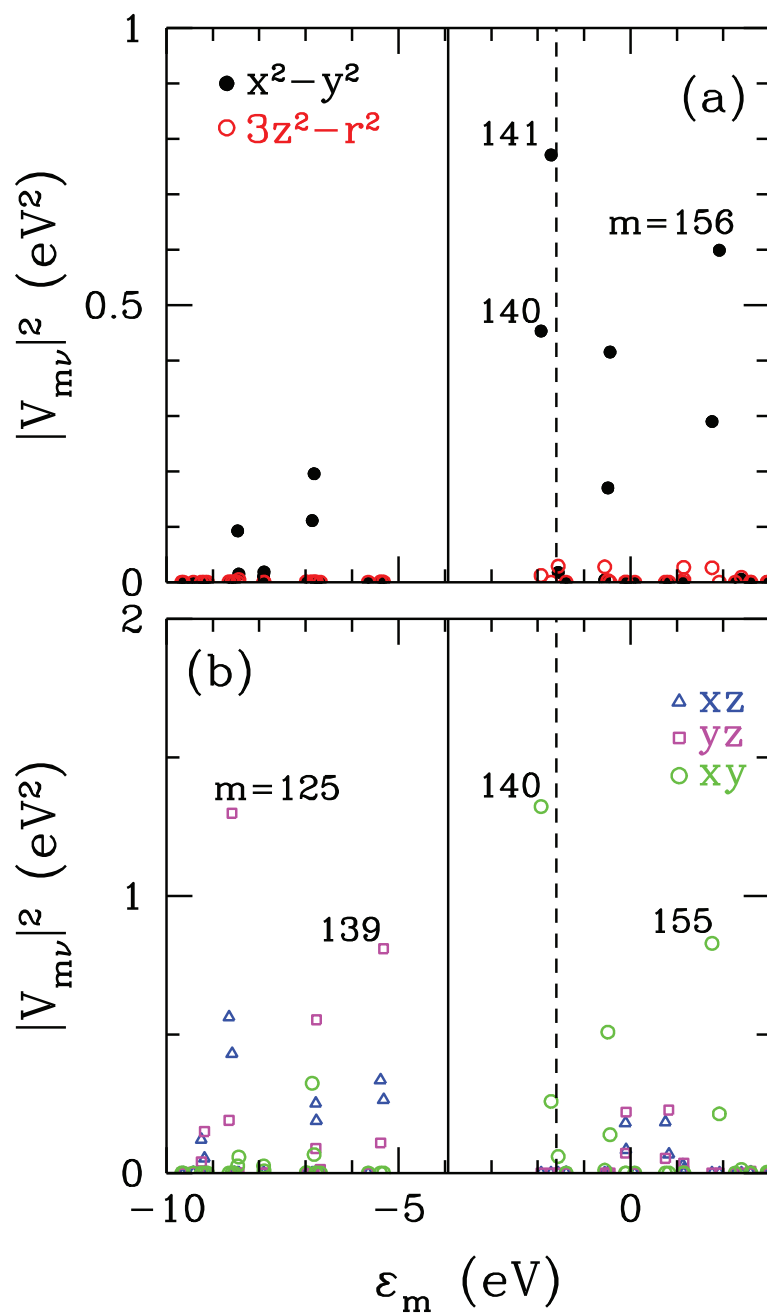
Figure 8.30. For Fe/3A-HGNS, DFT(BP86) results on the square of hybridization matrix elements $|V_{m\nu}|^2$ between the m'th host eigenstates and Fe($3d_\nu$) natural atomic orbitals as a function of the m'th host eigenvalues ε_m. In (a) results are shown for $3d_{x^2-y^2}$ and $3d_{3z^2-r^2}$ orbitals, and in (b) for $3d_{xz}$, $3d_{yz}$ and $3d_{xy}$ orbitals. Here, the vertical solid and dashed lines denote the values of the HOMO and LUMO, respectively. We observe that the host states $m = 140$th and 141st have the highest hybridization matrix elements.
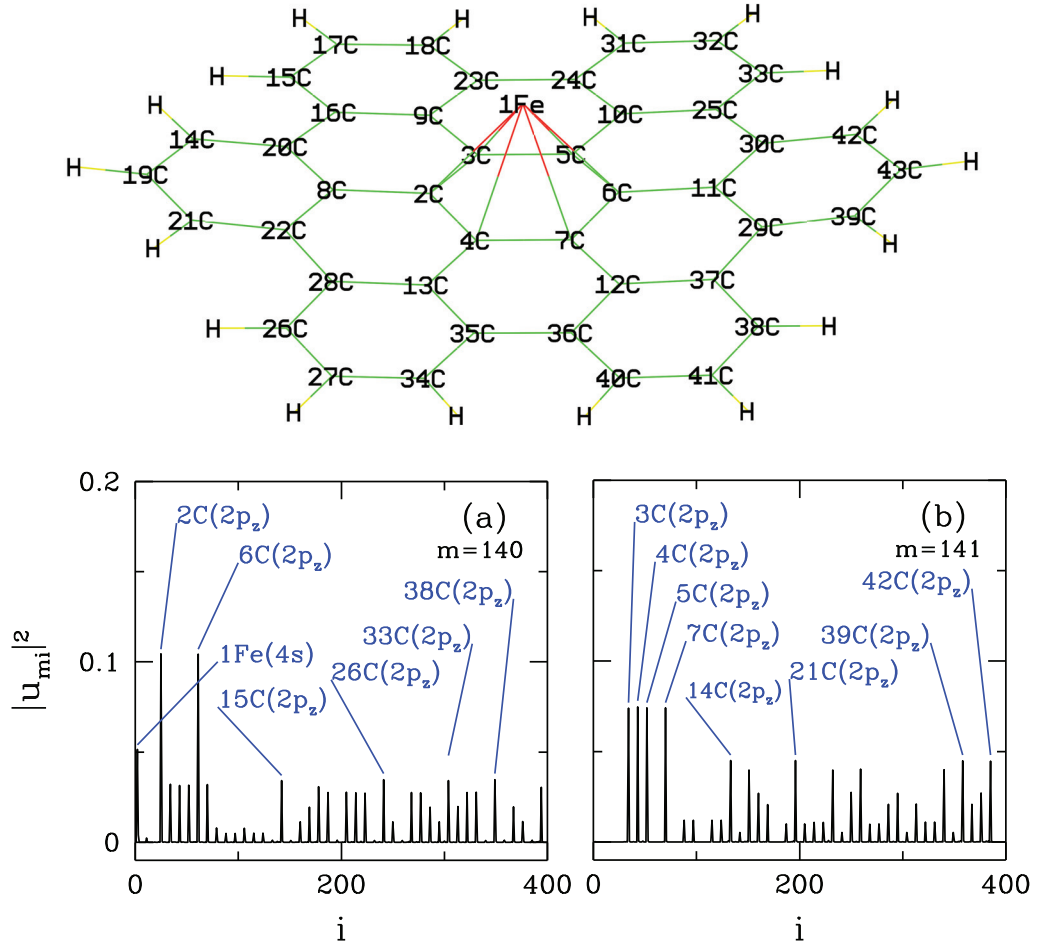
Figure 8.31. For Fe/3A-HGNS, schematic plot with label numbers and symbols of atoms. The DFT results on the square of the host eigenstate ($|u_{mi}|^2$) contributions versus the label i for (a) $m = 140$th and (b) 141st host states.

$J = 0.9$ eV. The new energies $\tilde{\varepsilon}_{d\nu}$ of Ni($3d_\nu$) orbitals are obtained that the bare Ni($3d_\nu$) energy levels $\varepsilon_{d\nu}$ are subtracted from double counting term μ_ν^{DC}. In Fig. 8.32 (b), they are located between -22 eV and -21 eV. The sort of new energies of Ni($3d_\nu$) orbitals is $3d_{3z^2-r^2}$, $3d_{x^2-y^2}$, $3d_{xz}$, $3d_{xy}$ and $3d_{yz}$ after shifting.

In Fig. 8.33, the square of the hybridization matrix elements $|V_{m\nu}|^2$ between the m'th host eigenstates and Ni($3d_\nu$) natural atomic orbitals as a function of the m'th host eigenvalues ε_m for Ni/3A-HGNS. We observed that the host states $m = 140$th and 141st have the highest hybridization matrix elements for $3d_{x^2-y^2}$ and $3d_{xy}$ orbitals. In Fig. 8.33 (a), $3d_{x^2-y^2}$ orbital has the noticeable hybridization contribution at $m = 140$th and 156th host states. Hybridization contribution of $3d_{xy}$ orbital is noticeable at $m = 141$st and 155th host states as shown in Fig. 8.33 (b).
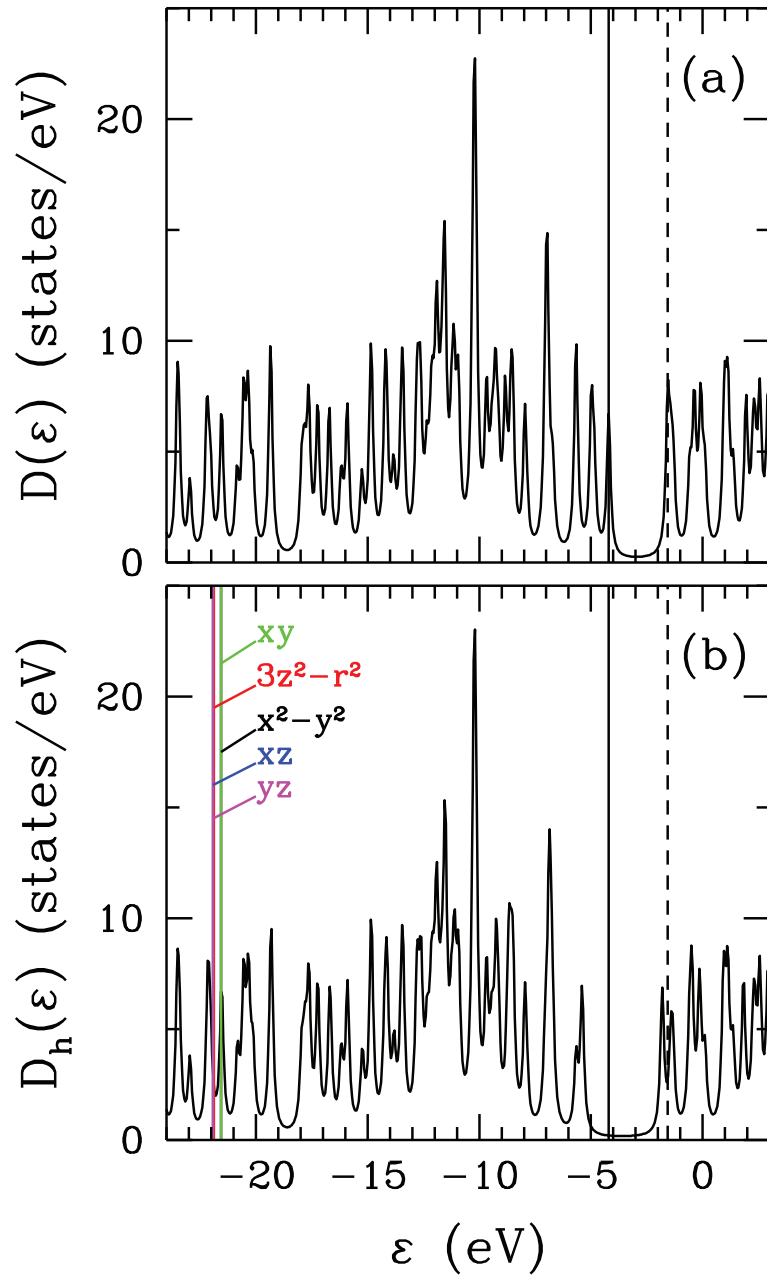
Figure 8.32. (a) For Ni/3A-HGNS, total density of states $D(\varepsilon)$ versus energy ε, obtained DFT(BP86) by using the Gaussian program. (b) For Ni/3A-HGNS, density of states of the host states $D_h(\varepsilon)$ of the extended Haldane-Anderson model. The Ni($3d_\nu$) levels have been shifted by the double counting term. This term is calculated for $U = 4$ eV and $J = 0.9$ eV. Here, the vertical solid and dashed lines denote the HOMO and LUMO levels, respectively.
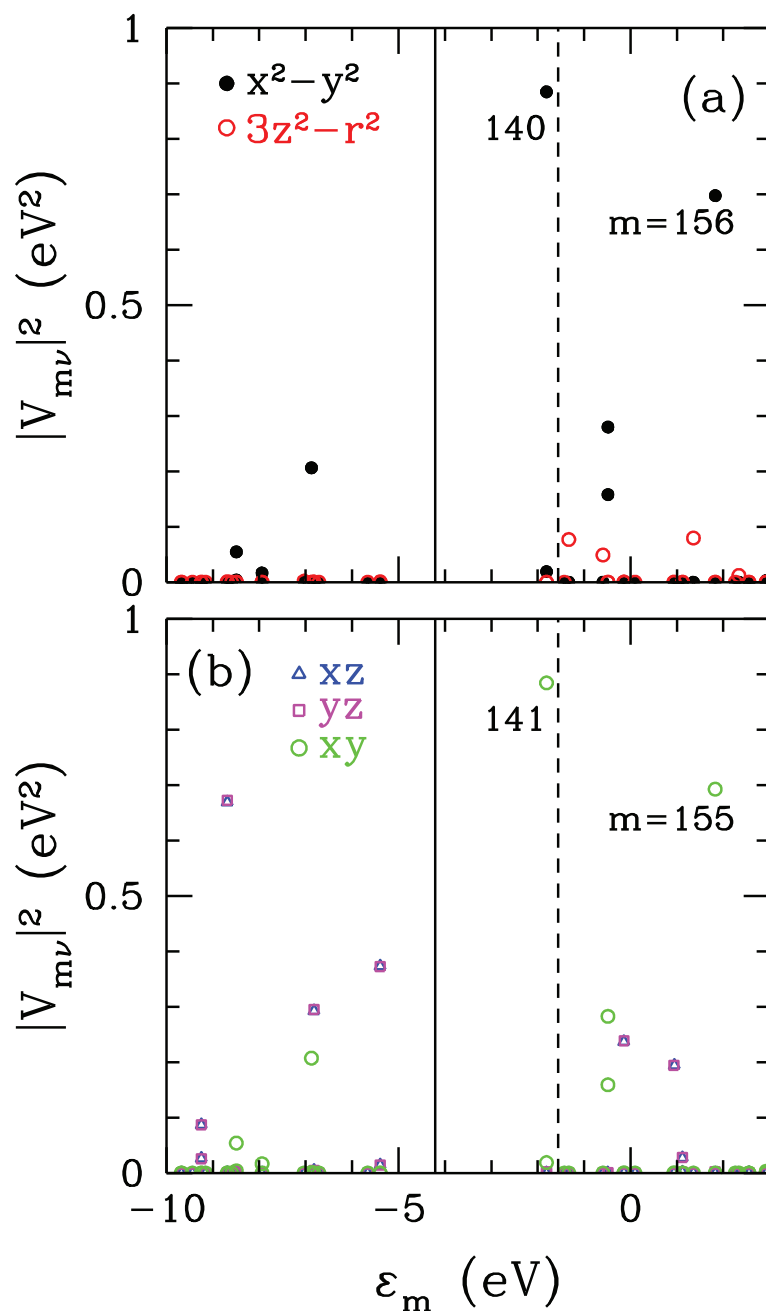
Figure 8.33. For Ni/3A-HGNS, DFT(BP86) results on the square of hybridization matrix elements $|V_{m\nu}|^2$ between the m'th host eigenstates and Ni($3d_\nu$) natural atomic orbitals as a function of the m'th host eigenvalues ε_m. In (a) results are shown for $3d_{x^2-y^2}$ and $3d_{3z^2-r^2}$ orbitals, and in (b) for $3d_{xz}$, $3d_{yz}$ and $3d_{xy}$ orbitals. Here, the vertical solid and dashed lines denote the values of the HOMO and LUMO, respectively. We observe that the host states $m = 140$th and 141st have the highest hybridization matrix elements.

(a) For m = 140th ε_m = −1.81 eV

i	host orbitals	$|u_{mi}|^2$
34	C 3(2pz)	0.103
43	C 4(2pz)	0.040
52	C 5(2pz)	0.040
70	C 7(2pz)	0.103
133	C14(2pz)	0.045
151	C16(2pz)	0.037
160	C17(2pz)	0.037
196	C21(2pz)	0.033
232	C25(2pz)	0.034
259	C28(2pz)	0.034
286	C31(2pz)	0.036
313	C34(2pz)	0.036
340	C37(2pz)	0.036
358	C39(2pz)	0.044
376	C41(2pz)	0.036

(b) For m = 141st ε_m = −1.80 eV

i	host orbitals	$|u_{mi}|^2$
25	C 2(2pz)	0.090
43	C 4(2pz)	0.065
52	C 5(2pz)	0.065
61	C 6(2pz)	0.091
142	C15(2pz)	0.045
169	C18(2pz)	0.041
178	C19(2pz)	0.031
187	C20(2pz)	0.040
223	C24(2pz)	0.039
268	C29(2pz)	0.041
277	C30(2pz)	0.018
322	C35(2pz)	0.040
349	C38(2pz)	0.047
367	C40(2pz)	0.042
394	C43(2pz)	0.032

Figure 8.34. For Ni/3A-HGNS, schematic plot with label numbers and symbols of atoms. The DFT results on the square of the host eigenstate ($|u_{mi}|^2$) contributions versus the label i for (a) $m = 140$th and (b) 141st host states.

Figure 8.34 shows the NAO (Glendening et al. (2013)) composition of the m'th host eigenstate for Ni/3A-HGNS. The Ref.(Kandemir et al. (2016); Kandemir (2013)) was explained more detail for NAO weight of the $|u_{mi}|^2$. The Ni atom is attached to the 2nd, 3rd, 4th, 5th, 6th and 7th carbon (C) atoms in the first part of Fig. 8.34. In Fig. 8.34 (a), NAO weights of the 3rd, 4th, 5th and 7th C $2p_z$ sites are the largest value for $m = 140$th host state. In Fig. 8.34 (b), NAO weights of $2p_z$ orbitals of the 2nd, 4th, 5th and 6th C sites are the largest value and other C sites are small for $m = 141$st host state. $m = 140$th and 141st host states have the highest hybridization matrix elements for $3d_{x^2-y^2}$ and $3d_{xy}$ orbitals.
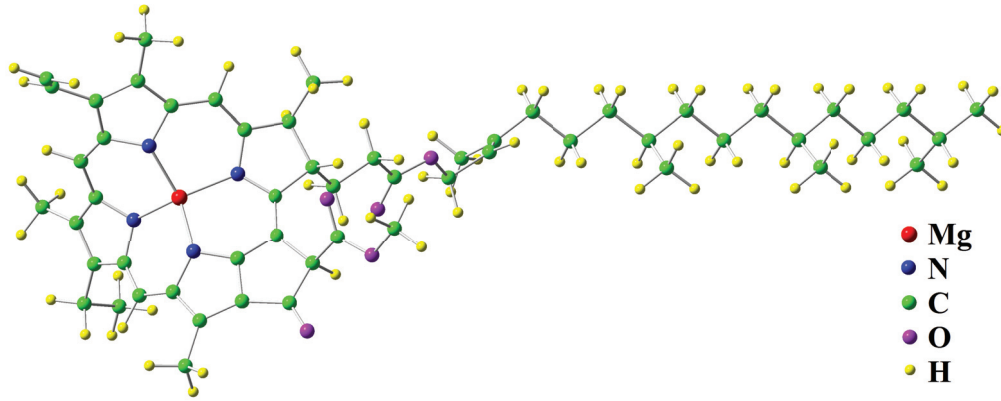
Figure 8.35. Molecular structures of chlorophyll-a (chl-a) molecule. Chl-a contains 137 atoms The chemical formula of chl-a is $C_{55}H_{72}MgN_4O_5$.

8.7.   DFT results for Chlorophyll-a

Chlorophyll-a (chl-a) molecule is found in all green plants. It plays a direct role in converting light energy into chemical energy. Therefore, it is the most important pigment for photosynthesis. Figure 8.35 shows the molecular structure of chlorophyll-a. In this molecule, magnesium atom is located at the center and binds four nitrogen atoms in the chlorin layer. Chl-a molecule contains 137 atoms and it has 482 electrons. The chemical formula of chl-a molecule is $C_{55}H_{72}MgN_4O_5$. The atomic coordinates of chlorophyll-a molecule are taken from PDB:CLA. Figure 8.36 (a) shows porphyrin plane where the iron atom is located and Fig. 8.36 (b) shows chlorophyll-a plane where the magnesium atom is located. The chlorin layer of chlorophyll-a is very similar to porphyrin layer of heme molecules.

For chlorophyll-a (chl-a) molecule, we perform the DFT calculation by using BP86 exchange-correlation energy functional and 6-31G(d) basis set for singlet state. Figure 8.37 (a) shows the total density of states $D(\varepsilon) = \sum_{n=1}^{N} \delta(\varepsilon - E_n)$ for chlorophyll-a. E_n is the eigenvalues of Kohn-Sham matrix. The HOMO and LUMO values are located at -4.24 eV and -3.10 eV, respectively. In Fig. 8.37 (b), the host density of states $D_h(\varepsilon) = \sum_{m=1}^{N-5} \delta(\varepsilon - \varepsilon_m)$ is shown without $Mg(3d_\nu)$ orbitals. The $Mg(3d_\nu)$ levels have been shifted by the double counting term (Mayda et al. (2017)). The double counting term μ_ν^{DC} includes U, $U'(= U - 2J)$ and $U' - J$ interactions. This term is calculated for Coulomb interaction $U = 4$ eV and Hund's coupling term $J = 0.9$ eV. The new energies $\tilde{\varepsilon}_{d\nu}$ of $Mg(3d_\nu)$ orbitals are obtained that the bare $Mg(3d_\nu)$ energy levels $\varepsilon_{d\nu}$ are
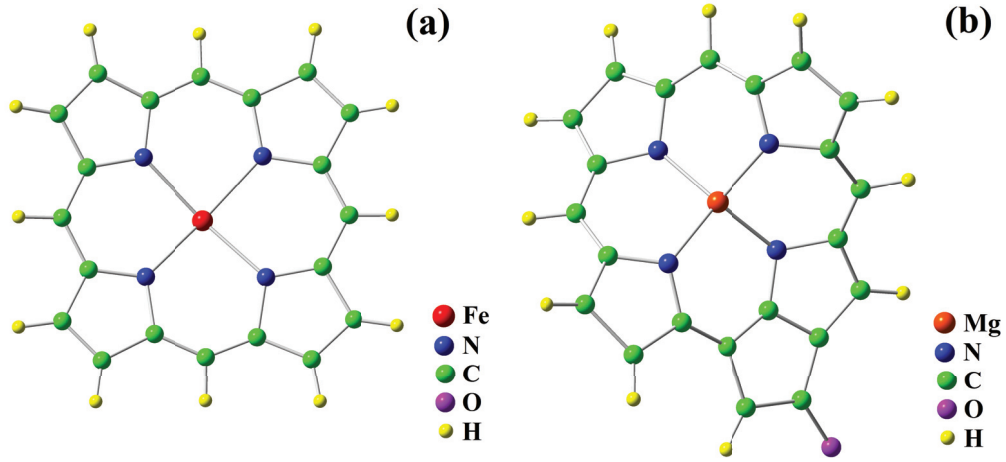
Figure 8.36. (a) Molecular structure of the porphyrin layer of heme molecules. It is located an iron (Fe) atom in the center of the porphyrin layer. (b) Molecular structures of chlorin layer of chlorophyll-a. It is located a magnesium (Mg) atom in the center of the chlorin layer. These molecules are very similar.

subtracted from double counting term μ_ν^{DC}. In Fig. 8.37 (b), they are located between 18 eV and 24 eV. The sort of new energies of Mg($3d_\nu$) orbitals is $3d_{yz}$, $3d_{xy}$, $3d_{3z^2-r^2}$, $3d_{xz}$ and $3d_{x^2-y^2}$ after shifting.

In Fig. 8.38, the square of the hybridization matrix elements $|V_{m\nu}|^2$ between the m'th host eigenstates and Mg($3d_\nu$) natural atomic orbitals as a function of the m'th host eigenvalues ε_m for chl-a molecule. We observed that the host states $m = 386$th, and 396th have the highest hybridization matrix elements for $3d_{3z^2-r^2}$ and $3d_{yz}$ orbitals. In Fig. 8.38 (a), $3d_{x^2-y^2}$ orbital has the noticeable hybridization contribution at $m = 440$th and 441st host states. In Fig. 8.38 (b), $3d_{xy}$ and $3d_{xz}$ orbitals have the noticeable hybridization contribution at $m = 385$th and 644th host states, respectively.

Figure 8.39 shows the NAO (Glendening et al. (2013)) composition of the m'th host eigenstate for chl-a. The Ref.(Kandemir et al. (2016); Kandemir (2013)) was explained more detail for NAO weight of the $|u_{mi}|^2$. The Mg atom is attached to the 2nd, 3rd, 4th and 5th nitrogen atoms in the first part of Fig. 8.39. In Fig. 8.39 (a), NAO weights of the Mg($4p$)'s orbitals are the largest value for $m = 382$nd, 385th, 386th and 396th host states.
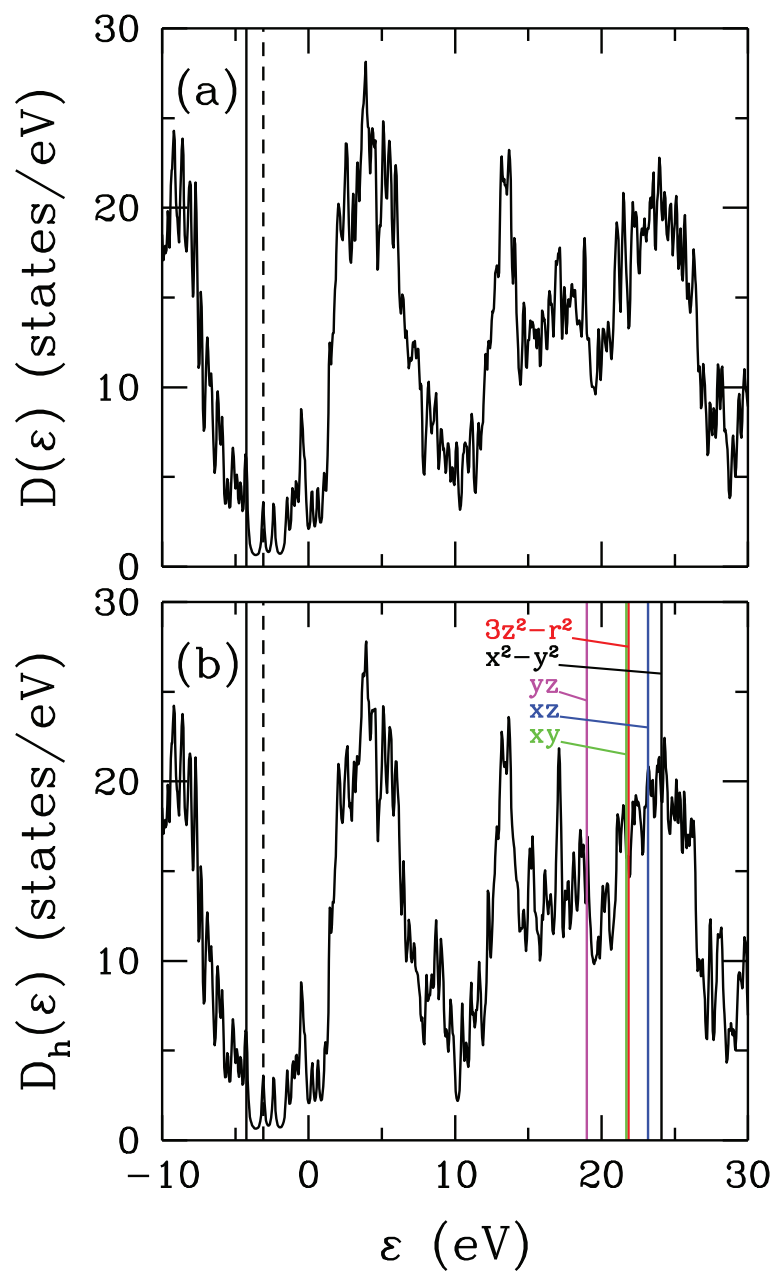
Figure 8.37. (a) For chlorophyll-a, total density of states $D(\varepsilon)$ versus energy ε, obtained DFT(BP86) by using the Gaussian program. (b) For chlorophyll-a, density of states of the host states $D_h(\varepsilon)$ of the extended Haldane-Anderson model. The Mg($3d_\nu$) levels have been shifted by the double counting term. This term is calculated for $U = 4$ eV and $J = 0.9$ eV. Here, the vertical solid and dashed lines denote the HOMO and LUMO levels, respectively.
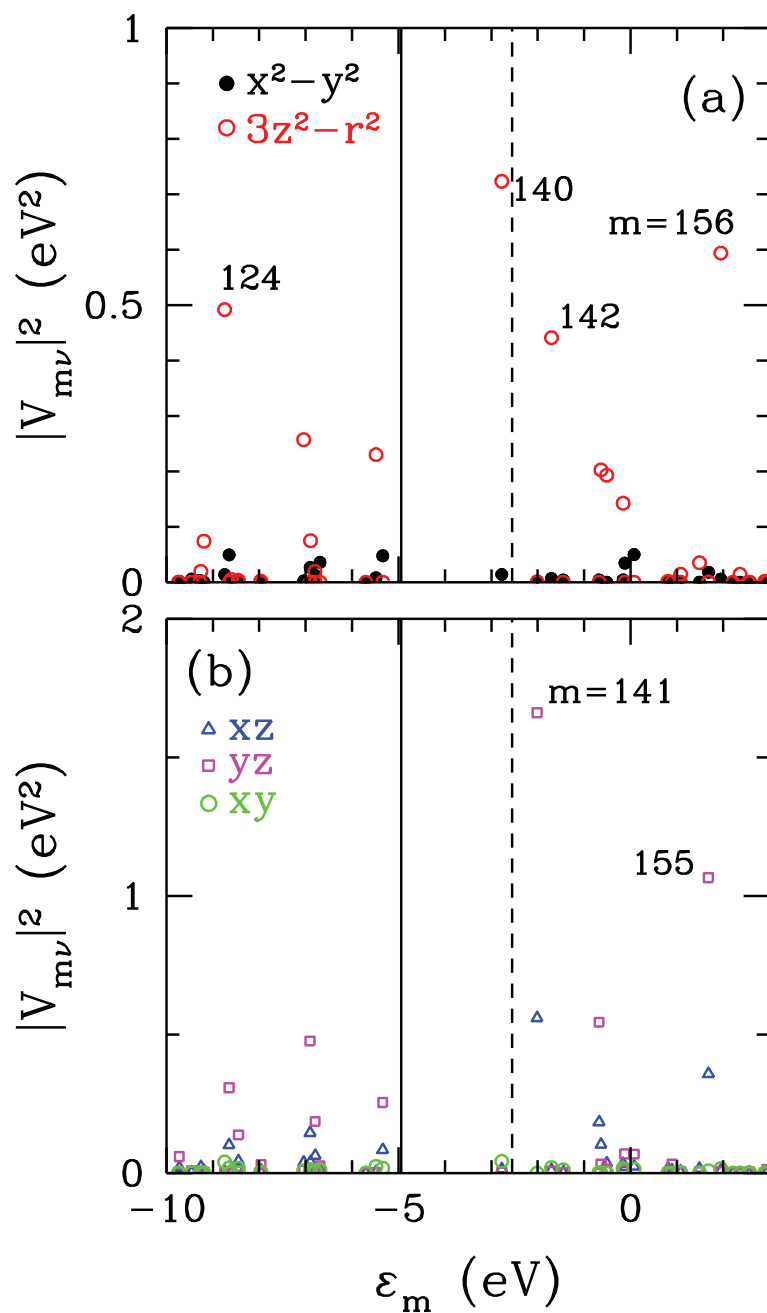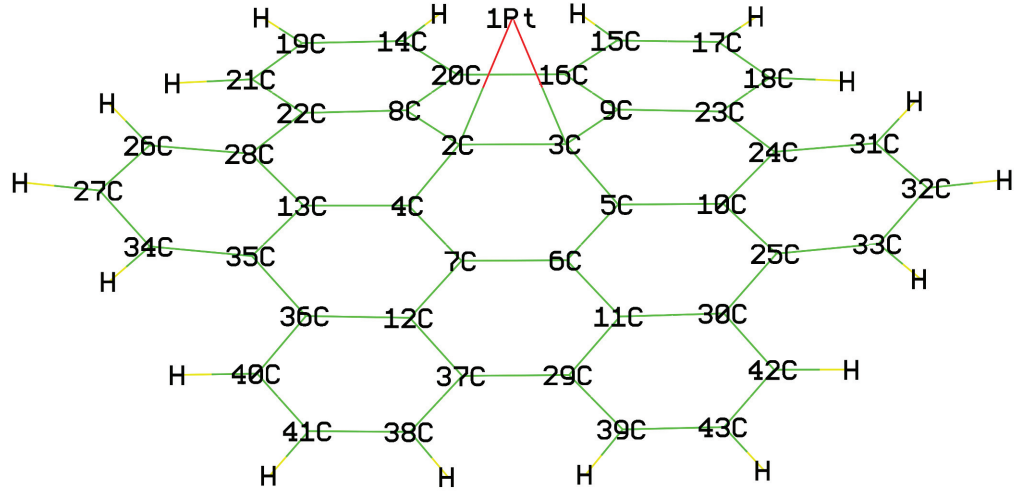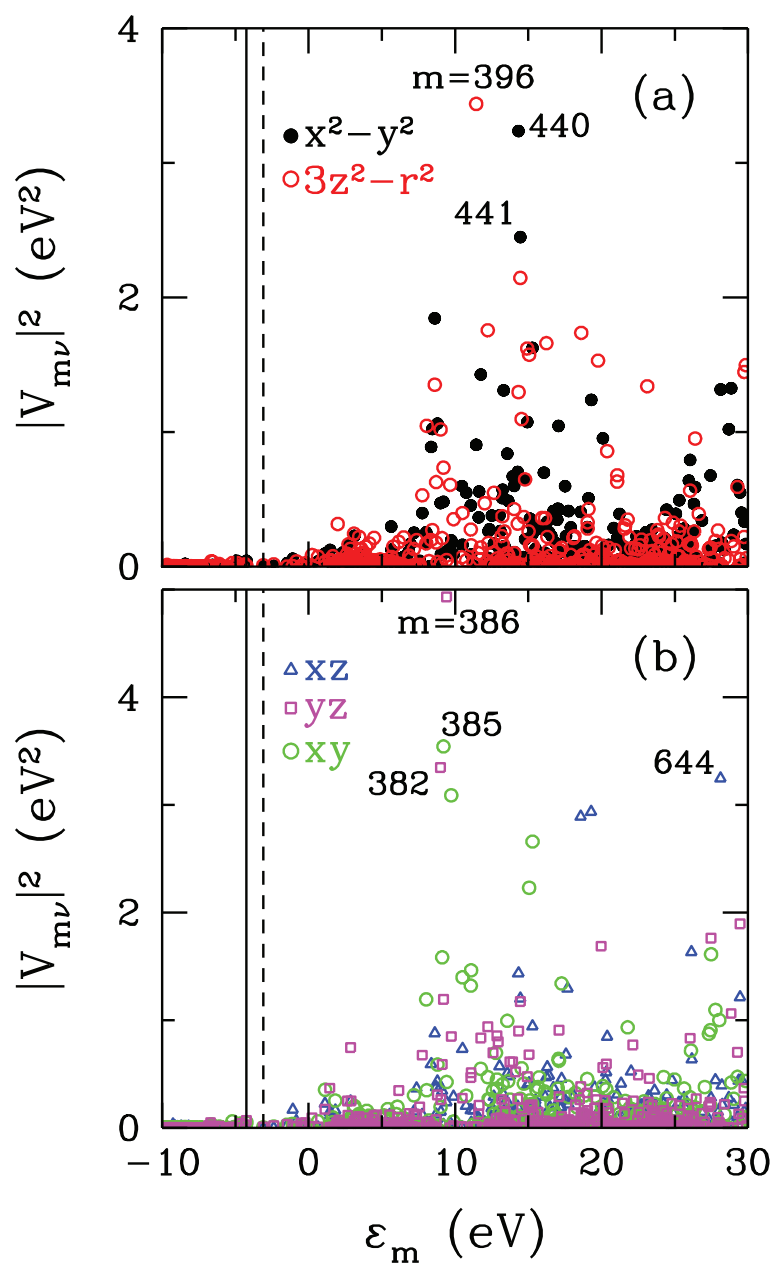
Figure 8.38. For chlorophyll-a, DFT(BP86) results on the square of hybridization matrix elements $|V_{m\nu}|^2$ between the m'th host eigenstates and Mg($3d_\nu$) natural atomic orbitals as a function of the m'th host eigenvalues ε_m. In (a) results are shown for $3d_{x^2-y^2}$ and $3d_{3z^2-r^2}$ orbitals, and in (b) for $3d_{xz}$, $3d_{yz}$ and $3d_{xy}$ orbitals. Here, the vertical solid and dashed lines denote the values of the HOMO and LUMO, respectively. We observe that the host states $m = 386$th, and 396th have the highest hybridization matrix elements for $3d_{3z^2-r^2}$ and $3d_{yz}$ orbitals.

For m = 382nd ε_m = 9.01 eV

i	host orbitals	$\|u_{mi}\|^2$
13	Mg 1(4pz)	0.035
19	N 2(2py)	0.038
22	N 2(3pz)	0.020
133	C10(2pz)	0.024
141	C11(2s)	0.039
169	C13(2s)	0.029
225	C17(2s)	0.024
365	C27(2s)	0.023
395	C29(2px)	0.022

For m = 385th ε_m = 9.21 eV

i	host orbitals	$\|u_{mi}\|^2$
7	Mg 1(4px)	0.081
13	Mg 1(4pz)	0.044
20	N 2(3py)	0.024
141	C11(2s)	0.022
183	C14(2s)	0.021
311	C23(2px)	0.026
505	C37(2s)	0.045
535	C39(2px)	0.021
561	C41(2s)	0.024

For m = 386th ε_m = 9.42 eV

i	host orbitals	$\|u_{mi}\|^2$
7	Mg 1(4px)	0.026
12	Mg 1(3pz)	0.021
13	Mg 1(4pz)	0.089
48	N 4(3py)	0.024
62	N 5(3py)	0.021
155	C12(2s)	0.051
156	C12(3s)	0.021
311	C23(2px)	0.036
353	C26(2px)	0.020

For m = 396th ε_m = 11.45 eV

i	host orbitals	$\|u_{mi}\|^2$
10	Mg 1(4py)	0.038
50	N 4(3pz)	0.024
64	N 5(3pz)	0.021
202	C15(3py)	0.025
211	C16(2s)	0.026

For m = 440th ε_m = 14.33 eV

i	host orbitals	$\|u_{mi}\|^2$
200	C15(3px)	0.021
382	C28(3px)	0.024
468	C34(3py)	0.022
484	C35(3pz)	0.031
536	C39(3pz)	0.024
538	C39(3py)	0.031
620	C45(3px)	0.075

For m = 441st ε_m = 14.46 eV

i	host orbitals	$\|u_{mi}\|^2$
162	C12(3pz)	0.022
218	C16(3pz)	0.036
372	C27(3pz)	0.034
400	C29(3pz)	0.031
412	C30(3py)	0.026

For m = 644th ε_m = 28.13 eV

i	host orbitals	$\|u_{mi}\|^2$
22	N 2(3pz)	0.032
46	N 4(3px)	0.023
86	C 7(3s)	0.020
88	C 7(3px)	0.029
256	C19(3px)	0.024
258	C19(3py)	0.030
282	C21(3s)	0.028

Figure 8.39. For chlorophyll-a, schematic plot with label numbers and symbols of atoms. The DFT results on the square of the host eigenstate ($\|u_{mi}\|^2$) contributions and eigenvalues (ε_m) of the m = 382nd, 385th, 386th, 396th, 440th, 441st and 644th host states. Here, we show the highest contributions with blue colors.

180

CHAPTER 9

CONCLUSION

In this thesis, we explore whether the electron correlations arising from the transition metal atoms have any special role in the functioning of the bioinorganic molecules. Hemoglobin which contains iron atom, vitamin B_{12} containing cobalt atom and ruthenium-based dye molecules are examples of the bioinorganic molecules. There are many experimental studies to understand the magnetic and electronic properties of hemoglobin molecules. From magnetic susceptibility measurements, each heme of deoxyhemoglobin has 5.46 μ_B (Pauling and Coryell (1936)). Oxyhemoglobin is zero magnetic moment and low-spin state (S=0) (Pauling and Coryell (1936); Pauling (1977); Cerdonio et al. (1977); Taylor and Coryell (1938)). In experimental measurements, deoxyhemoglobin exhibits high-spin to low-spin transition when oxygen binds. In this thesis, we use four different computational methods: DFT, DFT+U, DFT+MFA, and DFT+QMC to find this transition. We are going to concentrate on deoxy and oxy-heme molecules to determine whether these methods give accurate results. We compare the results of these methods with each other and the experimental data. We try to determine which one works best for deoxy and oxy-heme molecules.

We compute the DFT to study the electronic structure of deoxy-heme and oxy-heme molecules within the framework of the extended multi-orbital Haldane-Anderson model. Then, we have solved the extended multi-orbital Haldane-Anderson model by using the DFT+MFA and DFT+QMC methods to determine the spin-states and magnetic properties of these molecules. In addition, we study the charge and effective magnetic moment of Fe($3d$) orbitals of deoxy and oxy-heme by using the DFT+U method.

We perform the DFT calculations for deoxy and oxy-heme molecules by using BP86 energy functional and 6-31G basis set. In DFT results, we find that the ground state energy of deoxy-heme is the triplet-spin state and the ground state energy of oxy-heme is the open-shell singlet-spin state.

The impurity bound states (IBS's) play a significant role in determining the magnetic properties of the deoxy and oxy-heme molecules. The location of IBS's determines the spin-state and effective magnetic moment of these molecules. When the IBS's are located below (above) the Fermi level, the spin-state of deoxy-heme (oxy-heme) is high (low). DFT, DFT+MFA and DFT+QMC methods find IBS for these molecules. DFT

probably finds an IBS, but at the wrong energy. DFT finds IBS at about 0.5 eV above the Fermi level. Hence, IBS is unoccupied. This is why DFT finds triplet(intermediate)-spin (S=1) state. DFT does not find the high-spin (S=2) state for deoxy-heme. For deoxy-heme, DFT and DFT+U methods find the total effective magnetic moment $M_{tot}^{\text{eff}} = 2.0\mu_{\text{B}}$ because spin-state of deoxy-heme becomes triplet-spin state.

In DFT result of oxy-heme, we find that the ground state energy of oxy-heme is the open-shell singlet-spin state. For oxy-heme, DFT finds IBS is unoccupied and $M_{tot}^{\text{eff}} = 0\mu_{\text{B}}$. DFT finds IBS at about 2 eV above the Fermi level. However, the effective magnetic moments of Fe($3d$) orbitals and magnetic correlation function between host state and Fe($3d$) orbitals are very small. For the DFT+U result of oxy-heme, we find that the total effective magnetic moment is 0.07 μ_B in the ground state energy. However, DFT+U finds that the effective magnetic moments of Fe($3d$) orbitals of oxy-heme are very small.

For deoxy-heme molecule, DFT+MFA and DFT+QMC results on IBS agree very well. For DFT+MFA and DFT+QMC methods, the IBS is located at -4.0 eV which is about 1 eV below the Fermi level for deoxy-heme. The IBS is occupied by electrons in DFT+MFA and DFT+QMC results. Hence, DFT+MFA and DFT+QMC find that deoxy-heme has a large magnetic moment and is a high-spin state. Total effective magnetic moment M_{tot}^{eff} of deoxy-heme is $4.03\mu_{\text{B}}$ for DFT+MFA and $4.08\mu_{\text{B}}$ for DFT+QMC method.

For oxy-heme, DFT+MFA finds a high-spin state, which is wrong. DFT+MFA method does not give accurate results for oxy-heme. This technique does not obtain a low-spin state because it does not find the location of IBS correctly. IBS is at about -3.8 eV which is below the Fermi level. IBS is occupied by electrons. In DFT+MFA result of oxy-heme, $3d_{xy}$ orbital is not doubly occupied below the Fermi level, hence oxy-heme has a large magnetic moment.

DFT+QMC technique finds total effective magnetic moment $M_{tot}^{\text{eff}} = 2.0\mu_{\text{B}}$ at T=300 K and $M_{tot}^{\text{eff}} = 0.6\mu_{\text{B}}$ at T=150 K. DFT+QMC drops from $M_{tot}^{\text{eff}} = 4.1\mu_{\text{B}}$ in deoxy-heme to $M_{tot}^{\text{eff}} = 2.0\mu_{\text{B}}$ in oxy-heme because of IBS becoming unoccupied. In oxy-heme the decrease of $M_{tot}^{\text{eff}} = 2.0\mu_{\text{B}}$ at T=300 K to $M_{tot}^{\text{eff}} = 0.6\mu_{\text{B}}$ at T=150 K is due to charge transfer from O_2 to Fe.

In this thesis, we find that the DFT method is not alone a sufficient technique because of these results of deoxy and oxy-heme molecules. DFT and DFT+U methods do not yield the high-spin state for deoxy-heme. The DFT method does not find the location of IBS correctly. These methods obtain low-spin for oxy-heme, but they find that magnetic moment formations are very small. The DFT+MFA technique works well for high-spin, but this technique does not obtain a low-spin state because it does not find the

location of IBS correctly. DFT+QMC method gives high(low)-spin state for deoxy-heme (oxy-heme) and finds IBS and magnetic moment formations. We see that the DFT+QMC technique works better among these methods for deoxy and oxy-heme molecules.

In addition, we study the electronic and magnetic properties of the CNCbl molecule which is a cofactor of the vitamin B_{12} and Ru-based dye molecules as examples for bioinorganic molecules and the transition-metal adatom on graphene systems as examples for single-atom catalysts (SAC's). The CNCbl, N719, Z907, Pt/3A-HGNS, Fe/3A-HGNS, and Ni/3A-HGNS molecules have a low-spin state. The DFT+MFA method does not give accurate results for these molecules. In addition, this method does not find the location of the impurity bound state correctly for these molecules. The DFT+MFA method works best for molecules having a high-spin state. The deoxy-heme molecule has a high-spin state. In Chapter 5, the DFT+MFA results are compatible with the DFT+QMC results for deoxy-heme. In Chapter 7, we show the DFT+QMC results of the CNCbl, N719, Z907, Pt/3A-HGNS, Fe/3A-HGNS and Ni/3A-HGNS molecules. We find that the location of IBS is above the Fermi level in DFT+QMC results of these molecules. Thus, the CNCbl, N719, Z907, Pt/3A-HGNS, Fe/3A-HGNS, and Ni/3A-HGNS molecules have a low-spin state. We show the DFT results of these molecules in Chapter 8. In addition, we present the DFT results of carbonmonoxy-heme, cyanomet-heme, myoglobin derivatives and chlorophyll-a molecules in this chapter. The structure of myoglobin molecule is similar to the hemoglobin molecule. The myoglobin molecule has one heme group and contains only one iron atom in its active center. The structure of chlorin layer of chlorophyll-a molecule is similar to the porphyrin layer of heme molecules. The chlorophyll-a molecule contains one magnesium atom in its active center.

The IBS, magnetic moments and magnetic correlations are not only found in the deoxy and oxy-heme molecules but also in the vitamin B_{12}, Ru-based dye molecules and single-atom catalysts. We think that the IBS's play significant role in determining the magnetic and electronic properties of these molecules. We find that the DFT method is not alone a sufficient technique. The DFT+MFA method works best for molecules having a high-spin state. In addition, DFT+QMC technique should be used for molecules having high-spin and low-spin states instead of using purely the DFT method.

REFERENCES

Alpert, Y. and R. Banerjee (1975). Magnetic susceptibility measurements of deoxygenated hemoglobins and isolated chains. *Biochimica et Biophysica Acta (BBA) - Protein Structure 405*(1), 144 – 154.

Arcovito, A., M. Benfatto, M. Cianci, S. S. Hasnain, K. Nienhaus, G. U. Nienhaus, C. Savino, R. W. Strange, B. Vallone, and S. Della Longa (2007). X-ray structure analysis of a metalloprotein with enhanced active-site resolution using in situ x-ray absorption near edge structure spectroscopy. *Proceedings of the National Academy of Sciences 104*(15), 6211–6216.

Ayalew, W. A. and D. W. Ayele (2016). Dye-sensitized solar cells using natural dye as light-harvesting materials extracted from Acanthus sennii chiovenda flower and Euphorbia cotinifolia leaf. *Journal of Science: Advanced Materials and Devices 1*(4), 488–494.

Badaut, V., T. Shirakawa, and S. Yunoki (2012, dec). A Haldane-Anderson impurity model study for the spin- and charge-states of iron in heme proteins. *Journal of Physics: Conference Series 400*(3), 032006.

Barends, T. R., L. Foucar, A. Ardevol, K. Nass, A. Aquila, S. Botha, R. B. Doak, K. Falahati, E. Hartmann, M. Hilpert, et al. (2015). Direct observation of ultrafast collective motions in CO myoglobin upon ligand dissociation. *Science 350*(6259), 445–450.

Becke, A. D. (1988). Density-functional exchange-energy approximation with correct asymptotic behavior. *Physical Review A 38*(6), 3098.

Becke, A. D. (1993). Density-functional thermochemistry. III. The role of exact exchange. *The Journal of Chemical Physics 98*(7), 5648–5652.

Blumenthal, I. (2001). Carbon monoxide poisoning. *Journal of the Royal Society of Medicine 94*(6), 270–272.

Bruus, H. and K. Flensberg (2004). *Many-body quantum theory in condensed matter*

physics: an introduction. Oxford University Press.

Bulut, N., K. Tanikawa, S. Takahashi, and S. Maekawa (2007). Long-range ferromagnetic correlations between Anderson impurities in a semiconductor host: Quantum Monte Carlo simulations. *Physical Review B 76*(4), 045220.

Cerdonio, M., A. Congiu-Castellano, F. Mogno, B. Pispisa, G. L. Romani, and S. Vitale (1977). Magnetic properties of oxyhemoglobin. *Proceedings of the National Academy of Sciences 74*(2), 398–400.

Chu, K., J. Vojtchovskỳ, B. H. McMahon, R. M. Sweet, J. Berendzen, and I. Schlichting (2000). Structure of a ligand-binding intermediate in wild-type carbonmonoxy myoglobin. *Nature 403*(6772), 921–923.

Deng, J.-P., W.-H. Chen, S.-P. Chiu, C.-H. Lin, and B.-C. Wang (2014). Edge-termination and core-modification effects of hexagonal nanosheet graphene. *Molecules 19*(2), 2361–2373.

Dennington, R. D., T. A. Keith, J. M. Millam, et al. (2008). GaussView 5.0.8. Gaussian Inc.

Dunning Jr, T. H. (1989). Gaussian basis sets for use in correlated molecular calculations. I. The atoms boron through neon and hydrogen. *The Journal of Chemical Physics 90*(2), 1007–1023.

Fiamingo, F. G. and J. O. Alben (1985). Structures of photolyzed carboxymyoglobin. *Biochemistry 24*(27), 7964–7970.

Frisch, M. J., G. W. Trucks, H. B. Schlegel, G. E. Scuseria, M. A. Robb, J. R. Cheeseman, G. Scalmani, V. Barone, B. Mennucci, G. A. Petersson, H. Nakatsuji, M. Caricato, X. Li, H. P. Hratchian, A. F. Izmaylov, J. Bloino, G. Zheng, J. L. Sonnenberg, M. Hada, M. Ehara, K. Toyota, R. Fukuda, J. Hasegawa, M. Ishida, T. Nakajima, Y. Honda, O. Kitao, H. Nakai, T. Vreven, J. A. Montgomery, Jr., J. E. Peralta, F. Ogliaro, M. Bearpark, J. J. Heyd, E. Brothers, K. N. Kudin, V. N. Staroverov, R. Kobayashi, J. Normand, K. Raghavachari, A. Rendell, J. C. Burant, S. S. Iyengar, J. Tomasi, M. Cossi, N. Rega, J. M. Millam, M. Klene, J. E. Knox,

J. B. Cross, V. Bakken, C. Adamo, J. Jaramillo, R. Gomperts, R. E. Stratmann, O. Yazyev, A. J. Austin, R. Cammi, C. Pomelli, J. W. Ochterski, R. L. Martin, K. Morokuma, V. G. Zakrzewski, G. A. Voth, P. Salvador, J. J. Dannenberg, S. Dapprich, A. D. Daniels, . Farkas, J. B. Foresman, J. V. Ortiz, J. Cioslowski, and D. J. Fox (2009). Gaussian 09, Revision D.01. Gaussian, Inc., Wallingford CT.

Glendening, E., J. Badenhoop, A. Reed, J. Carpenter, J. Bohmann, C. Morales, C. Landis, and F. Weinhold (2013). NBO 6.0, Theoretical Chemistry Institute. University of Wisconsin, Madison, WI.

Godbout, N., D. R. Salahub, J. Andzelm, and E. Wimmer (1992). Optimization of Gaussian-type basis sets for local spin density functional calculations. Part I. Boron through neon, optimization technique and validation. *Canadian Journal of Chemistry 70*(2), 560–571.

Haldane, F. D. M. and P. W. Anderson (1976). Simple model of multiple charge states of transition-metal impurities in semiconductors. *Physical Review B 13*, 2553–2559.

Hao, S., J. Wu, Y. Huang, and J. Lin (2006). Natural dyes as photosensitizers for dye-sensitized solar cell. *Solar Energy 80*(2), 209–214.

Hay, P. J. and W. R. Wadt (1985). Ab initio effective core potentials for molecular calculations. Potentials for the transition metal atoms Sc to Hg. *The Journal of Chemical Physics 82*(1), 270–283.

Hendrickson, W. A. (1973). Structural effects accompanying ligand change in crystalline lamprey hemoglobin. *Biochimica et Biophysica Acta (BBA)-Protein Structure 310*(1), 32–37.

Hirsch, J. E. and R. M. Fye (1986). Monte Carlo method for magnetic impurities in metals. *Physical Review Letters 56*(23), 2521.

Hu, C., A. Roth, M. K. Ellison, J. An, C. M. Ellis, C. E. Schulz, and W. R. Scheidt (2005). Electronic configuration assignment and the importance of low-lying excited states in high-spin imidazole-ligated iron(II) porphyrinates. *Journal of the American Chemical Society 127*(15), 5675–5688. PMID: 15826208.

Hu, L., X. Hu, X. Wu, C. Du, Y. Dai, and J. Deng (2010). Density functional calculation of transition metal adatom adsorption on graphene. *Physica B: Condensed Matter 405*(16), 3337–3341.

Ichimura, M., K. Tanikawa, S. Takahashi, G. Baskaran, and S. Maekawa (2006). Magnetic impurity states and ferromagnetic interaction in diluted magnetic semiconductors. In *Foundations Of Quantum Mechanics In The Light Of New Technology*, pp. 183–186. World Scientific.

Jungwirth, T., J. Sinova, A. MacDonald, B. Gallagher, V. Novák, K. Edmonds, A. Rushforth, R. Campion, C. Foxon, L. Eaves, et al. (2007). Character of states near the Fermi level in (Ga, Mn) As: Impurity to valence band crossover. *Physical Review B 76*(12), 125206.

Kandemir, Z. (2013). Mapping of the electronic structure of metalloproteins onto multi-orbital Anderson model using the density functional theory. Master's thesis, Izmir Institute of Technology.

Kandemir, Z., S. Mayda, and N. Bulut (2016). Electronic structure and correlations of vitamin B_{12} studied within the Haldane-Anderson impurity model. *The European Physical Journal B 89*(5), 113.

Kresse, G. and J. Furthmüller (1996). Efficient iterative schemes for ab initio total-energy calculations using a plane-wave basis set. *Physical Review B 54*(16), 11169.

Kresse, G. and J. Hafner (1994). Ab initio molecular-dynamics simulation of the liquid-metal–amorphous-semiconductor transition in germanium. *Physical Review B 49*(20), 14251.

Kresse, G. and D. Joubert (1999). From ultrasoft pseudopotentials to the projector augmented-wave method. *Physical Review B 59*(3), 1758.

Kroeger, K. S. and C. E. Kundrot (1997). Structures of a hemoglobin-based blood substitute: insights into the function of allosteric proteins. *Structure 5*(2), 227–237.

Lee, C., W. Yang, and R. G. Parr (1988). Development of the Colle-Salvetti

correlation-energy formula into a functional of the electron density. *Physical Review B 37*(2), 785.

Liechtenstein, A., V. Anisimov, and J. Zaanen (1995). Density-functional theory and strong interactions: Orbital ordering in Mott-Hubbard insulators. *Physical Review B 52*(8), R5467.

Mayda, S. (2019). *Magnetic effect in the biological functioning of hemoglobin: DFT+QMC approach within an effective multi-orbital Anderson impurity model*. Ph. D. thesis, Izmir Institute of Technology.

Mayda, S., Z. Kandemir, and N. Bulut (2017). Electronic structure of cyanocobalamin: DFT+QMC study. *Journal of Superconductivity and Novel Magnetism 30*(11), 3301–3308.

Mayda, S., Z. Kandemir, and N. Bulut (2018). Future applications of artificially-synthesized organic molecules containing transition-metal atoms. In *Handbook of Nanomaterials for Industrial Applications*, pp. 386–391. Elsevier.

McLendon, G. and K. Sandberg (1978). Axial ligand effects on myoglobin stability. *Journal of Biological Chemistry 253*(11), 3913–3917.

Mebs, S., J. Henn, B. Dittrich, C. Paulmann, and P. Luger (2009). Electron densities of three B_{12} vitamins. *The Journal of Physical Chemistry A 113*(29), 8366–8378.

Mikroyannidis, J. A., P. Suresh, M. Roy, and G. Sharma (2010). Triphenylamine- and benzothiadiazole-based dyes with multiple acceptors for application in dye-sensitized solar cells. *Journal of Power Sources 195*(9), 3002–3010.

Norvell, J. C., A. C. Nunes, and B. P. Schoenborn (1975). Neutron diffraction analysis of myoglobin: structure of the carbon monoxide derivative. *Science 190*(4214), 568–570.

Novoselov, D., D. M. Korotin, and V. I. Anisimov (2016a, May). Spin state transition in the active center of the hemoglobin molecule DFT + DMFT study. *JETP Letters 103*(10), 658–662.

Novoselov, D. Y., D. M. Korotin, and V. I. Anisimov (2016b, Jan). Features of the electronic structure of the active center of an HbS molecule. *Russian Journal of Physical Chemistry A 90*(1), 113–116.

Nye, M. J. (2002). *The modern physical and mathematical sciences*. Cambridge University Press.

Park, S.-Y., T. Yokoyama, N. Shibayama, Y. Shiro, and J. R. Tame (2006). 1.25 Å resolution crystal structures of human haemoglobin in the oxy, deoxy and carbonmonoxy forms. *Journal of Molecular Biology 360*(3), 690 – 701.

Pauling, L. (1977). Magnetic properties and structure of oxyhemoglobin. *Proceedings of the National Academy of Sciences 74*(7), 2612–2613.

Pauling, L. and C. D. Coryell (1936). The magnetic properties and structure of hemoglobin, oxyhemoglobin and carbonmonoxyhemoglobin. *Proceedings of the National Academy of Sciences 22*(4), 210–216.

Perdew, J. P. (1986). Density-functional approximation for the correlation energy of the inhomogeneous electron gas. *Physical Review B 33*(12), 8822.

Perdew, J. P., K. Burke, and M. Ernzerhof (1996). Generalized gradient approximation made simple. *Physical Review Letters 77*(18), 3865.

Qin, Y. and Q. Peng (2012). Ruthenium sensitizers and their applications in dye-sensitized solar cells. *International Journal of Photoenergy 2012*, 21. Article ID 291579.

Roder, H., J. Berendzen, S. F. Bowne, H. Frauenfelder, T. B. Sauke, E. Shyamsunder, and M. B. Weissman (1984). Comparison of the magnetic properties of deoxy-and photodissociated myoglobin. *Proceedings of the National Academy of Sciences 81*(8), 2359–2363.

Rovira, C., K. Kunc, J. Hutter, P. Ballone, and M. Parrinello (1997). Equilibrium geometries and electronic structure of iron- porphyrin complexes: A density functional study. *The Journal of Physical Chemistry A 101*(47), 8914–8925.

Scherlis, D. A., M. Cococcioni, P. Sit, and N. Marzari (2007). Simulation of heme using DFT + U: A step toward accurate spin-state energetics. *The Journal of Physical Chemistry B 111*(25), 7384–7391. PMID: 17547444.

Scherlis, D. A. and D. A. Estrin (2002). Structure and spin-state energetics of an iron porphyrin model: An assessment of theoretical methods. *International Journal of Quantum Chemistry 87*(3), 158–166.

Schiffmann, F., J. VandeVondele, J. Hutter, R. Wirz, A. Urakawa, and A. Baiker (2010). Protonation-dependent binding of ruthenium bipyridyl complexes to the anatase (101) surface. *The Journal of Physical Chemistry C 114*(18), 8398–8404.

Smith, D. M. A., M. Dupuis, and T. P. Straatsma (2005). Multiplet splittings and other properties from density functional theory an assessment in iron-porphrin systems. *Molecular Physics 103*(2-3), 273–278.

Smith, F. R. and K. C. Simmons (1994). Cyanomet human hemoglobin crystallized under physiological conditions exhibits the Y quaternary structure. *Proteins: Structure, Function, and Bioinformatics 18*(3), 295–300.

Sosa, C., J. Andzelm, B. C. Elkin, E. Wimmer, K. D. Dobbs, and D. A. Dixon (1992). A local density functional study of the structure and vibrational frequencies of molecular transition-metal compounds. *The Journal of Physical Chemistry 96*(16), 6630–6636.

Sun, Y. (2009). *Sensitizer Molecule Engineering: The Development Of Novel Ru (II) Polypyridyl Complexes for Application in Dye Sensitized Solar Cells*. Ph. D. thesis, Bowling Green State University.

Tanaka, T., T. Kashimura, M. Ise, B. D. Lohman, and Y. Taira (2016). Light irradiation for treatment of acute carbon monoxide poisoning: an experimental study. *Journal of Intensive Care 4*(1), 58.

Taylor, D. S. and C. D. Coryell (1938). The magnetic susceptibility of the iron in ferrohemoglobin. *Journal of the American Chemical Society 60*(5), 1177–1181.

Tomoda, Y., N. Bulut, and S. Maekawa (2009). Inter-impurity and impurity–host

magnetic correlations in semiconductors with low-density transition–metal impurities. *Physica B: Condensed Matter 404*(8-11), 1159–1168.

Tsukahara, K. (1986). Ionic strength effect on the ascorbate reduction of sperm whale and horse heart metmyoglobins. *Inorganica Chimica Acta 124*(4), 199–202.

Waterman, M. R. (1978). [48] spectral characterization of human hemoglobin and its derivatives. In *Methods in enzymology*, Volume 52, pp. 456–463. Elsevier.

Woon, D. E. and T. H. Dunning Jr (1993). Gaussian basis sets for use in correlated molecular calculations. III. the atoms aluminum through argon. *The Journal of Chemical Physics 98*(2), 1358–1371.

Yamauchi, K., H. Maebashi, and H. Katayama-Yoshida (2003). Charge and spin states of transition-metal atoms in a hemoprotein based on the extended Haldane-Anderson model. *Journal of the Physical Society of Japan 72*(8), 2029–2032.

APPENDIX A

COMPUTATIONAL METHODS

In this chapter, we use four different computational methods to understand magnetic and electronic properties of hemoglobin, vitamin B_{12}, Ru-based dye molecules and single-atom catalysts. These methods are DFT, DFT+U, DFT+mean-field approximation (DFT+MFA) and DFT+quantum Monte Carlo (DFT+QMC). Here, we explain these methods as follow.

There are two main approaches for electronic structure calculations. The first approach is density functional theory (DFT). DFT is an approach that explains the ground state properties of many-body systems. Kohn and Sham showed ground state energy as a function of electron density. Kohn-Sham equations are a similar form of time independent Schrödinger equation. These equations describe independent particles moving within an effective potential. I have explained the details of this approach in my master's thesis (Kandemir (2013)). The other one is due to Anderson model. This model divides a system into two parts: impurity and host. The impurity part indicates d orbitals of a transition-metal atom and host part is the remaining orbitals. This model emphasizes the importance of Coulomb repulsions of d orbitals. For the first approach, we perform DFT and DFT+U calculations for deoxy and oxy-heme molecules. For the second approach, we perform DFT+MFA and DFT+QMC by using effective Anderson impurity model for these molecules.

A.1. DFT

We perform BP86 exchange-correlation energy functional and B3LYP hybrid functional with the Gaussian program (Frisch et al. (2009)) in order to obtain the DFT results. BP86 is comprised of the Becke 1988 (B, Becke (1988)) exchange functional and Perdew 1986 (P86, Perdew (1986)) correlation functional. This functional is defined by

$$E_{xc}^{BP86} = E_x^{B88} + E_c^{P86} \tag{A.1}$$

where the local density approximation (LDA) exchange energy is

$$E_x^{LDA} = -C\frac{3}{2}\left(\frac{3}{4\pi}\right)^{\frac{1}{3}}\sum_\sigma \int \rho_\sigma^{4/3}(r)d^3r, \tag{A.2}$$

with $C = \dfrac{2}{2^{4/3}}$ for local density approximation (LDA) and $C = 1$ for local spin density approximation (LSDA) (Becke (1988)). The correlation energy is defined by

$$E_c^{GGA}[\rho] = \int d^3r\rho(r)\epsilon_c(\rho(r), \nabla\rho(r)). \tag{A.3}$$

where GGA means generalized gradient approximation to the correlation energy as a function of density and its gradient.

B3LYP is formed by combining Becke's three parameters exchange functional (Becke (1993)) and Lee-Yang-Parr correlation functional (Lee et al. (1988)). I have explained this functional in detail in Ref. (Kandemir (2013)).

In our DFT calculations, we use 6-31G basis set. This set is a double split valence (Pople-style) basis set. The 6-31G basis set works for the elements located between hydrogen and krypton (H-Kr) atoms. For CNCbl molecule, we choose the 6-31G basis set for all atoms. N719 and Z907 molecules are Ru-based dye molecules. Ruthenium (Ru) atom is the 5th row of element in periodic table. The 6-31G basis set does not work for this atom, so we use LanL2DZ basis set. The LanL2DZ basis set is used with between sodium and bismuth (Na-Bi) elements. This basis set is double zeta effective core potential (ECP). We use the LanL2DZ basis set for Ru atom and 6-31G(d) basis set for C, H, O, N, and S atoms in dye molecules. There is only one difference between 6-31G(d) and 6-31G basis sets. The 6-31G(d) basis set contains the contributions of 3d orbitals in addition to 6-31G set for C, N, O and S atoms. Similarly, platinum (Pt) atom is the 6th row of element in periodic table, so we use the LanL2DZ basis set for Pt atom. We choose the 6-31G basis set for C and H atoms in 3A-HGNS graphene layer. In addition, we use the LanL2DZ basis set for Fe and Ni atoms in order to compare the results of Pt/3A-HGNS, Fe/3A-HGNS and Ni/3A-HGNS structures. We use the B3LYP hybrid functional for these structures, because BP86 energy functional does not converge.

A.2. DFT+U

The DFT plus Hubbard U (DFT+U) calculations of deoxy and oxy-heme molecules are performed with the Vienna Ab-initio Software Package (VASP) (Kresse and Hafner (1994); Kresse and Furthmüller (1996)). We use the Perdew-Burke-Ernzerhof (PBE) exchange correlation functionals as a type for the generalized gradient approximation (GGA) functional (Perdew et al. (1996)). The Fe, C, N, O and H ionic cores are indicated by the projector augmented-wave (PAW) (Kresse and Joubert (1999)) potentials with 8, 4, 5, 6 and 1 valence electrons, respectively. For each molecule, the k-point mesh of $1{\times}1{\times}1$ is used with a cutoff energy of 500 eV. We perform the DFT+U calculations by using the LDAUTYPE=4 (Liechtenstein et al. (1995)) in VASP. In this scheme, the total DFT+U functional is defined by the following equation

$$E^{DFT+U} = E^{DFT} + E^{U} - E^{DC} \tag{A.4}$$

where E^{DC} is the double-counting correction energy. For the LDAUTYPE=4, the double-counting energy is defined as

$$E^{DC} = \frac{U}{2}n_d(n_d - 1) - \frac{J}{4}n_d(n_d - 2) \tag{A.5}$$

where U and J are the effective on-site Coulomb and exchange interactions, respectively. The total occupation number of d orbitals denotes n_d. We choose $U = 4$ eV and $J = 0.9$ eV for the Fe($3d$) orbitals and $U = J = 0$ eV for the remaining orbitals.

A.3. DFT+MFA

The electron density at each $3d$ orbital is given by $n_\nu = n_{\nu\uparrow} + n_{\nu\downarrow}$ and the magnetization becomes $m_\nu = n_{\nu\uparrow} - n_{\nu\downarrow}$. In the mean-field approximation (Bruus and Flensberg (2004)), the occupancy of the $3d$ orbitals is rewritten as

$$n_{\nu\sigma} = \langle n_{\nu\sigma} \rangle + (n_{\nu\sigma} - \langle n_{\nu\sigma} \rangle) \tag{A.6}$$

where σ denotes spin state. While alpha occupancies of the $3d$ orbitals are spin-up $\sigma = \uparrow$, beta occupancies of the $3d$ orbitals are spin-down $\sigma = \downarrow$. Here, we use approximation that $n_{\nu\sigma} - \langle n_{\nu\sigma} \rangle$ is much less than $n_{\nu\sigma}$. Hence, we write

$$n_{\nu\uparrow} n_{\nu\downarrow} = \langle n_{\nu\uparrow} \rangle \langle n_{\nu\downarrow} \rangle + \langle n_{\nu\uparrow} \rangle (n_{\nu\downarrow} - \langle n_{\nu\downarrow} \rangle) + \langle n_{\nu\downarrow} \rangle (n_{\nu\uparrow} - \langle n_{\nu\uparrow} \rangle)$$
$$+ (n_{\nu\uparrow} - \langle n_{\nu\uparrow} \rangle)(n_{\nu\downarrow} - \langle n_{\nu\downarrow} \rangle) \tag{A.7}$$

where the last term is neglected due to it being very small. This way, we obtain

$$n_{\nu\uparrow} n_{\nu\downarrow} \cong n_{\nu\uparrow} \langle n_{\nu\downarrow} \rangle + n_{\nu\downarrow} \langle n_{\nu\uparrow} \rangle - \langle n_{\nu\uparrow} \rangle \langle n_{\nu\downarrow} \rangle \tag{A.8}$$

by using the mean-field approximation for the Anderson model. Similarly, we obtain

$$n_{\nu\sigma} n_{\nu',-\sigma} \cong n_{\nu\sigma} \langle n_{\nu',-\sigma} \rangle + n_{\nu',-\sigma} \langle n_{\nu\sigma} \rangle - \langle n_{\nu\sigma} \rangle \langle n_{\nu',-\sigma} \rangle \tag{A.9}$$

$$n_{\nu\sigma} n_{\nu'\sigma} \cong n_{\nu\sigma} \langle n_{\nu'\sigma} \rangle + n_{\nu'\sigma} \langle n_{\nu\sigma} \rangle - \langle n_{\nu\sigma} \rangle \langle n_{\nu'\sigma} \rangle. \tag{A.10}$$

Then, we use these relations (A.5, A.6 and A.7) for U, U' and $U' - J$ terms in extended multi-orbital Anderson model. With mean-field approximation, Anderson Hamiltonian becomes as follows

$$H = \sum_{m\sigma} (\varepsilon_m - \mu) c_{m\sigma}^\dagger c_{m\sigma} + \sum_{\nu\sigma} (\tilde{\varepsilon}_{d\nu} - \mu) d_{\nu\sigma}^\dagger d_{\nu\sigma} + \sum_{m\nu\sigma} \left(V_{\nu m} d_{\nu\sigma}^\dagger c_{m\sigma} + V_{\nu m}^* c_{m\sigma}^\dagger d_{\nu\sigma} \right)$$
$$+ \sum_\nu \left(U n_{\nu\uparrow} \langle n_{\nu\downarrow} \rangle + U n_{\nu\downarrow} \langle n_{\nu\uparrow} \rangle - U \langle n_{\nu\uparrow} \rangle \langle n_{\nu\downarrow} \rangle \right)$$
$$+ \sum_{\nu > \nu'} \sum_\sigma U' \left(n_{\nu\sigma} \langle n_{\nu',-\sigma} \rangle + n_{\nu',-\sigma} \langle n_{\nu\sigma} \rangle - \langle n_{\nu\sigma} \rangle \langle n_{\nu',-\sigma} \rangle \right)$$
$$+ \sum_{\nu > \nu'} \sum_\sigma (U' - J) \left(n_{\nu\sigma} \langle n_{\nu'\sigma} \rangle + n_{\nu'\sigma} \langle n_{\nu\sigma} \rangle - \langle n_{\nu\sigma} \rangle \langle n_{\nu'\sigma} \rangle \right) \tag{A.11}$$

where $n_{\nu\uparrow}$ $(n_{\nu\downarrow})$ is defined by $d^\dagger_{\nu\uparrow}d_{\nu\uparrow}$ $(d^\dagger_{\nu\downarrow}d_{\nu\downarrow})$. Here, we want to get the common paren-
thesis with $n_{\nu\uparrow}$ and $n_{\nu\downarrow}$ for U, U' and $(U'-J)$ terms. We define for $n_{\nu\uparrow}$

$$\sum_{\nu=2}^{5}\sum_{\nu'=1}^{\nu-1}\left[U'\langle n_{\nu\downarrow}\rangle + (U'-J)\langle n_{\nu\uparrow}\rangle\right]n_{\nu'\uparrow} = \sum_{\nu=1}^{4}\left(\sum_{\nu'=\nu+1}^{5}\left[U'\langle n_{\nu'\downarrow}\rangle\right.\right.$$
$$\left.\left. + (U'-J)\langle n_{\nu'\uparrow}\rangle\right]\right)n_{\nu\uparrow}, \quad \text{(A.12)}$$

similarly, for $n_{\nu\downarrow}$

$$\sum_{\nu=2}^{5}\sum_{\nu'=1}^{\nu-1}\left[U'\langle n_{\nu\uparrow}\rangle + (U'-J)\langle n_{\nu\downarrow}\rangle\right]n_{\nu'\downarrow} = \sum_{\nu=1}^{4}\left(\sum_{\nu'=\nu+1}^{5}\left[U'\langle n_{\nu'\uparrow}\rangle\right.\right.$$
$$\left.\left. + (U'-J)\langle n_{\nu'\downarrow}\rangle\right]\right)n_{\nu\downarrow}. \quad \text{(A.13)}$$

Consequently, this Hamiltonian is given by

$$H = \sum_{m\sigma}(\varepsilon_m - \mu)c^\dagger_{m\sigma}c_{m\sigma} + \sum_{m\nu\sigma}\left(V_{\nu m}d^\dagger_{\nu\sigma}c_{m\sigma} + V^*_{\nu m}c^\dagger_{m\sigma}d_{\nu\sigma}\right)$$
$$+ \sum_{\nu=1}^{5}\left((\tilde\varepsilon_{d\nu} - \mu) + U\langle n_{\nu\downarrow}\rangle + \sum_{\nu'=1}^{\nu-1}\left[U'\langle n_{\nu'\downarrow}\rangle + (U'-J)\langle n_{\nu'\uparrow}\rangle\right]\right)n_{\nu\uparrow}$$
$$+ \sum_{\nu=1}^{5}\left((\tilde\varepsilon_{d\nu} - \mu) + U\langle n_{\nu\uparrow}\rangle + \sum_{\nu'=1}^{\nu-1}\left[U'\langle n_{\nu'\uparrow}\rangle + (U'-J)\langle n_{\nu'\downarrow}\rangle\right]\right)n_{\nu\downarrow}$$
$$+ \sum_{\nu=1}^{4}\left(\sum_{\nu'=\nu+1}^{5}\left[U'\langle n_{\nu'\downarrow}\rangle + (U'-J)\langle n_{\nu'\uparrow}\rangle\right]\right)n_{\nu\uparrow}$$
$$+ \sum_{\nu=1}^{4}\left(\sum_{\nu'=\nu+1}^{5}\left[U'\langle n_{\nu'\uparrow}\rangle + (U'-J)\langle n_{\nu'\downarrow}\rangle\right]\right)n_{\nu\downarrow}$$
$$- \sum_{\nu}U\langle n_{\nu\uparrow}\rangle\langle n_{\nu\downarrow}\rangle - \sum_{\nu>\nu'}\sum_{\sigma}U'\langle n_{\nu\sigma}\rangle\langle n_{\nu',-\sigma}\rangle$$
$$- \sum_{\nu>\nu'}\sum_{\sigma}(U'-J)\langle n_{\nu\sigma}\rangle\langle n_{\nu'\sigma}\rangle \quad \text{(A.14)}$$

Finally, in mean-field approximation, the extended multi-orbital Anderson model

is obtained

$$H = \sum_{m\sigma}(\varepsilon_m - \mu)c_{m\sigma}^\dagger c_{m\sigma} + \sum_{m\nu\sigma}\left(V_{\nu m}d_{\nu\sigma}^\dagger c_{m\sigma} + V_{\nu m}^* c_{m\sigma}^\dagger d_{\nu\sigma}\right)$$
$$+ \sum_{\nu=1}^{5}\left[(\tilde{\varepsilon}_{d\nu} - \mu) + W_{\nu\uparrow}\right]n_{\nu\uparrow} + \sum_{\nu=1}^{5}\left[(\tilde{\varepsilon}_{d\nu} - \mu) + W_{\nu\downarrow}\right]n_{\nu\downarrow}$$
$$- \sum_{\nu}U\langle n_{\nu\uparrow}\rangle\langle n_{\nu\downarrow}\rangle - \sum_{\nu>\nu'}\sum_{\sigma}U'\langle n_{\nu\sigma}\rangle\langle n_{\nu',-\sigma}\rangle$$
$$- \sum_{\nu>\nu'}\sum_{\sigma}(U' - J)\langle n_{\nu\sigma}\rangle\langle n_{\nu'\sigma}\rangle \tag{A.15}$$

where

$$W_{\nu\sigma} = U\langle n_{\nu,-\sigma}\rangle + \sum_{\substack{\nu'=1 \\ \nu'\neq\nu}}^{5}\left[U'\langle n_{\nu',-\sigma}\rangle + (U' - J)\langle n_{\nu',\sigma}\rangle\right]. \tag{A.16}$$

Mean-field approximation equations were explained details in Ref. (Kandemir (2013)).

A.3.1. Self-consistent solution

For the impurity orbitals, we define the impurity Green's function

$$G_{\nu\nu'}^\sigma(\tau) = -\langle Td_{\nu\sigma}(\tau)d_{\nu'\sigma}^\dagger(0)\rangle, \tag{A.17}$$

which can be obtained from the following Feynman-diagram.

In Fig. A.1, we express these Feynman diagrams in terms of the Green's functions

Figure A.1. Feynman diagram representing the impurity Green's function $G^\sigma_{\nu\nu'}$ for $\sigma = \uparrow, \downarrow$. The double lines indicate $G^\sigma_{\nu\nu'}$ and $G^\sigma_{\nu''\nu'}$ (define the impurity Green's functions) while the single lines denote $G^{0\sigma}_\nu$ and G^0_m (define respectively the impurity and host Green's function for $U \neq 0$ and $V_{\nu m} = 0$). Here, the cross terms indicate the hybridization matrix elements between host and impurity.

at $T \neq 0$ as follows:

$$iG^\sigma_{\nu\nu'}(i\omega_n) = \delta_{\nu\nu'} iG^{0\sigma}_\nu(i\omega_n)$$
$$+ iG^{0\sigma}_\nu(i\omega_n)(-iV_{\nu m})(iG^0_m(i\omega_n))(-iV_{m\nu''})iG^\sigma_{\nu''\nu'}(i\omega_n), \quad \text{(A.18)}$$

$$G^\sigma_{\nu\nu'}(i\omega_n) = \delta_{\nu\nu'} G^{0\sigma}_\nu(i\omega_n)$$
$$+ G^{0\sigma}_\nu(i\omega_n) \sum_m V_{\nu m} G^0_m(i\omega_n) \sum_{\nu''} V_{m\nu''} G^\sigma_{\nu''\nu'}(i\omega_n). \quad \text{(A.19)}$$

Here, we leave $G^{0\sigma}_\nu$ term alone on the right hand side.

$$\sum_{\nu''} \left[\delta_{\nu\nu''} - G^{0\sigma}_\nu(i\omega_n) \left(\sum_m V_{\nu m} G^0_m(i\omega_n) V_{m\nu''} \right) \right] G^\sigma_{\nu''\nu'}(i\omega_n) = \delta_{\nu\nu'} G^{0\sigma}_\nu(i\omega_n), \quad \text{(A.20)}$$

where $(\tilde{Z}^\sigma(i\omega_n))_{\nu\nu''}$ is defined as follows

$$\sum_{\nu''} (\tilde{Z}^\sigma(i\omega_n))_{\nu\nu''} G^\sigma_{\nu''\nu'}(i\omega_n) = \delta_{\nu\nu'} G^{0\sigma}_\nu(i\omega_n) \quad \text{(A.21)}$$

where $(\tilde{Z}^\sigma(i\omega_n))_{\nu\nu''}$ is defined as follows

$$(\tilde{Z}^\sigma(i\omega_n))_{\nu\nu''} = \delta_{\nu\nu''} - G^{0\sigma}_\nu(i\omega_n) \left(\sum_m V_{\nu m} G^0_m(i\omega_n) V_{m\nu''} \right), \quad \text{(A.22)}$$

where G_m^0 is the host Green's function.

$$(\tilde{Z}^\sigma(i\omega_n))_{\nu\nu''} = \delta_{\nu\nu''} - G_\nu^{0\sigma}(i\omega_n)\left(\sum_m \frac{V_{\nu m}V_{m\nu''}}{i\omega_n - (\varepsilon_m - \mu)}\right), \qquad (A.23)$$

$$\left(\tilde{Z}^\sigma(i\omega_n)\right)_{\nu\nu''} = \delta_{\nu\nu''} - G_\nu^{0\sigma}(i\omega_n)F_{\nu\nu''}(i\omega_n) \quad \text{for } T \neq 0, \qquad (A.24)$$

where we define the impurity Green's function $G_\nu^{0\sigma}(i\omega_n)$ for $U \neq 0$, $U' \neq 0$, $J \neq 0$ and $V_{\nu m} = 0$

$$G_\nu^{0\sigma}(i\omega_n) = \frac{1}{i\omega_n - (\tilde{\varepsilon}_{d\nu} - \mu + W_{\nu\sigma})} \qquad (A.25)$$

and the self-energy term $F_{\nu\nu''}(i\omega_n)$

$$F_{\nu\nu''}(i\omega_n) = \sum_m \frac{V_{\nu m}V_{\nu''m}}{i\omega_n - (\varepsilon_m - \mu)}. \qquad (A.26)$$

Hence, we have

$$G_{\nu'\nu}^\sigma(i\omega_n) = \sum_{\nu''} \left[\left(\tilde{Z}^\sigma(i\omega_n)\right)^{-1}\right]_{\nu'\nu''} \delta_{\nu''\nu}G_{\nu''}^{0\sigma}(i\omega_n)$$
$$G_{\nu'\nu}^\sigma(i\omega_n) = \left[\left(\tilde{Z}^\sigma(i\omega_n)\right)^{-1}\right]_{\nu'\nu} G_\nu^{0\sigma}(i\omega_n). \qquad (A.27)$$

If $\nu' = \nu$,

$$G_{\nu\nu}^\sigma(i\omega_n) = \left[\left(\tilde{Z}^\sigma(i\omega_n)\right)^{-1}\right]_{\nu\nu} G_\nu^{0\sigma}(i\omega_n). \qquad (A.28)$$

Hence, we introduce the self-consistency condition for the Green's functions at each d-site for $\nu = \nu'$:

$$G_{\nu\nu}^\sigma(\tau = 0^-) = T\sum_{i\omega_n} e^{-i\omega_n 0^-} G_{\nu\nu}^\sigma(i\omega_n) = \langle n_{\nu\sigma}\rangle. \qquad (A.29)$$

We need to solve Eq.(A.29) for $\langle n_{\nu\sigma} \rangle$. Here, the local electron density can be defined

$$\langle n_{\nu\sigma} \rangle = T \sum_{n=-\infty}^{+\infty} e^{-i\omega_n 0^-} G_{\nu\nu}^{\sigma}(i\omega_n) \tag{A.30}$$

where ω_n is the Matsubara frequency as $\omega_n = (2n+1)\pi T$. Then, we can consider that the real part of $G_{\nu}^{0\sigma}(i\omega_n)$ is proportional to $\dfrac{1}{|\omega_n|}$. Hence, we define again

$$\langle n_{\nu\sigma} \rangle = T \sum_{n=-\infty}^{+\infty} e^{-i\omega_n 0^-} \left[G_{\nu\nu}^{\sigma}(i\omega_n) - G_{\nu}^{0\sigma}(i\omega_n) \right] + T \sum_{n=-\infty}^{+\infty} e^{-i\omega_n 0^-} G_{\nu}^{0\sigma}(i\omega_n),$$

$$\cong T \sum_{n=-n_{max}-1}^{n_{max}} \left[G_{\nu\nu}^{\sigma}(i\omega_n) - G_{\nu}^{0\sigma}(i\omega_n) \right] + T \sum_{n=-\infty}^{+\infty} e^{-i\omega_n 0^-} G_{\nu}^{0\sigma}(i\omega_n) \tag{A.31}$$

where $e^{-i\omega_n 0^-}$ goes 1 for the first term and the last term refers to Fermi distribution ($\mathcal{F}_{\nu}^{\sigma}$) because of the finite Green's function. Thus, we obtain

$$T \sum_{n=-\infty}^{+\infty} e^{-i\omega_n 0^-} G_{\nu}^{0\sigma}(i\omega_n) = \mathcal{F}_{\nu}^{\sigma} \left(\tilde{\varepsilon}_{d\nu} - \mu + W_{\nu\sigma} \right)$$

$$= \frac{1}{e^{\beta(\tilde{\varepsilon}_{d\nu} - \mu + W_{\nu\sigma})} + 1}. \tag{A.32}$$

Then, we obtained the local electron density

$$\langle n_{\nu\sigma} \rangle \cong T \sum_{n=-n_{max}-1}^{n_{max}} \left[G_{\nu\nu}^{\sigma}(i\omega_n) - G_{\nu}^{0\sigma}(i\omega_n) \right] + \mathcal{F}_{\nu}^{\sigma} \left(\tilde{\varepsilon}_{d\nu} - \mu + W_{\nu\sigma} \right),$$

$$\langle n_{\nu\sigma} \rangle \cong T \sum_{n=-n_{max}-1}^{n_{max}} \left[\left(\left[\left(\tilde{Z}^{\sigma}(i\omega_n) \right)^{-1} \right]_{\nu\nu} - 1 \right) G_{\nu}^{0\sigma}(i\omega_n) \right]$$

$$+ \mathcal{F}_{\nu}^{\sigma} \left(\tilde{\varepsilon}_{d\nu} - \mu + W_{\nu\sigma} \right). \tag{A.33}$$

We need to solve Eq.(A.30) for $\langle n_{\nu\sigma} \rangle$. Hence, we have ten equations with ten unknowns ($\nu = 1, 2, \ldots, 5$ for Fe($3d$) orbitals and $\sigma = \uparrow, \downarrow$ for spin up and down). We solve these
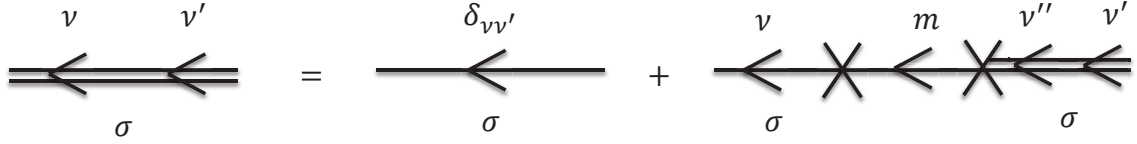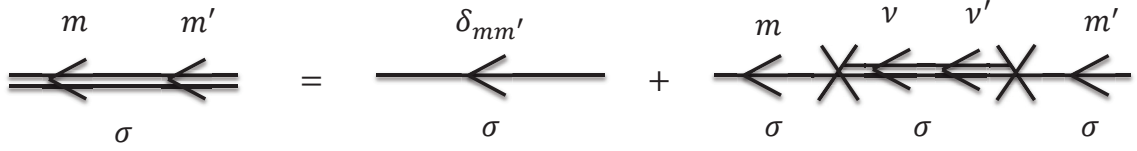
Figure A.2. Feynman diagram representing the host Green's function $G^{\sigma}_{mm'}$ for $\sigma = \uparrow$, $\downarrow$. The double lines indicate $G^{\sigma}_{mm'}$ (defines the host Green's function) and $G^{\sigma}_{\nu\nu'}$ (defines the impurity Green's function) while the single lines denote G^{0}_{m} and $G^{0}_{m'}$ (define the host Green's functions for $U = 0$). Here, the cross terms indicate the hybridization matrix elements between host and impurity.

equations by using iteration method. This method is performed

$$d^2 = \sum_{i=1}^{10} \left(x_i^{input} - x_i^{output} \right)^2 \tag{A.34}$$

where if the value of d is less than 10^{-12}, we obtain the electron number of impurity x_i^{output}.

Similarly, for the host orbitals we define the host Green's function

$$G^{\sigma}_{mm'}(\tau) = \langle T c_{m\sigma}(\tau) c^{\dagger}_{m'\sigma}(0) \rangle, \tag{A.35}$$

which can be obtained from the following Feynman-diagram. Thus, we introduce the self-consistency condition for the host Green's functions

$$G^{\sigma}_{mm}(\tau = 0^-) = T \sum_{i\omega_n} e^{-i\omega_n 0^-} G^{\sigma}_{mm}(i\omega_n) = \langle n_{m\sigma} \rangle. \tag{A.36}$$

In Fig. A.2, we express these Feynman diagrams in terms of the Green's functions

at $T \neq 0$ as follows

$$iG^{\sigma}_{mm'} = iG^0_m \delta_{mm'} + iG^0_m(-iV_{m\nu})iG^{\sigma}_{\nu\nu'}(-iV_{\nu'm'})iG^0_{m'},$$

$$G^{\sigma}_{mm'} = G^0_m \delta_{mm'} + G^0_m \sum_{\nu,\nu'} V_{m\nu} G^{\sigma}_{\nu\nu'} V_{\nu'm'} G^0_{m'}. \tag{A.37}$$

At finite temperatures, we then have

$$G^{\sigma}_{mm}(i\omega_n) = G^0_m(i\omega_n) + G^0_m(i\omega_n) \left(\sum_{\nu,\nu'} V_{m\nu} G^{\sigma}_{\nu\nu'}(i\omega_n) V_{\nu'm} \right) G^0_m(i\omega_n)$$

$$= G^0_m(i\omega_n) \left[1 + \left(\sum_{\nu\nu'} V_{m\nu} G^{\sigma}_{\nu\nu'}(i\omega_n) V_{\nu'm} \right) G^0_m(i\omega_n) \right]. \tag{A.38}$$

Here, $G^0_m(i\omega_n)$ is defined by

$$G^0_m(i\omega_n) = \frac{1}{i\omega_n - (\varepsilon_m - \mu)} \tag{A.39}$$

and from Eq.(A.21)

$$G^{\sigma}_{\nu\nu'}(i\omega_n) = \sum_{\nu''} \left[\left(\tilde{Z}^{\sigma}(i\omega_n) \right)^{-1} \right]_{\nu\nu''} \delta_{\nu''\nu'} G^{0\sigma}_{\nu''}(i\omega_n)$$

$$= \left[\left(\tilde{Z}^{\sigma}(i\omega_n) \right)^{-1} \right]_{\nu\nu'} G^{0\sigma}_{\nu'}(i\omega_n) \tag{A.40}$$

The last equation is obtained by setting the total number of electrons N_{el},

$$N_{el} = \sum_{m\sigma} \langle c^{\dagger}_{m\sigma} c_{m\sigma} \rangle + \sum_{\nu\sigma} \langle d^{\dagger}_{\nu\sigma} d_{\nu\sigma} \rangle \tag{A.41}$$

In Eq.(A.41), $\langle n_{\nu\sigma} \rangle = \langle d^{\dagger}_{\nu\sigma} d_{\nu\sigma} \rangle$ is obtained from Eq.(A.33)

$$\langle d^{\dagger}_{\nu\sigma} d_{\nu\sigma} \rangle = T \sum_{i\omega_n} e^{-i\omega_n 0^-} G^{\sigma}_{\nu\nu}(i\omega_n) \tag{A.42}$$

and $\langle n_{m\sigma} \rangle = \langle c_{m\sigma}^\dagger c_{m\sigma} \rangle$ is obtained from

$$\langle c_{m\sigma}^\dagger c_{m\sigma} \rangle = T \sum_{i\omega_n} e^{-i\omega_n 0^-} G_{mm}^\sigma(i\omega_n) \tag{A.43}$$

which is given in Eq.(A.38) with $G_{\nu\nu'}^\sigma(i\omega_n)$ substituted from Eq.(A.27)

$$G_{mm}^\sigma(i\omega_n) = G_m^0(i\omega_n) \left[1 + \left(\sum_{\nu,\nu'} V_{m\nu} V_{\nu'm} \left[\left(\tilde{Z}^\sigma(i\omega_n) \right)^{-1} \right]_{\nu\nu'} G_{\nu'}^{0\sigma}(i\omega_n) \right) G_m^0(i\omega_n) \right] \tag{A.44}$$

Thus, here

$$G_{mm}^\sigma(i\omega_n) = G_m^0(i\omega_n) \left[1 + Y_m^\sigma(i\omega_n) G_m^0(i\omega_n) \right]. \tag{A.45}$$

where $Y_m^\sigma(i\omega_n)$ is defined as

$$Y_m^\sigma(i\omega_n) = \sum_{\nu,\nu'} V_{m\nu} V_{\nu'm} \left[\left(\tilde{Z}^\sigma(i\omega_n) \right)^{-1} \right]_{\nu\nu'} G_{\nu'}^{0\sigma}(i\omega_n). \tag{A.46}$$

Then, we can consider that the real part of $G_m^0(i\omega_n)$ is proportional to $\frac{1}{|\omega_n|}$. Hence, we define again

$$\langle n_{m\sigma} \rangle = T \sum_{n=-\infty}^{+\infty} e^{-i\omega_n 0^-} \left[G_{mm}^\sigma(i\omega_n) - G_m^0(i\omega_n) \right] + T \sum_{n=-\infty}^{+\infty} e^{-i\omega_n 0^-} G_m^0(i\omega_n), \tag{A.47}$$

$$\langle n_{m\sigma} \rangle \cong T \sum_{n=-n_{max}-1}^{n_{max}} \left[G_{mm}^\sigma(i\omega_n) - G_m^0(i\omega_n) \right] + T \sum_{n=-\infty}^{+\infty} e^{-i\omega_n 0^-} G_m^0(i\omega_n) \tag{A.48}$$

where the last term refers to Fermi distribution (f_m) for the host orbitals because of the

finite Green's function. Thus, this Fermi distribution is defined by

$$T \sum_{n=-\infty}^{+\infty} e^{-i\omega_n 0^-} G_m^0(i\omega_n) = f_m(\varepsilon_m - \mu)$$

$$= \frac{1}{e^{\beta(\varepsilon_m - \mu)} + 1}. \tag{A.49}$$

Then, we obtain that electron occupation number of host orbitals $\langle n_{m\sigma} \rangle$ is

$$\langle n_{m\sigma} \rangle \cong T \sum_{n=-n_{max}-1}^{n_{max}} \left[G_{mm}^\sigma(i\omega_n) - G_m^0(i\omega_n) \right] + f_m(\varepsilon_m - \mu). \tag{A.50}$$

Finally, the last equation, which is given the total number of electrons N_{el}, is obtained with $G_{mm}^\sigma(i\omega_n)$ substituted from Eq.(A.45)

$$N_{el} = \sum_{m\sigma} \left[T \sum_{n=-n_{max}-1}^{n_{max}} G_m^0(i\omega_n) \left[\left(1 + Y_m^\sigma(i\omega_n)G_m^0(i\omega_n) \right) - 1 \right] + f_m(\varepsilon_m - \mu) \right]$$

$$+ \sum_{\nu\sigma} \langle d_{\nu\sigma}^\dagger d_{\nu\sigma} \rangle. \tag{A.51}$$

Then, we obtain the total number of electrons N_{el}:

$$N_{el} = \sum_{m\sigma} \langle n_{m\sigma} \rangle + \sum_{\nu\sigma} \langle n_{\nu\sigma} \rangle. \tag{A.52}$$

A.4. DFT+QMC

The QMC calculations are performed by using the Hirsch-Fye QMC algorithm (Hirsch and Fye (1986)). In particular, we have calculated the single-particle impurity Green's functions is defined by

$$G_{\nu\sigma}(\tau) = -\langle T_\tau d_{\nu\sigma}(\tau) d_{\nu\sigma}^\dagger(0) \rangle \tag{A.53}$$

where T_τ is the usual Matsubara τ-ordering operator and $d_{\nu\sigma}(\tau) = e^{H\tau} d_{\nu\sigma} e^{-H\tau}$. Similarly, the host Green's function is defined by

$$G_{m\sigma}(\tau) = -\langle T_\tau c_{m\sigma}(\tau) c_{m\sigma}^\dagger(0) \rangle. \tag{A.54}$$

We calculate the electron occupation number of impurity orbitals by using

$$\langle n_d \rangle = \sum_{\nu=1}^{5} \sum_\sigma \langle d_{\nu\sigma}^\dagger d_{\nu\sigma} \rangle. \tag{A.55}$$

We also calculate the electron occupation number of host orbital which is defined by

$$\langle n_h \rangle = \sum_{m=1}^{N-5} \sum_\sigma \langle c_{m\sigma}^\dagger c_{m\sigma} \rangle. \tag{A.56}$$

In addition, we calculate the effective magnetic moments M_ν^{eff} defined as $M_\nu^{\mathrm{eff}} = \sqrt{\langle (M_\nu^z)^2 \rangle}$ and magnetic correlations $\langle M_\nu^z M_{\nu'}^z \rangle$ of impurity orbitals, where $M_\nu^z = d_{\nu\uparrow}^\dagger d_{\nu\uparrow} - d_{\nu\downarrow}^\dagger d_{\nu\downarrow}$. In order to understand the correlations around the transition metal atom, we calculate the equal-time magnetic correlations between the impurity orbitals and host states $\langle M_\nu^z M_m^z \rangle$, where $M_m^z = c_{m\uparrow}^\dagger c_{m\uparrow} - c_{m\downarrow}^\dagger c_{m\downarrow}$.

APPENDIX B

FINITE SIZE EFFECTS FOR DEOXY-HEME CLUSTERS

In Section 3.1, we showed the DFT results for the deoxy-heme which contains 75 atoms. In Fig. 3.2 the energy of the $m = 165$th host state is close to the LUMO level which is obtained by the DFT calculation. The $m = 165$th host state consists of the $2p_x$ and $2p_y$ orbitals of 23rd C and 24th O atoms in Fig. 3.3. This energy state badly affects the DFT+QMC results because it is very close to the Fermi level which is obtained by the DFT+QMC. This energy state gives rise to a change of the Fermi level in DFT+QMC results. In the DFT calculation, we will check whether the $m = 165$th host state is real or artificial. Therefore, we add 12 atoms and 21 atoms to deoxy-heme 75 atoms cluster from the proximal histidine part as seen in Fig. B.1 (a) and (b). We use larger clusters containing 87 and 96 atoms by adding some ligands from proximal histidine. We will show the DFT results for these clusters. Then, we will observe that the host state arising from the boundary moves away from the Fermi level to higher energies.

B.1. Deoxy-heme cluster for 87 atoms

Figure B.1 (a) shows the molecular structure of the 87 atoms deoxy-heme cluster. The chemical formula of this cluster is $C_{35}H_{36}FeN_{12}O_3$. In addition, the total electron numbers of this cluster is 380 electrons. The energy values and the frontier molecular orbitals (FMO's) compositions of the first two HOMO's and the first two LUMO's of deoxy-heme 87 atoms cluster are shown in Fig. B.2. We calculate these FMO's compositions with directly DFT calculation. These compositions are plotted by using GaussView software program (Dennington et al. (2008)). The red and green bubbles show the positive and negative electron surfaces, respectively. These surfaces are located in porphyrin layer of deoxy-heme 87 atoms cluster for HOMO's and LUMO's. In the HOMO-LUMO region, there are no electron transfers from the porphyrin layer to proximal and distal histidine parts of the deoxy-heme molecule.

In Fig. B.3, the square of the hybridization matrix elements $|V_{m\nu}|^2$ between the m'th host eigenstates and Fe($3d_\nu$) natural atomic orbitals are shown as a function of the m'th host eigenvalues ε_m for deoxy-heme. We observed that the host states $m = 175$th,
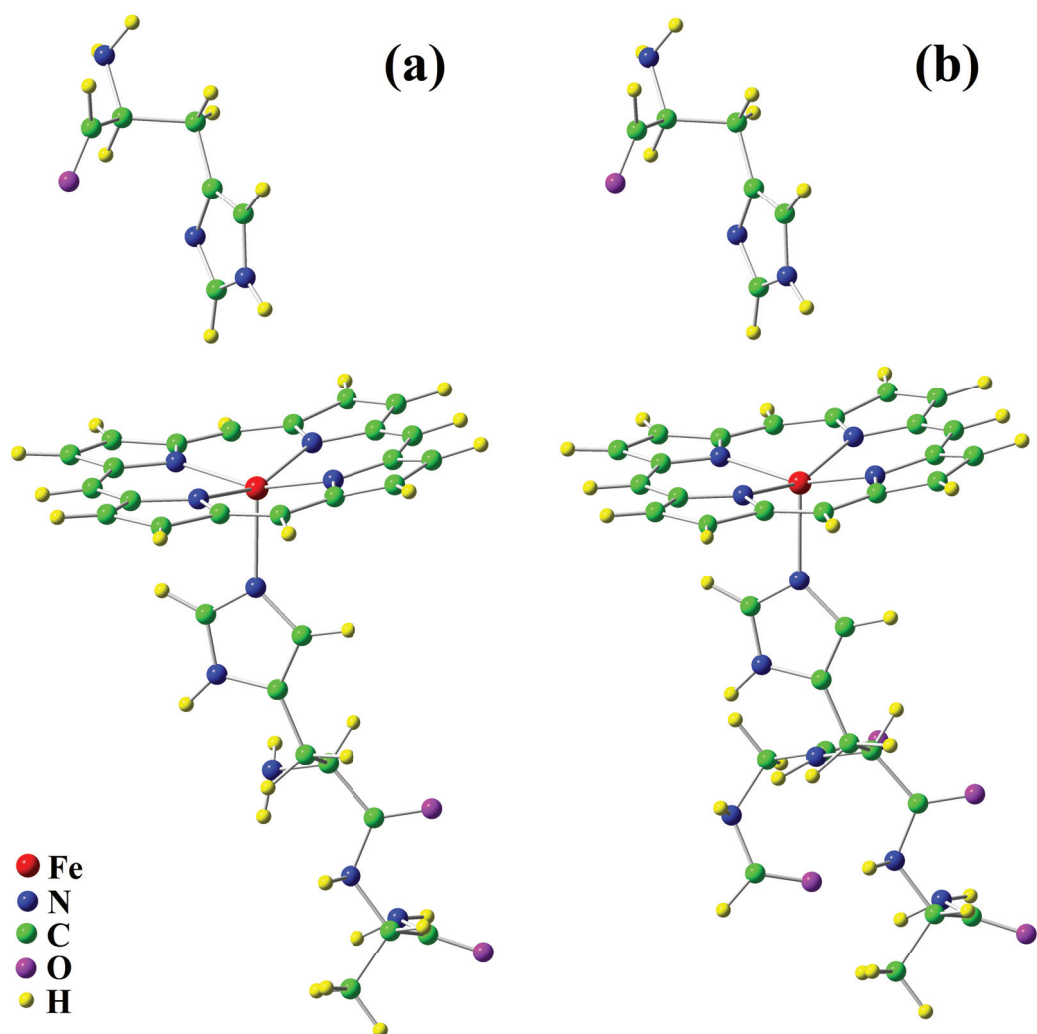
Figure B.1. Schematic plot of the molecular structure of the deoxy-heme (a) for 87 atoms cluster ($C_{35}H_{36}FeN_{12}O_3$) and (b) for 96 atoms cluster ($C_{38}H_{39}FeN_{13}O_5$).

and 165th have the highest hybridization matrix elements for $3d_{x^2-y^2}$ and $3d_{3z^2-r^2}$ orbitals. In Fig. B.3 (a), $3d_{3z^2-r^2}$ orbital has the noticeable hybridization contribution at $m = 163$rd, 167th, 176th and 186th host states. In Fig. B.3 (b), the hybridization of xz, yz and xy orbitals are relatively small compared to the hybridization of $x^2 - y^2$ and $3z^2 - r^2$ orbitals. The $m = 167$th and 168th host states have the hybridization with xz and yz orbitals, respectively. The hybridization contributions of $3d$ orbitals are very small for $m = 188$th, 189th and 190th host states in Fig. B.3.

The $m = 188$th, 189th and 190th host states are located above the LUMO level as shown in Fig. B.3. Host eigenstates (u_{mi}) contributions and eigenvalues (ε_m) of the $m = 188$th, 189th and 190th states for deoxy-heme 87 atoms cluster as shown in Fig. B.4. Here, the contributions of 23rd C and 24th O atoms go to the $m = 190$th host state. The energy value of the $m = 190$th host state is -1.62 eV. This state moves away from the LUMO (-2.89 eV) level. The $m = 188$th and $m = 189$th host states consist of $2p_z$ orbitals of C and N atoms in the porphyrin layer. In Fig. B.4, the electron densities which are located in the porphyrin layer have passed to the proximal histidine part of deoxy-heme molecule. The $m = 190$th host states consist of $2p$'s of of 23rd C, 24th O and 26th N atoms in the proximal histidine part of this molecule. The detailed compositions of these host states are shown in Fig. B.5. Here, we show the highest contributions with blue colors.

B.2. Deoxy-heme cluster for 96 atoms

Figure B.1 (b) shows the molecular structure of the 96 atoms deoxy-heme cluster. The chemical formula of this cluster is $C_{38}H_{39}FeN_{13}O_5$. In addition, the total electron numbers of this cluster is 424 electrons. The energy values and the frontier molecular orbital compositions of the first two HOMO's and the first two LUMO's of deoxy-heme 96 atoms cluster are shown in Fig. B.6. We calculate these FMO's compositions with directly DFT calculation. These compositions are plotted by using GaussView software program (Dennington et al. (2008)). The red and green bubbles show the positive and negative electron surfaces, respectively. In Fig. B.6, these surfaces are located in porphyrin layer of deoxy-heme 96 atoms cluster for HOMO's and LUMO's. In the HOMO-LUMO region, there are no electron transfers from the porphyrin layer to proximal and distal histidine parts of the deoxy-heme molecule.

In Fig. B.7, the square of the hybridization matrix elements $|V_{m\nu}|^2$ between the m'th host eigenstates and $Fe(3d_\nu)$ natural atomic orbitals are shown as a function of the

m'th host eigenvalues ε_m for deoxy-heme. We observed that the host states $m = 195$th, and 184th have the highest hybridization matrix elements for $3d_{x^2-y^2}$ and $3d_{3z^2-r^2}$ orbitals. In Fig. B.7 (a), $3d_{3z^2-r^2}$ orbital has the noticeable hybridization contribution at $m = 183$rd, 187th, 196th and 208th host states. In Fig. B.7 (b), the hybridization of xz, yz and xy orbitals are relatively small compared to the hybridization of $x^2 - y^2$ and $3z^2 - r^2$ orbitals. The $m = 187$th, 188th and 201st host states have the hybridization with xz and yz orbitals. The hybridization contributions of $3d$ orbitals are very small for $m =$210th, 211th and 212th host states in Fig. B.7.

The $m = 210$th, 211th, 212th and 217th host states are located above the LUMO level as shown in Fig. B.7. Host eigenstates (u_{mi}) contributions and eigenvalues (ε_m) of the $m = 210$th, 211th, 212th and 217th states for deoxy-heme 96 atoms cluster as shown in Fig. B.8. Here, the contributions of 23rd C and 24th O atoms go to the $m = 217$th host state. The energy value of the $m = 217$th host state is -1.25 eV. This state moves away from the LUMO (-3.08 eV) level. The $m = 210$th and 211th host states consist of $2p_z$ orbitals of C and N atoms in porphyrin layer. The electron densities which are located in porphyrin layer have passed to the proximal histidine part of deoxy-heme molecule. The $m = 212$th and 217th host states consist of $2p$'s of of C and N atoms in the proximal histidine part of this molecule. The $m = 212$th host state is composed of $2p$'s of 30th C and 31st O atoms. The detailed compositions of these host states are shown in Fig. B.9. Here, we show the highest contributions with blue colors.

HOMO−1   HOMO   LUMO   LUMO+1

Fe
N
C
O
H

$E_{\text{HOMO}-1} = -3.46$ eV $E_{\text{HOMO}} = -3.42$ eV $E_{\text{LUMO}} = -2.89$ eV $E_{\text{LUMO}+1} = -2.47$ eV
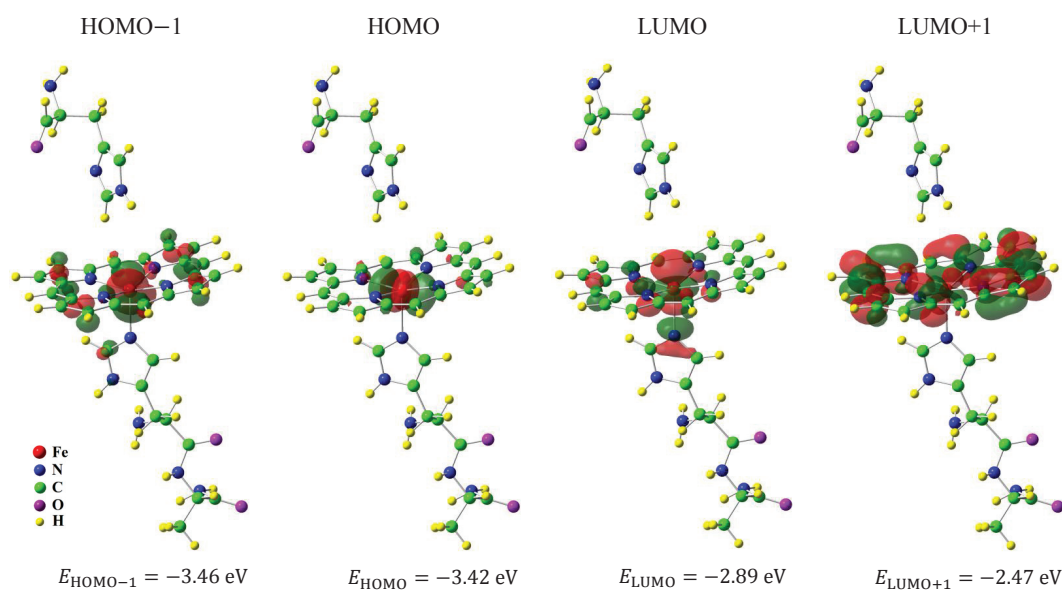
Figure B.2. Energy values and the frontier molecular orbital compositions of the first two HOMO's and LUMO's of deoxy-heme 87 atoms cluster. The red and green bubbles show the positive and negative contributions of the eigenstates, respectively.

Figure B.3. For deoxy-heme 87 atoms cluster, DFT(BP86/6-31G) results on the square of hybridization matrix elements $|V_{m\nu}|^2$ between the m'th host eigenstates and Fe($3d_\nu$) natural atomic orbitals as a function of the m'th host eigenvalues ε_m. In (a) results are shown for $3d_{x^2-y^2}$ and $3d_{3z^2-r^2}$ orbitals, and in (b) for $3d_{xz}$, $3d_{yz}$ and $3d_{xy}$ orbitals. Here, the vertical solid and dashes lines denote the values of the HOMO and LUMO, respectively. The HOMO and LUMO levels are obtained by the DFT method. We observe that the $m = 175$th host state has the highest hybridization matrix elements with $3d_{x^2-y^2}$ orbital.

$\varepsilon_{m=188} \approx -2.61$ eV $\qquad$ $\varepsilon_{m=189} \approx -2.48$ eV $\qquad$ $\varepsilon_{m=190} \approx -1.62$ eV
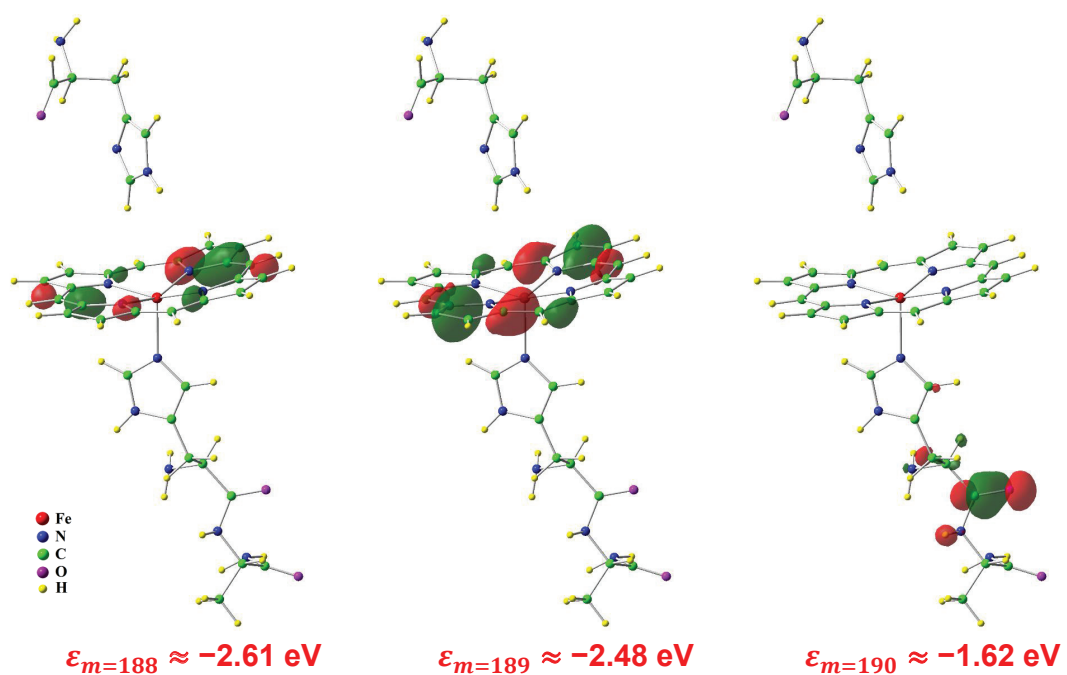
Figure B.4. For deoxy-heme 87 atoms cluster the DFT results on the host eigenstate (u_{mi}) contributions and eigenvalues (ε_m) of the $m = 188$th, 189th and 190th states. The red and green bubbles show the positive and negative contributions of the host eigenstates, respectively.

For m = 188th ε_m = -2.61 eV

i	host orbitals	$\|u_{mi}\|^2$
39	N 3(2pz)	0.052
57	N 5(2pz)	0.057
309	C33(2pz)	0.119
327	C35(2pz)	0.129
336	C36(2pz)	0.063
345	C37(2pz)	0.030
354	C38(2pz)	0.080
381	C41(2pz)	0.032
399	C43(2pz)	0.039
408	C44(2pz)	0.063
426	C46(2pz)	0.068
453	C49(2pz)	0.031
471	C51(2pz)	0.049
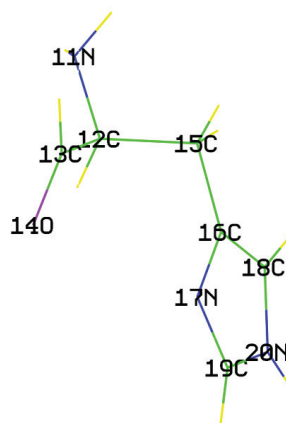
For m = 189th ε_m = -2.48 eV

i	host orbitals	$\|u_{mi}\|^2$
30	N 2(2pz)	0.058
48	N 4(2pz)	0.044
300	C32(2pz)	0.102
318	C34(2pz)	0.124
345	C37(2pz)	0.040
363	C39(2pz)	0.047
372	C40(2pz)	0.066
381	C41(2pz)	0.046
390	C42(2pz)	0.105
417	C45(2pz)	0.030
435	C47(2pz)	0.038
444	C48(2pz)	0.056
453	C49(2pz)	0.030
462	C50(2pz)	0.053
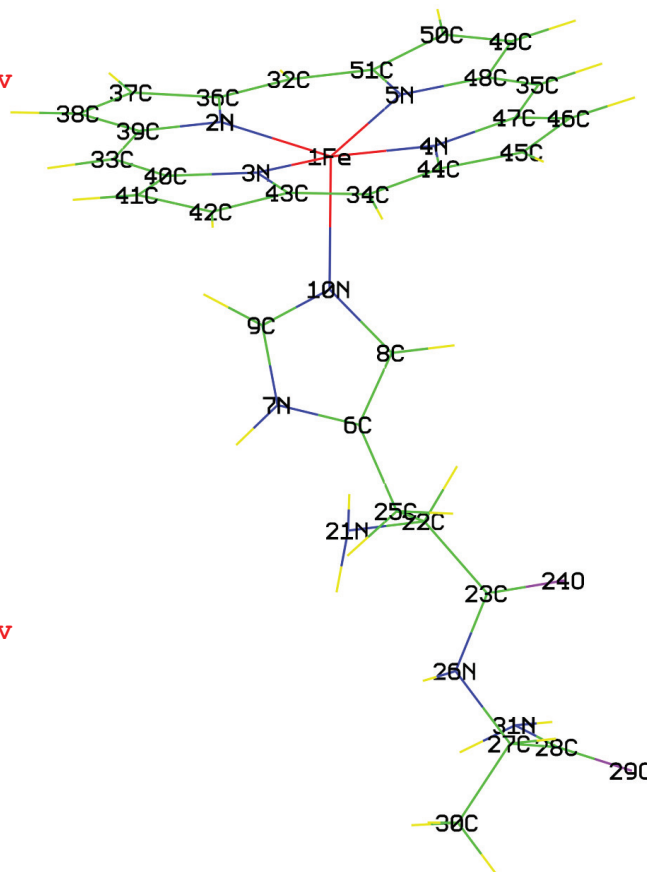
For m = 190th ε_m = -1.62 eV

i	host orbitals	$\|u_{mi}\|^2$
215	C23(2px)	0.327
217	C23(2py)	0.125
224	O24(2px)	0.177
226	O24(2py)	0.094
244	N26(2py)	0.056

Figure B.5. For deoxy-heme 87 atoms cluster, schematic plot with label numbers and symbols of atoms. The DFT results on the square of the host eigenstate ($|u_{mi}|^2$) contributions and eigenvalues (ε_m) of the m = 188th, 189th and 190th states. Here, we show the highest contributions with blue colors.

HOMO−1　　　　HOMO　　　　LUMO　　　　LUMO+1

$E_{\text{HOMO}-1} = -3.64$ eV　　$E_{\text{HOMO}} = -3.59$ eV　　$E_{\text{LUMO}} = -3.08$ eV　　$E_{\text{LUMO}+1} = -2.62$ eV

Figure B.6. Energy values and the frontier molecular orbital compositions of the first two HOMO's and LUMO's of deoxy-heme 96 atoms cluster. The red and green bubbles show the positive and negative contributions of the eigenstates, respectively.
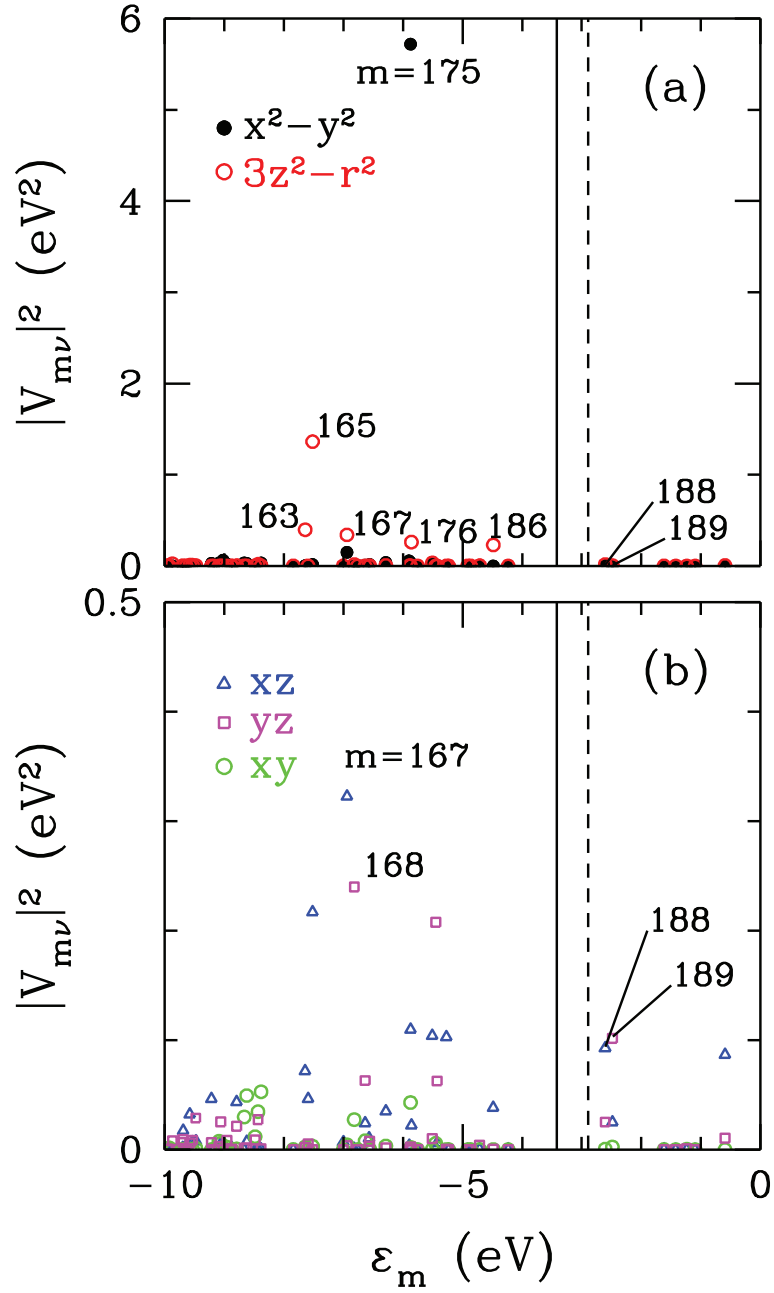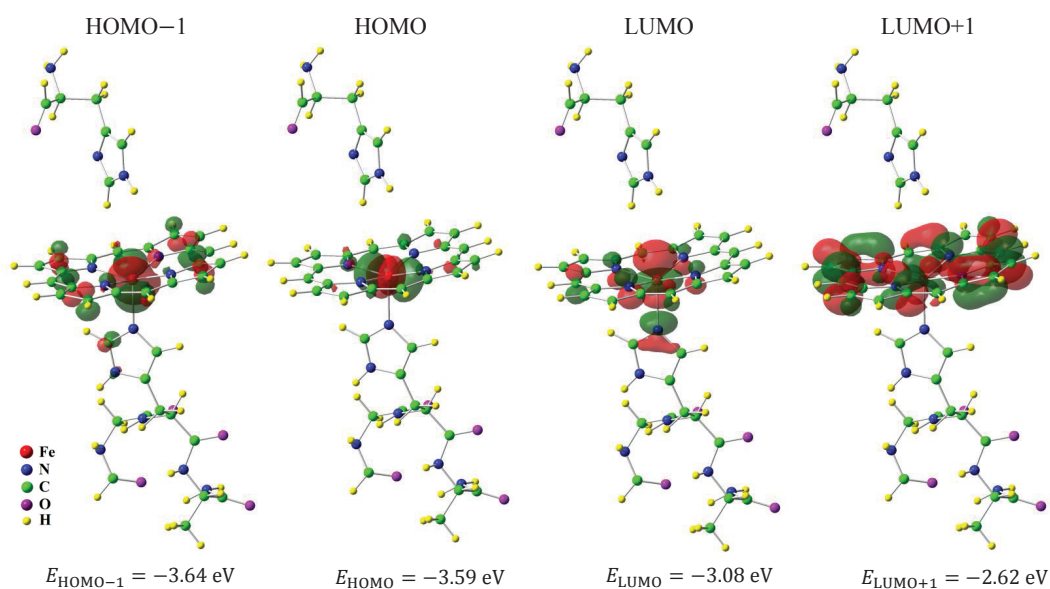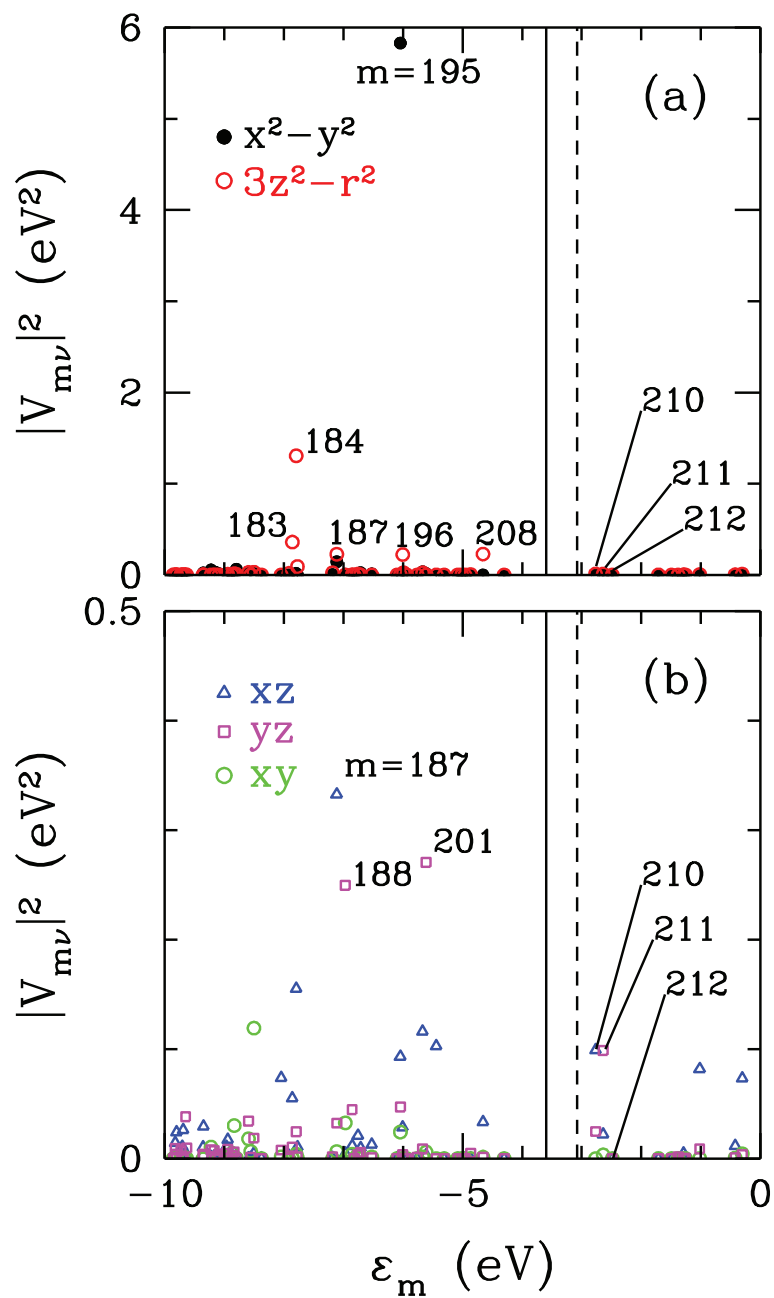
Figure B.7. For deoxy-heme 96 atoms cluster, DFT(BP86/6-31G) results on the square of hybridization matrix elements $|V_{m\nu}|^2$ between the m'th host eigenstates and Fe($3d_\nu$) natural atomic orbitals as a function of the m'th host eigenvalues ε_m. In (a) results are shown for $3d_{x^2-y^2}$ and $3d_{3z^2-r^2}$ orbitals, and in (b) for $3d_{xz}$, $3d_{yz}$ and $3d_{xy}$ orbitals. Here, the vertical solid and dashes lines denote the values of the HOMO and LUMO, respectively. The HOMO and LUMO levels are obtained by the DFT method. We observe that the $m = $ 195th host state has the highest hybridization matrix elements with $3d_{x^2-y^2}$ orbital.
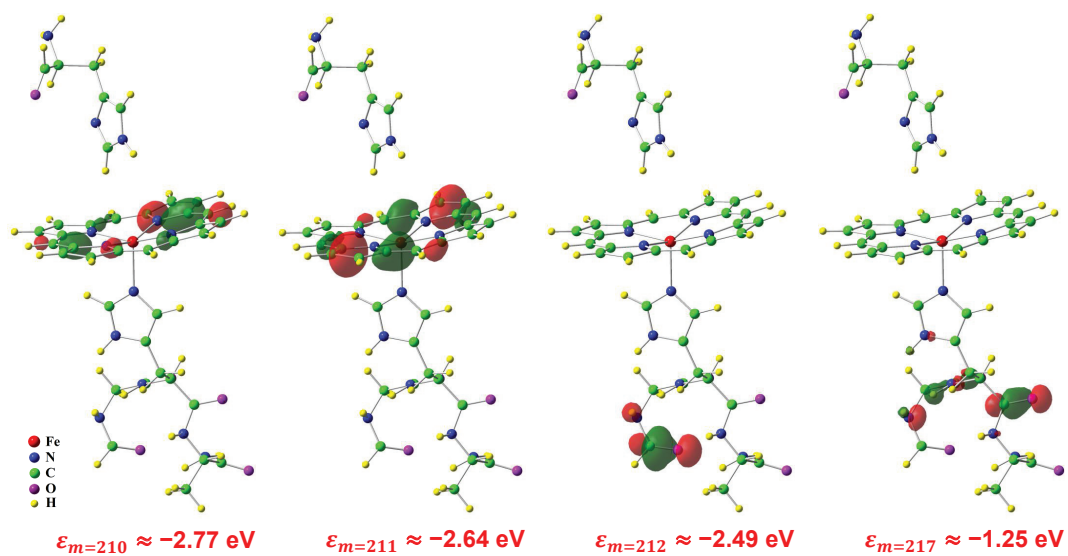
Figure B.8. For deoxy-heme 96 atoms cluster the DFT results on the host eigenstate (u_{mi}) contributions and eigenvalues (ε_m) of the $m = 210$th, 211th, 212th and 217th. The red and green bubbles show the positive and negative contributions of the host eigenstates, respectively.

```
For m = 210th          ε_m = -2.77 eV
   i   host orbitals     |u_mi|²
------------------------------
   39      N 3( 2pz)       0.052
   57      N 5( 2pz)       0.058
  363      C39( 2pz)       0.118
  381      C41( 2pz)       0.132
  390      C42( 2pz)       0.062
  399      C43( 2pz)       0.031
  408      C44( 2pz)       0.081
  435      C47( 2pz)       0.031
  453      C49( 2pz)       0.039
  462      C50( 2pz)       0.064
  480      C52( 2pz)       0.070
  507      C55( 2pz)       0.030
  525      C57( 2pz)       0.048
```
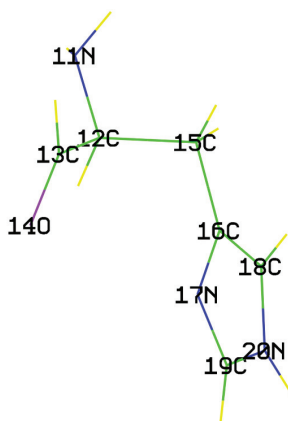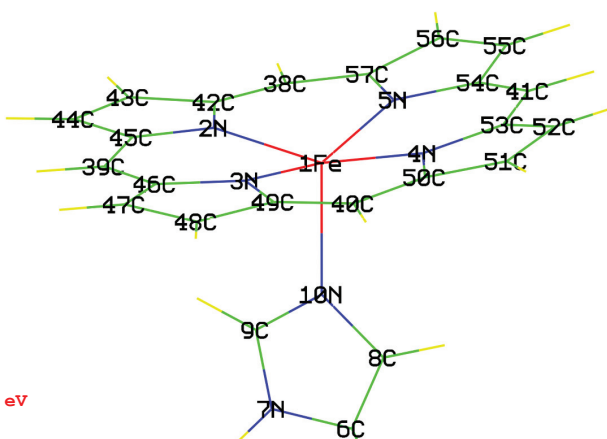
```
For m = 211th          ε_m = -2.64 eV
   i   host orbitals     |u_mi|²
------------------------------
   30      N 2( 2pz)       0.058
   48      N 4( 2pz)       0.046
  354      C38( 2pz)       0.097
  372      C40( 2pz)       0.126
  399      C43( 2pz)       0.038
  417      C45( 2pz)       0.045
  426      C46( 2pz)       0.066
  435      C47( 2pz)       0.047
  444      C48( 2pz)       0.105
  471      C51( 2pz)       0.032
  489      C53( 2pz)       0.040
  498      C54( 2pz)       0.057
  507      C55( 2pz)       0.030
  516      C56( 2pz)       0.054
```

```
For m = 212th          ε_m = -2.49 eV
   i   host orbitals     |u_mi|²
------------------------------
  278      C30( 2px)       0.195
  280      C30( 2py)       0.276
  282      C30( 2pz)       0.032
  287      O31( 2px)       0.092
  289      O31( 2py)       0.182
  298      N32( 2py)       0.062
```
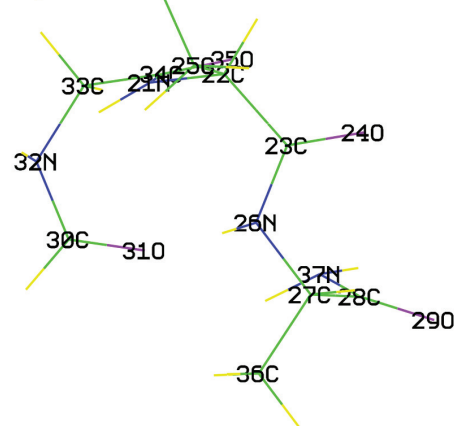
```
For m = 217th          ε_m = -1.26 eV
   i   host orbitals     |u_mi|²
------------------------------
  215      C23( 2px)       0.182
  217      C23( 2py)       0.082
  224      O24( 2px)       0.096
  226      O24( 2py)       0.058
  244      N26( 2py)       0.033
  296      N32( 2px)       0.021
  318      C34( 2pz)       0.041
  327      O35( 2pz)       0.030
```

Figure B.9. For deoxy-heme 96 atoms cluster, schematic plot with label numbers and symbols of atoms. The DFT results on the square of the host eigenstate ($|u_{mi}|^2$) contributions and eigenvalues (ε_m) of the $m = 210$th, 211th, 212th and 217th. Here, we show the highest contributions with blue colors.

VITA

Date and Place of Birth: 19.01.1988, İzmir-TURKEY

EDUCATION

2013 - 2019 Doctor of Philosophy in Department of Physics

Graduate School of Engineering and Sciences, İzmir Institute of Technology,
İzmir -Turkey
Thesis Title: Electronic Structure of Organic Molecules Containing Transition-Metal
Atoms
Supervisor: Prof. Dr. Nejat BULUT

2011 - 2013 Master of Science in Physics

Graduate School of Engineering and Sciences, İzmir Institute of Technology
İzmir -Turkey
Thesis Title: Mapping of the Electronic Structure of Metalloproteins onto
Multi-Orbital Anderson Model Using the Density Functional Theory
Supervisor: Prof. Dr. Nejat BULUT
Co-advisor: Prof. Dr. R. Tuğrul SENGER

SELECTED PUBLICATIONS

Kandemir, Z., Mayda, S., and Bulut, N.
(2016). "Electronic structure and correlations of vitamin B_{12} studied within
the Haldane-Anderson impurity model".
The European Physical Journal B, 89(5), 113.

Mayda, S., Kandemir, Z., and Bulut, N.
(2017). "Electronic structure of cyanocobalamin: DFT+QMC study".
Journal of Superconductivity and Novel Magnetism, 30(11), 3301–3308.

Mayda, S., Kandemir, Z., and Bulut, N.
(2018). "Future applications of artificially-synthesized organic molecules
containing transition-metal atoms".
Handbook of Nanomaterials for Industrial Applications, Elsevier, 386–391.